Johann V. Pototschnig

A theoretical study of metal containing diatomic molecules: Quantum chemical studies on selected systems featuring electric and magnetic dipole moments

DOCTORAL THESIS

to achieve the university degree of

Doktor der technischen Wissenschaften

submitted to

Graz University of Technology

Supervisor

Univ.-Prof. Dipl.-Phys. Dr.rer.nat. Wolfgang E. Ernst

Institute of Experimental Physics

Co-Supervisor
Mag.phil. Dipl.-Ing. Dr.phil. Dr.techn. Andreas W. Hauser

Graz, August 2016

AFFIDAVIT

I declare that I have authored this thesis independently, that I have not used other than the declared sources/resources, and that I have explicitly indicated all material which has been quoted either literally or by content from the sources used. The text document uploaded to TUGRAZonline is identical to the present doctoral thesis.

Date

Signature

Abstract

A theoretical study of metal containing diatomic molecules: Quantum chemical studies on selected systems featuring electric and magnetic dipole moments

Over the last decades quantum chemical calculations have become a valuable tool in understanding and predicting the behavior of molecules. In this work, computations for several metal containing molecules were performed which are relevant in current experiments of our group. Several *ab initio* methods have been used in the course of the work, for example multiconfigurational self-consistent field, multireference configuration interaction, and coupled cluster calculations. This study focuses on diatomic heteronuclear molecules, which have a permanent electric dipole moment of varying strength in their ground state. All molecules treated in this thesis have an open shell with a related magnetic dipole moment resulting from the unpaired spins of the valence electrons.

The chromium atom has one of the largest magnetic moment of all known elements. In a benchmark study we investigated how the electronic structure of this atom is influenced by a weakly interacting noble gas, the helium atom. To this end, several electronic states in different multiplicities were computed.

The main part of this thesis was concerned with the investigation of alkali-alkaline earth molecules (AK-AKE). In an earlier work it was shown that LiCa can be analyzed reliably by a combination of *ab initio* calculations and helium nanondroplet isolation spectroscopy. Two other molecules of this group were investigated in detail, RbSr and RbCa. Our theoretical results could be used to simulate spectra, which were then compared to experimental data of our group. Additionally, we studied the lowest doublet and quartet Σ^+ state for 16 AK-AKE molecules. Properties of the bonds and dipole moments were determined for the whole group and compared to each other.

Kurzfassung

Theoretische Untersuchungen an metallischen zweiatomigen Molekülen: Eine quantenchemische Betrachtung ausgewählter Systeme mit elektrischem und magnetischem Dipolmoment

In den letzten Jahrzehnten haben sich quantenchemische Berechnungen als ein wertvolles Instrument etabliert, das es uns erlaubt, das Verhalten von Molekülen zu verstehen und vorherzusagen. In dieser Arbeit wurden Berechnungen für eine Auswahl von Moleküle durchgeführt, die für die Experimente in unserer Gruppe relevant sind. Im Laufe der Arbeit wurden einige *ab initio* Methoden verwendet, wie zum Beispiel Multiconfigurational Self-Consistent Field, Multireference Configuration Interaction oder Coupled Cluster Berechnungen. Diese Studie beschränkt sich auf zweiatomige heteronukleare Moleküle, welche ein permanentes elektrisches Dipolmoment von variierender Stärke im Grundzustand haben. Alle betrachteten Moleküle zeichnen sich außerdem durch eine offene Schale mit einem dazugehörigen magnetischen Dipolmoment aus, das durch die ungepaarten Spins der Valenzelektronen verursacht wird.

Das Chromatom besitzt eines der größten magnetischen Momente aller Elemente. In der vorliegenden Arbeit wurde untersucht, wie sich die elektronische Struktur dieses Atoms durch ein schwach wechselwirkendes Edelgas, ein Heliumatom, verändert. Dazu wurden mehrere elektronische Zustände in unterschiedlichen Multiplizitäten berechnet.

Der größte Teil dieser Arbeit beschäftigt sich jedoch mit der Untersuchung von Alkali-Erdalkali Molekülen (AK-AKE). In einer früheren Arbeit wurde gezeigt, dass LiCa mit einer Kombination von *ab initio* Berechnungen und Helium Nanotröpfchen Matrix Isolations Spektroskopie zuverlässig beschrieben werden kann. Zwei weitere Moleküle aus dieser Gruppe, RbSr und RbCa, wurden im Detail untersucht. Die Resultate dieser Arbeit wurden zur Simulation molekularer Spektren verwendet, die darauf mit experimentellen Daten unserer Gruppe verglichen wurde. Des Weiteren wurden die niedrigsten Σ^+ Zustände der Dublett und Quartett Mutliplizität von 16 AK-AKE Molekülen untersucht. Bindungseigenschaften und Dipolmomente wurden für die ganze Gruppe bestimmt und miteinander verglichen.

Words bend our thinking to infinite paths of self-delusion, and the fact that we spend most of our mental lives in brain mansions built of words means that we lack the objectivity necessary to see the terrible distortion of reality which language brings.

Dan Simmons, Hyperion

Articles related to this work

[1] Spectroscopy of Lithium Atoms and Molecules on Helium Nanodroplets
by Florian Lackner, Johannes Poms, Günter Krois, Johann V. Pototschnig, and Wolfgang E. Ernst
Journal of Physical Chemistry A, **2013**, *117*, 11866

[2] Spectroscopy of Cold LiCa Molecules Formed on Helium Nanodroplets
by Günter Krois, Johann V. Pototschnig, Florian Lackner, and Wolfgang E. Ernst
Journal of Physical Chemistry A, **2013**, *117*, 13719

[3] An ab initio study of the CrHe diatomic molecule: The effect of van der Waals distortion on a highly magnetic multi-electron system
by Johann V. Pototschnig, Martin Ratschek, Andreas W. Hauser, and Wolfgang E. Ernst
Physical Chemistry Chemical Physics, **2014**, *16*, 9469

[4] Solvation and Spectral Line Shifts of Chromium Atoms in Helium Droplets Based on a Density Functional Theory Approach
by Martin Ratschek, Johann V. Pototschnig, Andreas W. Hauser, and Wolfgang E. Ernst
Journal of Physical Chemistry A, **2014**, *118*, 6622

[5] Helium Nanodroplet Assisted Preparation of Cold RbSr Molecules
by Florian Lackner, Günter Krois, Thomas Buchsteiner, Johann V. Pototschnig, and Wolfgang E. Ernst
Physical Review Letters, **2014**, *113*, 153001

[6] Characterization of RbSr molecules: spectral analysis on helium droplets
by Günter Krois, Florian Lackner, Johann V. Pototschnig, Thomas Buchsteiner, and Wolfgang E. Ernst
Physical Chemistry Chemical Physics, **2014**, *16*, 22373

[7] Ab initio study of the RbSr electronic structure: Potential energy surfaces, transition dipole moments and permanent electric dipole moments
by Johann V. Pototschnig, Günter Krois, Florian Lackner, and Wolfgang E. Ernst
Journal of Chemical Physics, **2014**, *141*, 234309

[8] Investigation of the RbCa molecule: Experiment and theory
by Johann V. Pototschnig, Günter Krois, Florian Lackner, and Wolfgang E. Ernst
Journal of Molecular Spectroscopy, **2015**, *310*, 126

[9] A classic case of Jahn-Teller effect theory revisited: Ab initio simulation of hyperfine coupling and pseudorotational tunneling in the $1^2E'$ state of Na_3
by Andreas W. Hauser, Johann V. Pototschnig, and Wolfgang E. Ernst
Chemical Physics, **2015**, *460*, 2

[10] Electric dipole moments and chemical bonding of diatomic alkali - alkaline earth molecules
by Johann V. Pototschnig, Andreas W. Hauser, and Wolfgang E. Ernst
Physical Chemistry Chemical Physics, **2016**, *18*, 5964

Note: The articles [3], [7], [8], and [10] are reprinted as part of this work and correspond to the chapters 2, 3, 4, and 5 respectively.

Contents

Abbreviations

AK	alkali atom
AKE	alkaline earth atom
ANO	atomic natural orbitals
Å	Ångström
aug	augmented
BSSE	basis set superposition error
CASSCF	complete active space self-consistent field calculation
CC	coupled cluster calculation
cc	correlation consistent
CCSD(T)	CC calculation with determinants produced by single and double excitations, most significant triple excitations added perturbatively
CI	configuration interaction calculation
CP	counterpoise correction
CSF	configuration state function
DFT	density functional theory
EMSL database	Environmental Molecular Science Laboratory database [11, 12]
EOM-CC	equation of motion coupled cluster
EPR	electron paramagnetic resonance
ESR	electron spin resonance
GTO	gauss type orbitals
He_N	helium-cluster consisting of N atoms
HF	Hartree Fock method
MBPT	many-body perturbation theory
MCSCF	multiconfigurational self-consistent field calculation
MD	molecular dynamics
MRCC	multireference coupled cluster calculation
MRCI	multireference configuration interaction calculation
(MRCI/CC)S	method with determinants produced by single excitations
(MRCI/CC)SD	method with determinants produced by single and double excitations
NIST	National Institute of Standards and Technology [13]
Nr.	number
PEC	potential energy curve
PEDM	permanent electric dipole moment
PES	potential energy surface

RHF	restricted Hartree-Fock calculation
ROHF	restricted open shell Hartree-Fock calculation
RS	Rayleigh - Schrödinger perturbation theory
SCF	self-consistent field calculation
STO	slater type orbitals
TDM	transition dipole moment
UHF	unrestricted Hartree-Fock calculation
ZPE	zero point energy

Chapter 1

Introduction

1.1 Motivation

This work was initiated by the demand for theoretical support of measurements performed in our group. In these measurements, atoms and small molecules were put on superfluid helium nanodroplets and investigated by multiphoton laser ionization and laser induced fluorescence. In the course of this work we simplified or neglected the interaction with the helium environment and computed properties for a selection of experimentally relevant diatomic open shell molecules. These molecules with one or more unpaired electrons in the ground state have a magnetic dipole moment which can be used to manipulate them. In a previous experiment single alkali atoms were put on superfluid helium nanodroplets and analyzed by optically detected magnetic resonances[14, 15]. A follow-up project was dedicated to the study of atomic chromium which has one of the largest magnetic moments of all elements. Its six unpaired electrons in the $^7\Sigma^+$ ground state result in a magnetic moment of $6\,\mu_B$. Chromium is the first atom for which the aufbau principle fails (occupation of [Ar] $3d^5\,4s^1$) due to the energetic proximity of the s- and d-orbitals. The experimental investigation was carried out by Andreas Kautsch[16–19]. In order to understand the experimental results for chromium on helium nanodroplets we started with a benchmark study of the interaction of a single Cr atom with a single He atom (chapter 2, [20]). Several excited states with differing multiplicity have been determined for this molecule. In a further analysis, performed by my colleague Martin Ratschek, the diatomic interaction was used to predict the behavior of chromium on superfluid nanodroplets[4, 21].

Later chapters of this work are concerned with the investigation of alkali-alkaline earth (AK-AKE) molecules. The alkali atom contributes one valence electron, the alkaline earth atom two. As a consequence, the resulting molecules possess a magnetic moment due to the remaining open shell. Additionally, these heteronuclear molecules have a permanent electric dipole moment of varying strength. This combination of magnetic and electric moment makes these molecules interesting for future experiments (see section 1.1.2). Experiments on these molecules were performed by Florian Lackner and Günter Krois[22, 23]. Initially, we studied the LiCa molecule[2]. This molecule was the benchmark for our approach since it had already been studied in the gas phase[24, 25]. The second molecule under investigation was RbSr, which shows promise for applications in ultracold molecular physics[26]. Multiphoton laser ionization spectra and laser induced fluorescence spectra were obtained by helium nanodroplet isolation spectroscopy and compared to computations[5–7]. RbCa was the third molecule studied in detail by experiment and theory[8], with no previous theoretical or experimental data available for excited states. Here we extended our theoretical investigation towards a whole series of AK-AKE molecules with the aim to understand and model trends in their properties. We were particularly interested in the permanent electric dipole moment and its behavior for the whole group. A simple empirical model was derived for this property and applied to a selection of molecules not treated in our ab initio computations.

1.1.1 Structure of the thesis

This thesis consists of a general introduction and four chapters that correspond to different publications.

- In chapter 1 we shortly summarize the applied methods and introduce denominations commonly used for diatomic molecules.
- Chapter 2 contains the results for CrHe with a short discussion of the relation to the experiment.
- Several electronic states for RbSr are presented in chapter 3 including spin-orbit interaction. These results are then used to understand laser induced fluorescence measurements of our group.
- A combined theoretical and experimental analysis of the RbCa molecule is given in chapter 4.
- Chapter 5 compares the potential energy curves and a selection of other properties in the lowest Σ^+ states of 16 AK-AKE molecules.

1.1.2 Ultracold molecules

Molecules with a temperature below 1 mK are considered "ultracold". A selection of recent reviews discussing the production and applications of these molecules is given in refs. 27–33. Ultracold molecules can either be produced directly by cooling or indirectly by the formation of molecules from ultracold atoms. There are several strategies for the direct cooling of molecules[31], as for example the deceleration of molecular beams, buffer gas cooling, and laser cooling[34, 35]. However, it is more challenging to cool molecules than atoms due to the additional degrees of freedom stemming from vibrations and rotations. The indirect production is achieved by the controlled formation of molecules from ultracold atoms. Common methods for this production are photoassociation, magnetoassociation (Feshbach resonances[36, 37]), coherent population transfer (for example stimulated adiabatic Raman passage – STIRAP) and combinations of these methods[28, 38–41].

The first molecules in the ultracold temperature regime were homonuclear alkali dimers, specifically Cs_2[42–45], K_2[46], and Rb_2[47]. Recently, an ultracold alkaline earth dimer, Sr_2[48], has been produced. These diatomic molecules have neither a permanent electric dipole moment nor a magnetic dipole moment. The requirement of a permanent electric dipole moment for certain applications[32] made the production of heteronuclear alkali molecules a logical consequence. Among the first ultracold polar molecules are KRb[49–53], RbCs[54–56], NaCs[57], and LiCs[58].

The next step is the production of ultracold molecules with a permanent electric dipole moment and a magnetic moment originating in an unpaired spin. Candidates for cooling to ultracold temperatures can roughly be separated in two groups corresponding to their proposed production. The first group, consisting of AKE halides or Yb halides, might be cooled down to ultracold temperatures by laser cooling or deceleration in magnetic or electric fields[59, 59]. The second group, AK-AKE and AK-Yb molecules, might be formed from precooled atoms in magneto-optical traps. These atoms are good candidates for this approach, because they can be trapped and cooled efficiently. For example, Bose-Einstein condensation was already achieved for alkali atoms [60–62], alkaline earth atoms[63, 64], ytterbium[65] and chromium[66, 67]. One step along the formation of ultracold molecules are combined traps for two quantum degenerate atomic gases which has been realized for RbSr[26] and LiYb[68–70].

Ultracold molecules are interesting because decoherence of the systems under investigation is reduced, which leads to an increased importance of quantum mechanical effects. On the other hand, the cold temperatures reduce the noise and allow for precise measurements and enhanced control in experiments. The quantum nature of ultracold ensembles can be used simulate quantum mechanical systems and quantum phase transitions with polar molecules[33, 71–78]. The additional magnetic moment of AK-AKE molecules would enable the realization of more complex systems[79]. Another possible future application is quantum computing[80], maybe using molecules captured on computer chips[81–84]. At cold and ultracold temperatures, only very few states are thermally populated, which enables precise control of chemical reactions starting from one or a few initial states[85–87]. The reduced noise in this temperature regime can also be used to increase the precision of measurements of fundamental physical properties[88]. One example is the measurement of the proton to electron mass ration and it variation with time[89–92]. Also, the invariance of the fine structure constant might be tested[93, 94]. Ultracold polar molecules without[95, 96] or with a magnetic[97, 98] moment have been suggested for high accuracy measurements of the electron electric dipole moment. This is of interest because certain extensions of the standard model predict a higher value of this property than the standard model[99, 100]. Finally, also the investigation of the anapole moment or fundamental symmetries have been discussed in the context of ultracold molecules[101, 102].

1.2 Diatomic molecules

This work is mainly concerned with diatomic molecules. Therefore, a short introduction in common concepts and notations is given here. The Hamiltonian of a system consisting of atoms A and B and N_{el} electrons can be written (in atomic units) as:

$$\widehat{H} = -\sum_{i=1}^{N_e} \frac{1}{2}\nabla_i^2 - \frac{1}{2M_A}\nabla_A^2 - \frac{1}{2M_B}\nabla_B^2 \\ + \sum_{i,j=1;i<j}^{N_e} \frac{1}{\left|\vec{r}_i - \vec{r}_j\right|^2} - \sum_{i=1}^{N_e} \left(\frac{Z_A}{\left|\vec{R}_A - \vec{r}_i\right|^2} + \frac{Z_B}{\left|\vec{R}_B - \vec{r}_i\right|^2} \right) + \frac{Z_A Z_B}{\left|\vec{R}_A - \vec{R}_B\right|^2} \tag{1.1}$$

R_I and r_i are the coordinates of the atomic cores and electrons, respectively. The masses of the atomic cores are given by M_I, their charges by Z_I. The Hamiltonian consists of following contributions:

$$\widehat{T}_e(\mathbf{r}) = -\sum_{i=1}^{N_e} \frac{1}{2}\nabla_i^2, \tag{1.2}$$

the kinetic energy of the electrons,

$$\widehat{T}_N(\mathbf{R}) = -\frac{1}{2M_A}\nabla_A^2 - \frac{1}{2M_B}\nabla_B^2 \tag{1.3}$$

the kinetic energy of the nuclei,

$$\widehat{V}_{ee}(\mathbf{r}) = \sum_{i,j=1;i<j}^{N_e} \frac{1}{\left|\vec{r}_i - \vec{r}_j\right|^2} \tag{1.4}$$

the energy of the interaction of electrons,

$$\widehat{V}_{NN}(\mathbf{R}) = \frac{Z_A Z_B}{\left|\vec{R}_A - \vec{R}_B\right|^2} \tag{1.5}$$

the energy of the interaction of nuclei, and

$$\widehat{V}_{Ne}(\mathbf{r},\mathbf{R}) = -\sum_{i=1}^{N_e} \left(\frac{Z_A}{\left|\vec{R}_A - \vec{r}_i\right|^2} + \frac{Z_B}{\left|\vec{R}_B - \vec{r}_i\right|^2} \right), \tag{1.6}$$

the energy of the interaction between electrons and nuclei.

The whole system is described by its wave function Ψ which can be determined by solving the time-independent Schrödinger equation ($\widehat{H}\Psi = E\Psi$). Typically, a separation of variables is applied to obtain solutions of this equation. With this approach the problem can be split into two parts. The first part is given by the electronic Schrödinger equation for a fixed set of nuclear coordinates,

$$\left(\widehat{T}_e(\mathbf{r}) + \widehat{V}_{ee}(\mathbf{r}) + \widehat{V}_{Ne}(\mathbf{r},\mathbf{R}) + \widehat{V}_{NN}(\mathbf{R})\right)\psi_n(\mathbf{r},\mathbf{R}) = E_n(\mathbf{R})\,\psi_n(\mathbf{r},\mathbf{R}), \tag{1.7}$$

with $\psi_n(\mathbf{r},\mathbf{R})$ denoting the electronic wave function. The corresponding energy eigenvalue $E_n(\mathbf{R})$ for the electronic state n can be determined for different positions of the nuclei, which yields the so called potential energy surface (PES). In the case of diatomic molecules there is only one significant intermolecular coordinate, the separation of the nuclei. Therefore, the potential energy surface is reduced to a potential energy curve (PEC). The determination and description of PECs is outlined in section 1.3. The term $\widehat{V}_{NN}$ is only a constant for fixed nuclear coordinates and shifts the energy eigenvalues. The total wave function can then be expanded in the basis of electronic excitations with expansion coefficients dependent on the nuclear coordinates:

$$\Psi_{tot} = \sum_n \Psi_n\left(\mathbf{R}\right) \cdot \psi_n\left(\mathbf{r},\mathbf{R}\right). \tag{1.8}$$

This wave function allows to calculate properties of the diatomic molecules (e.g. vibronic transition probabilities) which is described in section 1.4. Using this expression together with the abbreviations given by equations 1.2 to 1.6 we can write the Schrödinger equation for the total system as:

$$\left(\widehat{T}_N\left(\mathbf{R}\right) + \widehat{T}_e\left(\mathbf{r}\right) + \widehat{V}_{ee}\left(\mathbf{r}\right) + \widehat{V}_{Ne}\left(\mathbf{r},\mathbf{R}\right) + \widehat{V}_{NN}\left(\mathbf{R}\right) - E\right) \sum_n \Psi_n\left(\mathbf{R}\right) \cdot \psi_n\left(\mathbf{r},\mathbf{R}\right) = 0 \tag{1.9}$$

Using equation 1.7 this becomes:

$$\sum_n \left(\widehat{T}_N\left(\mathbf{R}\right) + E_n\left(\mathbf{R}\right) - E\right) \Psi_n\left(\mathbf{R}\right) \cdot \psi_n\left(\mathbf{r},\mathbf{R}\right) = 0 \tag{1.10}$$

We multiply this equation by ψ_m and integrate over all electron coordinates to obtain:

$$\sum_n \int \mathrm{d}\mathbf{r}\, \psi_m\left(\mathbf{r},\mathbf{R}\right) \left(\widehat{T}_N\left(\mathbf{R}\right) + E_n\left(\mathbf{R}\right) - E\right) \Psi_n\left(\mathbf{R}\right) \cdot \psi_n\left(\mathbf{r},\mathbf{R}\right) = 0 \tag{1.11}$$

Applying the orthogonality of the electronic wave functions ($\int \mathrm{d}\mathbf{r}\, \psi_m\left(\mathbf{r},\mathbf{R}\right) \psi_n\left(\mathbf{r},\mathbf{R}\right) = \delta_{mn}$) following expression is obtained:

$$\sum_n \left(\int \mathrm{d}\mathbf{r}\, \psi_m\left(\mathbf{r},\mathbf{R}\right) \widehat{T}_N\left(\mathbf{R}\right) \psi_n\left(\mathbf{r},\mathbf{R}\right) + \left(E_n\left(\mathbf{R}\right) - E\right) \delta_{mn}\right) \Psi_n\left(\mathbf{R}\right) = 0 \tag{1.12}$$

The nuclear kinetic energy operator yields the following expression if it is applied to the total wave function:

$$\int \mathrm{d}\mathbf{r}\, \psi_m^*\left(\mathbf{r},\mathbf{R}\right) \widehat{T}_N\left(\mathbf{R}\right) \psi_n\left(\mathbf{r},\mathbf{R}\right) \Psi_n\left(\mathbf{R}\right) = -\sum_I \frac{1}{2M_I} \left(\int \mathrm{d}\mathbf{r}\, \psi_m^*\left(\mathbf{r},\mathbf{R}\right) \frac{\partial^2 \psi_n\left(\mathbf{r},\mathbf{R}\right)}{\partial R_I^2} \Psi_n\left(\mathbf{R}\right) \right.$$
$$\left. + \int \mathrm{d}\mathbf{r}\, \psi_m^*\left(\mathbf{r},\mathbf{R}\right) \frac{\partial \psi_n\left(\mathbf{r},\mathbf{R}\right)}{\partial R_I} \frac{\partial \Psi_n\left(\mathbf{R}\right)}{\partial R_I} + \frac{\partial^2 \Psi_n\left(\mathbf{R}\right)}{\partial R_I^2} \delta_{mn}\right) \tag{1.13}$$

The third term on the right hand side of this equation is simply the nuclear kinetic energy operator applied to the nuclear wave function. The other two expressions contain derivatives of the electronic wave function with respect to the nuclear coordinates. Using this, equation 1.12 can be rewritten as:

$$\left(\widehat{T}_N(\mathbf{R}) + E_m(\mathbf{R}) - E\right)\Psi_m(\mathbf{R}) \\ -\sum_n \underbrace{\sum_I \frac{1}{2M_I}\int \mathrm{d}\mathbf{r}\,\psi_m^*(\mathbf{r},\mathbf{R})\left(\frac{\partial^2\psi_n(\mathbf{r},\mathbf{R})}{\partial R_I^2} + \frac{\partial\psi_n(\mathbf{r},\mathbf{R})}{\partial R_I}\frac{\partial}{\partial R_I}\right)}_{\Lambda_{mn}}\Psi_n(\mathbf{R}) = 0 \tag{1.14}$$

In this expression different electronic states are coupled to each other by the non-adiabatic coupling terms (Λ_{mn}). In most cases these terms are small, especially if the energies of the corresponding electronic states are significantly different for the relevant nuclear configurations. In this cases the Born-Oppenheimer or adiabatic approximation is applied and the coupling terms are neglected, which leads to following equation:

$$\left(\widehat{T}_N(\mathbf{R}) + E_m(\mathbf{R}) - E\right)\Psi_m(\mathbf{R}) = 0 \tag{1.15}$$

The Born-Oppenheimer approximation fails in the case of crossing (e. g. conical intersections) or nearly crossing potential energy surfaces (e. g. avoided crossing). An example for avoided crossings is plotted in figure 1.1, which contains a selection of electronically excited states of RbCa with the same symmetry and spin. In figure 1.1 there is an avoided crossing close to 10 Å for the $5^2\Pi$ and $6^2\Pi$ states and at about 11 Å for the $6^2\Pi$ and $7^2\Pi$ states. The PECs approach each other energetically at first but are repelled eventually. Related to this, a change of the permanent electric dipole moment (PEDM) can be observed, which is depicted in the last row of the figure. It is also obvious that the transition dipole moment is influenced by avoided crossings.

Within the Born-Oppenheimer approximation the PECs are continuous and do not cross, see figure 1.1. However, in regions of close lying electronic states the adiabatic approximation is no longer valid. With it also the concept of potential energy curves is lost, especially in the case of crossings or avoided crossings. A good discussion of non-adiabatic effects and their treatment in diatomic molecules can be found in the book by Lefebvre-Brion and Field[103]. In larger systems conical intersections become relevant which are treated in detail in ref. 104.

1.2.1 Hund's cases

For higher accuracy, the description of diatomic molecules needs to be extended by angular momentum coupling effects. The relevant physical quantities are listed in table 1.1.

For the complete system only the total energy, the parity and the total angular momentum ($\vec{F}$ in table 1.1) are good quantum numbers, i. e. conserved quantities. The relative magnitude of the contributions depends on the involved atoms, the bonding and the actual rovibronic state. The nuclear spin $\vec{I}$ only contributes a small magnetic dipole moment and can often be neglected. Other hyperfine interactions, such as the

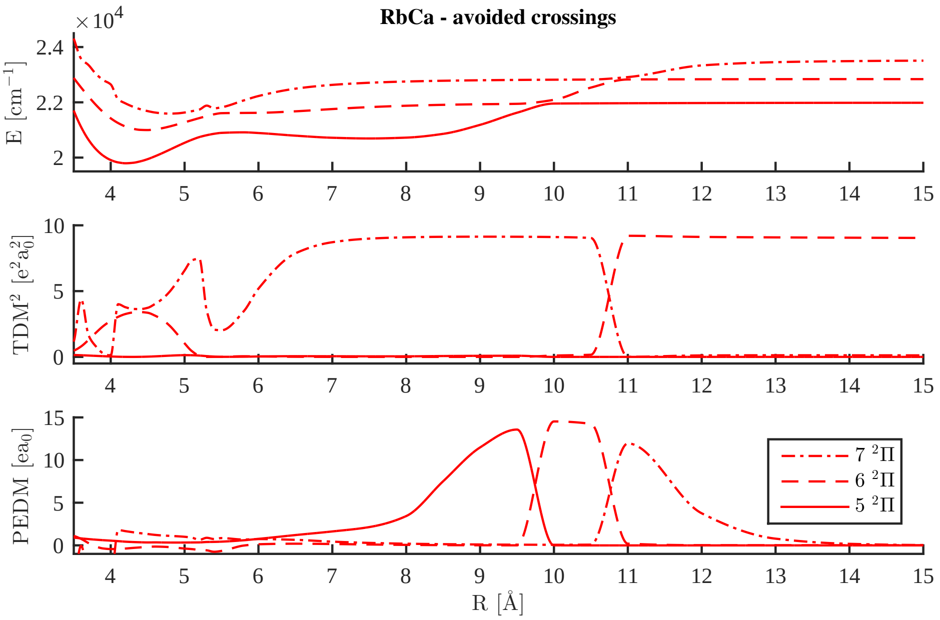

Figure 1.1: The energies (upper panel), the transition dipole moments with the ground state (middle panel) and the permanent electric dipole moments of several excited states in the doublet manifold of the RbCa molecule are shown as determined by a MRCI calculation. Two prominent avoided crossings can be observed.

electric quadrupole moment of the cores and the spin-rotation interaction, are also often omitted. In this approximation, the total angular momentum without nuclear spin $\vec{J}$ is a good quantum number and will be used for the discussion of Hund's cases (see table 1.2). In this approach fine structure effects are included, as for example interactions related to the spin of the electrons. In atoms, two cases arise for the coupling of the spins of the electrons and their orbital angular momentum. The theoretical treatment of spin-orbit coupling is described in section 1.6. In the case of LS-coupling the total orbital momentum of the electrons ($\vec{L}$) couples to the total spin of the electrons ($\vec{S}$). For jj-coupling, the spin and orbital angular momentum of each electron couple more strongly. The total angular momenta of the electrons ($\vec{j_i}$) are then coupled to each other. In the case of molecules, the coupling to the internuclear axis and the molecular rotation have to be considered as well. This leads to the Hund's cases listed in table 1.2, which differ in the relative strengths of their couplings.

For each Hund's case the dominant couplings are taken into account. This results in a specific splitting of states and related quantum numbers that are "good". These quantum numbers are listed in the second column of table 1.2 and can be used to address the states. In contrast, weak couplings lead to a small splitting, which is completely neglected in the context of the Hund's cases. The related states are all degenerate, but there is a difference in the number of degenerate states as can be seen in the fifth column of table 1.2. The third column shows the considered parts of the total Hamiltonian in

Table 1.1: Angular momenta and spins relevant for molecules. The projection for $\vec{L}$ and $\vec{N}$, as well as for $\vec{J}$ and $\vec{J}_e$ are the same because the projection of $\vec{R}$ on the molecular axis has to be zero for the molecule fixed coordinate system.

Description	Symbol and coupling	Projection
orbital angular momentum of one electron	$\vec{l}_i$	λ_i
total orbital angular momentum of the electrons	$\vec{L} = \sum_{i=1}^{N_{el}} \vec{l}_i$	Λ
spin of one electron	$\vec{s}_i$	σ_i
total spin of the electrons	$\vec{S} = \sum_{i=1}^{N_{el}} \vec{s}_i$	Σ
total angular momentum of the i$^{\text{th}}$ electron	$\vec{j}_i = \vec{l}_i + \vec{s}_i$	ω_i
total angular momentum of the electrons	$\vec{J}_e = \vec{L} + \vec{S}\ /\ \sum_{i=1}^{N_{el}} \vec{j}_i$	Ω
nuclear spin of the i$^{\text{th}}$ atom	$\vec{I}_i$	-
total spin of the nuclei	$\vec{I} = \sum_{i=1}^{N_N} \vec{I}_i$	-
angular momentum of the rotation of the nuclear framework	$\vec{R}$	0
total angular momentum without nuclear spin and electronic spin	$\vec{N} = \vec{R} + \vec{L}$	Λ
total angular momentum without nuclear spin and orbital angular momentum of the electrons	$\vec{O} = \vec{R} + \vec{S}$	-
total angular momentum without nuclear spin	$\vec{J} = \vec{R} + \vec{L} + \vec{S}$	Ω
total angular momentum	$\vec{F} = \vec{R} + \vec{L} + \vec{S} + \vec{I}$	-

the different cases. These contributions should be significantly larger than the other parts for the validity of a certain Hund's case. Solutions for the electronic Hamiltonian ($\widehat{H}_{el}$, equation 1.7) can be obtained by standard quantum chemistry packages. In these programs, Σ and S are well defined if spin-adapted configuration state functions are used. In certain cases, the projection of the orbital angular momentum of the electrons Λ can be assigned by symmetry considerations. Methods for molecules with heavy atoms which have a significant spin-orbit interaction ($\widehat{H}_{so}$) are discussed in section 1.6. The Hund's cases are applicable under following circumstances:

- Hund's case (a)

  This is the most widely used case and describes molecules comprised of light atoms with small spin-orbit splitting and low rotational quantum numbers. Here, the projection of the total orbital angular momentum (Λ), the projection of the total spin of the electrons (Σ), and the projection of the total angular moment of the electron hull (Ω) are good quantum numbers. In the reduced Hamiltonian parts of the rotational Hamiltonian and the spin-orbit Hamiltonian are neglected. The

Table 1.2: A summary of Hund's cases following ref. 103. Good quantum numbers are used to identify the unique states of a basis set, quantum numbers corresponding to the operators in the second column in table 1.1 are given by the same symbol without a vector arrow. The quantum number n represents additional quantum numbers which are not considered by Hund's coupling, as for example the vibrational quantum number. $C(\dots,\dots)$ represents the strength of coupling, $\vec{M}$ refers to the molecular axis.

case	basis	$\widehat{H}_{diag}$	strength of coupling	degeneracy
(a)	$\lvert nJS\Omega\Lambda\Sigma\rangle$	$\widehat{H}_{el} + B\vec{J}^2$	$C\left(\vec{L},\vec{M}\right) > C\left(\vec{L},\vec{S}\right) > C\left(\vec{L}+\vec{S},\vec{R}\right)$	2 / 1
(b)	$\lvert nJSN\Lambda\rangle$	$\widehat{H}_{el} + B\vec{N}^2$	$C\left(\vec{L},\vec{M}\right) > C\left(\vec{L}+\vec{S},\vec{R}\right) > C\left(\vec{L},\vec{S}\right)$	$(2S+1)\cdot$ 2 / 1
(c)	$\lvert nJ\Omega\rangle$	$\widehat{H}_{el} + \widehat{H}_{so} + B\vec{J}^2$	$C\left(\vec{L},\vec{S}\right) > C\left(\vec{L},\vec{M}\right) > C\left(\vec{L}+\vec{S},\vec{R}\right)$	2 / 1
(d)	$\lvert nJSNN^+\rangle$	$\widehat{H}_{el}+B\left(\vec{N}^+\right)^2 - B\left(\vec{J}^+\vec{l}^- + \vec{J}^-\vec{l}^+\right)$	$C\left(\vec{L}+\vec{S},\vec{R}\right) > C\left(\vec{L},\vec{M}\right) > C\left(\vec{L},\vec{S}\right)$	$(2L+1)\cdot$ $(2S+1)$
(e)	$\lvert nJJ_eR\rangle$		$C\left(\vec{L}+\vec{S},\vec{R}\right) > C\left(\vec{L},\vec{S}\right) > C\left(\vec{L},\vec{M}\right)$	

expression for rotational energy is given by $E_{rot} = B\left[J\left(J+1\right) - \Omega^2\right]$ (eq. V, 12 in ref. 105), which is also used in the Level 8.0 program[106].

- Hund's case (b)

  This case becomes relevant for high rotational quantum numbers. The coupling between the orbital angular momentum of the electrons ($\vec{L}$) and the rotation ($\vec{R}$) is more significant than the coupling between the orbital angular momentum and the spins of the electrons($\vec{L}$, $\vec{S}$). It is also the relevant coupling case for all states with $\Lambda = 0$.

- Hund's case (c)

  In this case there is significant coupling between the orbital angular momentum and the spin of the electron. This is mostly the case for heavy atoms in the lower rows of the periodic table (for example Rb and Sr). It has the smallest number of good quantum numbers.

- Hund's case (d)

  This Hund's case describes Rydberg complexes, molecules with highly excited electrons in a large orbital with a small probability density in the core region. The system is separated in a core part and in the Rydberg electron[103]: $\vec{L} = \vec{L}_{core} + \vec{l}$. N^+ is the operator for the core that corresponds to $\vec{N}$. This separation into core and Rydberg part also appears in the reduced Hamiltonian in table 1.2.

- Hund's case (e)

A rare case that describes a Rydberg complex with a core that shows spin-orbit splitting.

1.2.2 Designation of states

Hund's cases (a) and (b)

Depending on the Hund's case there are different notations used to address a state. The following expression is common for Hund's case (a):

$$\mathrm{N}\ {}^{2S+1}\Lambda^{sym}_{(g/u)/\Omega} \tag{1.16}$$

Different states which agree in all quantum numbers used in this expression are discerned by the index N, which labels them either by letters or by numbers. In the first case, an "X" is used for the ground state. Other states in the same multiplicity are then addressed by uppercase letters starting with "A". For states in a different multiplicity lowercase letters beginning with "a" are used. The second and more straightforward method is to use numbers for the states starting with "1" for the lowest state. The superscript $(2S + 1)$ is the multiplicity, which is determined by the total spin of the electrons. In table 1.3 values of the multiplicity relevant for this work are listed together with commonly used designations.

Table 1.3: The total spin of the electrons (S), the corresponding value in the designation of the states $(2S + 1)$ and the commonly used names for the different multiplicities are given.

S - value	0	1/2	1	3/2	2	5/2	3
$2S + 1$	1	2	3	4	5	6	7
name	singlet	doublet	triplet	quartet	quintet	sextet	septet

In the case of Λ, the projection of the total orbital angular momentum of the electrons, uppercase Greek letter corresponding to the common lowercase letters used for orbitals (s $\Leftrightarrow$ $l_i = 0$, p $\Leftrightarrow$ $l_i = 1$, d $\Leftrightarrow$ $l_i = 2$, $\ldots$) are used. The most common Λ-values and their assigned symbols are given in table 1.4.

Table 1.4: Symbols used to replace the value of the projection of the total orbital angular momentum of the electrons (third column in table 1.2).

Λ - value	0	1	2	3	...
symbol	Σ	Π	Δ	Φ	...

The superscript *sym* following the main expression in the designation is related to the reflection symmetry for a plane containing the internuclear axis (+ for symmetric and − for antisymmetric wave functions). In Hund's case (a) it is only used for Σ-states $(\Lambda = 0)$.

The possibilities for the subscript in expression 1.16 are more diverse. The numerical value of the projection of the total angular momentum of the electrons (Ω) might be used. For homonuclear molecules the subscripts g or u are used, abbreviations for gerade or ungerade, respectively. In the case of homonuclear dimers, if the atoms get close the orbitals interact and are split into two similar orbitals of different parity. For a gerade parity the system is symmetric for a point reflection at the center, for ungerade it is antisymmetric.

A similar notation can be used for Hund's case (b). However, the subscript Ω is omitted since the projection of total angular momentum of the electrons is ill defined in this case.

Hund's case (c)

For Hund's case (c) the following notation is used:

$$\mathrm{N}\ \Omega^{sym}_{(g/u)} \tag{1.17}$$

The counting of states with the same symmetry by "N" is done as described above. The states are addressed by the numerical value of the projection of the total angular momentum of the electrons (Ω). Additionally, in the case of $\Omega = 0$ the symmetry of the states is distinguished by a superscript (sym) that is either $+$ or $-$. For homonuclear diatomic molecules the parity can be given again by the subscripts g or u.

Vibrational and rotational states

Electronic states including angular momentum coupling can be addressed with the notation above. Additionally, they have vibrational and rotational sublevels. These levels are denoted by using the respective quantum numbers, ν for the vibrational states, and J or N for the rotational states. In figure 1.2, two electronic states including vibrational levels are shown, including some common spectroscopic quantities describing these states. In general, quantities associated with the ground state are denoted by a double prime ($''$, i. e. $\omega_0'' \ /\ \nu''$) and quantities associated with the excited state with a single prime($'$).

The subscript e identifies the values at the equilibrium position of the molecules. The values for the lowest vibrational level are denoted by the subscript 0. The vibrational constant ω_e is given by the curvature of the potential at the equilibrium internuclear separation. The energy difference of the two lowest vibrational levels ω_0 can be estimated with ω_e and the asymmetry parameter $\omega_e x_e$.

$$\omega_0 \approx \omega_e - 2\omega_e x_e \tag{1.18}$$

The calculated dissociation energy D_e and the observed one D_0 differ by the zero-point energy. The zero point energy can be estimated using the vibrational constants:

$$\mathrm{D}_e = \mathrm{D}_0 + \mathrm{ZPE} = \mathrm{D}_0 + \frac{\hbar\omega_0}{2} = \mathrm{D}_0 + \frac{\hbar\omega_e}{2} - \frac{\hbar\omega_e x}{4} + \ldots \tag{1.19}$$

The permanent electric dipole moment can either be given for the equilibrium distance of the molecule μ_e or averaged for the $\mathrm{n^{th}}$ vibrational level μ_n; the same can be done for the rotational constant B_n.

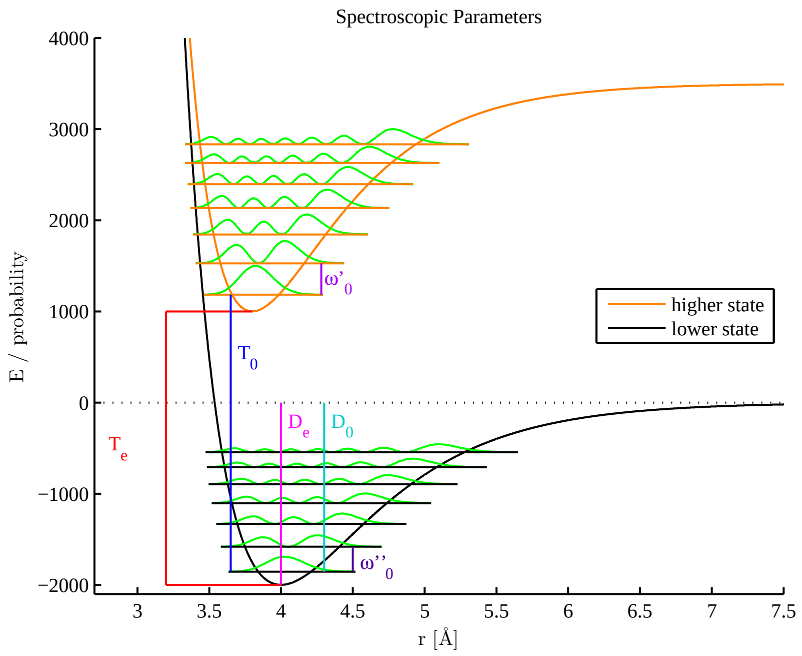

Figure 1.2: Showing the notations for vibronic transitions

1.2.3 Selection rules for molecular transitions

The selection rules for optical transitions for a certain Hund's case are given in table 1.5. These rules can be derived from symmetry considerations for the transition integrals.

Table 1.5: Selection rules for transitions if a certain Hund's case is assumed[105].

(a)	(b)	(c)	(d)
$\Delta J = 0/\pm 1$	$\Delta J = 0/\pm 1$	$\Delta J = 0/\pm 1$	$\Delta J = 0/\pm 1$
$J = 0 \not\leftrightarrow J = 0$	$J = 0 \not\leftrightarrow J = 0$	$J = 0 \not\leftrightarrow J = 0$	$J = 0 \not\leftrightarrow J = 0$
$\Delta\Lambda = 0/\pm 1$	$\Delta\Lambda = 0/\pm 1$	$\Delta\Omega = 0/\pm 1$	$\Delta N = 0/\pm 1$
$\Sigma^+ \not\leftrightarrow \Sigma^-$	$\Sigma^+ \not\leftrightarrow \Sigma^-$	$0^+ \not\leftrightarrow 0^-$	$\Delta L = 0/\pm 1$
$\Delta S = 0$	$\Delta S = 0$		$\Delta R = 0$
$\Delta\Sigma = 0$	$\Delta N = 0/\pm 1$		
for $\Omega = 0 \leftrightarrow \Omega = 0$:	for $\Sigma \leftrightarrow \Sigma$:	for $\Omega = 0 \leftrightarrow \Omega = 0$:	
$\Delta J \neq 0$	$\Delta N \neq 0$	$\Delta J \neq 0$	

For homonuclear diatomic molecules there is an additional rule, only transitions gerade to ungerade or ungerade to gerade are allowed ($g \leftrightarrow u$, $g \not\leftrightarrow g$, $u \not\leftrightarrow u$). The first two rules in table 1.5 hold for all coupling cases, because J is always a good quantum number if the nuclear spin is neglected. The multiplicity can not change ($\Delta S = 0$) in Hund's cases (a) and (b). These coupling schemes apply to molecules consisting of atoms found in the upper rows of the periodic table. Similarly, Hund's case (c), with strong spin-orbit coupling, is rather relevant for molecules containing heavy atoms. More details on selection rules and how they manifest in spectra of diatomic molecules can be found in the book by Herzberg[105] or the book by Lefebvre-Brion and Field[103]. In the case of polyatomic molecules and quantum chemical computations similar transition rules can be derived relying on symmetries and point groups, see section 1.3.10.

1.3 Theoretical Approach

The next sections give an outline of theoretical methods used in this thesis. First, the description of the electrons and the atomic core in wave function based *ab initio* computations is introduced. Next, the Hartree-Fock procedure is mentioned followed by several methods to obtain the correlation energy. Thereafter, some general considerations concerning these calculations are presented. Finally, the description of electronic states by potential energy curves is discussed in combination with vibrational considerations.

1.3.1 Description of the electronic wave function

The first part of the problem is to solve the electronic Schrödinger equation (equation 1.7) and to determine the potential energy curve $E_n(\mathbf{R})$. In general, this is done by describing the orbitals of the electrons with a set of localized or non-localized basis functions (χ_i). In this work localized, i.e. atom-centered, basis sets were used. The most common localized basis functions are Gaussian type orbitals, which allow integral evaluations via analytical expressions. In this case, the basis functions are of the following form:

$$\chi_i = \frac{1}{N} x^m y^n z^l e^{-a\cdot\left(x^2+y^2+z^2\right)} \tag{1.20}$$

N is the normalization factor, x, y and z are the Cartesian coordinates. The parameters m, n, l and a define the function and optimized values are available for each atom from different publications and databases such as EMSL[11, 12, 107]. More information on basis sets can be found in ref. 108. Localized basis sets are well suited for the description of molecules. However, an intrinsic problem of their application is the basis set superposition error (BSSE). If atoms are getting closer, the basis functions of one atom are used to describe the other. This causes a unphysical lowering of the energy for smaller internuclear separations in variational calculations. This error can be minimized by using large basis sets to reduce the impact of contributions from neighboring basis functions. The counterpoise correction (CP) of Boys and Bernadi[109] can be used to correct for this error, but requires additional calculations. In the case of a diatomic molecule, consisting of atoms A and B, the counterpoise correction is done by subtracting the energies of atoms calculated with the basis functions of both atoms from the energy of the molecule:

$$E^{CP}(AB) = E^{AB}(AB) - E^{AB}(A) - E^{AB}(B)\,. \tag{1.21}$$

General basis functions are non-orthogonal. A set of orthogonal orbitals ϕ_l is obtained by a specific linear combination of these functions(LCAO):

$$\phi_l = \sum_i^{N_B} C_{li}\chi_i \tag{1.22}$$

with N_B being the number of basis functions. An increase in the number of basis functions improves the results, although it is more important that the functions are suitable for the problem, i.e. atom. There are families of basis sets, similar basis sets with a different number of functions for the valence orbitals. These families can be used to estimate the results for an infinite or complete basis set. These formulas either extrapolate the total energy or the correlation energy. In this work we used a formula that only extrapolates the correlation energy[108, 110]:

$$E_{\mathrm{corr},\infty} = \frac{N^3 E_{\mathrm{corr},N} - M^3 E_{\mathrm{corr},M}}{N^3 - M^3}, \tag{1.23}$$

M and N denote the largest orbital angular momentum quantum number of the used basis set, $E_{\mathrm{corr},...}$ the correlation energy calculated with the respective basis.

The antisymmetry of the wave function is guaranteed by using Slater determinants, but a single Slater determinant might be insufficient to describe the electronic wave function. If the wave function should be an eigenstate of other operators, like the projection of the orbital angular momentum $(\widehat{L_z})$ or spin operators $(\widehat{S_z}, \widehat{S^2})$, it often is necessary to combine several Slater determinants. These symmetry adapted linear combinations of Slater determinants with the desired properties are called configuration state functions (CSFs):

$$\Phi_I = \sum_l a_{Il}\Pi_l. \tag{1.24}$$

Such a configuration state function describes the electronic wave function of a certain electronic configuration. There are cases where it is necessary to consider several configurations. One example are excited electronic states that cannot be enforced by symmetry restrictions. This is relevant for the current work. Another example are configurations that are close in energy. They influence each other and an accurate description of one of these states cannot be achieved without considering the other. In these cases several configurations are used to describe the electronic wave function:

$$\Psi_{el} = \sum_I c_I\Phi_I \tag{1.25}$$

The corresponding multireference or multiconfigurational computational methods are outlined in the sections 1.3.5 and 1.3.6.

1.3.2 Effective core potentials (ECPs) and core polarization potentials (CPPs)

For large atoms many closed shells need to be included in the computations, resulting in a large computational effort. However, the valence electrons are more significant for chemical interactions than core electrons. By replacing the inner shells with an effective core potential (ECP) the computational demand can be significantly reduced. This approach is mainly applied to heavy elements of the 4th to 7th period. Another advantage of effective core potentials is the simple and inexpensive inclusion of relativistic effects (see section 1.5), which are particularly important for heavy elements. In order to perform calculations with ECPs, the number of electrons described by the wave function is reduced (changes total energy) and the Coulomb-potential of the corresponding nucleus is replaced by the following function[111]:

$$V_{ECP} = -\frac{Z - n_{core}}{r} + V_{l_{max}} + \sum_{l=0}^{l_{max}-1} \left(V_l - V_{l_{max}}\right) \widehat{P}_l + \sum_{l=1}^{l'_{max}} \Delta V_l \widehat{P}_l \vec{l} \cdot \vec{s} \widehat{P}_l \tag{1.26}$$

The first contribution is the Coulomb potential of the remaining positive charge not included in the effective core potential (Z is the number of protons for the considered atom and n_{core} the number of electrons included in the ECP). $\widehat{P}_l$ denotes a projection operator for the spherical harmonics of the nucleus. The second and third term in equation 1.26 (V_{max},$(V_l - V_{l_{max}})$) are the scalar contributions. The fourth part (ΔV_l) is only important in calculations including spin-orbit interactions and set to zero otherwise. The different contributions are included by a sum of Gaussian functions (for each l):

$$V_{l_{max}} / \left(V_l - V_{l_{max}}\right) / \Delta V_l = \sum_{j=1}^{n} c_j r^{m_j - 2} e^{-\gamma_j r^2} \tag{1.27}$$

The coefficients n, c_j, m_j, and γ_j are specific for each element and can be retrieved from publications or online databases, similar to the ones for basis sets. One example is the collection of ECPs by the Stuttgart/Cologne group[112]. Typically, optimized basis sets for each effective core potential are also provided.

Effective core potentials can be classified by n_{core}, the number of electrons they comprise. If only the valence electrons are excluded, the pseudopotentials are called 'large core' ECPs. If additional closed shells are not included in the effective core potential, which then need to be considered in the computations, it is a 'small core' ECP. While the computational effort is larger for small core ECPs, the inclusion of closed shells often improves the accuracy. The pseudopotentials are also distinguished by the manner in which they have been determined. The parameters of energy consistent effective core potentials have been determined by comparing excitation and ionization energies to known values (mostly all electron *ab initio* results), as was done by the Stuttgart/Cologne group[112]. Alternatively, the effective core potentials can also be determined by adjusting the potential parameter in such a way that there is the best overlap with the all-electron wave functions except for positions close to the nuclei. An example are the shape-consistent ECPs by Ermler *et al.*[113, 114]. Nevertheless, for both approaches the orbitals change for small radii and the nodes of the orbitals vanish. The performances of an energy- and a shape-consistent ECP are compared in chapter 3.

A drawback of ECPs is that no correlation and polarization of the core electrons is included (The same is true if the core orbitals are frozen and no excitations from these orbitals are allowed in the calculations). This can significantly alter wave function properties such as the permanent electric dipole moment (see chapter 5). This deficiency can be reduced by applying core polarization potentials (CPPs)[115–117], which simulate a polarization of the cores. A core polarization potential is described by two parameters, the dipole polarizability of the core (α_c) and the cut-off radius (ρ_c). The core polarization is included by a potential of following form[116]:

$$V_{CPP} = -\frac{1}{2}\sum_c \alpha_c \vec{f}_c \cdot \vec{f}_c, \tag{1.28}$$

where $\vec{f}_c$ is the field generated by the other cores and the valence electrons, which act on the core and can be calculated by:

$$\vec{f}_c = \sum_i \frac{\vec{r}_{ci}}{\vec{r}^3_{ci}} \left(1 - e^{-\left(\frac{r_{ci}}{\rho_c}\right)^2}\right)^2 - \sum_{c' \neq c} \frac{\vec{R}_{cc'}}{\vec{R}^3_{cc'}} Z_{cc'}. \tag{1.29}$$

The Müller/Meyer cutoff-function $\left(1 - e^{-\left(\frac{r_{ci}}{\rho_c}\right)^2}\right)^2$ ensures that there are no divergences[116]. A different cutoff-function can be found in the work of Fuentealba[118]. This polarization contains the static and dynamic contribution. Therefore, the static SCF polarization needs to be subtracted to avoid double counting.

The description of the core polarization can be further improved by including higher multipole terms. Another successfully applied method is the use of cutoff radii that depend on the orbital angular momentum of the electron, as was done for example in refs. 119 and 120.

1.3.3 Self consistent field (SCF) / Hatree-Fock (HF) method

The Hartree-Fock method is the foundation of molecular orbital theory and includes the interaction of the electrons with each other by a mean field approximation. If the interaction with the electrons (equation 1.4, $\widehat{V}_{ee}$) is neglected, the electronic wave function is given by a product of orbitals, which are determined by a Schrödinger equation ($\widehat{h}(n)\,\varphi_i(x_n) = \epsilon_i \varphi_i(x_n)$) for the one electron operator $\widehat{h}(n)$:

$$\widehat{h}(n) = -\frac{1}{2}\nabla^2_n - \sum_{I=1}^{N_N} \frac{Z_I}{|R_I - r_n|} \tag{1.30}$$

Applying an antisymmetric product ansatz and taking electron-electron interaction into account, one obtains two additional terms, the Coulomb operator $\widehat{J}_j$ and the exchange operator $\widehat{K}_j$ for the spin-orbitals φ_i:

$$\widehat{J}_j(n)\,\varphi_i(x_n) = \varphi_i(x_n) \int \mathrm{d}x_m \frac{|\varphi_j(x_m)|^2}{|r_n - r_m|} \tag{1.31}$$

$$\widehat{K}_j(n)\,\varphi_i(x_n) = \varphi_j(x_n) \int \mathrm{d}x_m \frac{\varphi_j^*(x_m)\,\varphi_i(x_m)}{|r_n - r_m|} \tag{1.32}$$

These extra terms lead to a coupling of the single electron operators, which complicates the evaluation significantly. Three contributions define the Fock operator:

$$\widehat{f}(n) = \widehat{h}(n) + \sum_{j}^{N_{el}} \left(\widehat{J}_j(n) - \widehat{K}_j(n) \right), \tag{1.33}$$

which leads to the Hartree-Fock equations:

$$\widehat{f}(n)\,\varphi_i(x_n) = \epsilon_i \varphi_i(x_n), \tag{1.34}$$

a set of coupled integro-differential equations. The orbitals are in general described by a linear combination (equation 1.22) and their coefficients are optimized in the course of a computation. A self consistent procedure is necessary because the orbitals are already required for the evaluation of the Fock operator. This operator is then used to set up the equation that determines the coefficients of the orbitals. After successful convergence, the optimized orbitals can be used in subsequent computations, for example a coupled cluster calculation.

Note that spin-orbitals are used in the formulas above. There are different approaches how to describe the same orbital for different spin of the electrons. In a restricted Hatree-Fock calculation (RHF) the spatial orbitals for the two possible spin orientations are the same. The application of this approach for the coefficients in equation 1.22 leads to the Roothaan equations. The RHF method can only be applied to closed shell molecules because the approach requires that all orbitals are doubly occupied. Therefore, it is not applicable to the open-shell molecules treated in this thesis. Instead, an unrestricted Hartree-Fock computation (UHF) can be used for this class of molecules. In this case, each spin-orbital is treated independently and two sets of orbitals are obtained, one for each spin orientation. However, this leads to a non-physical difference in the spatial part of the orbitals, even for doubly occupied or completely empty orbitals. Since the doubly occupied orbitals do not completely overlap the spin is not completely compensated. This results in wave functions that are no longer eigenfunctions of the spin operator which is called spin-contamination. The restricted open shell Hartree-Fock method (ROHF) allows to calculate open-shell molecules with identical spatial orbitals for both spin orientations in the case of double occupation. This method is not applicable to all systems, but shows no spin-contamination. Therefore, ROHF was preferred for the molecules in this work.

In a Hartree-Fock computation, the interaction of the electrons among themselves is considered by an averaged potential (equations 1.31 and 1.32). The probability of finding an electron depends on the position of the nuclei, but the actual position of the other electrons is irrelevant, only their averaged distribution is taken into account. The missing part is defined as electron correlation. Parts of this missing contribution can be recovered by Post-Hartree-Fock methods which will be presented in the following sections. The contribution of the electron correlation to the total energy is small (about 1 %), but crucial for the correct estimate of relative energies. It has a significant impact on chemical bonds and other molecular properties. CrHe, for example, shows no bonding in the ground state if correlation is neglected.

1.3.4 Configuration interaction (CI)

A configuration interaction computation includes electron correlation and is based on a single CSF or Slater determinant. For example, a single configuration state function (Φ_0), optimized in a Hartree-Fock computation, may be used. Additional configurations are generated by moving electrons from occupied into unoccupied orbitals, which yields the expression

$$\Psi_{el} = c_0 \cdot \Phi_0 + \sum_{a}^{occ} \sum_{z}^{virt} c_a^z \Phi_a^z + \sum_{a<b}^{occ} \sum_{z<y}^{virt} c_{ab}^{zy} \Phi_{ab}^{zy} + \sum_{a<b<c}^{occ} \sum_{z<y<x}^{virt} c_{abc}^{zyx} \Phi_{abc}^{zyx} + \dots \tag{1.35}$$

The sum for the lowercase letters $\mathrm{a, b, c}, \dots$ includes all occupied orbitals, the lowercase indices $\mathrm{z, y, x}, \dots$ denote unoccupied (virtual) orbitals in the original CSF (Φ_0). For example, a new configuration state function Φ_a^z is generated by taking one electron out of orbital a and putting it into orbital z. This can be done for several electrons yielding higher terms in the expansion. The restrictions ($a < b, \dots$) ensure that every excited configuration only appears once. Equation 1.35 can be written in symbolic form as:

$$|\Psi_{el}\rangle = c_0 |\Phi_0\rangle + c_S |\Phi_S\rangle + c_D |\Phi_D\rangle + c_T |\Phi_T\rangle + \dots \tag{1.36}$$

The expression $|\Phi_S\rangle$ corresponds to single excitations, $|\Phi_D\rangle$ to double excitations and so on. The coefficient c_a^z, c_{ab}^{zy}, $\dots$ can be determined by a variational method. In this case, it corresponds to a diagonalization of the CI-Matrix ($|\Phi_N\rangle$ is a vector of all N times excited configurations):

$$\begin{pmatrix} \langle\Phi_0|\widehat{H}|\Phi_0\rangle & 0 & \langle\Phi_0|\widehat{H}|\Phi_D\rangle & 0 & \dots \\ 0 & \langle\Phi_S|\widehat{H}|\Phi_S\rangle & \langle\Phi_S|\widehat{H}|\Phi_D\rangle & \langle\Phi_S|\widehat{H}|\Phi_T\rangle & \dots \\ \langle\Phi_D|\widehat{H}|\Phi_0\rangle & \langle\Phi_D|\widehat{H}|\Phi_S\rangle & \langle\Phi_D|\widehat{H}|\Phi_D\rangle & \langle\Phi_D|\widehat{H}|\Phi_T\rangle & \dots \\ 0 & \langle\Phi_T|\widehat{H}|\Phi_S\rangle & \langle\Phi_T|\widehat{H}|\Phi_D\rangle & \langle\Phi_T|\widehat{H}|\Phi_T\rangle & \dots \\ \vdots & \vdots & \vdots & \vdots & \ddots \end{pmatrix} \tag{1.37}$$

Note that certain elements in equation 1.37 are zero by construction. More details concerning this method are given in refs. 108 and 121.

1.3.5 Multiconfigurational self-consistent field (MCSCF)

A self-consistent field calculation (section 1.3.3) can be extended to a multiconfigurational self-consistent field calculation by including several CSFs in the optimization procedure. Instead of a single configuration state function (Φ_0), a sum is used to describe the total electronic wave function (equation 1.25). The wave function in the equation describes either the ground state or an excited state. In order to optimize several states simultaneously, the state averaging technique can be used[122]:

$$E_{av} = \sum_{m}^{N_{st}} W_m E_m = \sum_{m}^{N_{st}} W_m \sum_{I,J}^{N_c} c_I^m c_J^m \langle\Phi_I|\widehat{H}|\Phi_J\rangle \tag{1.38}$$

Here, $\widehat{H}$ denotes the Hamilton operator of the electronic system and N_c is the number of CSFs. The number of states which are optimized simultaneously is N_{st} and the weight W_m determines the importance of state m during the optimization. Since the orbitals are optimized to describe several states simultaneously, the accuracy for a single state is slightly reduced, but all involved states are treated at similar accuracy. This is important if transition energies and probabilities involving several states are calculated.

The optimization procedure is more involved, since not only the coefficients C_{li} of equation 1.22 but also the coefficients c_I of equation 1.25 are determined in a MCSCF computation. This complicates the optimization since the coefficients C_{li} (equation 1.22) and c_I (equation 1.25) are not independent from each other. Details on how such a calculation can be set up can be found in refs. 122–126.

In general, CSFs are selected by the specification of an active space. The active space is defined by the number and symmetry of the orbitals and the number of electrons which can occupy these orbitals. In a complete active space calculation (CASSCF) all possible configuration state functions for a given number of electrons and orbitals are used. In contrast, the number of CSFs is reduced in a restricted active space calculation (RASSCF) by additional restrictions, mostly for orbital occupation. For larger atoms the computational demand can be reduced by defining a set of closed orbitals. The coefficients of these orbitals will be optimized, but no CSFs with partial occupation of these orbitals will be considered in the calculations. In contrast, an occupation of zero, one, or two electrons is possible for active orbitals if it is in agreement with the total number of electrons. In MOLPRO, the closed and active orbitals together are denoted as occupied. The virtual orbitals are always unoccupied and should have significantly higher energies. Using point groups and symmetries(see section 1.3.10) the computational cost might be reduced. This has to be done with care to avoid restricting the computation to a faulty or unwanted solution.

1.3.6 Multireference configuration interaction (MRCI)

In a multireference calculation the reference wave function is multiconfigurational, as given by equation 1.25. The CI wave function (equation 1.35) then contains an additional sum, as for example for a MRCI(SD) computation:

$$\Psi_{el} = \sum_I c_{I0}\Phi_{I0} + \sum_J \sum_a^{occ} \sum_z^{virt} c_{Ja}^z \Phi_{Ja}^z + \sum_K \sum_{a<b}^{occ} \sum_{z<y}^{virt} c_{Kab}^{zy} \Phi_{Kab}^{zy} \tag{1.39}$$

Details on the evaluation of the coefficients can be found in refs. 127 and 128.

1.3.7 Coupled cluster (CC)

Analogous to the CI ansatz a reference wave function is required for a coupled cluster calculation. In most cases a single configuration state function obtained by a Hartree-Fock calculation is used, but multireference coupled cluster methods are under development and some programs are already available[129–131]. In the coupled cluster approach an excitation operator ($\widehat{T}$) is defined which creates excited configurations. The operator can be split into contributions of different order:

$$\widehat{T} = \widehat{T}_1 + \widehat{T}_2 + \widehat{T}_3 + \widehat{T}_4 + \dots \tag{1.40}$$

$$\tag{1.41}$$

The first two terms of this series, for example, produce single and double excitations, if they are applied to a reference CSF:

$$\widehat{T}_1 \left|\Phi_0\right\rangle = \sum_{a}^{occ} \sum_{z}^{virt} t_a^z \left|\Phi_a^z\right\rangle \tag{1.42}$$

$$\widehat{T}_2 \left|\Phi_0\right\rangle = \frac{1}{4} \sum_{a<b}^{occ} \sum_{z<y}^{virt} t_{ab}^{zy} \left|\Phi_{ab}^{zy}\right\rangle \tag{1.43}$$

The CC wave function is now defined by the application of the cluster operator $\widehat{T}$ to the reference wave function in the form of an exponential function:

$$\begin{aligned}\left|\Psi_{CC}\right\rangle &= e^{\widehat{T}} \left|\Phi_0\right\rangle = \sum_{k=0}^{\infty} \frac{1}{k!} \widehat{T}^k \left|\Phi_0\right\rangle \\ &= \left[1 + \widehat{T}_1 + \left(\widehat{T}_2 + \frac{1}{2}\widehat{T}_1^{\,2}\right) + \left(\widehat{T}_3 + \widehat{T}_2\widehat{T}_1 + \frac{1}{6}\widehat{T}_1^{\,3}\right) + \dots\right] \left|\Phi_0\right\rangle \end{aligned} \tag{1.44}$$

In the lower line in equation 1.44 the operators have been sorted according to the excitation which they generate. This makes the difference to the CI wave function (equation 1.35) obvious: The coefficients of excited determinants also have contributions from lower orders in the excitation operator due to products (e.g. the coefficients of the single excitation operator t_a^z are included in the coefficients of double excited determinants via $\widehat{T}_1^{\,2}$). The coupled cluster equations are now obtained by evaluating the Schrödinger equation with this wave function. First the energy eigenvalues are split into the Hartree-Fock energy E_0 and the correlation energy E_{corr}:

$$\hat{H} \left|\Psi_{CC}\right\rangle = (E_0 + E_{corr}) \left|\Psi_{CC}\right\rangle \tag{1.45}$$

For simplicity we only consider double excitations (CCD):

$$\left|\Psi_{CCD}\right\rangle = \left[1 + \widehat{T}_2 + \frac{1}{2}\widehat{T}_2^{\,2} + \frac{1}{6}\widehat{T}_2^{\,3} + \dots\right] \left|\Phi_0\right\rangle \tag{1.46}$$

With this the Schrödinger equation becomes:

$$\begin{aligned}\left(\hat{H} - E_0\right) \left[\left|\Phi_0\right\rangle + \frac{1}{4} \sum_{a<b}^{occ} \sum_{z<y}^{virt} t_{ab}^{zy} \left|\Phi_{ab}^{zy}\right\rangle + \frac{1}{32} \sum_{a<b<c<d}^{occ} \sum_{z<y<x<w}^{virt} t_{ab}^{zy} t_{cd}^{xw} \left|\Phi_{abcd}^{zyxw}\right\rangle + \dots\right] = \\ E_{corr} \left[\left|\Phi_0\right\rangle + \frac{1}{4} \sum_{a<b}^{occ} \sum_{z<y}^{virt} t_{ab}^{zy} \left|\Phi_{ab}^{zy}\right\rangle + \frac{1}{32} \sum_{a<b<c<d}^{occ} \sum_{z<y<x<w}^{virt} t_{ab}^{zy} t_{cd}^{xw} \left|\Phi_{abcd}^{zyxw}\right\rangle + \dots\right]\end{aligned} \tag{1.47}$$

By multiplying from the left with $\langle\Phi_0|$ one obtains:

$$E_0 - E_0 + \frac{1}{4}\sum_{a<b}^{occ}\sum_{z<y}^{virt} t_{ab}^{zy} \langle\Phi_0|\, \hat{H}\, |\Phi_{ab}^{zy}\rangle = E_{corr}. \tag{1.48}$$

Now we multiply from the left with $\left\langle\Phi_{ef}^{vu}\right|$:

$$\begin{aligned}\left\langle\Phi_{ef}^{vu}\right| \hat{H}\, |\Phi_0\rangle + \frac{1}{4}\sum_{a<b}^{occ}\sum_{z<y}^{virt} t_{ab}^{zy} \left\langle\Phi_{ef}^{vu}\right| \left(\hat{H} - E_0\right) |\Phi_{ab}^{zy}\rangle & \\ +\frac{1}{32}\sum_{a<b<c<d}^{occ}\sum_{z<y<x<w}^{virt} t_{ab}^{zy} t_{cd}^{xw} \left\langle\Phi_{ef}^{vu}\right| \hat{H}\, |\Phi_{abcd}^{zyxw}\rangle &= E_{corr} t_{ef}^{vu}\end{aligned} \tag{1.49}$$

This set of equations is then solved to determine the coefficients of the coupled cluster wave function and its energy. The two equations describe a large set of coupled equations. Due to this truncated coupled cluster calculations are size extensive, but the computation is more demanding than a CI calculation for the same system.

Equation of motion / linear response coupled cluster

Approaches based on the coupled cluster method can also be used to calculate excited states and to consider multiconfigurational cases. One example is the linear response coupled cluster method[132]. Another one is the equation of motion coupled cluster (EOM-CC) approach[133, 134]. More information is provided in ref. 135.

1.3.8 Many-body perturbation theory

An alternative way of adding correlation energy is many-body perturbation theory. In order to apply perturbation theory the Hamiltonian of the system is split into two parts, a simplified system ($\widehat{H}^{(0)}$) for which the exact solutions are known ($\widehat{H}^{(0)}\Psi_i^{(0)} = E_i^{(0)}\Psi_i^{(0)}$) and a perturbation ($\widehat{H}^p$):

$$\widehat{H} = \widehat{H}^{(0)} + \lambda\widehat{H}^p \tag{1.50}$$

The parameter λ determines the strength of the perturbation. The exact wave function and energy eigenvalues can be expanded in a Taylor series for small λ:

$$E_i = E_i^{(0)} + \lambda E_i^{(1)} + \lambda^2 E_i^{(2)} + \ldots \tag{1.51}$$

$$\Psi_i = \Psi_i^{(0)} + \lambda\Psi_i^{(1)} + \lambda^2\Psi_i^{(2)} + \ldots \tag{1.52}$$

$$\tag{1.53}$$

These expressions are put into the equation 1.50. By direct comparison of terms of the same orders in λ the following expressions can be derived:

$$E_i^{(0)} = \left\langle \Psi_i^{(0)} \middle| \widehat{H}^{(0)} \middle| \Psi_i^{(0)} \right\rangle, \quad \Psi_i^{(0)} \tag{1.54}$$

$$E_i^{(1)} = \left\langle \Psi_i^{(0)} \middle| \widehat{H}^{p} \middle| \Psi_i^{(0)} \right\rangle, \quad \Psi_i^{(1)} = \sum_{n \neq i} \frac{\left\langle \Psi_n^{(0)} \middle| \widehat{H}^{p} \middle| \Psi_i^{(0)} \right\rangle}{E_i^{(0)} - E_n^{(0)}} \Psi_n^{(0)} \tag{1.55}$$

$$E_i^{(2)} = \sum_{n \neq i} \frac{\left| \left\langle \Psi_n^{(0)} \middle| \widehat{H}^{p} \middle| \Psi_i^{(0)} \right\rangle \right|^2}{E_i^{(0)} - E_n^{(0)}}, \quad \ldots \tag{1.56}$$

The denominator of the correction to the wave function of first order and to the energy of second order is given by the energy differences of the eigenstates in the simplified system. If there are states close in energy the corrections become large and many orders of perturbation theory need to be considered for accurate results. For states with the same energy the corrections diverge and perturbation theory for degenerate states has to be applied. In contrast to methods based on the variational principle, where the lowest energy is obtained for the best approximation to the wave function, the perturbative corrections can yield energies below the exact results.

The application of perturbation theory to the electronic structure problem can be outlined as follows. The exactly solved simplified system is the Hartree-Fock solution; the corresponding operator is the Fock-operator (equation 1.33). The perturbation is the exact interaction of the electrons without the averaged interaction already included in the Hartree-Fock calculation:

$$\widehat{H}^{p} = \frac{1}{2} \sum_{i/j=1, j \neq i}^{N_{el}} \frac{1}{|r_i - r_j|} - \widehat{g}_{HF} \tag{1.57}$$

This leads to the Møller-Plesset perturbation theory. With this definition, the zeroth order energy is simply the sum of the energies of the Fock orbitals. The first order energy corresponds to the Hartree-Fock result. The next order contains the first correction due to correlation. This is the MP2 method, which is implemented in most quantum chemistry software packages. It is the most common method of the MP series and shows a good balance of computational cost and correlation retrieved. However, it tends to overestimate the correlation contribution in some cases.

1.3.9 Truncation and size consistency

In multiconfigurational or multireference approaches expansions similar to equation 1.35 are used. The highest accuracy is achieved if all possible excitations from occupied to virtual orbitals are considered for a large set of virtual orbitals, but this is often not feasible and truncation becomes necessary. The excitations taken into account are then indicated by uppercase letters, as for example CISD or CCSD for configuration interaction or coupled cluster calculation using only single and double excitations. In the case of CC the triplet excitations are often considered by approximate methods which is then indicated by a uppercase T in brackets or with a dash in between. Currently, the CCSD(T) method is considered to be the gold standard of quantum chemistry.

In addition to the reduced accuracy, truncation can also lead to systematic errors. For example, there is no size consistency in truncated CI computations. The results are different if two non-interacting systems are computed separately or together. For small systems with few electrons a full CI calculation can be performed with optimized software to obtain size consistent results. If there are many virtual orbitals and electrons this is not possible and ad hoc corrections become necessary. In this work, the Davidson correction(+Q)[136, 137] was applied, which adds an energy term E_D given by:

$$E_D = E_c \frac{1 - c_0^2}{c_0^2} \tag{1.58}$$

E_c denotes the correlation energy and c_0 is the weight of the reference CSF in the CI expansion (equation 1.39 or 1.35). It was originally designed to estimate the CISDTQ energy from the CISD energy. It should give a more accurate energy and make the result approximately size consistent.

A stricter criterion than size consistency is size extensivity. If valid, the calculated energies scale linearly with the system size. HF, CC, full CI and MBPT are size extensive.

1.3.10 Symmetry

Symmetries are useful to derive general rules, to simplify calculations or to make them feasible in the first place. In the following, a short introduction into molecular symmetry of diatomic molecules will be given. In general, a symmetry is an invariance under a certain transformation. For the description of molecules either point groups or permutation inversion groups are used. The second class is only used in special cases such as large amplitude motion in polyatomic molecules and will be omitted in the following. An introduction into permutation inversion groups is given in refs. 138, 139. Our group recently applied it to the sodium trimer[9].

Point groups

Point groups are commonly applied to molecules and solids. The relevant transformations for the symmetry groups, which leave at least on point unaltered, are listed in table 1.6. In this work mainly diatomic molecules are treated. The relevant point groups are $\mathrm{D}_{\infty h}$ and $\mathrm{C}_{\infty v}$. These point groups have an infinite number of symmetry operations since arbitrary rotations about the internuclear axis do not change the molecule. Homonuclear diatomic molecules belong to the $\mathrm{D}_{\infty h}$ point group, heteronuclear to $\mathrm{C}_{\infty v}$. We will discuss this second point group in more detail, because all molecules of this work were heteronuclear. The table 1.7 is the character table of $\mathrm{C}_{\infty v}$. The first column lists the irreducible representations of the point group. For this infinite group there exists an infinite number of irreducible representations. A few of them are listed in the table. In

Symbol	Transformation
E	identity, no change of the coordinates
C$_n$	rotation by $\frac{2\pi}{n}$
i	inversion, reflection through a single point
σ	reflection through a plane
S$_n$	rotation by $\frac{2\pi}{n}$ with successive reflection through a plane perpendicular to the axis of rotation (improper rotation)

Table 1.6: transformations used to define point groups, symbols according to Schönflies notation

	E	$C_\infty\,(\phi)$	$\sigma_v\,(\infty)$	linear, rotations	quadratic
$A_1 \Leftrightarrow \Sigma^+$	1	1	1	z	z^2, x^2+y^2
$A_2 \Leftrightarrow \Sigma^-$	1	1	-1	R_z	
$E_1 \Leftrightarrow \Pi$	1	2 cos(ϕ)	0	x, y, R_x, R_y	xz, yz
$E_2 \Leftrightarrow \Delta$	1	2 cos(2ϕ)	0		xy, x^2-y^2
$E_3 \Leftrightarrow \Phi$	1	2 cos(3ϕ)	0		
...	...	...	...	...	...

Table 1.7: character table for C$_{\infty v}$

this special case the irreducible representations can be directly associated with a specific projection of the total orbital angular momentum of the electron (Λ). In the following columns the characters for the irreducible representations are listed for different symmetry operations. The number of columns depends on the number of symmetry operations. The last two columns, "linear, rotations" and "quadratic", list the position, rotation and quadratic operators which show the same behavior under the symmetry operations as the respective representations. The set of nuclei belongs to the totally symmetric irreducible representation A_1 for which all characters have a value of one. There is no change for any transformation listed in the table. The situation is different for wave functions, vibrational modes, orbitals or operators. They might, for example, change sign under a certain transformation. In this case, they would belong to an irreducible representation with the character -1 for this particular transformation. The previously mentioned infinite point groups are non-Abelian. This and the infinite number of symmetry elements makes these point groups problematic for computation. Instead, the

	E	$C_2\,(z)$	$\sigma_v\,(xz)$	$\sigma_v\,(yz)$	linear, rotations	quadratic
A_1	1	1	1	1	z	x^2, y^2, z^2
A_2	1	1	-1	-1	R_z	xy
B_1	1	-1	1	-1	x, R_y	xz
B_2	1	-1	-1	1	y, R_x	yz

Table 1.8: character table for C$_{2v}$

point group C_{2v} is used most of the time. Table 1.8 shows the corresponding character table. The infinite number of rotations C_∞ are now replaced with a rotation by 180 degree, C_2. This point group is, for example, applied in calculations of linear molecules with Molpro[140]. Character tables are highly useful for the evaluation of certain expressions. An integral can only be non-zero if the function belongs to the completely symmetric irreducible representation. If this is not the case, the antisymmetry of the function results in canceling contributions to the integral. Therefore, it is often helpful to know the irreducible representation of the product of two irreducible representations. The relevant product table for C_{2v} is given by table 1.9.

	A_1	A_2	B_1	B_2
A_1	A_1	A_2	B_1	B_2
A_2	A_2	A_1	B_2	B_1
B_1	B_1	B_2	A_1	A_2
B_2	B_2	B_1	A_2	A_1

Table 1.9: product table for the C_{2v} point group

1.3.11 Molecular orbitals

The molecular orbitals (ϕ_l, equation 1.22) are not uniquely defined. It is possible to perform a rotation, a unitary transformation, without changing the wave function and all its related observables:

$$\phi'_l = \sum_{j=1}^{N_{orb}} u_{lj}\phi_j \quad / \quad \phi' = \mathbf{U}\,\phi \tag{1.59}$$

The unitary transformation produces another set of orthogonal orbitals. In order to get a specific set of orbitals an additional restriction is required. A selection of common choices is mentioned below.

Canonical orbitals

Canonical orbitals are obtained by diagonalizing the Fock matrix (equation 1.33). Therefore, this representation of the orbitals is of advantage in energy computations since the corresponding eigenvalues are the orbital energies. However, canonical orbitals typically are delocalized over the whole molecule and respect the symmetry of the molecule (orbitals can be assigned to irreducible representations of the point group of the molecule, see section 1.3.10). The orbital energies from the canonical orbitals of a Hartree-Fock calculation can be used to estimate the ionization potential. This is referred to as Koopmans' theorem[108].

In the multiconfigurational self-consistent field approach an effective Fock operator (equation 21 in ref. 124) can be formulated. The orbitals which diagonalize this operator are denoted pseudo-canonical orbitals.

Natural orbitals

Natural orbitals are obtained by a diagonlization of the density matrix[141, 142], which yields the natural orbitals as eigenvectors and the occupation numbers as eigenvalues. The first order reduced density matrix is defined in Löwdin's normalization as[141]:

$$D\left(x_1, x_1'\right) = N_{el} \int \mathrm{d}x_2 \ldots \mathrm{d}x_{N_{el}}\, \Psi\left(x_1, x_2, \ldots, x_{N_{el}}\right) \Psi\left(x_1', x_2, \ldots, x_{N_{el}}\right). \tag{1.60}$$

After its diagonlization the resulting eigenvalues are the occupation numbers (integers) and the eigenvectors are the natural orbitals. The density matrix can simply be represented by a sum over all orbitals:

$$\rho\left(x_1, x_2\right) = \sum_{i}^{N_{orb}} \lambda_i \phi_i\left(x_1\right) \phi_i^*\left(x_2\right) \tag{1.61}$$

The occupation number for states consisting of a single CSF can either be 2 (for a doubly filled orbital, if spin-orbitals are not considered separately), 1 (for a single electron), or 0 (unoccupied). Such natural orbitals are displayed for a set of AK-AKE molecules in the appendix in section A.2.

If canonical orbitals are used, the orbital energies as diagonal elements of the Fock matrix are meaningful, but the diagonal elements of the density matrix are of limited value, since the density matrix is not diagonal in this basis. With natural orbitals meaningful occupation numbers are obtained, but the orbital energies have limited physical meaning, since the Fock matrix has non-zero off-diagonal elements.

Localized orbitals

Natural and canonical orbitals are typically delocalized over the whole molecule. For this reason, they can not be assigned to a certain part of the molecule (as for example a functional group) and it is not straight forward to associate them with specific bonds and their properties. In order to localize the orbitals, the expectation value of certain two electron operators $\widehat{O}$ can be optimized:

$$\left\langle \widehat{O} \right\rangle = \sum_{i=1}^{N_{orb}} \langle \phi_i \phi_i | \widehat{O} | \phi_i \phi_i \rangle \tag{1.62}$$

The following operators have been sugested in the past:[108]:

$\widehat{O} = \left(r_1 - r_2\right)^2$	maximization	Boys	(1.63)
$\widehat{O} = \dfrac{1}{r_1 - r_2}$	maximization	Edminston-Ruedenberg	(1.64)
$\widehat{O} = \sum_{I}^{N_{atoms}} \left\|\rho_I\right\|^2$	maximization	Pipek-Mezey[143]	(1.65)

with r_i being electronic coordinates and ρ_I partial atomic charges, as for example Mullikan charges.

Natural bond orbitals

This method of orbital localization was developed by Weinhold and co-workers[144, 145]. Natural bond orbitals are localized at a subset of atoms in a molecule and are generated from natural atomic orbitals. They have been developed to agree with common chemical concepts, like the Lewis picture.

Wannier orbitals

Wannier orbitals are localized orbitals generated from a non-local plane-wave basis set[146]. They are used to interpret the results of band structure computations and as basis functions for further calculations, for example in dynamical mean-field theory.

Brueckner orbitals

Brueckner orbitals are obtained under the condition that a single Slater determinant has the largest possible overlap with the correlated many-body wave function. For example, in the CI representation of the total electronic wave function (equation 1.35), the molecular orbitals are sought which minimize the coefficients c_a^z, c_{ab}^{zy}, ... and result in the largest possible coefficient c_0. A short discussion of Brueckner orbitals can be found in ref. 147 and the determination of Brueckner orbitals for coupled cluster calculations is presented in ref. 148.

Dyson orbitals

Dyson orbitals can be determined by electron propagator theory[147, 149, 150]. These orbitals are determined by the overlap of the original wave function (Ψ^N) with a wave function containing one electron more or less(Ψ^{N+1}, Ψ^{N-1}). They are not necessarily normalized and form an over-complete set[147].

1.3.12 Description of the potential energy curves and vibrational energy levels

Ab initio computations result in single point evaluations of the potential energy surface, but analytical expressions for the potential are often required, for example in order to calculate rovibrational levels. Besides spline interpolation several analytical expressions have been applied and will be mentioned in the following sections. Analytical expressions often allow a direct extraction of spectroscopic parameters. Parameters listed in the various chapters of this thesis have been determined by fitting a Morse potential to approximately the lowest 8 points of the potential. These parameters can then be used to estimate the energy of vibrational levels:

$$E\left(n\right) = -D_e + \hbar\omega_e\left(n + \frac{1}{2}\right) - \hbar\omega_e x_e\left(n + \frac{1}{2}\right)^2 \tag{1.66}$$

Power series

A rough approximation with the wrong long range behavior is a power series with the equilibrium distance as expansion center:

$$V\left(r\right) = c_S + a_2 * \left(r - r_e\right)^2 + a_3 * \left(r - r_e\right)^3 + \dots \tag{1.67}$$

with r the distance between the two atoms, r_e the position of the minimum of the potential, c_S a constant shift and a_2 a constant related to the bond strength. The vibrational frequency is then given by

$$\omega = \sqrt{\frac{2 * a_2}{\mu}} \qquad \text{with the reduced mass} \qquad \mu = \frac{m_A m_B}{m_A + m_B}. \tag{1.68}$$

Mie and Lennard-Jones potential

The models discussed so far show the wrong long range behavior. A diatomic potential should approach a constant value for $r \to \infty$ and diverge for $r \to 0$. A simple potential showing this behavior is the Lennard-Jones potential[151, 152]:

$$V\left(r\right) = c_S + D_e * \left[\left(\frac{r_e}{r}\right)^{12} - 2\left(\frac{r_e}{r}\right)^{6}\right], \tag{1.69}$$

with r_e as the position of the minimum of the potential, c_S as a constant shift and the potential depth D_e. This potential form has originally been derived for collision processes in gases and shows a characteristic long range behavior (r^{-6}). The Lennard-Jones potential contains only two parameters, the potential depth and the equilibrium distance, which means that there is no parameter left to determine the force constant of the bond. A more generalized form is the so called Mie-potential[152, 153] which contains two additional parameters:

$$V\left(r\right) = c_S + D_e * \left(\frac{n}{n-m}\right) * \left(\frac{n}{m}\right)^{\frac{m}{n-m}} * \left[\left(\frac{r_e}{r}\right)^{n} - \left(\frac{r_e}{r}\right)^{m}\right], \tag{1.70}$$

with n and m being two arbitrary integer numbers fulfilling the condition $n \neq m$. However, the determination of the vibrational constants from these potentials is not straight forward.

Morse potential

The Morse potential has only three free parameters, but is a very good approximation. The well known diatomic potential function is given by[154]

$$V\left(r\right) = c_S + D_e * \left[1 - e^{-a(r-r_2)}\right]^2 = \tag{1.71}$$

$$c_S' + D_e * \left[e^{-2a(r-r_2)} - 2e^{-a(r-r_2)}\right], \tag{1.72}$$

with c_S being the shift to the long range energy and c'_S the shift to the potential minimum. The vibrational frequency and the asymmmetry parameter can be determined analytically for this potential with the following expressions:

$$\omega_e = \frac{a}{2\pi}\sqrt{\frac{2D_e}{\mu}}, \qquad \omega_e x_e = \frac{\omega_e^2}{4D_e}. \tag{1.73}$$

Dunham expansion

The Dunham expansion is based on a description of the potential with a power series in the variable $\xi = \frac{r-r_e}{r_e}$.

$$V\left(\xi\right) = a_0 \xi^2 \left(1 + \sum_{n=1,2,3,\ldots} a_n \cdot \xi^n\right) \tag{1.74}$$

Since it is a power series, the derivatives of the potential are simply given by

$$\begin{aligned}
V'(r_e) =& 0, && (1.75)\\
V''(r_e) =& \frac{2}{r_e^2} \cdot a_0 = \frac{2}{r_e^2}\frac{\omega_e^2}{4B_e}, && (1.76)\\
V^{n+2}(r_e) =& \frac{(n+2)!}{r_e^{n+2}} \cdot a_0 \cdot a_n. && (1.77)
\end{aligned}$$

Spectroscopic parameters can be calculated from the coefficients a_n as determined by Dunham[155] and Varshni[156]:

$$\begin{aligned}
B_e =& \frac{h}{8\pi^2 m r_e^2 c} && (1.78)\\
\omega_e =& \sqrt{4B_e a_0} && (1.79)\\
Y_{00} =& \frac{B_e}{8}\left(3a_2 - \frac{7}{4}a_1^2\right) && (1.80)\\
Y_{10} =& \omega_e\left[1 + \frac{B_e^2}{4\omega_e^2}\left(25a_4 - \frac{95}{2}a_1a_3 - \frac{67}{4}a_2^2 + \frac{459}{8}a_1^2a_2 - \frac{1155}{64}a_1^4\right)\right] && (1.81)\\
Y_{01} =& B_e\left[1 + \frac{B_e^2}{2\omega_e^2}\left(15 + 14a_1 - 9a_2 + 15a_3 - 23a_1a_2 + \frac{21}{2}\left(a_1^2 + a_1^3\right)\right)\right] && (1.82)\\
Y_{01} =& \frac{B_e^2}{\omega_e}\left[6\left(1+a_1\right) + \frac{B_e^2}{\omega_e^2}\left(175 + 285a_1 - \frac{335}{2}a_2 - 190a_3 - \frac{225}{2}a_4 + 175a_5\right.\right.\\
&+ \frac{2295}{8}a_1^2 - 459a_1a_2 + \frac{1425}{4}a_1a_3 - \frac{795}{2}a_1a_4 + \frac{1005}{8}a_2^2 - \frac{715}{2}a_2a_3 + \frac{1155}{4}a_1^3\\
&\left.\left.- \frac{9639}{16}a_1^2a_2 + \frac{5145}{8}a_1^2a_3 + \frac{4677}{8}a_1a_2^2 + \frac{14259}{16}a_1^3a_2 + \frac{31185}{128}\left(a_1^4 + a_1^5\right)\right)\right] && (1.83)\\
&\ldots
\end{aligned}$$

Dunham denoted the spectroscopic constants with Y_{ij}, which allow the calculation of energy levels with the rotational quantum number N and the rotational quantum number ν:

$$E\left(N,\nu\right)=\sum_{i,j}Y_{ij}\cdot\left(\nu+\frac{1}{2}\right)^{l}\cdot N^{j}(N+1)^{j} \tag{1.84}$$

Relations of this set of constant to commonly used spectroscopic parameters are listed in table 1.10.

Table 1.10: Assignment of Dunham coefficients to spectroscopic parameters.

$Y_{00}\approx T_e$	$Y_{10}\approx\omega_e$	$Y_{20}\approx-\omega_e x_e$	$Y_{30}\approx-\omega_e y_e$
$Y_{01}\approx B_e$	$Y_{11}\approx-\alpha_e$	$Y_{21}\approx-\gamma_e$	
$Y_{02}\approx-D_e$	$Y_{12}\approx-\beta_e$		
$Y_{03}\approx H_e$			

LEVEL and BETAFIT programs

Other examples for analytical expressions, for example the Morse/long-range potential function, are available in software packages such as LEVEL 8.2[157] and betaFit[158]. In both programs, it is possible to fit these functions to a set of *ab initio* data points. In the course of this work the betaFit package was used extensively for potential fits. Afterwards, surface parameters were extracted and used in the LEVEL software package to calculate the rovibrational energy levels and Frank-Condon factors between them. This program uses the Numerov shooting method to determine the nuclear wave function for diatomic molecules. A one-dimensional grid is set up for the radius and the values of the wave function are fixed at the boundaries. Then, the wave function is propagated according to the Schrödinger equation from one to the other boundary. A possible wave function has been found if it fulfills the boundary condition. In the analysis presented here only the first rotational sublevel was considered since only the vibrational structure was resolved in the experiments.

1.4 Properties of diatomic molecules

1.4.1 Atomic constituents

The properties of atoms can be used to estimate the behavior of these atoms in a bound molecule. An example is the calculation of the long range behavior of alkali-alkaline earth molecules by Jiang *et al.*[159] from static dipole and quadrupole polarizabilities. In order to understand the behavior of the atoms in a diatomic molecule we list several atomic properties in table 1.11.

Table 1.11: Atomic properties of the elements used in this work. Explanations of properties and abbreviations are given in the text. The sources of the values are listed in the header 'Ref.' and their units in the header 'un.'.

	IP	EA	EN	EN	η	α	r_{VdW}	r_{cov}	$\alpha(^3P)$
Ref.	13	160	160			160, 161	162	163	here[b]
un.	cm^{-1}	cm^{-1}	Paul.	Mull.	eV	a.u.	Å	Å	a.u.
Li	43487	4985	0.98	3.00	2.39	164.2	2.12	1.28	
Na	41449	4419	0.93	2.84	2.30	162.7	2.50	1.66	
K	35010	4045	0.82	2.42	1.92	290.8	2.73	2.03	
Rb	33691	3919	0.82	2.33	1.85	318.8	3.21	2.2	
Cs	31406	3804	0.79	2.18	1.71	401	3.48	2.44	
Fr	32849	3710	0.70	2.27	1.81	313.7		2.6	
Be	75193	not st.	1.57	4.66[a]	4.66[a]	37.7	1.98	0.96	38
Mg	61671	not st.	1.31	3.82[a]	3.82[a]	71.7	2.51	1.41	130
Ca	49306	198	1.00	3.07	3.04	169	2.62	1.76	301
Sr	45932	387	0.95	2.87	2.82	186	2.84	1.95	542
Ba	42035	1166	0.89	2.68	2.53	268	3.03	2.15	
Ra	42573	807	0.90	2.69	2.59	248		2.21	
He	198311	not st.	–	12.29[a]	12.29[a]	1.384	1.43	0.28	
Cr	54576	5380	1.66	3.72	3.05	78.3	2.45	1.39	

[a] ... An electron affinity of zero was used for the calculation of these values since there is no bound state with an additional electron.

[b] ... In the course of this work the polarizabilities of the excited ^3P states were calculated for a selection of atoms.

The first column of table 1.11 contains the ionization energy or ionization potential (IP). Helium with its closed shell has the highest value and its excited states have also a larger separation from the ground state than in other atoms, which makes it a good matrix for spectroscopic investigations[164]. In general, the ionization potentials decrease for heavier atoms. This can be observed for the series of AK and AKE atoms. Similarly sized alkaline earth atoms have a larger ionization potential due to the closed subshell. This closed subshell also makes it more difficult to attach an electron, which explains the small electron affinities (EA) of the AKE atoms. The electron affinities of the alkali atoms are also significantly smaller than their ionization potentials. Both values, IP and EA, can be used to calculate the electronegativity[165]:

$$EN(\text{Mulliken}) = \frac{IP\,[eV] + EA\,[eV]}{2} \approx -\mu \tag{1.85}$$

These values are listed in the 5th column of table 1.11 and are an estimation of the pull on the electrons in a molecule. Thermodynamically, this is described by the chemical potential (μ) for the electrons, which can roughly be estimated by the negative electronegativity (equation 1.85). In contrast to the Mulliken values, the Pauling electronegativity (4th column in table 1.11) is derived from dissociation energies. For helium, no value can be found in the literature because it rarely forms a stable molecule. The highest value in the Pauling scale is about 4 which is obtained for fluorine. In the Mulliken scale used in the table, fluorine has a value of 10.4, a smaller value than the one listed for helium in table 1.11. In addition to this rough estimation, the chemical potential can be determined with density functional theory as the first derivative of the energy with respect to the number of electrons. The second derivative gives the chemical hardness (η):

$$\mu = \frac{\partial E}{\partial N} \qquad \eta = \frac{\partial^2 E}{\partial N^2} \tag{1.86}$$

The latter can again be estimated from the IP and EA via

$$\eta \approx \frac{\mathrm{IP} - \mathrm{EA}}{2} \tag{1.87}$$

and is listed in the 6th column of table 1.11.

The electronegativity (Pauling scale) will be used in chapter 5 to model the permanent electric dipole moment. Another atomic property which is relevant for the model, is the atomic polarizability (α, 7th column of table 1.11). This quantity gives the magnitude of the induced change of the electron density by an external field, as for example caused by another atom. In general, the size of the orbitals and the related polarizability increases within the same group in the periodic table. An exception to this behavior are Fr and Ra, see table 1.11.

The 8th and 9th column of table 1.11 contain the estimated van der Waals and covalent radii. In chapter 5, they will be compared to bond distances determined by *ab initio* methods.

The values listed in the last column of table 1.11 were computed in the course of this work by a finite field method. The same approach was used to calculate polarizabilities for the ground state. Differences of less than 20 a.u. from the values presented in the table were obtained. The excited ^{3}P state of Be has a similar polarizability as the ground state; for the heavier AKE atoms the excited state values are significantly higher.

1.4.2 Permanent electric dipole moment (PEDM)

The permanent electric dipole moment of a molecule is given by the following formula for fixed nuclear coordinates:

$$\mu = \mu_{el} + \mu_N = \sum_{i=1}^{N_{el}} \int \psi^* (\mathbf{r_i}) \left(-e\hat{\mathbf{r}}\right) \psi (\mathbf{r_i})\, \mathbf{dr_i} + \sum_{I=1}^{N_N} Z_I \mathbf{R_I}. \tag{1.88}$$

For a specific vibrational state the PEDM is determined by averaging over different nuclear coordinates using the vibrational wave function. A non-zero electric dipole moment is obtained, if the center of the positive charges (atomic nuclei) and the center of the negative charges are not the same, as shown in figure 1.3. This sketch depicts the situation for AK-AKE molecules in the $^2\Sigma^+$ ground state. The core orbitals and nuclei are combined because they have the same center. Only the charge of the remaining valence electrons and the remaining charge of the cores are shown. The positive charges are centered at the position of the nuclei, one positive charge representing the alkali core, the other two representing the alkaline earth core. The valence electrons are distributed over the molecule. Additionally, the center of mass, of negative and positive charge are indicated by arrows. In this case, the center of negative charge is closer to the alkaline earth than the alkali atom. For our choice concerning the coordinate system (axis pointing from the AK atom to the AKE atom) the permanent electric dipole moment is positive. In addition to the permanent electric dipole moment an induced electric dipole or quadrupole moment might arise in an external field, as for example produced by another atom or molecule. The total electric dipole moment is given by:

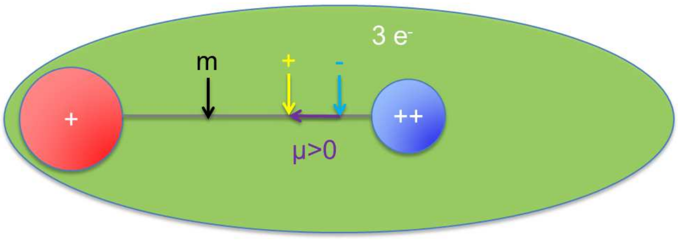

Figure 1.3: center of charges for the ground state of an AK-AKE molecule.

$$\mu = \mu_p - \alpha \mathbf{E} + \frac{1}{2}\mathbf{E}\beta\mathbf{E} + \ldots, \tag{1.89}$$

with the permanent dipole moment μ_p, the dipole polarizability α, and the quadrupole polarizability β in an external electric field $\mathbf{E}$.

In appendix B some models predicting the permanent electric dipole moment are mentioned. These models are mainly concerned with molecules showing a large charge transfer, like AK halides or AKE halides.

Ionic character - Pauling criterion

The Pauling criterion is a simple parameter to estimate the ionic character of a molecule. This is done using PEDM (μ) and the equilibrium distance (r_e), either obtained experimentally or from *ab initio* computations.

$$f_{ION} = \frac{|\mu|}{e \cdot r_e} \tag{1.90}$$

The f_{ION} value gives the fraction of ionic character in %. However, this crude approximation does not work for strong deformations and highly ionic systems.

Experimental relevance of the PEDM

In the following experimental observations relying on the PEDM and applications of it are listed.

A) Stark effect

The Stark effect or Stark shift is the shift and splitting of spectral lines of atoms and molecules in external electric fields. The linear Stark effect is observed if the molecule or atom has a permanent electric dipole moment. In this case, the energies change linearly with the electric field. Depending on the orientation of the dipole in the electric field the energies are different. This leads to an additional splitting of the levels in discrete number of states due to the limitation of quantized alignments. The permanent electric dipole moment can be determined from observed spectral splittings. The quadratic Stark effect, described by second order perturbation theory, is relevant for atoms and molecules without a permanent electric dipole moment. For such systems the electric field induces a dipole moment, which leads to a splitting of the states with a quadratic field dependence.

B) Rotational spectroscopy

Rotational energy differences correspond to microwave and far-infrared electromagnetic waves. Direct transition between rotational states are only possible if there is a non-zero permanent electric dipole moment. This means rotational spectroscopy is not possible for molecules with symmetries that forbid permanent electric dipole moments, as for example in homonuclear diatomics.

C) Alignment of molecules

The permanent electric dipole moment leads to an alignment of molecules in an electric field because an energy is associated with the orientation of the dipole moment. Both, the permanent electric dipole moment and the polarizability, are relevant for the alignment of ultracold molecules[166, 167].

D) Coupling of molecules in optical lattices

It was suggested to use adjustable couplings of molecules for experiments in optical lattices[31]. Such couplings can be realized by microwave radiation, which can only interact with the molecules if there is a permanent electric dipole moment.

Finite field calculations

Certain molecular properties in this thesis have been determined by the response (change) of the molecular energy to a small electric field. This approach[168, 169] is particularly useful since it requires energy evaluations only and can be applied to any *ab initio* method. The energy E of a molecule shows following dependence on a uniform external electric field $\vec{F}$:

$$E\left(\vec{F}\right) = E_0 + \vec{\mu}\vec{F} + \frac{1}{2}\vec{F}\alpha\vec{F} + \dots \tag{1.91}$$

Using this definition, the dipole moment and the polarizability can be determined in the following manner:

$$\mu_i = -\left.\frac{\partial E\left(F_i\right)}{\partial F_i}\right|_{F_i=0}, \tag{1.92}$$

$$\alpha_{ij} = -\left.\frac{\partial^2 E\left(F_i, F_j\right)}{\partial F_i \partial F_j}\right|_{F_i=0, F_j=0}, \tag{1.93}$$

with i and j standing for the three Cartesian components (x, y, z). These properties can now be determined by the influence of a small field (ΔF) on the undisturbed molecule: The derivative is then approximated by finite field differences (3 point formula):

$$\mu_i|_{F=0} = -\frac{E\left(\Delta F_i\right) - E\left(-\Delta F_i\right)}{2\Delta F_i}, \tag{1.94}$$

$$\alpha_{ij}|_{F=0} = -\frac{E\left(\Delta F_{ij}\right) + E\left(-\Delta F_{ij}\right) - 2E\left(0\right)}{\Delta F_{ij}^2}. \tag{1.95}$$

More accurate approximations are available but need additional energy calculations (5 point formula):

$$\mu_i|_{F=0} = -\frac{-E\left(2\Delta F_i\right) + 8E\left(\Delta F_i\right) - 8E\left(-\Delta F_i\right) + E\left(-2\Delta F_i\right)}{12\Delta F_i}, \tag{1.96}$$

$$\alpha_{ij}|_{F=0} = -\frac{-E\left(2\Delta F_i\right) + 16E\left(\Delta F_i\right) - 30E\left(0\right) + 16E\left(-\Delta F_i\right) - E\left(-2\Delta F_i\right)}{12\Delta F_i^2}. \tag{1.97}$$

1.4.3 Transition dipole moment

In section 1.3 the calculation of the energies of vibronic levels was outlined. This determines the position of the spectral lines, but does not give information on intensities. One quantity describing the intensity is the line strength between an initial and final state (S_{if}). It can be calculated as a sum over the squared transition dipole moments of all degenerate states:

$$S_{if} = \sum_{i,f} \left|\mu_{if}\right|^2 \tag{1.98}$$

The transition dipole moment for a transition from an initial state i to final state f takes the following form:

$$\mu_{if} = \int \Psi_{tot,i}\left(\mathbf{X}\right) \hat{\mu}\, \Psi_{tot,f}\left(\mathbf{X}\right) \mathrm{d}\mathbf{X}\,, \tag{1.99}$$

with a dipole moment operator that comprises electronic and nuclear contributions:

$$\widehat{\mu} = \widehat{\mu_{el}} + \widehat{\mu_N} = \sum_{i=1}^{N_{el}} -e\,\hat{\mathbf{r}}_{\mathbf{i}} + \sum_{I=1}^{N_N} Z_I \widehat{\mathbf{R}_{\mathbf{I}}}. \tag{1.100}$$

This operator is relevant for electric dipole transitions which are the strongest and only transitions treated in this work. Weaker transitions, such as magnetic dipole or electric quadrupole transitions, have been neglected. More details on the derivation of the transition probabilities and the treatment of higher moments (magnetic dipole, electric quadrupole) can be found in ref. 170.

Within the Born-Oppenheimer approximation, the wave function can be written as a product of an electronic and a nuclear part and the transition dipole moment splits into two parts:

$$\mu_{if} = \int\int \Psi_{el,i}\left(\mathbf{r},\mathbf{R}\right)\ \Psi_{N,i}\left(\mathbf{R}\right)\left[\widehat{\mu_{el}} + \widehat{\mu_N}\right]\Psi_{el,f}\left(\mathbf{r},\mathbf{R}\right)\ \Psi_{N,f}\left(\mathbf{R}\right)\mathrm{d}\mathbf{r}\,\mathrm{d}\mathbf{R} \tag{1.101}$$

$$= \int\left[\int \Psi_{el,i}\left(\mathbf{r},\mathbf{R}\right)\ \Psi_{el,f}\left(\mathbf{r},\mathbf{R}\right)\mathrm{d}\mathbf{r}\right]\ \Psi_{N,i}\left(\mathbf{R}\right)\ \widehat{\mu_N}\ \Psi_{N,f}\left(\mathbf{R}\right)\mathrm{d}\mathbf{R} \tag{1.102}$$

$$+ \int\left[\int \Psi_{el,i}\left(\mathbf{r},\mathbf{R}\right)\widehat{\mu_{el}}\ \Psi_{el,f}\left(\mathbf{r},\mathbf{R}\right)\mathrm{d}\mathbf{r}\right]\ \Psi_{N,i}\left(\mathbf{R}\right)\ \Psi_{N,f}\left(\mathbf{R}\right)\mathrm{d}\mathbf{R} \tag{1.103}$$

The first part (equation 1.102) is zero if the initial and final electronic wave function ($\Psi_{el,i}$,$\Psi_{el,f}$) are not the same, because the electronic wave functions are orthonormal. This means in such a transition the electronic state stays the same, but the vibrational state changes. This term is relevant for pure vibrational spectroscopy in a single electronic state. The second term (equation 1.103) is relevant for this work, since it treats transitions between different electronic states. The expression for an electronic transition can be simplified assuming that the electric dipole moment remains more or less constant for the range of the vibrational wave function. This approximation is suitable for deeply bound initial states with a well localized wave function, as for example the lowest vibrational level of the ground state. Such a situation is encountered for the majority of the experimental measurements discussed in this work because helium nanodroplets cool the molecules efficiently. Following approximation was used for the total transition dipole moment:

$$\mu_{if} = \int\left[\int \Psi_{el,i}\left(\mathbf{r},\mathbf{R}\right)\widehat{\mu_{el}}\ \Psi_{el,f}\left(\mathbf{r},\mathbf{R}\right)\mathrm{d}\mathbf{r}\right]\ \Psi_{N,i}\left(\mathbf{R}\right)\ \Psi_{N,f}\left(\mathbf{R}\right)\mathrm{d}\mathbf{R} \tag{1.104}$$

$$\approx \int \Psi_{el,i}\left(\mathbf{r},R_e\right)\widehat{\mu_{el}}\ \Psi_{el,f}\left(\mathbf{r},R_e\right)\mathrm{d}\mathbf{r}\int \Psi_{N,i}\left(\mathbf{R}\right)\ \Psi_{N,f}\left(\mathbf{R}\right)\mathrm{d}\mathbf{R}\,, \tag{1.105}$$

with R_e being the equilibrium internuclear separation of the initial state: The first part forms the electronic transition dipole moment (TDM) and can be calculated from the involved electronic wave functions:

$$TDM_{if} = \int \Psi_{el,i}\left(\mathbf{r},R_e\right)\widehat{\mu_{el}}\ \Psi_{el,f}\left(\mathbf{r},R_e\right)\mathrm{d}\mathbf{r}\,. \tag{1.106}$$

The square of the vibrational part of equation 1.105 is the so called Franck-Condon (FC) factor:

$$FC_{if} = \left|\int \Psi_{N,i}\left(\mathbf{R}\right)\ \Psi_{N,f}\left(\mathbf{R}\right)\mathrm{d}\mathbf{R}\right|^2 \tag{1.107}$$

1.5 Relativistic effects

The Schrödinger equation (equation 1.7) is not Lorentz invariant and violates the laws of special relativity. The corresponding relativistic equations are the Klein-Gordon equation for spin 0 particles and the Dirac equation for spin 1/2 particles like electrons. The time-dependent Dirac equation is given as:

$$\left[c\alpha \cdot p + \beta mc^2 + \mathbf{V}\right] \Psi = i\frac{\partial \Psi}{\partial t}, \tag{1.108}$$

with α and β denoting the following 4×4 matrices:

$$\alpha_{x/y/z} = \begin{pmatrix} 0 & \sigma_{x/y/z} \\ \sigma_{x/y/z} & 0 \end{pmatrix} \qquad \sigma_x = \begin{pmatrix} 0 & 1 \\ 1 & 0 \end{pmatrix} \quad \sigma_y = \begin{pmatrix} 0 & -i \\ i & 0 \end{pmatrix} \quad \sigma_z = \begin{pmatrix} 1 & 0 \\ 0 & -1 \end{pmatrix} \tag{1.109}$$

$$\beta = \begin{pmatrix} \mathbf{I} & 0 \\ 0 & \mathbf{I} \end{pmatrix} \qquad \mathbf{I} = \begin{pmatrix} 1 & 0 \\ 0 & 1 \end{pmatrix} \tag{1.110}$$

The wave function describing the system Ψ now has four components, two spin states for electrons and two spin states for positrons. p is the 4-component momentum vector, m the mass of the particle and $\mathbf{V}$ the matrix of potentials for interaction with other particles. In the more accurate treatment of quantum electrodynamics the potential is no longer a simple Coulomb potential as in equation 1.7, because new effects such as retardation have to be considered. A software package which solves the Dirac equation (equation 1.108) for small molecular systems is the DIRAC code[171]. It determines both spinors and includes spin-orbit interaction by default.

One relativistic effect is the velocity dependence of the mass of the particle. In the case of molecules and atoms this becomes relevant for strongly bound electrons with a probability density close to the core. By including the relativistic contributions, the corresponding orbitals are contracted and the binding energy is increased. Another relativistic effect is the spin-orbit coupling, which is discussed in section 1.6. Typically, relativistic contributions become increasingly important for heavy molecules. The Dirac equation is more complex than the Schrödinger equation and finding a solution is computationally costly. Under this aspect, several approximations have been developed to include relativism.

One widespread and simple method for the inclusion of relativistic effects are effective core potentials (see section 1.3.2). In this case, the inner core orbitals, which experience the largest influence of relativistic effects, are replaced by an effective potential. In the current work this approach was used in many cases concerning multiconfigurational configuration interaction calculations for heavy AK or AKE atoms.

Another method is to add corrections to the Hamiltonian. One example is the Douglas-Kroll-Hess Hamiltonian[172–175], which can be applied in one component computations. In the current work this was done for the CrHe molecule.

Further information on relativistic computations and effects can be found in refs. 176 and 177.

1.6 Spin-orbit coupling

The spin is an important property of elementary and composite particles, which manifests in two ways. Firstly, depending on the spin, the particles show different statistical behavior. For an integer spin the Bose-Einstein statistic is relevant, for a half-integer spin the Fermi-Dirac statistic. Secondly, the spin also corresponds to a magnetic dipole which interacts with the environment. One example of magnetic interaction between the spin and an external magnetic field is the deflection of atoms with an unpaired spin in an inhomogeneous magnetic field as was demonstrated by Stern and Gerlach[178].

This magnetic moment interacts in relativistic quantum mechanics with the magnetic field generated by the movement of the electrons within the orbitals, which is known as spin-orbit coupling. In the beginning, empirical formulas were used to describe this interaction, see section 1.6.1. As has been stated, the Dirac equation allows to compute this effect directly (equation 1.108), but obtaining solutions for this equation is rather expensive. Therefore, several approximations have been derived. One example is the Breit-Pauli Hamiltonian presented in section 1.6.2.

1.6.1 Empirical approach

For this approach the interaction energy of the two magnetic dipoles (spin and orbital angular momentum) is calculated by:

$$\hat{H}_{so} = A\,\vec{L} \cdot \vec{S} \tag{1.111}$$

where A is an effective spin-orbit constant, which can be adjusted to the atomic spin-orbit splitting, $\vec{L}$ is the total orbital angular momentum and $\vec{S}$ is the total spin of the electrons. This can now be applied to the lowest states of alkali-alkaline earth molecules using the correct angular momentum coupling. This was done in ref. 179 and yielded the following results:

For the ^2P-asymptote of the alkali atom in the non-relativistic case one $^2\Sigma^+$ and two degenerate $^2\Pi$ states can be obtained. They couple via their spin (S $= \frac{1}{2}$, doublet state), and three spin-orbit states with values of $|\Omega| = \frac{1}{2}$ and $|\Omega| = \frac{3}{2}$ for the projection of the total angular momentum are obtained by matrix diagonlization:

$$\widehat{H}_{|\Omega|=\frac{3}{2}} = E\left(^2\Pi, R\right) + 2A_{AK} \tag{1.112}$$

$$\widehat{H}_{|\Omega|=\frac{1}{2}} = \begin{pmatrix} E\left(^2\Sigma^+, R\right) & \sqrt{2}A_{AK} \\ \sqrt{2}A_{AK} & E\left(^2\Pi, R\right) + A_{AK} \end{pmatrix} \tag{1.113}$$

$E\left(\ldots, R\right)$ are the distance-dependent energies of the respective non-relativistic state, and A_{AK} is the effective spin-orbit constant of the alkali atom in this state.

The ^3P-asymptote of the alkaline earth atom corresponds to one $^2\Sigma^+$, one $^4\Sigma^+$, two degenerate $^2\Pi$, and two degenerate $^4\Pi$ states. The nine spin-orbit coupled states can be determined by the following matrices:

$$\widehat{H}_{|\Omega|=\frac{5}{2}} = E\left({}^4\Pi, R\right) + 2A_{AKE} \tag{1.114}$$

$$\widehat{H}_{|\Omega|=\frac{3}{2}} = \begin{pmatrix} E\left({}^2\Pi, R\right) + \frac{2}{3}A_{AKE} & \sqrt{\frac{1}{3}}A_{AKE} & -\frac{\sqrt{2}}{3}A_{AKE} \\ \sqrt{\frac{1}{3}}A_{AKE} & E\left({}^4\Sigma^+, R\right) & \sqrt{\frac{2}{3}}A_{AKE} \\ -\frac{\sqrt{2}}{3}A_{AKE} & \sqrt{\frac{2}{3}}A_{AKE} & E\left({}^4\Pi, R\right) + \frac{1}{3}A_{AKE} \end{pmatrix} \tag{1.115}$$

$$\widehat{H}_{|\Omega|=\frac{1}{2}} = \begin{pmatrix} E\left({}^2\Sigma^+, R\right) & \sqrt{\frac{8}{9}}A_{AKE} & 0 & -\frac{1}{3}A_{AKE} & \sqrt{\frac{1}{3}}A_{AKE} \\ \sqrt{\frac{8}{9}}A_{AKE} & E\left({}^2\Pi, R\right) - \frac{1}{3}A_{AKE} & \frac{1}{3}A_{AKE} & -\frac{\sqrt{2}}{3}A_{AKE} & 0 \\ 0 & \frac{1}{3}A_{AKE} & E\left({}^4\Sigma^+, R\right) & \sqrt{\frac{8}{9}}A_{AKE} & \sqrt{\frac{2}{3}}A_{AKE} \\ -\frac{1}{3}A_{AKE} & -\frac{\sqrt{2}}{3}A_{AKE} & \sqrt{\frac{8}{9}}A_{AKE} & E\left({}^4\Pi, R\right) - \frac{1}{3}A_{AKE} & 0 \\ \sqrt{\frac{1}{3}}A_{AKE} & 0 & \sqrt{\frac{2}{3}}A_{AKE} & 0 & E\left({}^4\Pi, R\right) - A_{AKE} \end{pmatrix}. \tag{1.116}$$

1.6.2 Breit-Pauli Hamiltonian

Approximate expressions can be derived from the Dirac equation in quantum electrodynamics. One example is the Breit-Pauli Hamiltonian (taken from ref. 180):

$$\hat{H}_{SO} = \frac{e^2\hbar}{2m^2c^2}\sum_i\sum_K \frac{Z_K\mathbf{r}_{iK}\times\hat{\mathbf{p}}\left(i\right)}{r_{iK}^3}\cdot\hat{\mathbf{s}}\left(i\right) - \frac{e^2\hbar}{2m^2c^2}\sum_{i,j,i\neq j}\frac{\mathbf{r}_{ij}\times\hat{\mathbf{p}}\left(i\right)}{r_{ij}^3}\left[\hat{\mathbf{s}}\left(i\right)+2\hat{\mathbf{s}}\left(j\right)\right], \tag{1.117}$$

with the spin-operators $\hat{\mathbf{s}}$ and orbital angular momentum operators $\mathbf{r}\times\hat{\mathbf{p}}$. It can be evaluated using the wave functions and orbitals of a non-relativistic calculation. Each doubly occupied orbital is then split up into two spin-orbitals. The Breit - Pauli Hamiltonian has been used as implemented in MOLPRO by Berning and Schweizer[181].

Chapter 2

A weakly bound system – CrHe

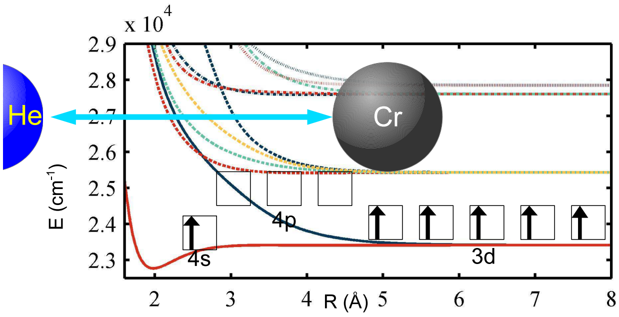

This chapter corresponds to the publication:
An ab initio study of the CrHe diatomic molecule: The effect of van der Waals distortion on a highly magnetic multi-electron system
by Johann V. Pototschnig, Martin Ratschek, Andreas W. Hauser, and Wolfgang E. Ernst
in *Physical Chemistry Chemical Physics*, **2014**, *16*, 9469,
which was written by the author of the thesis.

The author of the thesis was responsible for:

- author of the publication
- realization and implementation of the *ab initio* calculations
- interpretation of the result, comparison to experiments by Andreas Kautsch

The contributions of the co-authors are listed below:

- M. Ratschek: editing, assistance with the *ab initio* calculations, help with the computational infrastructure
- A. W. Hauser: supervision, editing, help with the interpretation of the results
- W. E. Ernst: supervision, editing, funding

Reproduced from ref. 3 with permission from the PCCP Owner Societies. The article is available at https://doi.org/10.1039/c4cp00559g.

Abstract

The interaction between He and Cr is investigated by means of post-Hartree-Fock molecular orbital theory. We analyze the influence of the van der Waals forces on the complex electronic structure of the chromium atom, starting with its septet manifold and cover the first few electronically excited states up to 30000 cm^{-1}. For the sake of a direct comparison to ongoing experiments on Cr-doped helium nanodroplets we extend our analysis to selected states of the quintet manifold in order to explain a non-radiating relaxation from y $^7\mathrm{P}^\circ$ to z $^5\mathrm{P}^\circ$.

2.1 Introduction

Small transition metal clusters have gained much attention in recent years due to the vast amount of their potential applications[182–184]. The partial occupation of the nd and $(n+1)$s shells in transition metal (TM) atoms, which results in outstanding magnetic properties and high densities of low lying electronically excited states, makes a theoretical treatment of systems containing TM atoms particularly challenging. Among them, the chromium atom may be considered as one of the most demanding cases: the half-filled 3d and 4s subshells give rise to a septet ground state with a huge magnetic moment of 6 μ_B[185]. From this configuration it is already obvious that any quantum-chemical treatment of electronically excited states must be based on a comprehensive multi-reference approach to properly account for the statical part of electronic correlation. Since the calculation of electronic excitations of a single Cr atom is still a challenging task for the available methods, the appropriate description of larger Cr-clusters and their numerous spin manifolds, especially the spin-parallel configurations, is beyond the scope of current simulation techniques. Much effort is undertaken, theoretically[186–188] as well as experimentally[189–191], to at least understand the basic magnetic properties of the mostly antiferromagnetic Cr clusters, which strongly depend on the shape and size of the investigated nanostructures. The magnetic state of bulk chromium at room temperature and atmospheric pressure was experimentally determined to be the spin-density-wave antiferromagnetism[192].

Hence, from a theoretical point of view, but also from the experimental, as will be explained below, it makes sense to tackle the problem of finding a suitable description for the formation and the electronic excitation of high-spin clusters of TM atoms on a much simpler route: We suggest a basic analysis of the van der Waals forces, which keep the atoms of high-spin systems together, and the effect of these weak interactions on the electronic structure of a Cr atom in the smallest possible system – the CrHe diatomic molecule.

It is the aim of this article to provide potential curves for the first few electronically excited states of the CrHe diatomic molecule in its septet manifold. Furthermore, we include selected states of the quintet manifold for a direct comparison to recent experimental results of our group on Cr-doped helium nanodroplets. This is the second reason why we choose the CrHe diatomic system: Helium Nanodroplet Isolation Spectroscopy

(HENDI)[164, 193] offers this unique chance to study small metal clusters exclusively in their high-spin states, as has been shown in the past for K, Rb and Ag clusters[164, 194–197]. This selectivity is based on the fact that the helium nanodroplet, acting as an almost inert and extremely cold environment of about 0.37 K[198], is more likely to survive multiple dotations[199, 200], e.g. with Cr atoms, if the binding energies released into the droplet are low. While the low-spin cluster formation of metal atoms, which may be interpreted as growth of metallic complexes, necessitates the dissipation of binding energies in the range of several thousands of wave numbers, the binding energies of van der Waals bound, spin parallel clusters are significantly lower. This makes HENDI a promising method for the generation of high-spin clusters of chromium atoms. Although practically inert, the helium environment does affect the electronic structure. This became particularly evident in recent experiments of our group on photoinduced ejection of Cr atoms from the droplet[17, 18]. The whole process, a two photon excitation, is supposed to contain a nonradiative relaxation from the y^7P° to the z^5P° state. We discuss this phenomenon of an intersystem crossing between the septet and the quintet manifold on the simplified model of a Cr-He diatomic molecule.

Charged chromium-helium systems have been extensively analyzed in the past[201–204] . The inelastic collision rates and elastic cross sections for Cr and He were determined in experiments using He buffer gas cooling for loading a magnetic trap with chromium[205]. The ground state of the chromium dimer was investigated by several authors, using a wide range of theoretical methods[206–209]. Excited states of the chromium dimer and the heteronuclear diatomic molecules of V, Cr, Mo, and W are discussed in refs. 210 and 211, respectively. The high magnetic moment of chromium raises its prospects for atomic traps[66, 185, 212]. To our knowledge, this article contains the first theoretical study of electronic excitations of the neutral CrHe diatomic molecule.

2.2 Computational aspects

We start our computational approach with a series of benchmark calculations on the ground state of the charged $CrHe^+$ diatomic molecule and the excited states of a single Cr atom. Both systems are well studied and allow a direct comparison to experiment. In a second step, we calculate the potential energy curves for the neutral CrHe diatomic molecule in its lowest electronic states of the triplet, quintet and septet spin manifolds. We use the basis set families aug-cc-pVNZ-DK and aug-cc-pVNZ (with N=T,Q,5) which were provided by Balabanov and Peterson[213] for Cr and by Woon and Dunning[214] for He. The Douglas Kroll (DK) optimized basis sets were only used in ground state calculations and benchmark calculations for excitations of the Cr atom using the Douglas-Kroll-Hess Hamiltonian for relativistic corrections[174] (marked DK). All calculations were performed with the MOLPRO software package[140]. Orbitals and state-averaged wave functions (CSFs) are presented in the program-specific internal ordering for the C_{2v} point group ($A_1/B_1/B_2/A_2$), which was used for all systems. For the lowest state in each multiplicity two different molecular-orbital based post-Hartree-Fock methods were compared: a) a single-reference restricted open-shell variant of the coupled cluster method with single, double and non-iterative triple excitations (CCSD(T))[215] based on a restricted open-shell Hartree-Fock reference function (ROHF), and b) a state-averaged multiconfigurational self-consistent field method, the complete active space SCF (CASSCF) approach of Werner and Knowles[122, 123, 125, 216], followed by a multi-reference configuration interaction calculation (MRCI) of second order[217]. Scalar relativistic effects were taken into account by applying the Douglas-Kroll-Hess correction of the 8^{th} order. To improve the accuracy of the lowest state in each spin manifold we extrapolate to the basis set limit via the formula[108, 110]

$$\Delta E_{\mathrm{corr},\infty} = \frac{N^3 E_{\mathrm{corr},N} - M^3 E_{\mathrm{corr},M}}{N^3 - M^3}, \tag{2.1}$$

with M and N denoting the largest angular momentum quantum numbers of the two basis sets used for the extrapolation. This formula yields an estimation for the correlation energy itself, which has to be added to the Hartree-Fock result to obtain the estimated total energy. The energies were further corrected for the Basis Set Superposition Error (BSSE) before extrapolation to avoid artificial oscillations. The method of choice was the counterpoise (CP) correction suggested by Boys and Bernardi[109]. Excited states in the different multiplicities were treated within CASSCF/MRCI theory. In these cases, neither an extrapolation to the basis set limit, nor CP corrections were applied.

2.3 Results and discussion

2.3.1 Benchmark results for CrHe$^+$ and atomic Cr

In table 2.1 we compare our results for the X $^6\Sigma^+$ ground state of the CrHe$^+$ cation to previous calculations[203] and available experimental data[218, 219]. The equilibrium distance and the vibrational constant agree better with experimentally observed values than previous theory using a MRCI-approach[203]. Especially the coupled cluster results reproduce the experimental results, which also holds for the potential depth, while the MRCI-results underestimate the potential depth.

Table 2.1: Comparison of different results regarding CrHe$^+$

Source	$\mathrm{R_e}$ / Å	$\mathrm{D_e}$ / cm^{-1}	ω_e / cm^{-1}
Kemper *et al.*[218]	2.25 ± 0.15	430 ± 30	185 ± 30
von Helden *et al.*[219]	2.18 ± 0.30	490 ± 160	210 ± 42
Wilson *et al.*[203]	2.363	476	138
MRCI	2.328	373	149
MRCI+DK	2.290	396	156
CCSD(T)	2.260	427	173
CCSD(T)+DK	2.218	458	183

The PES obtained with the two methods described above are shown in figure 2.1. For internuclear distances larger than 3.5 Å the potentials are nearly identical. The coupled cluster curves show a slightly steeper repulsive wall and a deeper potential than the MRCI-results.

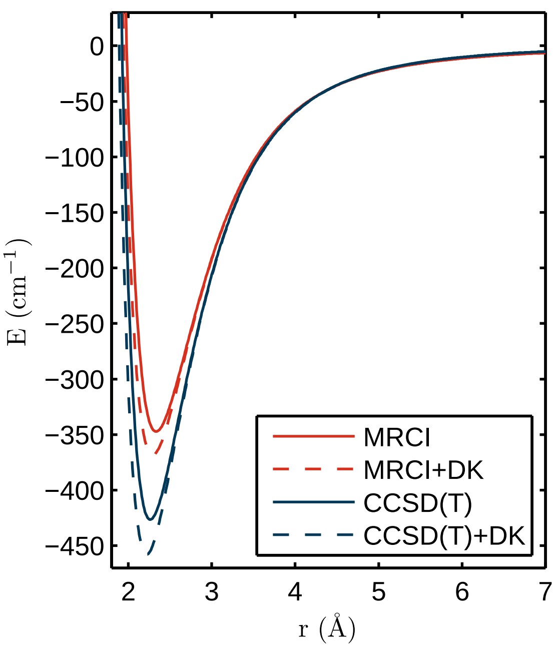

Figure 2.1: PES of the CrHe$^+$ cation in its X $^6\Sigma^+$ ground state, calculated at the CASSCF/MRCI and CCSD(T) level of theory. Equation 2.1 has been used to extrapolate the results obtained with quadruple- and quintuple-zeta basis sets to the basis set limit.

In the next step we calculate the first few electronically excited states of a single Cr atom at the CASSCF/MRCI level of theory. The ground state of Cr (a $^7S_3$) is a septet state with the occupational scheme [Ar] $4s^1\,3d^5$. The active space for the first 19 states of the septet manifold includes all occupied orbitals as well as the virtual 4p and 4d orbitals. To reduce the computational expense, the orbitals of the [Ar] configuration are optimized, but kept doubly occupied in all calculations. This leads to an accessible, yet representative active space consisting of 14 orbitals (6/3/3/2) and 6 electrons, comprising 772/ 752/ 752/ 727 state-averaged wave functions (CSFs) for the symmetries.[1]

Table 2.2 compares our results for the aug-cc-pVTZ, the aug-cc-pVQZ and the larger aug-cc-pV5Z basis set with experimental data taken from the NIST database[13] . The states were identified using symmetry and energetic position. Although the multiplicities

---

[1] The active space for the other multiplicities was chosen differently to obtain a similar accuracy and computational effort. For the same active space the quintet and triplet multiplicity would give many more CSFs, since the Pauli Exclusion Principle only forbids electrons of the same spin to occupy the same orbital. For the quintet multiplicity an active space of 9 orbitals (4/2/2/1) and 6 electrons has been used, for the triplet multiplicity the active space contained 14 orbitals (6/3/3/2) and 4 electrons. This resulted in 270/ 260/ 260/ 260 and 932/ 1032/ 1032/ 1038 CSFs for the quintet and triplet manifold, respectively.

Table 2.2: Transition energies (cm^{-1}) obtained for the Cr atom for differrent multiplicities. The NZ column headings refer to the aug-cc-pVNZ basis sets, whereas 5Z-DK denotes the aug-cc-pV5Z-DK basis set

Transition	NIST [13]	TZ	QZ	5Z	5Z-DK
z ^{7}P$^\circ$$\leftarrow$ a ^{7}S	23415	21458	21828	21844	21773
z ^{7}F$^\circ$$\leftarrow$ a ^{7}S	25432	23665	24256	24279	23054
z ^{7}D$^\circ$$\leftarrow$ a ^{7}S	27607	26030	26603	26623	25413
y ^{7}P$^\circ$$\leftarrow$ a ^{7}S	27848	26168	26771	26787	26444
a ^{5}S $\leftarrow$ a ^{7}S	7593	6435	7071	7037	7440
a ^{5}D $\leftarrow$ a ^{7}S	8090	9443	10181	10177	8487
a ^{5}G $\leftarrow$ a ^{7}S	20251	22389	22869	22688	22554
a ^{5}P $\leftarrow$ a ^{7}S	21846	23744	24125	23936	23762
b ^{5}D $\leftarrow$ a ^{7}S	24292	26770	27220	27056	26863
z ^{5}P$^\circ$$\leftarrow$ a ^{7}S	26793	25582	26301	26299	27110
a ^{3}P $\leftarrow$ a ^{7}S	23796	25778	26219	25615	23776
a ^{3}H $\leftarrow$ a ^{7}S	24080	26118	26733	26104	24274
a ^{3}F $\leftarrow$ a ^{7}S	25177	27378	27962	27236	25372

were treated with different active spaces they show similar deviations, indicating that a similar amount of electron correlation was included. The numbers correspond to energy difference between the lowest state in the septet multiplicity and the respective states. The last column contains the results obtained with the Douglas-Kroll correction and basis sets. For the excited states in the septet multiplicity the order of the states is reproduced correctly. Relative energy deviations for the largest basis set are below 8 % for the septet states. On average, the discrepancy between TZ and QZ energies is about 600 cm^{-1}, but shrinks to about 20 cm^{-1} between QZ and 5Z. Such a convergence with basis set size could not be observed for atomic excitations within the quintet multiplicity. The changes between the aug-cc-pVTZ and the aug-cc-pVQZ basis set are similar to the changes between the aug-cc-pVQZ and the aug-cc-pV5Z basis set. The order of the states z ^{5}P$^\circ$ and b ^{5}D was found to be wrong for all tested basis sets except aug-cc-pV5Z-DK after inclusion of the DK-correction. The triplet states have an error of similar magnitude as the other states. By including the DK-correction the results for the triplet multiplicity were improved. While the inclusion of the Douglas-Kroll (DK) correction increased the error in the septet multiplicity to at most 10 %, the results for the quintet multiplicity were improved, especially for the second transition. Since problems with convergence arose after including the Douglas-Kroll correction in calculating the excited states of the diatomic molecule CrHe and no significant improvement was observed for the atomic transitions, no DK correction was applied to the excited diatomic states.

2.3.2 The neutral CrHe diatomic molecule: method comparison and relativistic corrections

Figure 2.2 shows a comparison of the CC and the MRCI potential energy curves obtained for the electronic $X\,^7\Sigma^+$ ground state of the CrHe molecule. The CCSD(T) potential is deeper and the minimum is found at a smaller equilibrium distance of 5.04 Å (5.24 Å for MRCI). We explain this discrepancy by a lack of dynamic correlation in the case of the MRCI approach, which seems to be essential for a correct description of the weak van der Waals interaction. The CCSD performance is comparable to MRCI, which underlines the importance of the (in both cases missing) triple excitations correction. MRCI calculations are not size consistent, but can be corrected e.g. by a multiconfigurational analogue to the Davidson method (MRCI+Q). The corrected potentials show a deeper well depth than the CCSD results. The Douglas-Kroll correction increases the potential depth for all methods. However, these changes are smaller than those introduced by triply excited amplitudes or the Davidson correction. The inclusion of DK corrections caused similar changes in the other manifolds: It reduces the Cr-He bond length by 0.2 Å on average, and increases the potential energy depth by about 0.54 cm^{-1}.

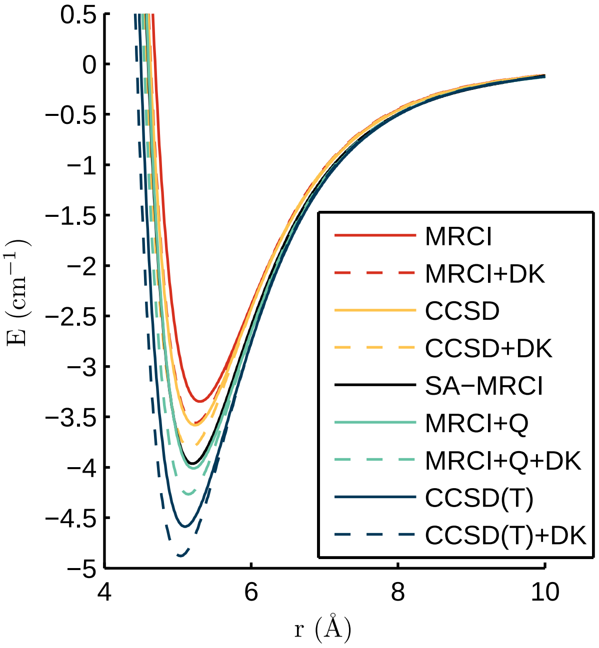

Figure 2.2: PES of the CrHe diatomic molecule in its $X\,^7\Sigma^+$ ground state, calculated at the CASSCF/MRCI and CCSD(T) level of theory, after basis set extrapolation according to equation 2.1.

The same methods were applied to determine the lowest electronic states in the quintet (a^5S) and the triplet (a^3P) manifold (see figures 2.3 and 2.4). Here we obtain huge qualitative differences for both methods, indicating the breakdown of the single-reference assumption for these spin manifolds. Technically, this can be derived from the T_1 and

D_1 values of the CC approach, which are above the recommended threshold for states of the quintet and triplet manifold[220, 221]. It is obvious from a simple orbital picture that a single reference approach must fail: The possible distribution of the electrons over the available energetically close s- and d- orbitals leads to several configurations of similar energies in the case of the quintet and triplet multiplicity. Note that the a^5S potential curve is almost congruent with the $X^7\Sigma^+$ curve. This indicates a severe mixing of septet character into the quintet wave function through a double excitation.

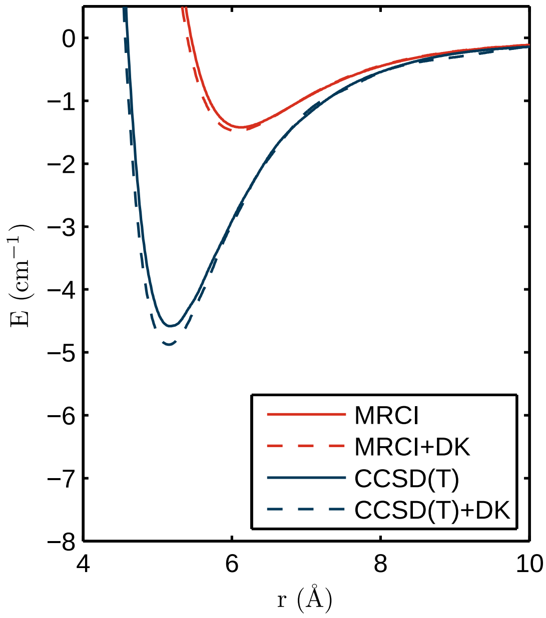

Figure 2.3: Comparison of the CASSCF/MRCI and CCSD(T) results obtained for the lowest electronic state in the quintet manifold (a^5S) of CrHe.

We note further that all PES shown in figures 2.1-2.4 have been corrected for BSSE by application of the counterpoise correction method of Boys and Bernardi[109]. As can be seen in figure 2.5 this correction turns out to be essential for an appropriate description within the CC approach, while the MRCI results are far less affected. For the lowest states of the neutral system the error is below 0.2 cm^{-1}, whereas the results for $CrHe^+$ cation show a difference of about 5 cm^{-1}, which, however, is also small compared to the potential depth of the system (see table 2.1). Hence, no BSSE correction is applied to the MRCI-derived excited states in the next section.

Table 2.3 summarizes the potential parameters in each multiplicity determined with different methods. Relativistic corrections are considered within the Douglas-Kroll formalism. In general, CASSCF/MRCI-calculations underestimate the potential depth and overestimate the equilibrium distance. As can be seen in table 2.3, the state averaged (SA) CASSCF/MRCI-calculations give values closer to the CC results. The MRCI-calculations for the ground state were improved by applying the Davidson-correction to correct for size inconsistency (MRCI+Q).

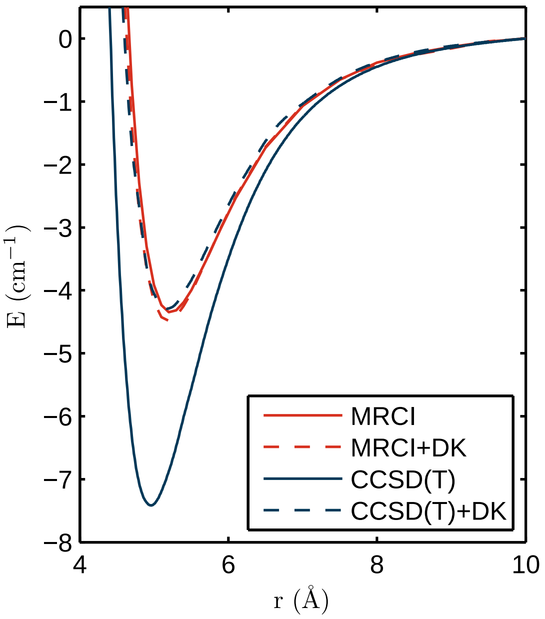

Figure 2.4: Comparison of the CASSCF/MRCI and CCSD(T) results obtained for the lowest electronic state in the triplet manifold (a^{3}P) of CrHe.

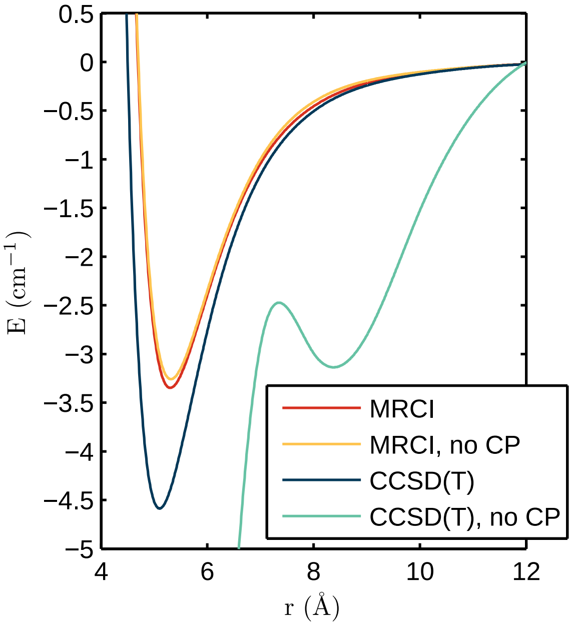

Figure 2.5: PES of the CrHe diatomic molecule in its X $^7\Sigma^+$ ground state, calculated at the CASSCF/MRCI and CCSD(T) levels of theory, after basis set extrapolation according to equation 2.1. The figure displays results with and without counterpoise correction (CP)

Table 2.3: Potential parameters of the lowest states of CrHe in the different multiplicities

M	Method	R_e / Å	D_e / cm^{-1}	ω_e / cm^{-1}
Septet	CCSD	5.235	3.58	9.1
	CCSD+DK	5.170	3.81	9.5
	CCSD(T)	5.100	4.59	10.4
	CCSD(T)+DK	5.038	4.88	10.9
	MRCI	5.301	3.35	8.8
	MRCI+DK	5.235	3.56	9.1
	MRCI+Q	5.211	4.01	9.7
	MRCI+Q+DK	5.145	4.27	10.0
	MRCI - SA	5.203	3.96	9.6
Quintet	CCSD(T)	5.176	4.59	11.0
	CCSD(T)+DK	5.146	4.88	11.1
	MRCI	6.125	1.42	5.2
	MRCI+DK	6.067	1.49	5.3
Triplet	CCSD(T)	4.953	7.42	14.9
	CCSD(T)+DK	5.164	4.30	11.1
	MRCI	5.224	4.35	10.9
	MRCI+DK	5.189	4.48	11.1

2.3.3 The neutral CrHe diatomic molecule: electronically excited states in the quintet and septet manifold

In this section we extend our CASSCF/MRCI approach to the first electronically excited states of the neutral CrHe diatomic molecule. The active space schemata used for the single Cr atom are extended by the helium contribution, which consists of one additional, doubly occupied orbital in A_1 symmetry. PES for the septet manifold are shown in figure 2.6. All calculations were performed with the aug-cc-pV5Z basis sets. Interestingly, of all the states considered, only the $1\,^7\Pi$ state shows a noticeable potential minimum. However, this somewhat unusual finding can also be observed in other heteronuclear diatomic molecules including He (see table 2.4)[222–228].

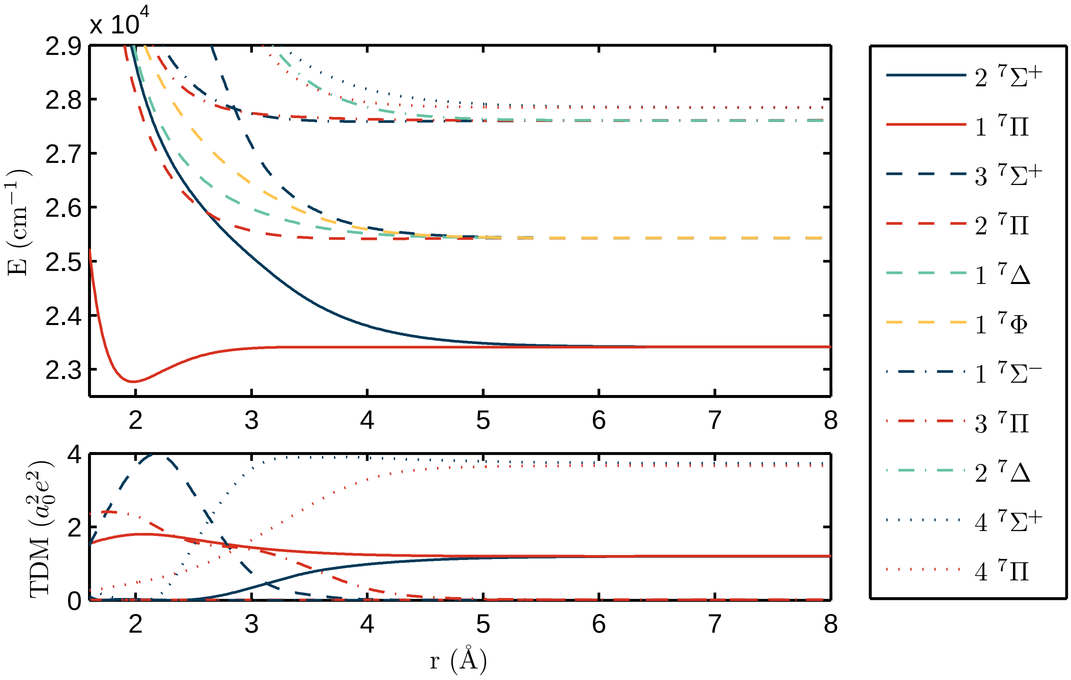

Figure 2.6: The first 11 electronically excited states of CrHe in the septet manifold. Zero energy is set to the asymptote of the X $^7\Sigma^+$ ground state (not shown). Excited states are asymptotically corrected based on atomic energies taken from the NIST database[13]. Additionally the non-zero transition dipole moments from the X $^7\Sigma^+$ ground state are shown.

It seems that a weakly bound X Σ^+ and a more strongly bound $1\,\Pi$ state is typical for these systems. The binding strength for the first excited state is especially strong for elements where the first electronic transition excites an electron from a singly occupied s-orbital into a p-orbital. This effect can be observed for the alkali metals, the coinage metals and, as we found for chromium. In general, the binding strength decreases with increasing period in the periodic table. The d-orbitals also influence the interaction, which can be seen for the fourth period. Potassium with no occupied d-orbitals shows the weakest bonding, copper is in between with completely filled orbitals, and chromium

Table 2.4: Comparing the potential parameters of the two lowest states of several heteronuclear diatomic molecules including He.

	X Σ^+		1 Π	
Element	R_e / Å	D_e / cm^{-1}	R_e / Å	D_e / cm^{-1}
LiHe [222]	6.09	1.50	1.80	1015
NaHe [222]	6.56	1.20	2.33	425
KHe [223]	7.78	0.45	2.90	163
RbHe [224]	$\approx$ 7.40	$\approx$ 1.50	3.30	134
CsHe [224]	7.94	1.30	3.49	112
MgHe [225]	5.06	5.84	3.82	40
CaHe [226]	5.85	4.20	4.76	10
CrHe	5.04	4.88	1.98	629
CuHe [227, 228]	4.59	6.23	2.03	461
AgHe [227, 228]	4.60	7.42	2.52	272

shows the strongest bond with its half-filled d-orbitals. Overall copper shows the greatest similarity with chromium for the elements included in table 2.4.

The potential parameters of the states in figure 2.6 were determined by fitting a Morse-potential and collected in table 2.5.

For the ground state the potential depth is slightly underestimated and the bond length is slightly overestimated, but it compares well with the above coupled cluster results. Only the states $1\,^7\Pi$, $2\,^7\Pi$ and $1\,^7\Sigma^-$ show a significant binding. These three states are the only ones with an equilibrium position below or around 4 Å. This becomes important when looking at the transition dipole moments (TDM) (see figure 2.6) .

The TDM values (figure 2.6) for large internuclear distances approach the atomic values, see last column of table 2.6. Down to 4 Å the TDM remain nearly at the atomic values. If no relaxation in the states $1\,^7\Pi$, $2\,^7\Pi$ and $1\,^7\Sigma^-$ is considered, the atomic dipole moments should be a good approximation. Taking this into account, the states with the atomic limits y $^7P^\circ$ and z $^7P^\circ$ are of interest, since they can be reached from the ground state by excitation. The diatomic states corresponding to the y $^7P^\circ$ level are similar in shape, showing weak binding and long equilibrium distances. The states corresponding to the z $^7P^\circ$ atomic asymptote, on the other hand, differ considerably in shape. While the $2^7\Sigma^+$ state is only weakly bound, the $1^7\Pi$ state shows a potential depth of 629 cm^{-1}. This strongly bound state could lead to the formation of a CrHe* excimer, but this becomes less likely if spin-orbit coupling is included (see section 2.3.4).

The results for the quintet states are summarized in table 2.7 and figure 2.7. No strongly bound states occur in the quintet manifold. The levels are well separated and only cross each other for internuclear distances smaller than 2 Å. A closer look at table 2.7 reveals a correlation between binding strength and electronic configurations.

Table 2.5: Potential parameters of the excited states of CrHe in the septet-multiplicity

At. limit	Term	R_e / Å	D_e / cm^{-1}	ω_e / cm^{-1}
a ^{7}S	X $^7\Sigma^+$	5.20	3.96	9.6
z ^{7}P°	2 $^7\Sigma^+$	7.87	0.57	2.8
	1 $^7\Pi$	1.97	638.38	321.7
z ^{7}F°	3 $^7\Sigma^+$	6.46	1.58	5.3
	2 $^7\Pi$	4.03	16.36	23.4
	1 $^7\Delta$	5.97	2.24	5.5
	1 $^7\Phi$	6.32	1.67	5.6
z ^{7}D°	1 $^7\Sigma^-$	4.00	19.91	25.1
	3 $^7\Pi$	5.53	2.64	6.7
	2 $^7\Delta$	6.77	1.23	4.5
y ^{7}P°	4 $^7\Sigma^+$	7.86	0.66	2.9
	4 $^7\Pi$	6.00	1.99	5.8

The states belonging to the a ^{5}D asymptote show the strongest binding. This electronic state is the only one with an electronic configuration of [Ar] 3d^4 4s^2. The configuration which led to the strongest bond in the septet multiplicity, [Ar] 3d^5 4p (z ^{7}P° state), shows intermediate bond strengths (the z ^{5}P° atomic limit). The remaining states correspond to the configuration [Ar] 3d^5 4s, like the ground state in the septet multiplicity. The configuration [Ar] 3d^4 4s 4p gives rise to most calculated states in the septet multiplicity (z ^{7}F°, z ^{7}D°, y ^{7}P° limits), but no states with this configuration were calculated in the quintet multiplicity. In general, the potentials in the quintet-multiplicity show less variation with the projection of the total orbital angular momentum than septet states, but this seems unrelated to the different orbital occupations that are possible for quintet states.

Table 2.6: Comparison of MRCI transition dipole moments (J-averaged, TDM^2) to experimental data obtained from Younger *et al.*[229] for selected Cr transitions in the septet manifold. Experimental line strengths ($\mathrm{S_{if}}$) are divided by the number of degenerate final states ($\mathrm{g_f}$).

transition	$\mathrm{S_{if}}$ / a. u.	$\mathrm{g_f}$	$(\mathrm{S_{if}/g_f})$ / a. u.	$(\mathrm{TDM})^2$ / a. u.
z $^7\mathrm{P}^\circ{}_2 \leftarrow$ a $^7\mathrm{S}_3$	6.10	5	1.22	1.20
z $^7\mathrm{P}^\circ{}_3 \leftarrow$ a $^7\mathrm{S}_3$	8.25	7	1.18	
z $^7\mathrm{P}^\circ{}_4 \leftarrow$ a $^7\mathrm{S}_3$	10.80	9	1.20	
z $^7\mathrm{D}^\circ{}_4 \leftarrow$ a $^7\mathrm{S}_3$	0.01	9	0.00	0.00
y $^7\mathrm{P}^\circ{}_2 \leftarrow$ a $^7\mathrm{S}_3$	18.70	5	3.74	3.67
y $^7\mathrm{P}^\circ{}_3 \leftarrow$ a $^7\mathrm{S}_3$	24.00	7	3.43	
y $^7\mathrm{P}^\circ{}_4 \leftarrow$ a $^7\mathrm{S}_3$	30.20	9	3.36	

Table 2.7: Potential parameters of the excited states of CrHe in the quintet-multiplicity

at. limit	Term	$\mathrm{R_e}$ / Å	$\mathrm{D_e}$ / cm^{-1}	ω_e / cm^{-1}
a ^{5}S	1 $^5\Sigma^+$	6.00	1.60	5.4
a ^{5}D	2 $^5\Sigma^+$	5.29	4.38	10.7
	1 $^5\Pi$	5.23	4.69	11.2
	1 $^5\Delta$	5.15	5.03	11.5
a ^{5}G	*a*	5.37 - 5.47	2.81 - 3.03	≈ 8.0
a ^{5}P	1 $^5\Sigma^-$	5.37	2.99	8.1
	3 $^5\Pi$	5.45	2.88	8.1
b ^{5}D	4 $^5\Sigma^+$	5.32	3.17	8.6
	4 $^5\Pi$	5.29	3.28	8.5
	3 $^5\Delta$	5.55	2.67	7.6
z $^5\mathrm{P}^\circ$	5 $^5\Sigma^+$	5.60	2.51	7.4
	5 $^5\Pi$	5.40	3.04	8.2

[a] …The 3 $^5\Sigma^+$, 2 $^5\Pi$, 2 $^5\Delta$, 1 $^5\Phi$, 1 $^5\Gamma$ states belong to the a ^{5}G limit.

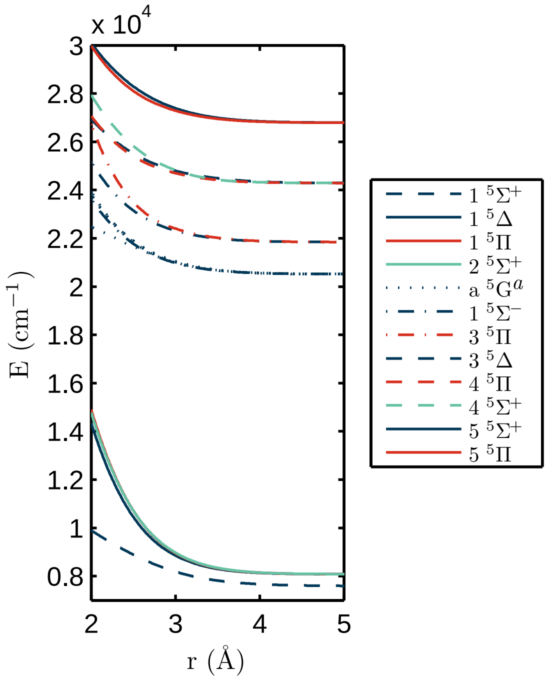

Figure 2.7: The first electronically excited states of CrHe in the quintet manifold. Excited states are asymptotically corrected based on atomic energies taken from the NIST database[13].

[a] . . . The 3 $^5\Sigma^+$, 2 $^5\Pi$, 2 $^5\Delta$, 1 $^5\Phi$, 1 $^5\Gamma$ states belong to the a ^{5}G limit.

2.3.4 The neutral CrHe diatomic molecule: spin-orbit coupling

To allow for a direct comparison to experimental data we further consider spin-orbit coupling in our analysis of the electronically excited states in the septet manifold. This is achieved *via* an effective correction based on the Breit-Pauli-Hamiltonian[181], as it is included in the MOLPRO software package[140]. Including the spin-orbit-coupling leads to extensive state splitting as it is expected for Cr. For higher energies a unique identification of states is only possible down to an internuclear distance of 5 Å due to the high density of states.

Table 2.8: Comparing experimental transition energies for Cr[13] and calculated asymptotic values for the J-substates of CrHe

Transition	Δ E[13] / cm^{-1}	Δ E^a / cm^{-1}	Δ E^b / cm^{-1}
z $^7\mathrm{P}°_2 \leftarrow$ a $^7\mathrm{S}_3$	23305	21642	23302
z $^7\mathrm{P}°_3 \leftarrow$ z $^7\mathrm{P}°_2$	81	87	85
z $^7\mathrm{P}°_4 \leftarrow$ z $^7\mathrm{P}°_3$	112	116	112
z $^7\mathrm{F}°_0 \leftarrow$ z $^7\mathrm{P}°_4$	1472	1755	1497
z $^7\mathrm{F}°_1 \leftarrow$ z $^7\mathrm{F}°_0$	39	37	36
z $^7\mathrm{F}°_2 \leftarrow$ z $^7\mathrm{F}°_1$	79	73	73
z$^7\mathrm{F}°_3 \leftarrow$ z $^7\mathrm{F}°_2$	117	111	109
z $^7\mathrm{F}°_4 \leftarrow$ z $^7\mathrm{F}°_3$	154	146	146
z $^7\mathrm{F}°_5 \leftarrow$ z $^7\mathrm{F}°_4$	189	182	182
z $^7\mathrm{F}°_6 \leftarrow$ z $^7\mathrm{F}°_5$	223	220	218
z $^7\mathrm{D}°_1 \leftarrow$ z $^7\mathrm{F}°_6$	1529	1701	1555
z $^7\mathrm{D}°_2 \leftarrow$ z $^7\mathrm{D}°_1$	82	73	72
z $^7\mathrm{D}°_3 \leftarrow$ z $^7\mathrm{D}°_2$	118	110	109
z $^7\mathrm{D}°_4 \leftarrow$ z $^7\mathrm{D}°_3$	149	152	146
z $^7\mathrm{D}°_5 \leftarrow$ z $^7\mathrm{D}°_4$	176	184	187
y $^7\mathrm{P}°_2 \leftarrow$ z $^7\mathrm{D}°_5$	-97	-39	-107
y $^7\mathrm{P}°_3 \leftarrow$ y $^7\mathrm{P}°_2$	91	97	90
y $^7\mathrm{P}°_4 \leftarrow$ y $^7\mathrm{P}°_3$	115	128	132

[a] …This work

[b] …This work, corrected by a shift of the asymptotic MRCI energies to atomic values[13].

The level splitting of the different states is well reproduced, as can be seen in table 2.8 and figure 2.8. The mean of the energies of m_J-sublevels was used to determine the energy of each J-state. For J-states belonging to the same term the error of the level-differences is smaller than 10 cm^{-1}, which indicates an appropriate description of the SO-coupling. Larger deviations are obtained for differences between different terms due to inaccuracies in the electronic energies. As a consequence the order of two sublevels deviates from experimental observation[13] . In the second column in table 2.8 the state y $^7\mathrm{P}°_3$ lies energetically above the state z $^7\mathrm{D}°_5$, not below. This is related to the deviation in the transition y ^{7}P°$_2$ ← z ^{7}D°$_5$, where instead of a value of -97 cm^{-1}a value of -39 cm^{-1}is determined (table 2.8). In an additional step, the results were improved by shifting the CI-energies at 100 Å to the experimental values. The modified values are shown in figure 2.8 and in the fourth column of table 2.8.

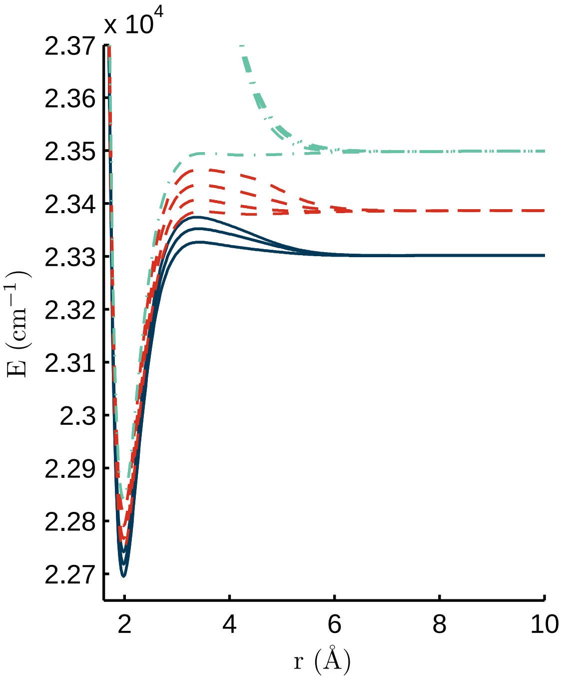

Figure 2.8: The electronically excited states of CrHe corresponding to the z ^{7}P° atomic excitation of Cr in the septet manifold after inclusion of SO-coupling. Zero energy is set to the asymptote of the X $^7\Sigma^+$ ground state.

2.4 Comparison with experiment

Up to now there are no experimental verifications of the CrHe diatomic molecule, but spectroscopic studies of Cr in He droplets shall be compared in the following. In recent beam depletion measurements of chromium doped superfluid helium nanodroplets blueshifts of about 200 to 300 cm^{-1} were observed for the transitions z ^{7}P°←a^{7}S and y ^{7}P°←a^{7}S[18]. A shift for the state y ^{7}P° can already be seen in calculations for CrHe at the MRCI-level. Vertical excitations in the diatomic molecule from the ground state to the 4 $^7\Sigma^+$ or to the 4 $^7\Pi$ state are blue shifted by about 70 cm^{-1}and 15 cm^{-1}, respectively, with respect to the corresponding atomic transitions. An enhancement of this effect by having the Cr atom surrounded by helium might be an explanation of the larger shifts as they occur for nanodroplets. A similar extrapolation for a shift of the atomic z ^{7}P° excitation energy on a droplet based on the corresponding CrHe states is less straightforward. While the 2 $^7\Sigma^+$ state is also blue shifted by 80 cm^{-1}, the 1 $^7\Pi$ state shows a slight red shift at the MRCI level. However, after inclusion of spin-orbit coupling it becomes obvious that a simple extrapolation of trends is no longer sufficient: For the z ^{7}P° asymptote strongly and weakly bound potentials were determined, which differ significantly in the onset of the repulsive part of the potential. The phenomenon of blue shifted atomic excitations for Cr is even more pronounced in matrix isolation spectroscopy, where the atoms are embedded in a less inert argon or krypton environment. Significantly larger blue shifts of 1600 cm^{-1} and 2200 cm^{-1} were reported for the z ^{7}P°←a ^{7}S and y ^{7}P°←a ^{7}S transitions in Kr and Ar matrix, respectively[230].

While atomic Cr excitations are shifted in HENDI experiments, the fluorescence is not. This interesting finding indicates that chromium atoms leave the droplet after excitation[18]. A possible explanation for such an ejection could be the population of more weakly bound states (y ^{7}P°, z ^{5}P°) during the relaxation process after the initial excitation. The interaction of superfluid He droplets with single atom dopants has been investigated by Ancilotto *et al.*[231]. In short, the behavior of a single atom X on helium droplets correlates with simple parameters of the XHe potential. In general, increased potential depth or X-He bond length raises the probability for a full immersion into the droplet. However, the ground state of chromium is a borderline case. It has a slight tendency to favor a position inside the droplet[17, 18], but a minimal reduction of the potential depth would already suggest a position on the surface of the He droplet. Applying the above argumentation to the CrHe potentials, our tentative explanation may be summarized as follows: the deeper CrHe ground state potential suggests that the chromium atom is residing in the center before excitation. The sublevels corresponding to the y ^{7}P° state on the other hand are weakly bound and their population would therefore favor a position on the surface of the droplet. Hence, the supplied excitation energy might be sufficient for a complete detachment from the helium droplet simply due to a reduced attractive interaction. We note that in the z ^{7}P° state the formation of an excimer might be a possible scenario ($1\,^7\Pi$), but SO-corrected results indicate a potential barrier for certain states which makes such a formation less likely.

Fluorescence emissions from the z ^{5}P° state to the a ^{5}S state have been observed in HENDI-experiments[17, 18]. The transitions a ^{5}G → a ^{5}D and a ^{5}P → a ^{5}D appear in matrix isolation spectroscopy[230], and their difference corresponds to the gas phase level difference of a ^{5}P and a ^{5}G. This indicates a similar interaction of these states (which share the same electronic configuration) with the matrix environment. Pellin *et al.*[230] determined a strong matrix dependence of the level difference of a ^{5}S and a ^{5}D, two states with different configuration, and that the state a ^{5}S is a trapped state with long lifetime. These findings are also reflected in our calculated potentials (see table 2.7 and figure 2.7): The curves related to a ^{5}S differ more strongly from the potentials corresponding to the a ^{5}P state than the potential curves with the a ^{5}G atomic asymptote.

HENDI as well as matrix-isolation spectroscopy experiments report transitions into the quintet multiplicity for embedded Cr atoms, which indicates the presence of a mechanism for populating quintet-states enabled by the rare gas environment. Our CrHe model approach reaches a limit in this regard since there is no level crossing between the relevant states. The states corresponding to z ^{5}P° are lower in energy and more strongly bound than those belonging to y ^{7}P°. However, considering more pronounced effects due to the helium environment, we offer the following suggestion: the states corresponding to the y ^{7}P° atomic limit have a smaller potential depth and a larger equilibrium distance than the ground state. The same is valid for the states corresponding to z ^{5}P°, although not to the same extent. The differences in binding strength can be understood by taking a look at the configuration: The z ^{5}P° has the same configuration as the strongly bound state z ^{7}P°([Ar] $3d^5\,4p$), whereas the state y ^{7}P° has a configuration of [Ar] $3d^4\,4s\,4p$. The chromium atom will be most likely ejected in the state y ^{7}P°, while it might even reside inside the droplet in the state z ^{5}P°. For the excitation a ^{7}S → y ^{7}P° the chromium atom needs to create a large 'bubble' within the helium droplet. A change of the bubble size in the liquid helium would be much smaller for the transition a ^{7}S → z ^{5}P°, which includes a spin flip. This indicates a pressure-induced spin-flip as it is also observed for bulk chromium[232], which undergoes a first order phase transition at 122 K between two different spin-density-wave antiferromagnetic states. The pressure dependence of the magnetic properties of bulk chromium is well known and has been used to study the quantum critical point, see ref. 233 and references therein. In theoretical approaches an accurate lattice constant has proven essential to determine accurate magnetic moments and states of bulk Cr, see ref. 234 and references therein. Our results suggest that even non-magnetic atoms like helium affect the magnetic properties of chromium noticeable, simply due to Pauli repulsion. Pellin *et al.*[230] also observed a strong system crossing *via* the a ^{3}P → a ^{5}D transition. It shows a line shift of less than 80 cm^{-1}, which can be considered minimal for this type of spectroscopy, and independent of the rare gas matrix. Again, this is to be expected since both states share the same configuration ([Ag] $3d^4\,4s^2$), so the effects of the matrix should be similar to both states. In our case, this similarity is apparent in the potential parameters for the lowest state in the triplet multiplicity in table 2.3 and the quintet states listed in table 2.7.

2.5 Conclusion

The interaction of a single Cr atom with He has been analyzed at the CCSD(T) and CASSCF/MRCI level of theory. We validated our computational approach by comparison to experimental data available for the charged $CrHe^+$ system and the well-known atomic excitations of a single Cr atom. Our CCSD(T) results for the ground state potential curve of $CrHe^+$ are in good agreement with experiment and lie within the reported experimental uncertainties. Deviations in relative energy for the first few electronically excited states of Cr up to 3.36 eV obtained with MRCI are less than 10 percent in the septet manifold and somewhat higher for quintet and triplet states.

The $X^7\Sigma^+$ ground state of CrHe shows a binding length of 5.04 Å and a binding energy of about 4.9 cm^{-1} with CCSD(T). MRCI on top of a moderately sized CASSCF(8,14) gives comparable results, but slightly underestimates the strength of the van der Waals binding. Our MRCI analysis of excited states reveals a strongly bound state ($1^7\Pi$, D_e=638 cm^{-1}) in the septet manifold. This somewhat unusual finding is in line with previous results for heteronuclear diatomic molecules of helium and alkali or alkaline earth metals. Spectroscopically, the $1^7\Pi$ and the $2^7\Sigma^+$ state are of particular interest due to their z ^{7}P° atomic asymptote, which has a high dipole transition moment for an excitation from the atomic ground state of Cr. In the quintet manifold all excited states of CrHe up to our energy threshold of 3.36 eV show a weak bonding of about 5 cm^{-1} or less.

Looking at the CrHe diatomic molecule as a highly simplified toy model for the complex interactions of Cr with larger He-nanodroplets we find agreement between vertical excitations from the ground state at R_e and the experimentally observed blueshifts with respect to energy differences tabulated for the corresponding transitions in free Cr atoms ($\mathrm{z}\,{}^7\mathrm{P}^\circ \leftarrow \mathrm{a}^7\mathrm{S}$ and $\mathrm{y}\,{}^7\mathrm{P}^\circ \leftarrow \mathrm{a}^7\mathrm{S}$). Transitions between the septet and the quintet manifold as reported in HENDI and matrix-isolation spectroscopy experiments are not accessible within our CrHe model due to the lack of intersystem crossings in this system for the relevant states ($\mathrm{z}\,{}^5\mathrm{P}^\circ$ and $\mathrm{y}\,{}^7\mathrm{P}^\circ$). However, we find that CrHe states corresponding to the $\mathrm{z}\,{}^5\mathrm{P}^\circ$ asymptote are slightly stronger bound than those with $\mathrm{y}\,{}^7\mathrm{P}^\circ$ asymptote. Secondly, their $[\mathrm{Ar}]3\mathrm{d}^5 4\mathrm{p}$ electronic configuration is assumed to be less interfering with the helium droplet. Thirdly, the latter configuration is identical to the configuration of the strongly bound $1^7\Pi$ state. We believe that the combination of these three factors is the driving force for the intersystem crossing as it occurs in larger Cr-He_N systems.

2.6 Remark

The solvation of Cr atoms in He-nanodroplets and the induced shift of energy levels was further investigated in ref. 4 and quantitative results were obtained. This study used the so-called Orsay-Trento functional for the He density. This bosonic density functional has been optimized to describe the properties of liquid ^{4}He[235–237]. However, the calculated diatomic potential energy curves of CrHe can not be directly applied in the DFT computation, because there are many He atoms and the potential energy curves are only given for one direction. Therefore, the potentials were mixed by the diatomic in molecules approach[4]. The potentials were then used in DFT calculations for droplets of 10 to 2000 helium atoms. The interaction of Cr with He_N was investigated and for the ground state the Cr atom prefers a position inside the helium droplet with a solvation energy of 40-50 cm^{-1}. Several experimentally relevant excited states ($4\,{}^7\Pi$, $4\,{}^7\Sigma^+$, $1\,{}^5\Sigma^+$, $6\,{}^5\Pi$, $6\,{}^5\Sigma^+$) of Cr were also considered and in these cases Cr attaches to the surface with binding energies of about 20 cm^{-1}. Additionally, the line shift introduced by the helium environment was studied.

Chapter 3

Electronic structure and spin-orbit coupling of RbSr

This chapter corresponds to the publication:
Ab initio Study of the RbSr electronic structure: Potential energy curves, transition dipole moments and permanent electric dipole moments
by Johann V. Pototschnig, Günter Krois, Florian Lackner, and Wolfgang E. Ernst
in *Journal of Chemical Physics*, **2014**, *141*, 234309,
which was written by the author of the thesis.

The author of the thesis was responsible for:

- author of the publication
- realization and implementation of the *ab initio* calculations
- determination of the vibronic spectra based on the *ab initio* calculations
- interpretation of the result, comparison to experiments

The contributions of the co-authors are listed below:

- G. Krois: experiment and data acquisition
- F. Lackner: experiment, comparison to experiment, editing
- W. E. Ernst: supervision, editing, funding

The article is available at http://dx.doi.org/10.1063/1.4903791.

Details on the experimental investigation can be found in the doctoral thesis by Günter Krois[23] and in two other publications[5, 6].

Abstract

Excited states and the ground state of the diatomic molecule RbSr were calculated by post Hartree-Fock molecular orbital theory up to 22000 cm^{-1}. We applied a multireference configuration interaction calculation based on multiconfigurational self-consistent field wave functions. Both methods made use of effective core potentials and core polarization potentials. Potential energy curves, transition dipole moments and permanent electric dipole moments were determined for RbSr and could be compared with other recent calculations. We found a good agreement with experimental spectra, which have been obtained recently by helium nanodroplet isolation spectroscopy. For the lowest two asymptotes (Rb (5s ^{2}S) + Sr (5s4d ^{3}P°) and Rb (5p ^{2}P°) + Sr (5s^2 ^{1}S)), which exhibit a significant spin-orbit coupling, we included relativistic effects by two approaches, one applying the Breit-Pauli Hamiltonian to the multireference configuration interaction wave functions, the other combining a spin-orbit Hamiltonian and multireference configuration interaction potential energy curves. Using the results for the relativistic potential energy curves that correspond to the Rb (5s ^{2}S) + Sr (5s4d ^{3}P°) asymptote, we have simulated dispersed fluorescence spectra as they were recently measured in our lab. The comparison with experimental data allows to benchmark both methods and demonstrate that spin-orbit coupling has to be included for the lowest states of RbSr.

3.1 Introduction

The recent years have seen a considerable growth of interest in polar molecules with unpaired electrons because of the intriguing applications, which have been proposed for these molecules in the ultracold temperature regime. With their permanent electric dipole moment (PEDM) and magnetic dipole moment, they offer many opportunities for a controlled manipulation. Possible applications range from the realization of quantum simulations[80] and lattice spin models[79] to precise measurements of fundamental physical constants with high resolution spectroscopy[90].

Especially alkali (AK) atoms and alkaline earth (AKE) atoms are promising constituents for such diatomic molecules, because these elements can be cooled efficiently and quantum degenerate systems were already produced[61, 63, 64, 238]. Up to now several homonuclear and heteronuclear diatomic molecules were investigated consisting either of two AK atoms or two AKE atoms, especially in the ultracold temperature regime[28, 29]. In contrast to homonuclear dimers, the heteronuclear molecules can posses a significant PEDM[239], however they have no unpaired electron. Mixed AK-AKE molecules have one unpaired electron, which gives rise to a magnetic dipole moment in the $^2\Sigma^+$ ground state. Among the AK-AKE molecules, RbSr is the most promising candidate for the production of ultracold molecules, because the production of spatially overlapping quantum degenerate systems has recently been demonstrated[26]. Theoretical calculations of the ground state of RbSr have been performed by several groups[119, 167, 240]. For excited states of RbSr only two theoretical studies are known to the authors. Żuchowski *et al.*[179] compared two methods: A full configuration interaction calculation (FCI) was performed with the CIPSI method (configuration interaction by perturbation of a multiconfigurational wave function selective iteratively) applying large effective core potentials (ECPs) and core polarization potentials (CPPs). They compared their results to equation of motion coupled cluster theory (EOM-CC) using small ECPs. Chen *et al.*[241] applied Kramers restricted multireference configuration interaction (KR-MRCI) and determined the ground state as well as three excited states corresponding to the Rb (5p ^{2}P°) + Sr (5s^2 ^{1}S) asymptote within their all-electron approach.

So far, excited states of RbSr have only been investigated experimentally by helium nanodroplet (He_N) isolation spectroscopy[5, 6], an approach that has recently been introduced for the characterization of AK-AKE molecules[2]. This work extends the previous calculations[179, 241] to higher states up to an asymptotic energy of 22000 cm^{-1} and utilizes a different method. Our results will be compared to recent experimental results for RbSr formed on He_N[5, 6].

Furthermore, we include spin-orbit interaction for the lowest states, which correspond to the Rb (5s ^{2}S) + Sr (5s4d ^{3}P°) and Rb (5p ^{2}P°) + Sr (5s^2 ^{1}S) asymptotes by using two different approaches. The two sets of relativistic potential energy curves (PECs) and their transition dipole moments (TDMs) were calculated (i) by evaluating the Breit-Pauli Hamiltonian as implemented in the MOLPRO software package[140] and (ii) by extending the MRCI results with a spin-orbit Hamiltonian as described in ref. 179.

As will be shown for the states originating from the Rb (5s ^{2}S) + Sr (5s4d ^{3}P°) asymptote, this is essential for a proper simulation of the dispersed fluorescence spectra[5] in the respective energy range. The aim of this study is to provide PECs, TDMs and PEDMs for several excited states of RbSr in order to explain experimentally recorded spectra[5, 6] and to aid the envisaged experiments with ultracold RbSr molecules[167, 240–242].

3.2 Methods and computational details

The calculations were performed with the MOLPRO software package[140]. A multiconfigurational self-consistent field calculation (MCSCF)[125, 216] in combination with a second order multireference configuration interaction calculation (MRCI)[128, 217] was applied. These molecular orbital based methods enable the calculation of the PECs, PEDMs, and TDMs for several excited states and the ground state. The number of states as well as the orbitals will be given in the program-specific ordering of irreducible representations ($A_1/B_1/B_2/A_2$) of the C_{2v} point group. According to this notation the active space consisted of 16/8/8/3 orbitals filled with 19 electrons, whereas the innermost 4/2/2/0 orbitals were optimized but kept doubly occupied. The remaining 56 electrons were considered by applying two different ECPs, one for each atom. The 28 inner electrons of Rb and Sr were replaced by the relativistic ECP ECP28MDF provided by Lim *et al.*[243, 244]. The corresponding basis sets were used, but modified such that they were completely decontracted and several exponents[2] were added. This procedure led to a basis of Rb[14s 11p 7d 4f 2g], Sr[15s 12p 8d 5f 2g] elementary functions. The addition of further d-functions was especially important for higher states. Benchmark calculations on atomic Rb and Sr in the molecular basis indicate a negligible basis set superposition error of about ~ 20 cm^{-1} for the given basis set and method. The results were improved by Müller/Meyer type[117] CPPs with cutoff parameters of 0.3238 Å^{-2} for Rb and 0.2609 Å^{-2} for Sr. For the static dipole polarizabilities of the atomic cores replaced by the ECPs, values of 9.215 a. u. for Rb and 9.127 a. u. for Sr show the best results. These values for the CPPs were obtained by optimizing the energies at large internuclear separations (table 3.1). 13/8/8/4 doublet states and 3/2/2/1 quartet states were calculated with the MRCI approach. With the method described above (in the following this approach which applies the ECPs from Lim *et al.*[243, 244] will be referred to as ST) the asymptotic values have been well reproduced, with a deviation of less than 0.8 % for Rb and a deviation of at most 6.1 % for Sr at the atomic limit ($r = 30$ Å).

A second calculation was performed with the same basis set, but a different ECP and CPP. The 28 innermost electrons of Rb and Sr were replaced by the CRENBL ECP[114]. (This approach is in the following referred to as CR.) In contrast to the ST approach, an improvement was achieved by applying a CPP of the Müller/Meyer type[117] with a static dipole polarizability of 9.79 a. u. and a cutoff parameter of 0.322 Å^{-2} for the core of Rb. For Sr, values of 8.92 a. u. and 0.264 Å^{-2} were used. These values were again determined by optimizing the energies at large internuclear separations (table 3.1). At the atomic limit ($r = 30$ Å) the energy levels could be reproduced with a deviation of less then 0.4 % and 4.8 % for Rb and Sr, respectively.

In section 3.3.8 the results of two relativistic approaches will be presented, both based on the ST MRCI calculation. By including the spin-orbit interaction, Hund's case (a) notation as used for the MRCI PECs becomes inappropriate. In the relativistic treatment, Hund's case (c) notation is appropriate for RbSr and will be used in section 3.3.8. In the first approach (SO) the MRCI PECs in Hund's case (a) notation are transformed into Hund's case (c) states utilizing Clebsch-Gordon coefficients and the spin-orbit interaction was included with a spin-orbit Hamiltonian, following the approach outlined in ref. 179. Upon diagonalization of the resulting matrix the relativistic PECs are obtained. Note that this approach assumes the spin-orbit coupling to be constant and independent of the internuclear separation. The TDMs were calculated by multiplying the TDMs determined by the ST approach with the eigenvectors of the diagonalized states. As a second approach (BP), we used a more sophisticated method for the calculation of relativistic PECs, which is then compared to the first method. The Breit-Pauli Hamiltonian was evaluated using the MRCI wave functions, as it is implemented in the Molpro software package[140, 245]. The calculated states were identified with the assistance of the corresponding results for the SO method.

---

[2] Following functions were added to the basis sets: Rb(s: 0.0036; p: 0.0042; d: 0.0116, 2.860; f: 0.0624; g: 0.33) Sr(s: 0.0030; p: 0.0035; d: 8.337, 3.257, 0.0116; f: 0.0486: g: 0.45)

Table 3.1: Comparison of experimentally observed atomic level energies[13] to calculated transition energies for the diatomic states at an internuclear distance of 30 Å for the two different approaches (ST/CR). Values are given in cm^{-1}.

State	NIST[13]	ST	CR
Rb (5p ^{2}P°)	12737	12507	12555
Sr (5s5p ^{3}P°)	14703	14517	14476
Sr (5s4d ^{3}D)	18254	19292	19043
Rb (4d ^{2}D)	19355	19360	19425
Rb (6s ^{2}S)	20133	19952	20051
Sr (5s4d ^{1}D)	20149	21363	21110
Sr (5s4d ^{1}P°)	21698	21163	21112
Rb (6p ^{2}P°)	23767	23514	23616

3.3 Results and discussion

3.3.1 Comparison of asymptotic values to atomic energy levels

In order to estimate the accuracy of the results, the calculated asymptotic values are compared to atomic energy levels. Table 3.1 shows the asymptotic values for the energies at an internuclear distance of 30 Å as well as atomic energy levels obtained from the NIST database[13]. As can be seen, the overall agreement is good. Only the Sr (5s4d ^{1}D) ← Sr (5s^2 ^{1}S) and Sr (5s4d ^{3}D) ← Sr (5s^2 ^{1}S) atomic transitions show stronger deviations from their calculated counterparts. The energies for these two states are overestimated by about 1000 cm^{-1}, whereas a slight underestimation of about 500 cm^{-1} is found for Sr (5s4d ^{1}P°) ← Sr (5s^2 ^{1}S). All other transitions deviate by less than 260 cm^{-1}. These deviations result in a wrong energetic order of the Sr (5s4d ^{1}D) and Sr (5s4d ^{1}P°) states, which lie very close to each other. Similar deviations have been observed for calculated Sr asymptotes of the SrYb molecule in ref. 242, where the same ECP as in the ST calculation has been used. It was observed that different values of the core polarization potential and the cutoff parameter for the CPPs resulted only in minor changes of the form and depth of the potential. Instead the whole PEC was shifted upwards or downwards, giving varying agreement between energies at 30 Å and the atomic energy levels. This was only observed for states without avoided crossings, since the locations of these crossings depend strongly on the energy differences of the involved states and change the form of the potential. An avoided crossing appears if the PECs of two states of the same symmetry come close, then the states repel each other and their character changes.

The calculated TDMs in the atomic limit (at 30 Å internuclear separation) agree well with listed values in the NIST database[13]. The calculated values are shown in table 3.2, note that only states with non-negligible TDM are shown. Line strengths for different J-values are listed for the experimental values. In the ST and CR calculations no spin-orbit interaction was included and therefore only one value is shown in table 3.2.

Table 3.2: Experimentally obtained line strengths[13] (S_{ik}) are compared with calculated TDMs at 30 Å for the two different calculations (ST and CR). The squares of the TDMs (TDM^2) equal the line strengths, if the degeneracy of the excited states (g_k) is considered (fifth column).

State	J	S_{ik}[13] ($e^2a_0^2$)	g_k[13]	(S_{ik}/g_k)[13] ($e^2a_0^2$)	TDM^2 (ST) ($e^2a_0^2$)	TDM^2 (CR) ($e^2a_0^2$)
Rb (5p ^{2}P°)	1/2	17.9	2	9.0	10.1	10.1
	3/2	35.7	4	8.9		
Sr (5s5p ^{1}P°)	1	29.1	3	9.7	10.8	10.8
Rb (6p ^{2}P°)	1/2	0.1	2	0.1	0.1	0.0
	3/2	0.3	4	0.1		

3.3.2 Overview

The PECs as calculated by the ST approach are plotted in the figures 3.1, 3.2, 3.3, 3.4, and 3.5. An overview plot for the ST calculation can be found in ref. 5. The parameters of 22 PECs up to an excitation energy of 22000 cm^{-1} have been calculated and are shown in table 3.3. The lower states can be compared to previous results determined by Żuchowski *et al.*[179], where good overall agreement has been found. Some trends can be observed: The FCI[179] calculation shows the smallest equilibrium distances. The potential depths obtained by the EOM-CC[179] are smaller than those obtained with the other approaches. The potential depths of the quartet states show the largest value for calculations performed in this work. The largest differences between the different methods were found for the $3^2\Sigma^+$ state. The potential depths have a difference larger than 20 % and the vibrational constants differ by more than 10 cm^{-1}.

The calculated potentials were fitted by the betafit-program[158] and the Franck-Condon factors (FCFs) were calculated with the Level 8-program[106]. Transition probabilities were determined by multiplying the squares of the TDMs at the equilibrium position of the ground state with the FCFs. These transition probabilities enabled the assignment of transitions observed in the excitation spectrum of the RbSr molecule on He$_N$ (see ref. 6). Therein, an assignment of states with an energy up to 20500 cm^{-1} was possible.

Table 3.3: Molecular parameters of excited states and the ground state of RbSr. Related excited atomic states are given in brackets.

State	Parameters	ST[a]	CR[a]	FCI[b]	EOM-CC[b]	Exp.
$X^2\Sigma^+$	R_e (Å)	4.59	4.58	4.60	4.67	
	ω_e (cm^{-1})	42.2	42.1	39.0	38.1	42 ± 5[5]
	D_e (cm^{-1})	1273.3	1283.5	1073.3	1040.5	
$2^2\Sigma^+$	R_e (Å)	4.53	4.52	4.45	4.50	
(Rb, 5p $^2P^\circ$)	ω_e (cm^{-1})	58.5	58.9	58.4	60.2	
	D_e (cm^{-1})	5077.5	5144.3	4982.9	4609.6	
	T_0 (cm^{-1})	8710.6	8702.7	8837.4	9179.3	
$1^2\Pi$	R_e (Å)	3.92	3.91	3.87	3.93	
(Rb, 5p $^2P^\circ$)	ω_e (cm^{-1})	79.3	79.5	79.5	83.2	
	D_e (cm^{-1})	8704.8	8770.2	8439.8	8038.6	
	T_0 (cm^{-1})	5093.7	5087.1	5391.1	5761.8	
$3^2\Sigma^+$	R_e (Å)	4.18	4.15	4.06	4.13	
(Sr, 5s5p $^3P^\circ$)	ω_e (cm^{-1})	52.8	57.4	65.3	62.5	
	D_e (cm^{-1})	3609.5	3677.8	3828.0	2892.4	
	T_0 (cm^{-1})	12186.4	12089.6	11961.0	12862.9	~ 12200[6]
$2^2\Pi$	R_e (Å)	4.15	4.13	4.05	4.17	
(Sr, 5s5p $^3P^\circ$)	ω_e (cm^{-1})	65.2	65.8	67.6	63.4	
	D_e (cm^{-1})	4405.7	4450.3	4421.2	3303.5	
	T_0 (cm^{-1})	11396.5	11321.3	11369.0	12452.2	~ 11800[6]
$4^2\Sigma^+$	R_e (Å)	4.51	4.51			
(Sr, 5s4d ^3D)	ω_e (cm^{-1})	78.0	77.5			86(3)[6]
	D_e (cm^{-1})	6282.4	6138.8			
	T_0 (cm^{-1})	14301.2	14205.2			14028(1)[6]
$3^2\Pi$	R_e (Å)	4.36	4.36			
(Sr, 5s4d ^3D)	ω_e (cm^{-1})	56.9	56.4			
	D_e (cm^{-1})	5596.9	5372.6			
	T_0 (cm^{-1})	14976.1	14960.8			~ 14900[6]
$1^2\Delta$	R_e (Å)	3.93	3.93			
(Sr, 5s4d ^3D)	ω_e (cm^{-1})	73.8	73.8			
	D_e (cm^{-1})	7758.8	7637.4			
	T_0 (cm^{-1})	12822.6	12704.7			
$5^2\Sigma^+$	R_e (Å)	4.51	4.50			
(Rb, 5d ^2D)	ω_e (cm^{-1})	51.9	52.2			
	D_e (cm^{-1})	4466.3	4555.4			
	T_0 (cm^{-1})	16172.1	16158.0			
$4^2\Pi$	R_e (Å)	4.56	4.53			
(Rb, 5d ^2D)	ω_e (cm^{-1})	31.7	32.5			
	D_e (cm^{-1})	2758.0	2939.5			
	T_0 (cm^{-1})	17870.4	17764.0			~ 16600[6]
$2^2\Delta$	R_e (Å)	4.58	4.56			
(Rb, 5d ^2D)	ω_e (cm^{-1})	44.7	44.7			
	D_e (cm^{-1})	1531.2	1639.6			
	T_0 (cm^{-1})	19103.7	19070.0			
$6^2\Sigma^+$	R_e (Å)	4.55	4.54			
(Rb, 6s ^2S)	ω_e (cm^{-1})	48.0	47.8			
	D_e (cm^{-1})	1899.1	1996.0			
	T_0 (cm^{-1})	19328.8	19341.2			~ 19700[6]

Table 3.3: *Continued.*

State	Parameters	ST[a]	CR[a]	FCI[b]	EOM-CC[b]	Exp.
$7^2\Sigma^+$	R_e (Å)	4.37	4.36			
(Sr, 5s4d ^{1}D)	ω_e (cm^{-1})	60.0	60.5			
	D_e (cm^{-1})	2306.6	2246.9			
	T_0 (cm^{-1})	20139.0	20155.5			
$5^2\Pi$	R_e (Å)	4.38	4.37			
(Sr, 5s4d ^{1}D)	ω_e (cm^{-1})	54.7	52.6			
	D_e (cm^{-1})	1910.5	1856.5			
	T_0 (cm^{-1})	20532.5	20541.9			
$3^2\Delta$	R_e (Å)	4.76	4.77			
(Sr, 5s4d ^{1}D)	ω_e (cm^{-1})	35.1	34.2			
	D_e (cm^{-1})	1386.9	1329.1			
	T_0 (cm^{-1})	21245.3	21060.1			
$8^2\Sigma^+$	R_e (Å)	5.17	5.04			
(Sr, 5s5p ^{1}P°)	ω_e (cm^{-1})	35.5	33.5			
	D_e (cm^{-1})	965.1	821.0			
	T_0 (cm^{-1})	21667.4	21570.3			
$6^2\Pi$	R_e (Å)	4.72	4.70			
(Sr, 5s5p ^{1}P°)	ω_e (cm^{-1})	40.0	37.4			
	D_e (cm^{-1})	919.0	970.4			
	T_0 (cm^{-1})	21715.7	21422.8			
$1^4\Sigma^+$	R_e (Å)	6.17	6.16	6.15	6.25	
(Sr, 5s5p ^{3}P°)	ω_e (cm^{-1})	16.2	16.3	15.4	15.0	
	D_e (cm^{-1})	390.3	396.7	336.3	329.2	
	T_0 (cm^{-1})	15387.4	15350.2	15427.8	15402.4	
$1^4\Pi$	R_e (Å)	4.33	4.32	4.27	4.36	
(Sr, 5s5p ^{3}P°)	ω_e (cm^{-1})	56.9	57.6	57.0	55.0	
	D_e (cm^{-1})	3036.1	3053.9	2838.1	2655.7	
	T_0 (cm^{-1})	12761.9	12713.6	12946.8	13095.8	
$2^4\Sigma^+$	R_e (Å)	4.72	4.72			
(Sr, 5s4d ^{3}D)	ω_e (cm^{-1})	38.2	37.8			
	D_e (cm^{-1})	1670.6	1630.5			
	T_0 (cm^{-1})	18893.0	18693.6			
$2^4\Pi$	R_e (Å)	4.78	4.78			
(Sr, 5s4d ^{3}D)	ω_e (cm^{-1})	44.5	43.7			
	D_e (cm^{-1})	2098.5	2026.2			
	T_0 (cm^{-1})	18468.3	18300.9			
$1^4\Delta$	R_e (Å)	5.02	5.03			
(Sr, 5s4d ^{3}D)	ω_e (cm^{-1})	26.1	25.7			
	D_e (cm^{-1})	726.0	707.8			
	T_0 (cm^{-1})	19831.6	19610.3			

[a] This work

[b] Values are taken from ref. 179. Transition energies (T_0) are derived from atomic energy levels in the NIST-database[13].

3.3.3 Ground state

Due to the high interest in the RbSr molecule, recently several theoretical studies[119, 167, 179, 240, 241] and one experimental investigation[5] have targeted the electronic ground state. In comparison to the other theoretical results, the approach used in this work leads to a larger binding energy for the ground state (10 - 20 % deeper than the others, see table 3.4). A similar effect was observed with the same approach for the LiCa molecule[2]. Slightly higher values were obtained for the PEDM and the vibrational constant in our calculation than in previous theoretical work. Recently the vibrational constant was determined experimentally and a value of 42 ± 5 cm^{-1} was reported[5], which is in excellent agreement with the theoretical values in table 3.4. The equilibrium distance agrees with the result obtained by Guérout *et al.*[119], whereas the other authors found slightly larger values (see table 3.4).

Table 3.4: Compilation of different theoretical results for the ground state. The value for the PEDM is taken at the respective equilibrium position of the ground state.

Source	R_e (Å)	D_e (cm^{-1})	PEDM (a.u.)	ω_e (cm^{-1})
Gopakumar[167]	4.72	916	0.55	36
Chen [241]	4.67	1018		36
Żuchowski[179]	4.66	1059	0.61	38
Guérout[119]	4.60	1073	0.61	32
This work	4.59	1274	0.71	42

Figure 3.1 shows the PEC and PEDM obtained for the ground state. The local maximum of the PEDM is at about 4.1 Å, at a smaller internuclear separation than the equilibrium position of the ground state. The behavior and position of the PEDM curve agrees with previous results[119, 167, 179], although the amplitude is slightly larger. The vector for the PEDM points from Sr to Rb. Consequently, the positive value in figure 3.1 indicates an increased probability density of the electron close by the Sr atom. This result is reasonable, considering the higher electronegativity of Sr compared to Rb.

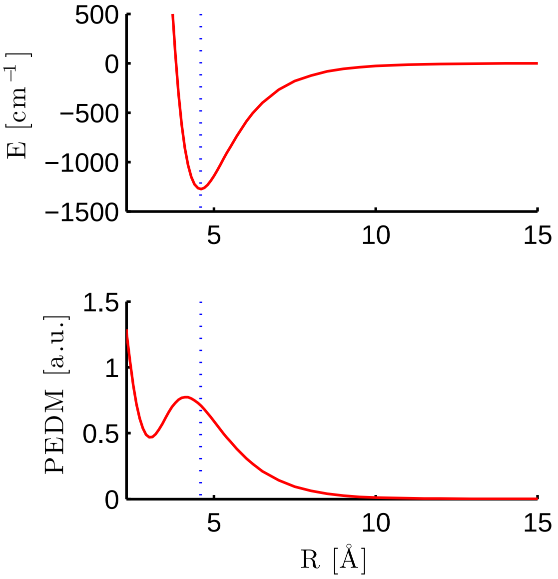

Figure 3.1: PEC and PEDM for the ground state of RbSr as determined by the ST calculation. The dotted line marks the minimum of the potential energy curve.

3.3.4 Diatomic states corresponding to the Rb (5p ^{2}P°) + Sr (5s^2 ^{1}S) asymptote

In the non-relativistic picture, the Rb (5p ^{2}P°) state gives rise to two diatomic PECs, the $2^2\Sigma^+$ and the $1^2\Pi$ doublet states. The $1^2\Pi$ state shows the smallest equilibrium separation and largest potential depth of all calculated states. The internuclear distance dependent properties (PECs, TDMs, PEDMs) of these states are displayed in figure 3.2. The transition Rb (5p ^{2}P°) ← Rb (5s ^{2}S) has the highest line strength of all transitions for the Rb and Sr atoms, which include the ground state. Consequently, the $2^2\Sigma^+$ and the $1^2\Pi$ states have a high TDM at large internuclear separation. The value of the TDM for the $2^2\Sigma^+$ state even increases for smaller internuclear separations and reaches a maximum at 6.5 Å. This state has the highest TDM of all calculated states at the equilibrium distance of the RbSr ground state. The TDM of the $1^2\Pi$ state becomes smaller with decreasing internuclear separation and is small for the equilibrium distance. The PEDM of the states displayed in figure 3.2 are mainly positive and their amplitudes are larger than the one for the ground state. This is in agreement with the behavior of the TDMs and PEDMs reported in ref. 179.

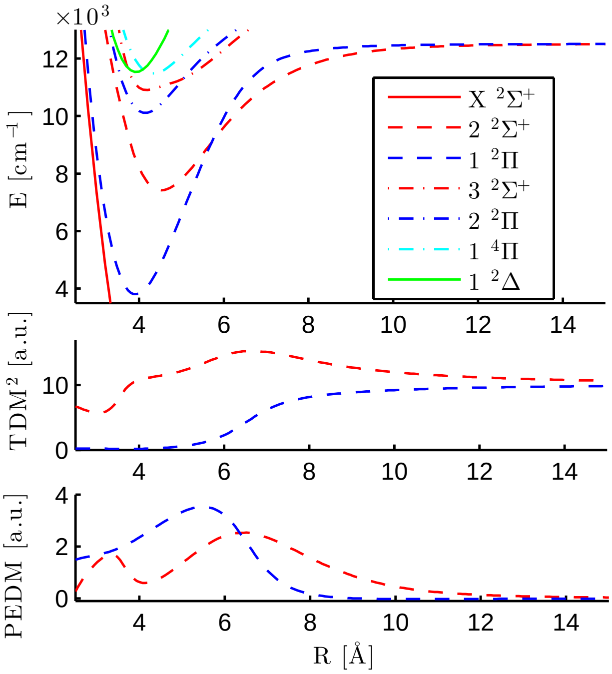

Figure 3.2: The PECs, PEDMs and TDMs for the lowest excited states of RbSr determined with ST calculation. The TDMs were calculated for a transition from the ground state into the denoted excited states.

3.3.5 Diatomic states corresponding to the Rb (5s ^{2}S) + Sr (5s4d ^{3}P°) asymptote

Figure 3.3 contains the PECs, TDMs and PEDMs for molecular states approaching the Sr (5s4d ^{3}P°) atomic state at long distances. The two doublet states, $3^2\Sigma^+$ and $2^2\Pi$, as well as the two quartet states, $1^4\Sigma^+$ and $1^4\Pi$, show crossings with the strongly bound $1^2\Delta$ state (see figures 3.2 and 3.3). The calculations provide valuable information for the interpretation of dispersed fluorescence spectra obtained for the free RbSr molecule, formed on helium nanodroplets[5] .In these experiments RbSr molecules have been excited initially into the $4^2\Sigma^+$ state. The majority of the molecules relaxed into lower states and a strong fluorescence originating from the $3^2\Sigma^+$ and $2^2\Pi$ states has been observed. The $1^2\Delta$ state, which has the same asymptote as the $4^2\Sigma^+$ state, provides a relaxation path into the $3^2\Sigma^+$ and $2^2\Pi$ states, which is accessed by the interaction with He$_N$. Furthermore, the $3^2\Sigma^+$ and $2^2\Pi$ states have been experimentally studied for RbSr on He$_N$ by resonance enhanced multiphoton ionization time-of-flight spectroscopy (REMPI-TOF), giving rise to a broadened double peak structure. In comparison to free molecules, transitions of AK-AKE molecules on the surface of He$_N$[2, 6] are shifted by a few cm^{-1}. For the $3^2\Sigma^+$ state the measured energy (T_0[2]≈ 12200 cm^{-1}) agrees well with the calculated value ($T_0 \approx 12200\,\mathrm{cm}^{-1}$). The accuracy of the experimental value for the $2^2\Pi$ state (T_0[2]≈ 11800 cm^{-1}) is limited, because it is cut off by the end of the laser tuning range, but it corresponds well to theory ($T_0 \approx 11400\,\mathrm{cm}^{-1}$). These

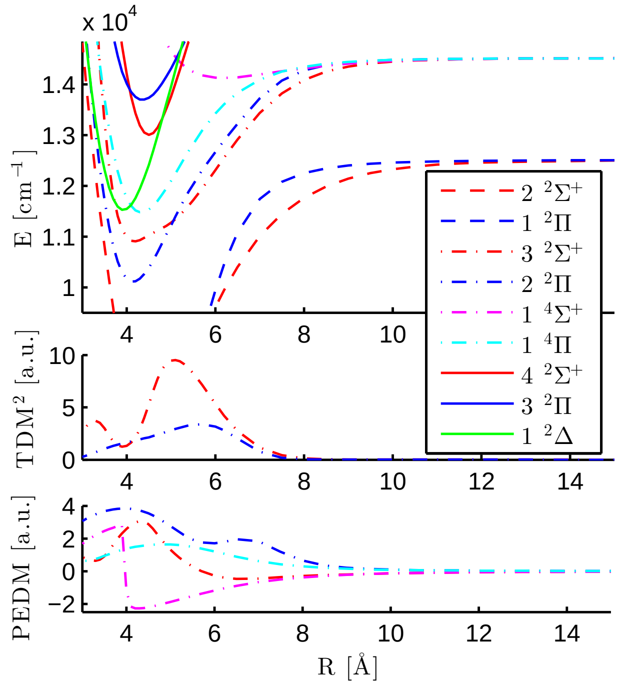

Figure 3.3: The PECs, PEDMs and TDMs for excited states of RbSr determined with ST calculation are shown in the figure.

states have a transition dipole moment of zero in the asymptotic limit, as expected for the Sr (5s4d ^{3}P°) ← Sr (5s^2 ^{1}S) transition. The TDM of the $3^2\Sigma^+$ state has two maxima, the $2^2\Pi$ has only one within the calculated distances. Comparing this result with previous calculations, it can be seen that it agrees better with the EOM-CC[179] calculation than the FCI[179] calculation, which applies a large effective core potential. The FCI approach shows a weaker TDM with a maximum at smaller internuclear separation than the results presented here. The higher TDM obtained with our approach seems more reliable, because the calculated transition probabilities agree well with the experiment[6]. A possible explanation for the deviation of the FCI calculation is offered by the application of larger ECPs. The TDMs of the quartet states are zero for all internuclear separations, as demanded by the selection rules. The PEDMs for the doublet states more closely resemble the FCI results than the EOM-CC results[179]. The quartet states show a different behavior than reported in ref. 179. The calculations presented here consider higher quartet states and their interaction with each other. Especially in the case of the $1^4\Sigma^+$ state this leads to a strong change of the PEDM at 4 Å, as can be seen in figure 3.3. The $3^2\Sigma^+$ state has a slightly negative PEDM at about 7 Å and the $1^4\Sigma^+$ state shows negative values down to 4 Å, indicating a charge transfer towards the Rb atom.

3.3.6 Diatomic states corresponding to the Rb (5s ^{2}S) + Sr (5s4d ^{3}D) and Rb (4d ^{2}D) + Sr (5s^2 ^{1}S) asymptotes

Six doublet states ($4^2\Sigma^+$, $3^2\Pi$, $1^2\Delta$, $5^2\Sigma^+$, $4^2\Pi$, $2^2\Delta$) and three quartet states ($1^4\Sigma^+$, $1^4\Pi$, $1^4\Delta$) correlate to the excited Sr (5s4d ^{3}D) and Rb (4d ^{2}D) atomic states, the corresponding PECs, TDMs, and PEDMs are shown in figure 3.4. The $4^2\Sigma^+$ and $5^2\Sigma^+$ states show two avoided crossings, the first at 12 Å, the second at 6 Å. These avoided crossings alter the PEC and related properties. The potential depth and the vibrational states within the potential depend on the avoided crossing, especially if the crossing lies in a region of the potential well with a strong gradient. The first avoided crossing was determined with 9.5 Å (FCI) and 8.5 Å (EOM-CC) by Żuchowski *et al.*[179] These values for the position of the avoided crossing are expected to be more accurate, since the Rb (5s ^{2}S) + Sr (5s4d ^{3}D) asymptote is better described by the calculations in ref. 179. The disagreement is related to the small slope of the PECs. The second avoided crossing appears at ≈ 6.8 Å (FCI) / 6.3 Å (EOM-CC), in agreement with our result. This avoided crossing leads to a distinct change of the PECs and other electronic properties at 6 Å for the $4^2\Sigma^+$ and $5^2\Sigma^+$ states (see figure 3.4). The $3^2\Pi$ and $4^2\Pi$ states exhibit an avoided crossing at 10 Å. Żuchowski *et al.*[179] reported a value of 8.5 Å, the deviation is again linked to the weak slope of the potential.

In REMPI-TOF and laser induced fluorescence (LIF) measurements of RbSr on He$_N$ the $4^2\Sigma^+$ state was observed and vibrationally resolved (see Figure 4 in ref. 6). The energy T_e = 14006(4) cm^{-1} and vibrational constant ω_e = 86(3) cm^{-1} agree satisfactorily with our calculations (T_e = 14321.8 cm^{-1}, ω_e = 76 cm^{-1}). The experimental and theoretical energy levels for the $3^2\Pi$ state compare well, T_0[2]≈ 14900 cm^{-1} and

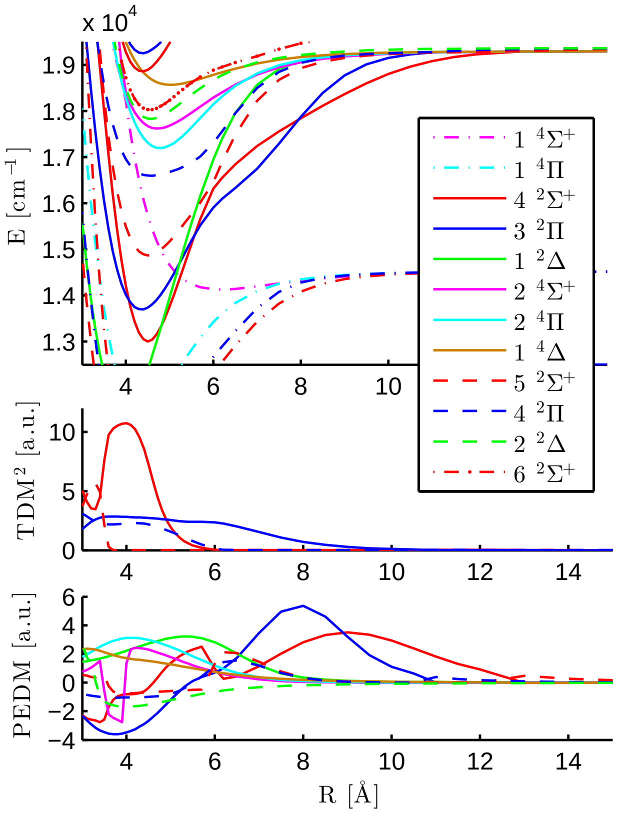

Figure 3.4: PECs, TDMs, and PEDMs for diatomic states originating from the Rb (4d ^{2}D) + Sr (5s^2 ^{1}S) and Rb (5s ^{2}S) + Sr (5s4d ^{3}D) asymptotes as calculated by the ST approach.

$T_0 \approx 15000\,\mathrm{cm}^{-1}$ respectively. The $5^2\Sigma^+$ state was not observed experimentally, which can be explained by its small TDM (see figure 3.4). An energy of T_0[6]$\approx 16600\,\mathrm{cm}^{-1}$ was found for the $4^2\Pi$ state in REMPI-TOF measurements, whereas the theoretical prediction gives a value of $T_0 \approx 17900\,\mathrm{cm}^{-1}$. This difference can be understood by the similar deviation for the asymptote Rb (5s ^{2}S) + Sr (5s4d ^{3}D) (see table 3.1), which might be transferred to this state via the avoided crossing. This assumption is supported by a value of $T_0 \approx 17800\,\mathrm{cm}^{-1}$ obtained with the CR calculation, where the deviation for the Rb (5s ^{2}S) + Sr (5s4d ^{3}D) asymptote is smaller.

3.3.7 Higher excited diatomic states

In figure 3.5 several higher excited states are shown. These molecular states correspond to the Rb (6s ^{2}S) + Sr (5s^2 ^{1}S), Rb (5s ^{2}S) + Sr (5s4d ^{1}D), and Rb (5s ^{2}S) + Sr (5s4d ^{1}P°) asymptotes, which lie very close to each other (see table 3.1). As mentioned above, the calculated asymptotic energies show the wrong energetic order. The results in figure 3.5 indicate avoided crossings between the displayed diatomic electronic states. Even higher electronic states influence the results, as can be observed in figure 3.5 for the $7^2\Pi$ and

$9^2\Sigma^+$ states. The four states, $5^2\Pi$, $6^2\Pi$, $7^2\Sigma^+$, and $8^2\Sigma^+$, have relatively high TDMs at the equilibrium position of the ground state and give rise to experimentally detectable transitions, see Figure 2 in ref. 6.

Among the states discussed in this section, the $6^2\Sigma^+$ state lies energetically lowest and has the smallest TDM at the equilibrium position of the ground state. However, it gives rise to a signal in the experiment at $T_0[2] \approx$ 19700 cm^{-1}, whereas the theoretical value is given by $T_0 \approx$ 19300 cm^{-1}. For higher excited states the calculation is less reliable and an unambiguous identification of spectral features is no longer possible, because the states start to overlap. In figure 3.5 avoided crossings can be observed for the $7^2\Sigma^+$ and $8^2\Sigma^+$ states as well as for the $5^2\Pi$ and $6^2\Pi$ states. These avoided crossings vanish if the order of the Sr (5s4d ^{1}D) and Sr (5s4d ^{1}P°) states would be reproduced correctly. This provides a possible explanation for the high TDM of the $8^2\Sigma^+$ and $6^2\Pi$ states which correspond to the Sr (5s4d ^{1}P°) atomic state with a high TDM (table 3.2), if the avoided crossing is taken into account. The PEDM for the $6^2\Sigma^+$ state has the largest negative value of all considered states, which is reasonable, because the excited electron resides in the 6s orbital, the largest one of the considered Rb orbitals.

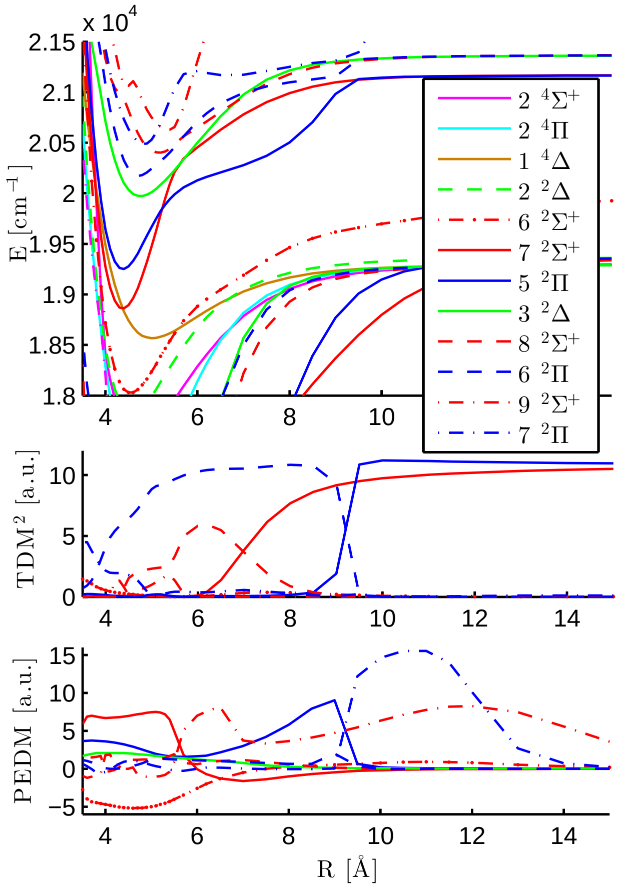

Figure 3.5: PECs, TDMs, and PEDMs are shown for the higher diatomic states treated in the MRCI (ST) calculation.

3.3.8 Relativistic potential energy curves for the diatomic states corresponding to the Rb (5s ^{2}S) + Sr (5s4d ^{3}P°) and Rb (5p ^{2}P°) + Sr (5s^2 ^{1}S) asymptotes

In this section we present two relativistic approaches, which include spin-orbit interaction for the diatomic RbSr molecule. Due to the increased effort of these calculations, only states correlating to the Rb (5s ^{2}S) + Sr (5s4d ^{3}P°) and Rb (5p ^{2}P°) + Sr (5s^2 ^{1}S) asymptotes were treated. As will be shown, this relativistic treatment is necessary for an accurate description of these states, because Rb and Sr are both heavy atoms with a significant spin-orbit splitting. For the atoms, the spin-orbit splitting amounts to 238 cm^{-1} ($^2\mathrm{P°}_{3/2}$-$^2\mathrm{P°}_{1/2}$) for Rb as well as 187 cm^{-1} ($^3\mathrm{P°}_1$-$^3\mathrm{P°}_0$) and 394 cm^{-1} ($^3\mathrm{P}_2$°-$^3\mathrm{P°}_1$) for Sr[13].

The results of the two relativistic approaches are shown in figure 3.6. The PECs on the left side (SO) were obtained with a spin-orbit Hamiltonian with constant spin-orbit coupling[179]. On the right side the findings for an evaluation of the Breit-Pauli Hamiltonian are displayed. The PECs and TDMs determined with the two different approaches are in good agreement. A notable difference can be observed in the proximity of the avoided crossings, which appears more smoothly for the SO method. The PECs which correspond to the Rb (5s ^{2}S) + Sr (5s4d ^{3}P°) asymptote show a significant difference for the two methods in the range from 7 to 8 Å. A stronger influence of the PECs onto each other and changes in the slopes are observed for the BP approach. The inset on the right side shows results for a Breit-Pauli calculation including states beyond the Rb (5s ^{2}S) + Sr (5s4d ^{3}P°) atomic asymptote. An unambiguous assignment of these states was not possible, but the crossing PECs are related to the $1^2\Delta$ state in the MRCI-calculations.

In table 3.5 the spectroscopic parameters of relativistic PECs calculated in this work are compared to the results of Chen *et al.*[241]. Therein the authors performed a Kramers-restricted MRCI calculation within a four-component framework. In general our potentials are deeper, whereas for the equilibrium distances no clear trend is observed.

Dispersed fluorescence measurements for RbSr on He_N have been presented in ref. 5. The RbSr diatomic molecules desorb after excitation and consequently the emission signal is not influenced by the helium environment. A strong signal was observed at 12400 cm^{-1}, shown in figure 3.7 with the label 'exp. data'. The spectrum was simulated by using three different sets of PECs, from the MRCI (ST), the spin-orbit matrix (SO), and the Breit-Pauli (BP) calculation. The PECs were fitted using the betafit-program[158]. With the determined analytical potentials the vibrational states and the Franck-Condon factors were calculated by using the Level 8-program[106]. Subsequently the FCFs were summed up and weighted with the square of the TDMs at a internuclear separation of 4.6 Å. Therefore only two states from the MRCI calculation ($3^2\Sigma^+$, $2^2\Pi$) and three states from the spin-orbit calculation ($4\left(\Omega = \frac{1}{2}\right)$, $2\left(\Omega = \frac{3}{2}\right)$, $5\left(\Omega = \frac{1}{2}\right)$) were taken into account. The relativistic states are denoted according to Hund's case (c) notation and numbered starting from the lowest state (see figure 3.6 and table 3.5). All other states have either a negligible transition dipole moment or their energy levels are

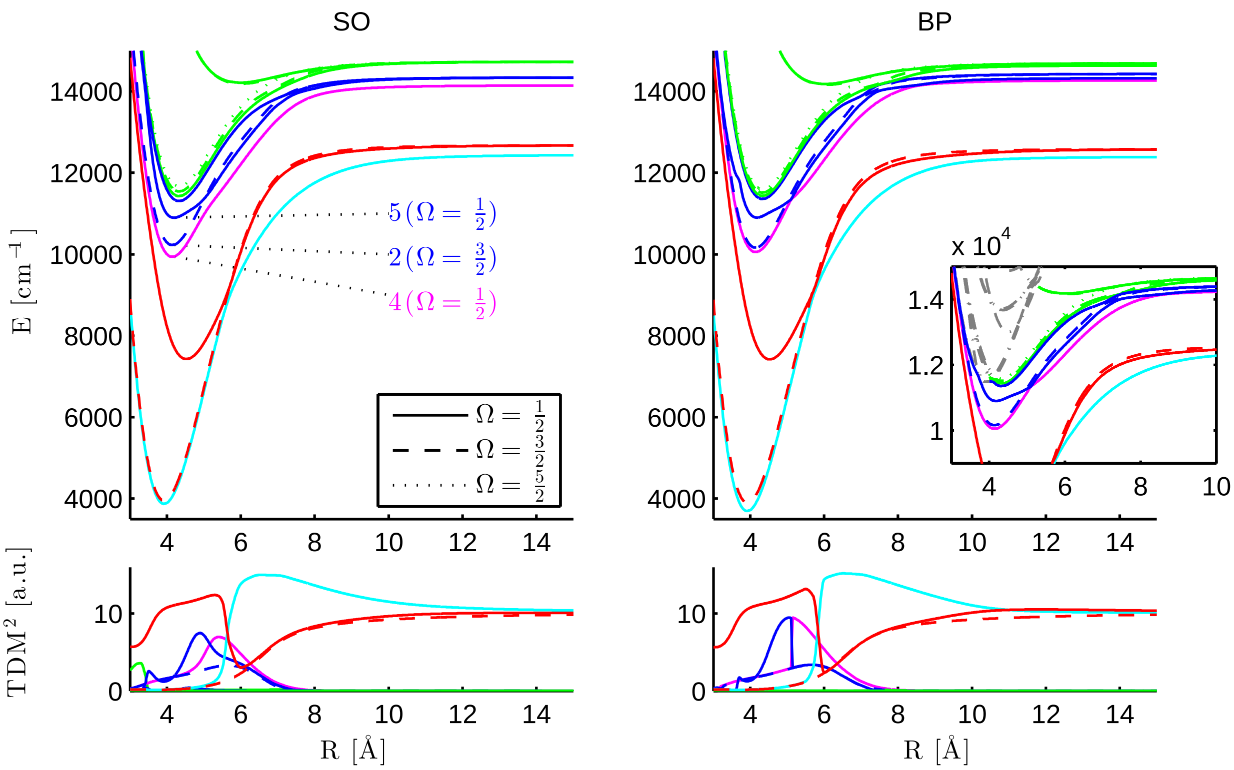

Figure 3.6: The PECs and the TDMs for the lowest excited states including spin orbit coupling. The results on the left were obtained by the SO method[179] the results on the right with Breit-Pauli calculation as implemented in the Molpro-Package[140]. The inset on the right side shows PECs for a Breit-Pauli calculation including higher states.

far off. For the simulation of the emission spectrum an assumption for the distribution of occupied excited states is required. The most successful assumption was a normal distribution with a mean at 12750 cm^{-1} and a standard deviation of 100 cm^{-1}. This distribution of the occupation coincides with the lowest vibrational levels of the $1^2\Delta$ state, assuming a similar shift as for the other states. A maximum of the population of vibrational levels levels at the minimum of the $1^2\Delta$ state strongly indicates that this state which crosses also the $4^2\Sigma^+$ potential close to its minimum, is responsible for the experimentally observed population transfer. Note that the relaxation process in ref. 5 is enabled by the helium environment. After a shift of the potentials to the correct asymptotes the shape of the signal was reproduced, but not the energetic position. An additional shift of about 280 cm^{-1} to smaller photon energies was necessary, which is probably related to the overestimation of the potential depth of the ground state. A similar deviation was found for the transition $4^2\Sigma^+ \leftarrow \mathrm{X}\ ^2\Sigma^+$ in ref. 6, which uses the results from the ST calculation. Finally the determined intensities are convoluted with a normal distribution with a width of 6 cm^{-1}, representing the instrument limited line width.

Table 3.5: Comparison of the relativistic PECs with previously published results, numbering of states as in figure 3.6. The excited atomic states, which the diatomic states approach for large distances, are given in brackets.

State	Parameters	SO[a]	BP[a]	Chen *et al.*[241]
1 $\left(\Omega = \frac{1}{2}\right)$	R_e (Å)	4.59	4.58	4.67
	ω_e (cm^{-1})	42.2	42.0	36.0
	D_e (cm^{-1})	1274.2	1274.5	1017.6
2 $\left(\Omega = \frac{1}{2}\right)$	R_e (Å)	3.93	3.92	3.85
(Rb, 5p $^2P_{\frac{1}{2}}$°)	ω_e (cm^{-1})	79.6	77.4	85.7
	D_e (cm^{-1})	8569.0	8675.7	7883.1
1 $\left(\Omega = \frac{3}{2}\right)$	R_e (Å)	3.92	3.93	3.86
(Rb, 5p $^2P_{\frac{3}{2}}$°)	ω_e (cm^{-1})	80.4	77.3	87.2
	D_e (cm^{-1})	8727.6	8665.4	7957.3
3 $\left(\Omega = \frac{1}{2}\right)$	R_e (Å)	4.53	4.53	4.44
(Rb, 5p $^2P_{\frac{3}{2}}$°)	ω_e (cm^{-1})	58.7	57.8	58.4
	D_e (cm^{-1})	5252.3	5158.0	4683.6
4 $\left(\Omega = \frac{1}{2}\right)$	R_e (Å)	4.14	4.14	
(Sr, 5s5p $^3P_0$°)	ω_e (cm^{-1})	64.1	65.8	
	D_e (cm^{-1})	4202.3	4215.9	
2$\left(\Omega = \frac{3}{2}\right)$	R_e (Å)	4.14	4.14	
(Sr, 5s5p $^3P_1$°)	ω_e (cm^{-1})	64.5	66.1	
	D_e (cm^{-1})	4107.4	4262.5	
5 $\left(\Omega = \frac{1}{2}\right)$	R_e (Å)	4.20	4.18	
(Sr, 5s5p $^3P_1$°)	ω_e (cm^{-1})	52.4	53.7	
	D_e (cm^{-1})	3436.2	3419.2	

[a] This work.

Note that the simulated spectrum applying the BP approach has already been presented in Figure 3 in ref. 5. In contrast to the simulation therein, we first shifted the BP potential energy curves such that the calculated asymptotes match the spin-orbit split atomic states. This explains the difference in the assumed population maximum as well as the difference in the final shift between this work and ref. 5. The results for the three different sets of PECs are shown in figure 3.7. Without considering spin-orbit coupling the experimental emission is represented poorly, as can be seen from the MRCI (ST) simulation in figure 3.7. The smaller features are not reproduced at all and the contour shows an additional peak. The two simulations, which apply the relativistic potentials resemble the fine structure in the experimental spectra with a spacing of about 10 cm^{-1}. The overall structure with a spacing of about 60 cm^{-1} is well reproduced, especially with the PECs obtained by the SO method. The main contribution to the observed emission originates from the 5 $\left(\Omega = \frac{1}{2}\right)$ state, which is the state with the largest transition dipole moment. The vibrational spacing in the region of the assumed maximum of the vibrational population for the 5 $\left(\Omega = \frac{1}{2}\right)$ PEC is about 45 cm^{-1}. The small structure

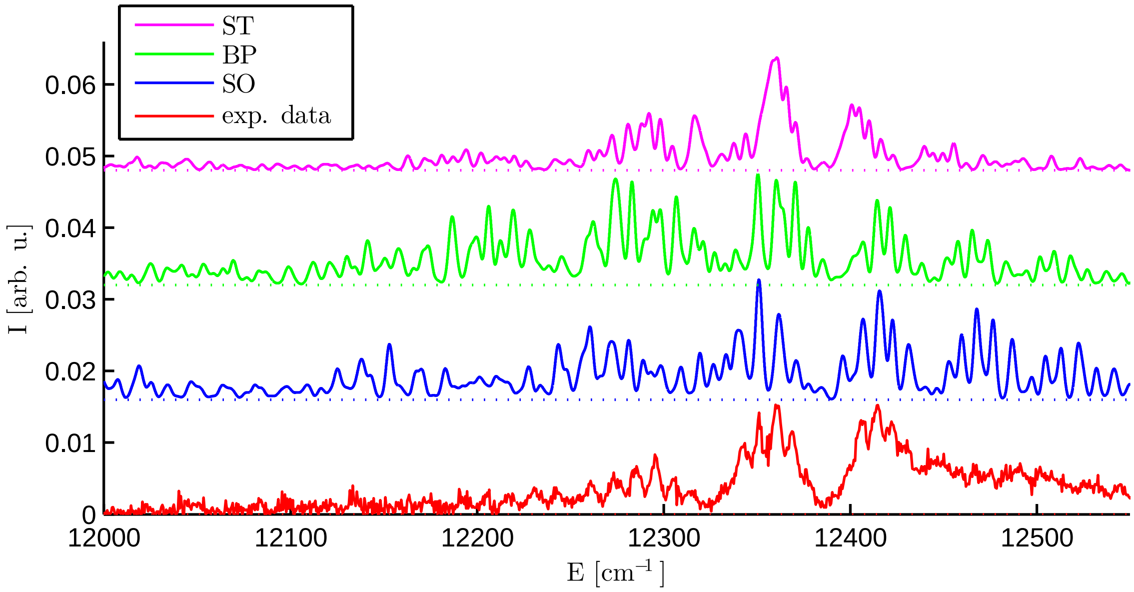

Figure 3.7: Comparison of a dispersed fluorescence spectrum[5] (exp. data) and several simulated spectra. The non-relativistic simulation (ST) differs significantly from the measurement. The simulations including spin-orbit interaction (BP, SO) resemble the experimental structure.

($\approx 10\,\mathrm{cm}^{-1}$) originates from the difference in the vibrational spacing of the excited state ($\approx 45\,\mathrm{cm}^{-1}$) and of the ground state ($\approx 36\,\mathrm{cm}^{-1}$) in the Franck-Condon window. The 4 ($\Omega = \frac{1}{2}$) state contributes significantly to the signal especially for the lower part of the spectrum.

3.4 Conclusion

We have presented *ab initio* calculations for the ground and excited states of the RbSr molecule, encompassing potential energy curves, transition dipole moments and permanent electric dipole moments. Our approach utilizes a multireference configuration interaction calculation based on multiconfigurational selfconsistent field wave functions, applying ECPs and CPPs. We compared two different sets of ECPs and CPPs, which are in excellent agreement with each other. The results are compared to available REMPI excitation spectra, which have been recorded recently for RbSr molecules formed on the surface of helium nanodroplets[5, 6]. This allowed to draw conclusions on the reliability of the calculations: while the lower states deviate by less than $250\,\mathrm{cm}^{-1}$ from the experimentally observed energy levels, the difference between experiment and theory increases for higher excited states.

The large spin-orbit interaction in the lowest excited states of Rb and Sr (Rb 5p $^2\mathrm{P}^o$ and Sr 5s5p $^3\mathrm{P}^o$ states) calls for a relativistic treatment of the related molecular RbSr potentials. For the calculation of relativistic potential energy curves and the corresponding transition dipole moments, two different methods have been compared: (i) the Breit-Pauli Hamiltonian, as implemented in the MOLPRO package[140], has been evaluated, (ii) following the approach of Żuchowski *et al.*[179] we calculated relativistic potentials from the MRCI results by diagonalizing the matrices for the respective sets of Hund's case (c) states, which include the respective spin-orbit Hamiltonians. The two different methods are compared to experimentally recorded dispersed fluorescence spectra. In both cases, the agreement between experimental and simulated spectra is good. Although the Breit-Pauli method accounts for a variation of the spin-orbit coupling with the internuclear separation, the spin-orbit Hamiltonian based method leads to slightly better results, which is attributed to the smoother potentials in the region of the avoided crossing, which lies in the proximity of the population maximum of vibrational states in the simulation.

The presented calculations in combination with the experiments[5, 6], which have been used to benchmark our results, give a thorough description of the electronic structure of the RbSr system. The presented results may serve as a valuable contribution for the quest for the production of ultracold ground state RbSr molecules as the first ultracold molecule with an electric and magnetic dipole moment, thus offering intriguing new possibilities for its controlled manipulation. As our theoretical approach has now been successfully applied to RbSr and LiCa, it may easily be adapted in a future work for the RbCa molecule. Besides RbSr, RbCa molecules may represents another promising candidate for both, the formation of ultracold molecules (a Ca BEC has already been reported[63]) as well as the formation and investigation of RbCa on the surface of helium nanodroplets.

3.5 Remark

More comparisons between experimental and theoretical results can be found in refs. 5, 6 and in the PHD thesis of Günter Krois[23]. Two methods to include spin-orbit coupling were presented in section 1.6 and applied to RbSr in section 3.3. During peer review, the question arose of how these methods compare to each other.

In the SO method, the matrices given in section 1.6.1 are diagonalized applying potential energy curves obtained by MRCI. The spin-orbit coupling is included *via* parameters that are held constant for different internuclear separations. The coupling parameter A_{Rb} and A_{Sr} are one third of the level splitting of the related atomic states. For Rb the value is A_{Rb} = 79.2 cm^{-1}, derived from a splitting of 237.595 cm^{-1}[13] between the $^2P_{\frac{1}{2}}$ and $^2P_{\frac{3}{2}}$ states. The relevant level splitting for Sr between the $^3P_0$ and $^3P_2$ states is given by 581.038 cm^{-1}[13]. Therefore, the coupling parameter for Sr amounts to $A_{Sr} = 193.7$ cm^{-1}.

In the BP method, on the other hand, the determined wave functions are employed and the operator presented in section 1.6.2 is evaluated. An better approximation to the BP result should be given by a matrix diagonlization with the SO method for variable coupling coefficients. Following this idea we determined the coupling parameters (A_{Rb}, A_{Sr}) for each internuclear separation by minimizing the difference between the SO and BP energies. The resulting curves are presented in figure 3.8. In ref. 246 a similar approach was used and the spin-orbit splitting for RbCs was described with distance dependent coupling parameters which were extracted from experimental data.

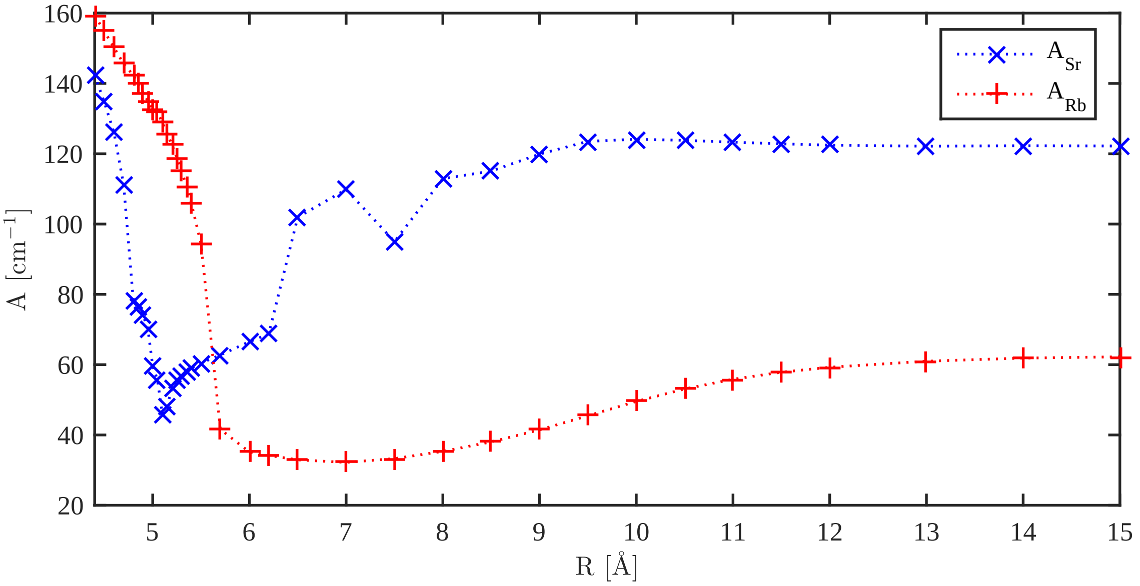

Figure 3.8: This figure displays the distance dependent spin-orbit coupling parameters, which yield the best agreement between Breit-Pauli results and the SO diagonlization. Both of the results are based on the ST approach.

The asymptotic value of the coupling parameter A_{Rb} in figure 3.8 is 62 cm^{-1}, close to the atomic value of 79.2 cm^{-1}. For A_{Sr} the calculation yields 122 cm^{-1} in somewhat worse agreement with the atomic value of 193.7 cm^{-1}. The strong change in the coupling parameter of Sr at 5 Å is probably related to the crossing of two potential energy curves in the Hund's case (a) description. Here, the $3\,^2\Sigma^+$ and $2\,^2\Pi$ states cross. It is not an avoided crossing because the states have different symmetry, but if spin-orbit interaction is included these states interact and split up. This interaction is differently described by the two methods, which is probably the cause for the tip in the curve. Since more Hund's case (c) states are involved, the description of the spin-orbit interaction with only one parameter seems to be insufficient, leading to the jumps in the curve. The coupling coefficients for the Rb and Sr states show a similar behavior. There is a small change of the coupling parameter for large internuclear separations. For distances smaller than 10 Å the coupling coefficient and its associated interaction is lowered at first but increases again afterwards. A significant change of the spin-orbit parameter, a lowering to about half its value occurs around 6 Å, appears already near the equilibrium distance of most states.

Chapter 4

Investigation of the diatomic molecule RbCa

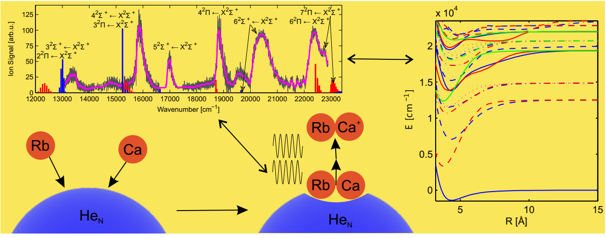

This chapter corresponds to the publication:
Investigation of the RbCa molecule: Experiment and theory
by Johann V. Pototschnig, Günter Krois, Florian Lackner, and Wolfgang E. Ernst
in *Journal of Molecular Spectroscopy*, **2015**, *310*, 126,
which was written by the author of the thesis.

The author of the thesis was responsible for:

- author of the publication
- realization and implementation of the *ab initio* calculations
- determination of the vibronic spectra based on the *ab initio* calculations
- interpretation of the result, comparison to experiments

The contributions of the co-authors are listed below:

- G. Krois: experiment and data acquisition, author of the experimental parts
- F. Lackner: experiment, interpretation of the results, editing
- W. E. Ernst: supervision, editing, funding

Reproduced from ref. 8. Published by Elsevier Inc. The article is available at http://dx.doi.org/10.1016/j.j

Abstract

We present a thorough theoretical and experimental study of the electronic structure of RbCa. The mixed alkali-alkaline earth molecule RbCa was formed on superfluid helium nanodroplets. Excited states of the molecule in the range of 13000 - 23000 cm^{-1} were recorded by resonance enhanced multi-photon ionization time-of-flight spectroscopy. The experiment is accompanied by high level *ab initio* calculations of ground and excited state properties, utilizing a multireference configuration interaction method based on multiconfigurational self consistent field calculations. With this approach the potential energy curves and permanent electric dipole moments of 24 electronic states were calculated. In addition we computed the transition dipole moments for transitions from the ground into excited states. The combination of experiment and theory allowed the assignment of features in the recorded spectrum to the excited $3^2\Sigma^+$, $4^2\Sigma^+$, $3^2\Pi$, $5^2\Sigma^+$, $4^2\Pi$, $6^2\Sigma^+$, $6^2\Pi$, and $7^2\Pi$ states, where the experiment allowed to benchmark the calculation. This is the first experimental work giving insight into the previously unknown RbCa molecule, which offers great prospects in ultracold molecular physics due to its magnetic and electronic dipole moment in the $^2\Sigma^+$ ground state.

4.1 Introduction

Alkali-alkaline earth (AK-AKE) molecules, such as RbCa, are of growing interest in ultracold molecular physics, because they possess a permanent electric dipole moment in combination with a magnetic dipole moment in their $^2\Sigma^+$ ground state. These properties enable new exciting applications and experiments, such as precise measurements of fundamental physical constants[31, 90] or simulations of spin models in optical lattices[77, 79]. The replacement of the AKE by Yb leads to a class of molecules with similar features which have been studied theoretically[242, 247–251] as well as experimentally in combined traps of ultracold AK and Yb atoms[68, 69, 252, 253]. AKE monohalides, such as CaF or SrF[35, 59, 254, 255], also possess a magnetic and permanent electric dipole moment in their $^2\Sigma^+$ ground state. While AKE monohalides are typically produced at elevated temperatures and need to be cooled as molecules, AK and AKE atoms are individually cooled into the ultracold temperature regime for a subsequent laser assisted formation of molecules. The latter method has been successfully applied to form ultracold homo- and heteronuclear AK diatomic molecules[53, 256] and does not require the more difficult cooling of the many degrees of freedom in molecules.

Due to this interest in AK-AKE molecules their ground states have been studied extensively by theory[89, 119, 167, 240, 257–260]. Experimentally, LiBa and LiMg were investigated by means of spectroscopy[261–264] also in combination with calculations[265]. LiCa is the best studied AK-AKE molecule including several experiments[2, 24, 25, 266] and theoretical calculations[2, 266–268]. Among the AK-AKE molecules, RbSr appears to be the most promising candidate for the preparation of ultracold ground state molecules. Rb and Sr atoms have been prepared in combined traps[26, 269] and quantum degenerate mixtures have been obtained[26]. Consequently, excited states of RbSr were investigated theoretically[3, 179, 241] and experimentally on He nanodroplets[5, 6].

RbCa represents the other interesting molecule, because Rb and Ca are well under control in ultracold atomic physics. Ultracold Rb_2 ground state molecules[256] as well as Bose Einstein condensates of Rb[60] and Ca[63] have been reported. Furthermore, a combined trap of Rb atoms and Ca^+ cations has been applied in the study of cold reactive collisions[270]. The electronic structure of RbCa is unknown; to the best of our knowledge neither calculations nor experimental investigations of excited states have been reported. The ground state has been addressed in recent calculations[167] as well as the ground and excited states of the $RbCa^+$ cation[270–272]. Considering these prospects for RbCa, a spectroscopic investigation of this molecule is of great interest. Gas phase formation of RbCa is impeded by the very different vapor pressure curves of Rb and Ca. Here, matrix isolation spectroscopy comes to mind, which has been the starting point of many free radical studies in the past. Many examples were reported in a special issue in 2000[273] and we want to draw special attention to the extensive and pioneering work by Marilyn Jacox[274]. While perfect for the preparation of radicals in the cold environment of a rare gas host, matrices usually induce some perturbation and non-negligible spectral line shifts. About 20 years ago, doping helium nanodroplets with foreign atoms and molecules[198, 275] turned out to evolve as a new form of matrix isolation spectroscopy, named helium nanodroplet isolation (HENDI) spectroscopy[276]. As the new nano-matrix is created in a molecular beam apparatus, most methods of molecular beam spectroscopy, including double-resonance techniques, can be applied. A detailed survey is given in a recent book chapter[164], which also addresses the much smaller influence on spectral lines in comparison with conventional matrix isolation spectroscopy. Helium droplets have a constant temperature of 0.37 K for ^{4}He[164, 193] maintained by evaporative cooling, which greatly simplifies excitation spectra because the dopant molecules are in their vibronic ground state. AK and AKE atoms have been previously investigated with HENDI spectroscopy[277–280] and except for Mg, were all found to reside on the droplet surface. Besides atoms, several homo- and heteronuclear diatomic molecules consisting of alkali atoms[281, 282] as well as AK trimers[194, 195, 283] have been studied on He nanodroplets. Recently HENDI spectroscopy was successfully extended to AK-AKE diatomic molecules[2, 5, 6], which were formed on helium droplets by applying a sequential pick up scheme.

In this manuscript we present an application of the HENDI approach to the RbCa molecule. The experimental results for the excited states have been obtained by resonance enhanced multi-photon ionization time-of-flight (REMPI-TOF) spectroscopy. In our theoretical treatment the potential energy curves (PECs), the transition dipole moments (TDMs) and the permanent electric dipole moments (PEDMs) were determined for the neutral RbCa molecule with post Hartree-Fock molecular orbital theory. The combination of experiment and calculations enables the assignment of experimentally recorded features and allows for an estimate of the accuracy of the calculation. The knowledge gained from this work is essential for experiments envisaging the creation of ultracold molecules from quantum degenerated gas mixtures, which is based on the navigation via various potential energy curves with multiple lasers to the molecular ground state[28, 29, 31].

4.2 Theory

We calculated the ground state and the excited states of the diatomic molecule RbCa with post Hartree-Fock molecular orbital theory applying the MOLPRO software package[140]. Potential energy curves and electronic properties of the excited states were computed by a multireference configuration interaction[127] calculation of second order based on a multiconfigurational self consistent field calculation[125]. The inner core of the Rb atom, containing 28 electrons, was described by the relativistic effective core potential ECP28MDF[243] and the corresponding basis set. The basis set was slightly modified and a core polarization potential was applied as described in ref. 3. The 10 innermost electrons of the Ca atom were replaced by the effective core potential ECP10MDF[244]. The cc-pV5Z basis set[284] was applied with a core polarization potential following the approach in ref. 2. The calculation was performed in the C_{2v} point group, the orbitals will be given in the program-specific order of the irreducible representations (A_1/ B_1/ B_2/ A_2). The active space comprised 19 electrons in 37 orbitals (17/9/9/2). Out of them, eight orbitals (4/2/2/0) were kept doubly occupied at all times, but were included in the coefficient optimization. In the multiconfigurational self consistent field calculation (15/9/9/5) states were determined with doublet symmetry and (3/2/2/1) states for the quartet symmetry. This was necessary in order to obtain reasonable results for the 37 states calculated with the multireference configuration interaction, including (12/7/7/3) doublet states and (3/2/2/1) quartet states. The states, determined in the irreducible representations of C_{2v} for computational ease, can be assigned to diatomic states by inclusion of additional information, e. g. based on their energetic order. This approach yielded a good agreement of the results with atomic energy levels in the asymptotic limit at 30 Å, as is shown in table 4.1. The calculated values agree within 3.5% with the values reported in the NIST-database[13]. The excitation energies of diatomic states corresponding to atomic D-states are slightly overestimated. For all other states an underestimation of the energies is observed.

TDMs between the ground and excited states were computed by the same level of theory. At 30 Å, the majority of excited states have a TDM of zero in agreement with the selection rules for the corresponding atomic transitions. For the $8^2\Sigma^+$ and $6^2\Pi$ states a TDM^2 of 8.96 $e^2a_0^2$ was obtained at 30 Å, corresponding to a line strength of S_{ik}/g_k=8.13 $e^2a_0^2$ for the Ca (4s4p $^1P°$) ← Ca (4s^2 ^1S) transition as found in the NIST-database[13]. The literature value for the Rb (5p $^2P°$) ← Rb (5s ^2S) transition is S_{ik}/g_k=8.94 $e^2a_0^2$[13], the corresponding $2^2\Sigma^+$ and $1^2\Pi$ states show a TDM^2 of 10.12 $e^2a_0^2$. The $9^2\Sigma^+$ and $7^2\Pi$ states also have a noticeable TDM^2 of 0.10 $e^2a_0^2$ at 30 Å. For the corresponding Rb (6p $^2P°$) ← Rb (5s ^2S) transition a value of S_{ik}/g_k=0.06 $e^2a_0^2$[13] is given.

The ground state of the cation RbCa$^+$ was investigated with the same basis set and methods. An ionization potential of IP=33482.18 cm^{-1} was determined at 30 Å, comparable to the Rb atom with an ionization potential of IP=33690.81 cm^{-1} as found in the NIST-database[13].

Table 4.1: This table compares atomic energy levels as found in the NIST-database to calculated asymptotic excitation energies (30 Å). The values are given in cm^{-1}.

State	NIST[13]	This work
Rb (5p ^{2}P°)	12737	12516
Ca (4s4p^{3}P°)	15263	14849
Rb (4d ^{2}D)	19355	19367
Rb(6s ^{2}S)	20133	19962
Ca (3d4s ^{3}D)	20357	20721
Ca (3d4s ^{1}D)	21850	21987
Ca (4s4p ^{1}P°)	23652	22843
Rb(6p ^{2}P°)	23767	23525

4.3 Experiment

The following paragraph provides a short overview of the experimental setup. Details can be found in refs. 194, 285, and 286. A beam of He nanodroplets is generated by a supersonic jet expansion of He gas at 60 bar through a 5 μm nozzle at 15 K. The obtained droplet size distribution shows a maximum at $\hat{N}_{60,15} = 6000$ and a mean value of $\bar{N}_{60,15} = 14000$, corresponding to radii of $\hat{R}_{60,15} = 40\,\AA$ and $\bar{R}_{60,15} = 54\,\AA$, respectively, assuming spherical droplets[193].

The established He cluster beam is extracted by a 5 μm skimmer and subsequently enters the pickup chamber. There it passes through two resistively heated pickup cells, which contain the dopant materials Rb and Ca. The probability of a dopant pickup by the He droplets follows a Poisson distribution and depends on the length of the pickup cell, the droplet size and the vapor pressure of the dopants in the pickup cells[287]. The molecular beam and pickup conditions for different experiments may vary and the signals were optimized for the respective conditions. The optimum pickup temperature to obtain a maximum RbCa signal has been found to be around $T_{Rb} = 85\,°\mathrm{C}$ and $T_{Ca} = 400\,°\mathrm{C}$.

An excitation spectrum for RbCa molecules on He nanodroplets was recorded over a large wavelength range with resonance enhanced multi-photon ionization time-of-flight (REMPI-TOF) spectroscopy, using a dye laser (Lambda Physik FL 3002) to excite the molecule and a fraction of the pump laser (Radiant Dyes RD-EXC 200 XeCl laser, 26 ns pulse duration, 100 Hz) to ionize it. Above an energy of $\sim$14000 cm^{-1} only the dye laser was used for excitation and ionization. A time-of-flight mass spectrometer (Jordan D-850 AREF) with angular reflectron served to record the ion signal. Laser induced fluorescence spectroscopy was applied for an investigation of molecular transitions found in the REMPI-TOF spectrum, however no fluorescence light originating unambiguously from excited RbCa was observed in the experiment.

4.4 Results and discussion

4.4.1 Overview

In total we calculated 24 electronic states of the neutral RbCa molecule, corresponding asymptotically to the ground states of the atomic constituents, four excited states of Rb, and four excited states of Ca. The potential parameters of the 24 states have been determined and collected in table 4.2, as well as the values for the ground state of the RbCa$^+$ cation. There are two strongly bound states with an equilibrium radius smaller than 4 Å, the $1^2\Pi$ and $1^2\Delta$ states. These strongly bound states as well as a very weakly bound $1^4\Sigma^+$ state were also observed for LiCa[2] and RbSr[3]. The PECs of the electronic states are displayed in figure 4.1. Avoided crossings appear where two PECs of the same symmetry approach each other, altering the PECs and electronic properties of the involved states. Within the energy range of figure 4.1, two zones of prominent avoided crossings are marked by rectangles. The corresponding portions have been blown up and are depicted together with the plots of TDMs and PEDMs in figures 4.5 and 4.9. There, strong changes in the TDMs and PEDMs are related to the avoided crossings.

An excitation spectrum of RbCa has been recorded with REMPI-TOF spectroscopy in a spectral range of $13000 - 23000\,\text{cm}^{-1}$. The experimental spectrum has been divided in three parts, which will be shown and addressed individually in the following sections. The energetic positions of the rising edges of the recorded spectral features are given in table 4.2. Note that for transitions which show a steep rising edge followed by an extended blue tail (i. e. the potential minima of the ground and excited state have a similar equilibrium separation), the rising edge can be assumed to coincide with the potential minimum, because all molecules are initially in their vibronic ground state[2, 5, 6]. For other transitions, the position of the rising edge serves as an upper limit for the potential minimum. The spectra are comprised of peaks recorded with various laser dyes. They have been offset-corrected, but not scaled, with laser pulse energies within a range of $0.5 - 1.5\,\text{mJ}$, depending on the laser dye. Therefore, the relative heights of the peaks shown in the figures can only be tentatively compared to each other.

It can be expected that the line shift introduced by the helium environment is small for RbCa. Rb and Ca are both heliophobic atoms, like all alkali atoms and most alkaline earth atoms. They reside on the surface of the helium droplet, which limits the perturbations of the electronic states to some extent. Recently, a REMPI-TOF spectrum of LiCa formed on helium nanodroplets was compared with gas phase measurements[2]. The results show a small line shift of a few cm^{-1} in the REMPI-TOF spectrum in agreement with a surface location. Additionally, a broad (10-100 cm^{-1}) phonon wing accompanies each vibronic transition resulting in an unresolvable merged structure for most transitions.

For a more thorough comparison of the theoretical and experimental data, the Franck-Condon factors (FCFs) have been used. The FCFs for the PECs in figure 4.1 were calculated using the program Level 8.0 of Le Roy[106]. The corresponding transition probabilities (FCF*TDM^2) were determined by multiplying the FCFs with the square of the TDMs at 4.4 Å (ground state minimum) and are indicated in the figures 4.4, 4.6,

Table 4.2: Parameters for the calculated PECs of the RbCa diatomic molecule are shown in the table. The potential depth (D_e), the vibrational constant (ω_e) and the excitation energy (T_0) are given in cm^{-1}. The values of the internuclear distances (r_e) are given in Å. T_0 (exp.) refers to the position of the rising edges of the experimentally observed transitions. The corresponding asymptote for each state is denoted in the last column.

State	r_e	ω_e	D_e	T_0 (calc.)	T_0 (exp.)	Asymptote
$X\ ^2\Sigma^+$	4.37	58	1406			Rb (5s ^{2}S) + Ca (4s^2 ^{1}S)
$2\ ^2\Sigma^+$	4.34	78	5446	8487		Rb (5p ^{2}P$^\circ$) + Ca (4s^2 ^{1}S)
$1\ ^2\Pi$	3.75	108	9175	4772		Rb (5p ^{2}P$^\circ$) + Ca (4s^2 ^{1}S)
$3\ ^2\Sigma^+$	4.02	62	3367	12891	13100	Rb (5s ^{2}S) + Ca (4s4p ^{3}P$^\circ$)
$2\ ^2\Pi$	4.02	79	4156	12110		Rb (5s ^{2}S) + Ca (4s4p ^{3}P$^\circ$)
$1\ ^4\Sigma^+$	5.98	19	336	15901		Rb (5s ^{2}S) + Ca (4s4p ^{3}P$^\circ$)
$1\ ^4\Pi$	4.13	77	3220	13045		Rb (5s ^{2}S) + Ca (4s4p ^{3}P$^\circ$)
$4\ ^2\Sigma^+$	4.32	96	5551	15241	15700	Rb (4d ^{2}D) + Ca (4s^2 ^{1}S)
$3\ ^2\Pi$	4.14	79	5523	15261	15700	Rb (4d ^{2}D) + Ca (4s^2 ^{1}S)
$1\ ^2\Delta$	3.74	100	7014	13781		Rb (4d ^{2}D) + Ca (4s^2 ^{1}S)
$5\ ^2\Sigma^+$	4.34	68	4739	16635	16900	Rb (6s ^{2}S)+ Ca (4s^2 ^{1}S)
$6\ ^2\Sigma^+$	4.36	63	2492	19638	20100	Rb (5s ^{2}S) + Ca (3d4s ^{3}D)
$4\ ^2\Pi$	4.48	35	3405	18712	18750	Rb (5s ^{2}S) + Ca (3d4s ^{3}D)
$2\ ^2\Delta$	4.39	58	2621	19507		Rb (5s ^{2}S) + Ca (3d4s ^{3}D)
$2\ ^4\Sigma^+$	4.52	47	1574	20549		Rb (5s ^{2}S) + Ca (3d4s ^{3}D)
$2\ ^4\Pi$	4.59	47	2001	20121		Rb (5s ^{2}S) + Ca (3d4s ^{3}D)
$1\ ^4\Delta$	4.92	28	653	21460		Rb (5s ^{2}S) + Ca (3d4s ^{3}D)
$7\ ^2\Sigma^+$	4.20	77	2498	20906		Rb (5s ^{2}S) + Ca (3d4s ^{1}D)
$5\ ^2\Pi$	4.21	74	2192	21210		Rb (5s ^{2}S) + Ca (3d4s ^{1}D)
$3\ ^2\Delta$	4.59	40	1158	22227		Rb (5s ^{2}S) + Ca (3d4s ^{1}D)
$8\ ^2\Sigma^+$	5.19	59	1618	22632		Rb (5s ^{2}S) + Ca (4s4p ^{1}P$^\circ$)
$6\ ^2\Pi$	4.47	59	1843	22406	22100	Rb (5s ^{2}S) + Ca (4s4p ^{1}P$^\circ$)
$9\ ^2\Sigma^+$	5.00	42	1855	23069		Rb (6p ^{2}P$^\circ$) + Ca (4s^2 ^{1}S)
$7\ ^2\Pi$	4.80	49	1933	22994	22700	Rb (6p ^{2}P$^\circ$) + Ca (4s^2 ^{1}S)
RbCa$^+$	4.24	75	3925	30972		Rb$^+$ (^{1}S) + Ca (4s^2 ^{1}S)

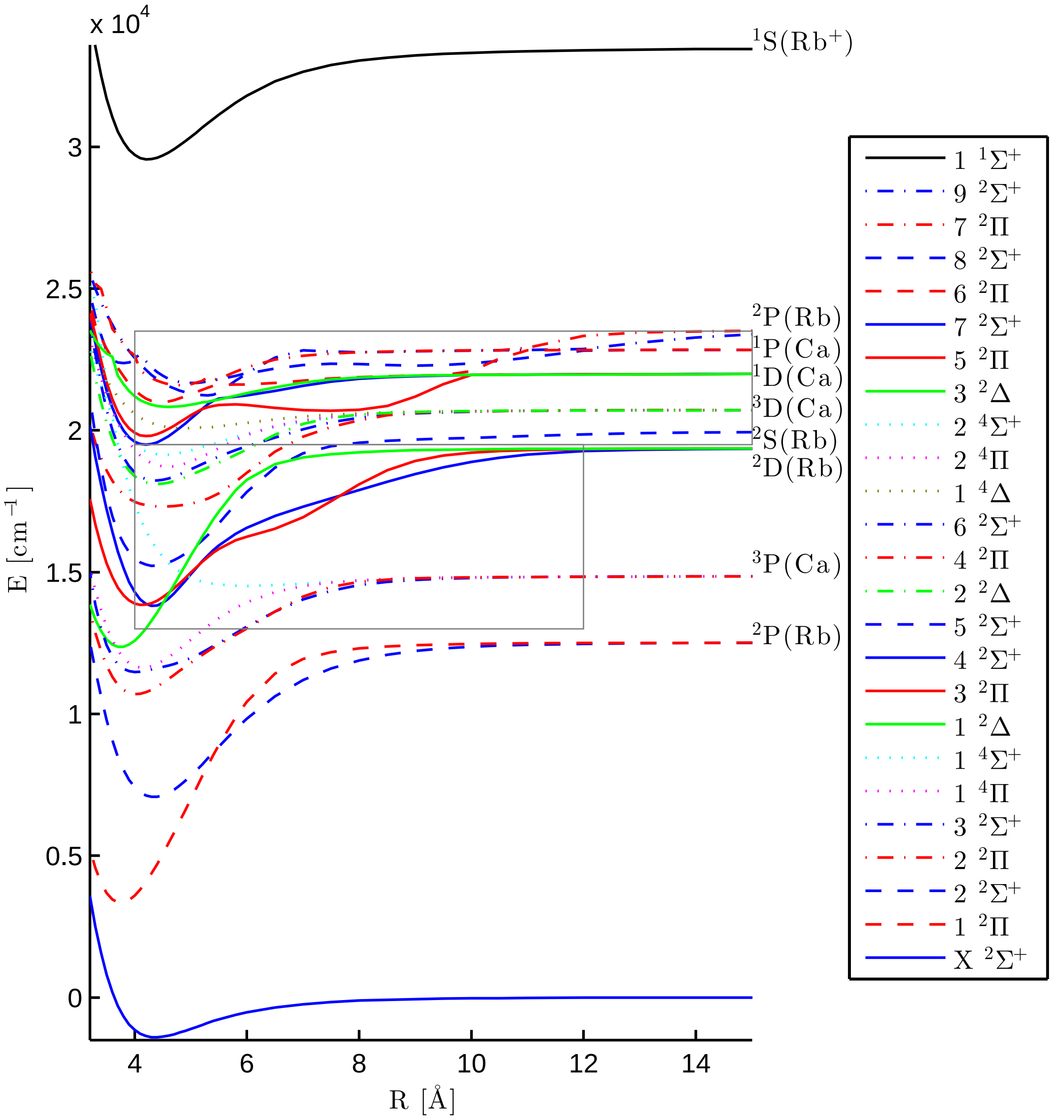

Figure 4.1: PECs of electronic states of RbCa and the ground state of RbCa$^+$ are displayed, for each multiplicity and symmetry a distinct color is used. Note, that a few PECs show the same color and line style. At the long range limit the corresponding atomic energy levels are denoted. All states above the $9^2\Sigma^+$ state have been neglected, except for the $1^1\Sigma^+$ state of the molecular ion. The gray rectangles mark the areas that are shown in more detail in figures 4.5 and 4.9.

and 4.8 as vertical bars. The calculations allowed to assign the peaks in the experimental spectra. Generally, the theoretical values for the molecular transitions lie slightly lower in energy than the experimental values ($\sim 40-400\,\mathrm{cm}^{-1}$) for all states below an excitation energy of $22000\,\mathrm{cm}^{-1}$.

4.4.2 Ground state

The results for the ground state can be compared to previous calculations for RbCa as well as experimental and theoretical results for similar molecules. The parameters determined for the ground state potential (D_e= $1406\,\mathrm{cm}^{-1}$, r_e =4.37 Å, ω_e= $58\,\mathrm{cm}^{-1}$) lie in between the experimental values for LiCa (D_e= $2605\,\mathrm{cm}^{-1}$, r_e= 3.36 Å, ω_e= $202\,\mathrm{cm}^{-1}$[24]) and the theoretical values for RbSr (D_e = 1041/ 916/ $1273\,\mathrm{cm}^{-1}$, r_e= 4.67/ 4.72/ 4.59 Å, ω_e= 38 / 36 / $42\,\mathrm{cm}^{-1}$[3, 167, 179]). These intermediate values for RbCa are reasonable because both RbSr and LiCa share one atom with RbCa, paired with a heavier (Sr) or lighter (Li) atomic partner. In a previous calculation for ground states of several AK-AKE diatomic molecules Gopakumar *et al.*[167] found for RbCa a potential depth of D_e=$921\,\mathrm{cm}^{-1}$, an equilibrium distance of r_e=4.53 Å, and a vibrational constant of ω_e=$49\,\mathrm{cm}^{-1}$. We determined a larger potential depth, a similar result as in our former calculations at the same level of theory[2, 3], using the same method (multireference configuration interaction), basis sets, core polarization potentials, and effective core potentials. This multireference configuration interaction approach is suitable for the description of higher states, but at the cost of higher uncertainties for the ground state. The dependence of the permanent electric dipole moment (PEDM) of the ground state on the internuclear distance is shown in figure 4.2. The observed behavior is similar to the one reported in ref. 167. The absolute value differs with d_e=$1.00\,\mathrm{ea}_0$ for our calculation and d_e=$0.69\,\mathrm{ea}_0$ determined in ref. 167. RbCa has a larger PEDM than LiCa[2] and RbSr[3], in agreement with the calculations in ref. 167, where RbCa showed the largest PEDM of several investigated AK-AKE molecules. Positive electronic dipole moments refer to a net negative charge on the Ca end and a net positive charge on Rb for our

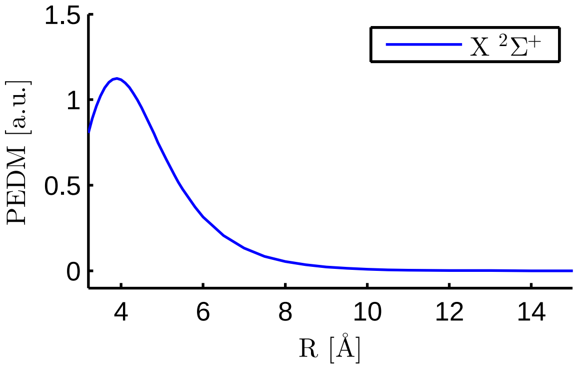

Figure 4.2: This figure displays the PEDM of the ground state of RbCa as a function of the internuclear separation of the atoms.

selection of the coordinate system. The PEDM is positive at all considered internuclear distances, which indicates an increased probability density for electrons around the Ca atom.

4.4.3 Lowest excited states

The two lowest excited states of the RbCa molecule, $2^2\Sigma^+$ and $1^2\Pi$, correlate to the Rb (5p ^{2}P°) + Ca (4s^2 ^{1}S) asymptote. They were only treated theoretically, because the excitation energies (see table 4.2) lie too far in the infrared for our laser systems. Figure 4.3 shows the corresponding TDMs and PEDMs. The TDMs between the ground state and these excited states are the highest among all transitions in the asymptotic limit (at 30 Å), which is expected from the transitions of the atomic constituents, i. e. Rb (5p ^{2}P°) ← Rb (5s ^{2}S)[13]. For the $2^2\Sigma^+$ state, the TDM even increases for smaller internuclear separations, resulting in the highest TDM for all treated states. The PEDMs are positive with a single maximum, the $2^2\Sigma^+$ state has its maximum at larger internuclear separation. Both states have similar amplitudes of the PEDMs. The same behavior, at slightly larger internuclear separations, was observed for the two lowest states of RbSr with similar amplitudes, see figure 2 in ref. 3. This could be interpreted as a contribution of the 5p of Rb to a bonding orbital. For LiCa, the $2^2\Sigma^+$ state shows only a small positive maximum, but the dent, as seen for RbCa in figure 4.3, is more pronounced and results in negative values[2]. It is probably related to the much smaller 2p orbital of Li.

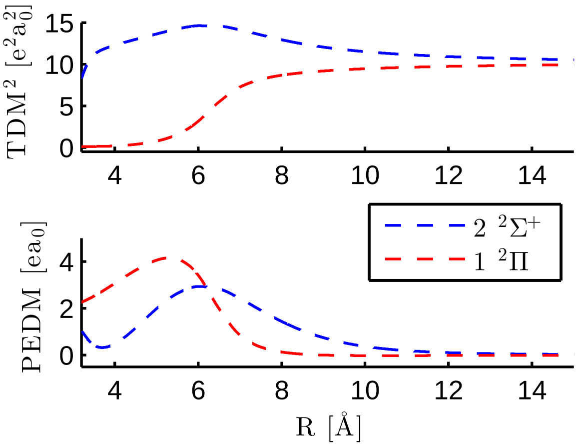

Figure 4.3: The upper panel of the figure contains the square of the TDMs for a transition from the ground state into the excited states of the diatomic molecule RbCa corresponding to the Rb (5p ^{2}P°) + Ca (4s^2 ^{1}S) asymptote. The lower panel presents the PEDMs of the same states.

4.4.4 Excitation spectrum from 13000 to 16500 cm^{-1}

The REMPI-TOF signal in figure 4.4 has been achieved with a two-color two-photon ionization up to ~14000 cm^{-1} and with a one-color two-photon ionization above this excitation energy. The threshold energy for a one-color two-photon ionization can only be roughly estimated. The ground state potential well depth of the RbCa molecule was only treated here and in one other publication[167] and can be estimated as 1200 cm^{-1}. There are two publications in which the ground and several excited states of the RbCa$^+$ cation have been computed. Therein a potential depth of about ~4100 cm^{-1} and equilibrium separation of ~8 a_0 have been reported[270, 271], in good agreement with our result (see table 4.2). Using these depths, one-color two-photon ionization may become possible around ~15400 cm^{-1}. Additionally, the effects of the helium environment have to be considered (known to lower the ionization threshold[288, 289]). We started the one-color two-photon ionization at 14000 cm^{-1} in order to detect a possible rise of the signal in the energy range where the ionization threshold was expected. The slight rise in the signal around ~14800 cm^{-1} might be an indicator for this, but cannot be assigned with certainty.

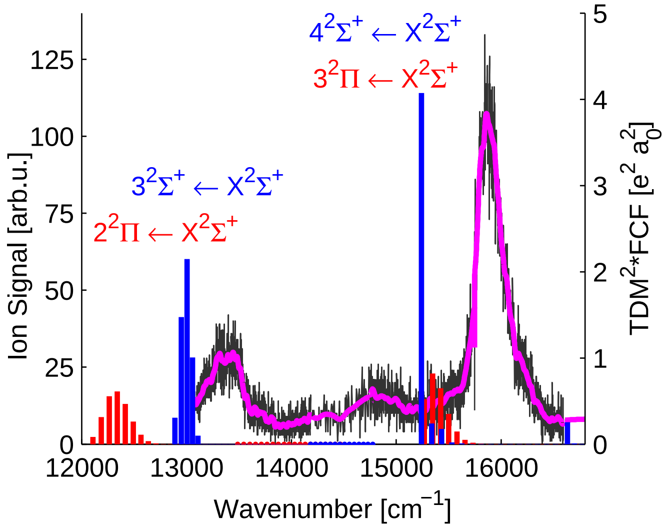

Figure 4.4: REMPI-TOF excitation spectrum in the range of 13000 − 16500 cm^{-1}, the original data points are shown in gray, the magenta line shows the data smoothed by convolution with a Gaussian. The transition probabilities (FCF*TDM^2) are shown as vertical sticks, in blue for transitions into $^2\Sigma^+$ states and in red for transitions into $^2\Pi$ states.

The small structure at 13000 cm^{-1} is assigned to the $3^2\Sigma^+ \leftarrow X^2\Sigma^+$ transition on basis of theoretical calculations. The $3^2\Sigma^+$ state is related to the Rb (5s ^{2}S) + Ca (4s4p ^{3}P°) asymptote. As shown in figure 4.4, the calculations underestimate the position by about ~200 cm^{-1}. This can be explained by the fact that the PEC approaches a value approximately ~400 cm^{-1} below the Rb (5s ^{2}S) + Ca (4s4p ^{3}P°) asymptote for large internuclear separations, see table 4.1. A comparison with RbSr[2] shows that the $3^2\Sigma^+$ state of RbCa lies ∼600 cm^{-1} higher in energy, which is as expected since the Ca (4s4p ^{3}P°) state also lies ∼560 cm^{-1}[13] above the corresponding Sr state. The $2^2\Pi$ state also has a significant TDM at the equilibrium distance (see figure 4.5), but is more strongly bound than the $3^2\Sigma^+$ state. Therefore this state lies below the experimentally recorded wave length range. The PEDM of the $1^4\Sigma^+$ state becomes negative close to 4 Å, whereas the other three states corresponding to this asymptote show positive PEDMs, see figure 4.5.

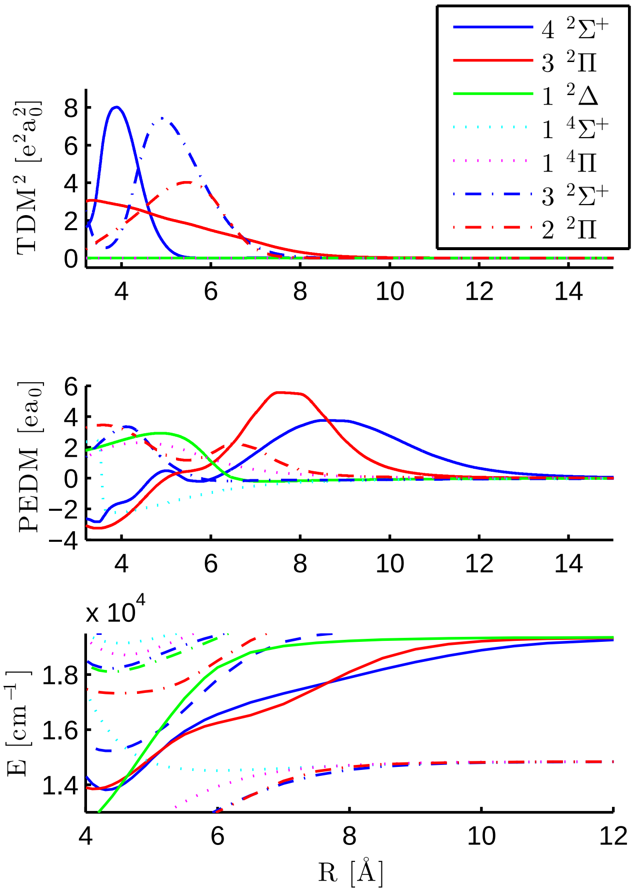

Figure 4.5: TDMs, PEDMs and PECs for excited states of the RbCa molecule corresponding to the Rb (5s ^{2}S) + Ca (4s4p ^{3}P°) and Rb (4d ^{2}D) + Ca (4s^2 ^{1}S) asymptotes are shown in this figure. These states give rise to the signal in the REMPI-TOF spectrum in figure 4.4.

The structure around ∼15900 cm^{-1} in figure 4.4 shows a steep rising edge on the low energy side and a broad shoulder to higher energies. The calculations suggest an assignment of this structure to the molecular states originating from the Rb (4d ^{2}D) + Ca (4s^2 ^{1}S) asymptote. According to the calculated transition probabilities in figure 4.4 and the PECs in figure 4.1, the transitions into these two molecular states are overlapped. Hence, the structure at 15900 cm^{-1} is assigned to the superimposed $3^2\Pi/4^2\Sigma^+ \leftarrow X^2\Sigma^+$ transitions. The $4^2\Sigma^+$ state has shown vibrational resolution for LiCa[2] as well as for

RbSr[6]. There are several reasons for the different structure of the $4^2\Sigma^+ \leftarrow X^2\Sigma^+$ excitation spectrum of RbCa compared to LiCa and RbSr counterparts. In LiCa and RbSr, the $4^2\Sigma^+$ state correlates to a ^{3}D state asymptote of the alkaline earth, which corresponds to the $6^2\Sigma^+$ state in RbCa. The $4^2\Sigma^+$ state of RbCa, however, dissociates into ground state Ca and Rb (4d ^{2}D). Ground and excited state potentials look similar for this transition in RbCa with the ($\nu' = 0 - \nu'' = 0$) band having a Franck-Condon factor of about 0.9. The single vertical blue bar in figure 4.4 represents this result and is followed to higher energies by some small structure that stand for the higher ν' levels of $4^2\Sigma^+$ and the weaker but strongly overlapping $3^2\Pi \leftarrow X^2\Sigma^+$excitation bands. In LiCa and RbSr the corresponding transitions are well separated.

The spectral range between 14450 and 16450 cm^{-1} was additionally investigated with laser induced fluorescence spectroscopy in order to find an emission signal of RbCa. In this wavelength range, both, a Rb_2 (Rb_2 $(1)^1\Pi_u \leftarrow a^1\Sigma_g^+$ [194]) and a Ca_2 (Ca_2 $A^1\Sigma_u^+ \leftarrow X^1\Sigma_g^+$ [290]) transition can be found. The Rb dimer transition overlaps with a Rb_3 transition (Rb_3 $3^4E' \leftarrow 1^4A_2'$ [194]). However, no emission could be found for RbCa excited around ~15900 cm^{-1} in the laser induced fluorescence spectrum. The complete absence of fluorescence can either be explained by a non-radiative relaxation of the RbCa molecules into low lying excited states, from which an emission is beyond our detection limit, or by the transfer of excited RbCa into metastable states. Helium mediated relaxation into the metastable $1^2\Delta$ and further to the $1^4\Pi$ states might be possible. For free molecules, fluorescence emission from $4^2\Sigma^+$ and $3^2\Pi$ can be expected.

4.4.5 Excitation spectrum from 16500 to 19500 cm^{-1}

The REMPI-TOF spectrum for transitions in the range of 16500 – 19500 cm^{-1} is shown in figure 4.6. Two peaks at 17000 cm^{-1} and 18800 cm^{-1} can be identified, which have been assigned to the molecular $5^2\Sigma^+ \leftarrow X^2\Sigma^+$ and $4^2\Pi \leftarrow X^2\Sigma^+$ transitions, respectively. The assignment is based on the comparison to calculations, which are shown in form of stick spectra in figure 4.6.

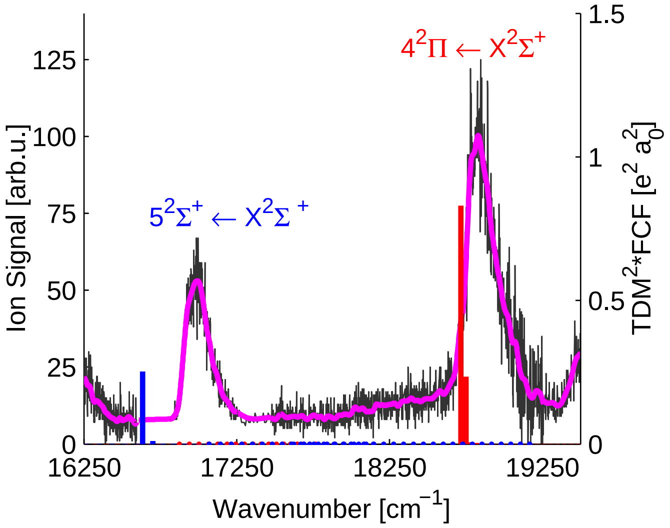

Figure 4.6: REMPI-TOF excitation spectrum in the range of 16500 – 19500 cm^{-1}, the original data points are shown in gray, the magenta line shows the data smoothed by convolution with a Gaussian. The transition probabilities (FCF*TDM^2) are shown as vertical sticks, in blue for transitions into $^2\Sigma^+$ states and in red for transitions into $^2\Pi$ states.

Both states are underestimated by the calculations ($\sim$ 300 cm^{-1} for the $5^2\Sigma^+$ state and $\sim$ 40 cm^{-1} for the $4^2\Pi$ state). For the $5^2\Sigma^+$ state, this can be explained by an underestimation of the asymptotic value by the theoretical calculations as can be seen in table 4.1, which also affects the PEC at smaller internuclear separations. In contrast, the asymptotic value of the $4^2\Pi$ state is overestimated by a few hundred cm^{-1}, but there is an avoided crossing between the $4^2\Pi$ and $5^2\Pi$ states at 9 Å, see the PECs in figure 4.9. This avoided crossing results in a strong change of the PEDM at the same distance, as can be seen in figure 4.7. The $5^2\Sigma^+$ state has a negative PEDM and corresponds to the Rb (6s ^{2}S)+ Ca (4s^2 ^{1}S) asymptote, this negative value was also obtained for the same state in RbSr. The TDMs in the upper part in figure 4.7 are small beyond an internuclear separation of 5 Å, but become large at the equilibrium distance of the ground state. For both transitions, the Franck-Condon factors favor $(\nu' = 0 - \nu'' = 0)$ transitions. Again, no fluorescence was detected after excitation of the observed RbCa bands.

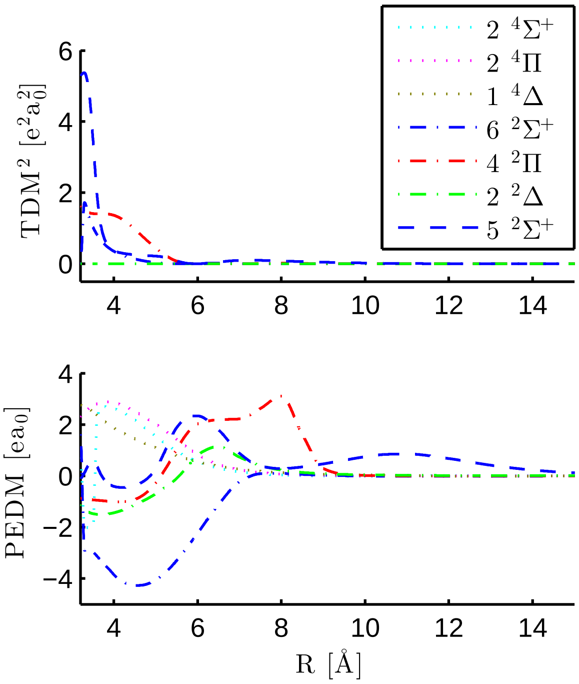

Figure 4.7: PEDMs and TDMs for excited states of the RbCa molecule related to the Rb (6s ^{2}S)+ Ca (4s^2 ^{1}S) and Rb (5s ^{2}S) + Ca (3d4s ^{3}D) asymptotes. The $4^2\Pi$ and $5^2\Sigma^+$ states give rise to a signal in the REMPI-TOF spectrum in figure 4.6.

4.4.6 Excitation spectrum from 19500 to 23000 cm^{-1}

Figure 4.8 shows the excitation spectrum of RbCa above 19500 cm^{-1} as recorded with REMPI-TOF spectroscopy. Several distinct structures can be identified. Between the two broad structures at 20400 cm^{-1} and 22400 cm^{-1} several resolved lines appear. The peaks are Gauss-shaped and have a spacing of $\sim$200(10) cm^{-1}. The series can be followed from the maximum of the peak of the lower lying structure (20400 cm^{-1}) to the onset of the transition at higher energies (22100 cm^{-1}). These structures have been reproduced in several experiments, but could not be separated better from the energetically higher or lower-lying transitions. The peaks only occur for the mass window of the RbCa isotopologues and a contribution of dimers or triatomic molecules ($\mathrm{Rb_2Ca}$ or $\mathrm{Ca_2Rb}$) can be excluded. However, neither the calculations nor the comparison to RbSr indicate a PEC for such high excitation energies, bound deeply enough to harbor vibrational lines with a spacing of $\sim$200(10) cm^{-1} (see table 4.2). The $7^2\Sigma^+$ and $5^2\Pi$ states lie in this range, but their vibrational spacing is significantly smaller and they have negligible TDMs, see figure 4.9. This structure might be related to the first excited state of the cation, $1^3\Sigma^+$ [270–272]. It lies at about 43000 cm^{-1}, an energy that can be supplied with two photons in this energy range.

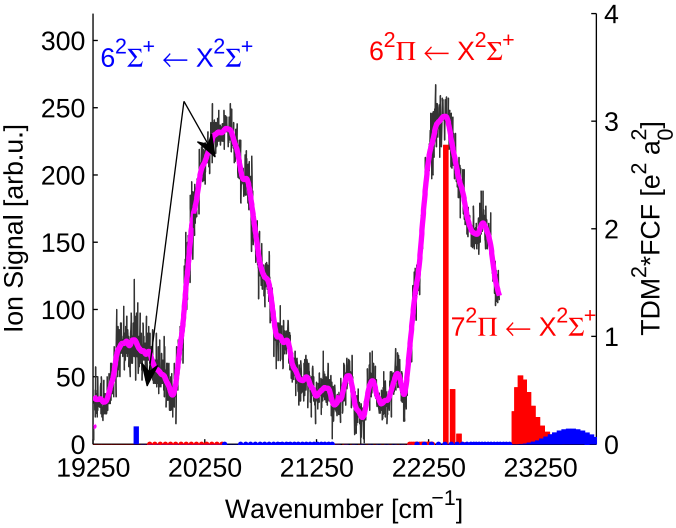

Figure 4.8: REMPI-TOF excitation spectrum in the range of 19500 – 23000 cm^{-1}, the original data points are shown in gray, the magenta line shows the data smoothed by convolution with a Gaussian. Between the two strong transitions around 20400 cm^{-1} and 22400 cm^{-1} a resolved structure can be seen. The transition probabilities (FCF*TDM^2) are shown as vertical sticks, in blue for transitions into $^2\Sigma^+$ states and in red for transitions into $^2\Pi$ states.

The structure at 20400 cm^{-1} is tentatively assigned to the $6^2\Sigma^+ \leftarrow X^2\Sigma^+$ transition, since the peak around 19600 cm^{-1} has been found not to originate from a RbCa molecular transition, *vide infra*. Theoretical calculations suggest the assignment of the structure at 22400 cm^{-1} to the $6^2\Pi \leftarrow X^2\Sigma^+$ transition and the shoulder at higher en-

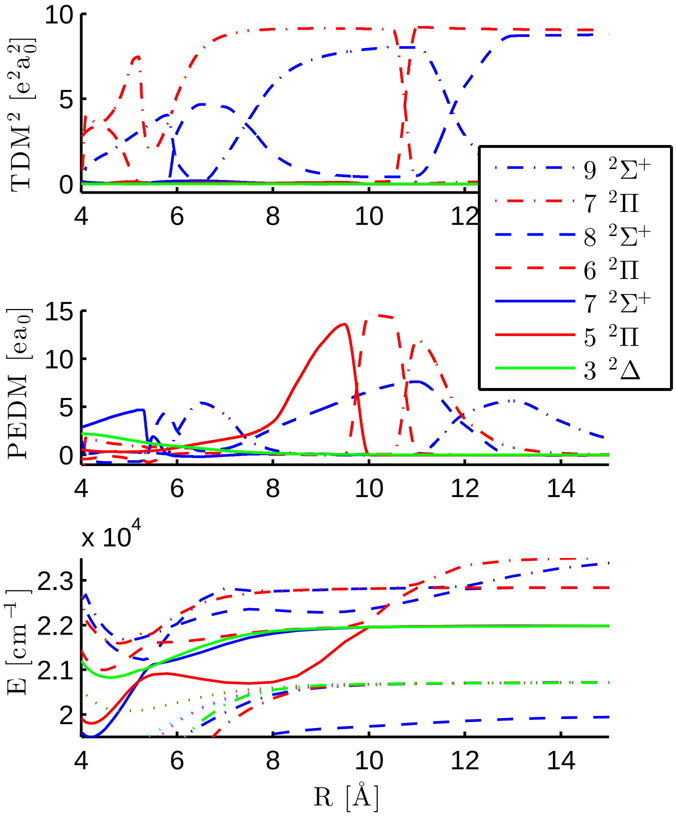

Figure 4.9: TDMs, PEDMs, and PECs for excited states of RbCa with the Rb (5s ^{2}S) + Ca (3d4s ^{1}D), Rb (5s ^{2}S) + Ca (4s4p ^{1}P°), and Rb (6p ^{2}P°) + Ca (4s^2 ^{1}S) asymptotes are displayed. The abrupt changes are related to avoided crossings, where the molecular states change their character.

ergies (22700 cm^{-1}) to the $7^2\Pi \leftarrow X^2\Sigma^+$ transition. The TDMs for transitions into $^2\Sigma^+$ states above $6^2\Sigma^+$ are negligible at 4.4 Å, see figure 4.9.

The strong interactions of the energetically highest states with each other are obvious in figure 4.9. The TDMs and the PEDMs change their values, indicating avoided crossings, which are observable in figures 4.1 and 4.9. The two states corresponding to the Rb (6p ^{2}P°) + Ca (4s^2 ^{1}S) asymptote ($9^2\Sigma^+$, $7^2\Pi$) show avoided crossings at 11 and 12 Å and corresponding changes in the PEDMs and TDMs. These two states are influenced by higher states for small internuclear separations.

4.4.7 Structure at 19600 cm^{-1}

Figure 4.8 reveals the presence of a small peak slightly below the $6^2\Sigma^+ \leftarrow X^2\Sigma^+$ transition with a maximum around 19600 cm^{-1}. A comparison of different ion traces recorded in the REMPI experiment suggests that this structure is not related to a RbCa transition. The REMPI spectra for different ions are presented in figure 4.10, the ion yield originating from RbCa is shown in red, Ca in blue, Rb in black and RbHe in green. The atomic Rb (4d ^{2}D) ← Rb (5s ^{2}S) transition is indicated by the vertical black line. It is remarkable that the main feature in figure 4.10 can be unambiguously identified in the Rb, RbHe and the RbCa ion signal. Also, the Ca signal seems to weakly follow the other signals. The rising edge of the transition coincides exactly with the free atom transition in Rb, followed by a blue shifted maximum and an extended blue wing. This is the typical form of Rb-He$_N$ transitions in the lower energy region[291–294]. Following the pseudo-diatomic molecule notation for alkali doped helium droplets [291, 295], this transition corresponds to the merged 4^2D ($^2\Pi$) ← 5^2S$_{1/2}$ ($^2\Sigma_{1/2}$) and 4^2D ($^2\Sigma$) ← 5^2S$_{1/2}$ ($^2\Sigma_{1/2}$) transitions in Rb-He$_N$. These transitions have been previously observed[294, 296] and are in excellent agreement with the REMPI spectra in figure 4.10, consequently we assign the Rb and RbHe ion signal to these transitions.

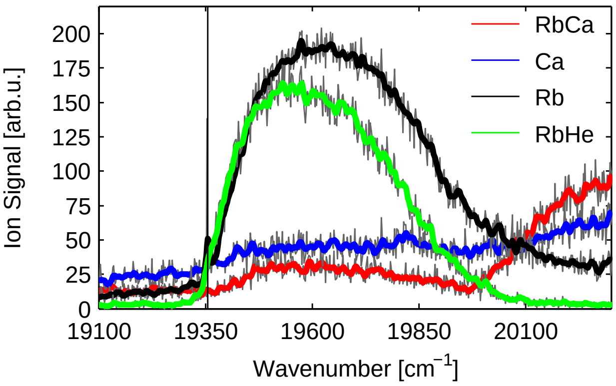

Figure 4.10: Close- up of the transition around 19600 cm^{-1} in the RbCa ion yield. The ion yields for ^{40}Ca (blue), ^{85}Rb+^{87}Rb (black), ^{85}RbHe+^{87}RbHe (green) and ^{85}Rb^{40}Ca+^{87}Rb^{40}Ca (red) are shown, the vertical line indicates the free atom Rb (4d ^{2}D) ← Rb (5s ^{2}S) transition. It can be seen that the RbCa signal follows the Rb and Rb-He signal. The peak in the RbCa ion yield is not correlated to a RbCa transition, as explained in the text.

The observation of this transition in the Rb and RbHe signal is not surprising. Due to the statistical nature of the doping process, monomers are always present at doping conditions optimized for RbCa. However, it is remarkable that the RbCa and, very weakly, the Ca signal follow the Rb-He$_N$ transition. This can only be explained if it is assumed that a fraction of Rb and Ca atoms are initially found separated from each other on the helium droplet. The laser excitation and subsequent ionization of the Rb atom changes the interaction with the helium environment. (Neutral Rb is heliophobic, but the Rb ion is heliophilic[297].) This initiates a dynamic process in which the Rb ion (or excited atom) finds a Ca atom and forms RbCa, which explains the RbCa signal. Subsequent fragmentation of a fraction of the formed molecular ions may lead to a weak signal in the Ca mass window. Similar processes have been observed for Na and K doped He droplets in ref. 281.

4.5 Conclusion

In this manuscript we applied a combined theoretical and experimental approach in the analysis of RbCa. *Ab initio* calculations were performed for 24 electronic states of RbCa and their energies and permanent electric dipole moments were determined. The combination of the transition dipole moments at equilibrium position of the ground state and the Franck-Condon factors allowed to calculate a theoretical spectrum, which was subsequently compared to experimental measurements. In the experiment, the RbCa molecule was synthesized on helium nanodroplets by a sequential pick up scheme and then analyzed by resonance enhanced multiphoton ionization time-of-flight spectroscopy. With the aid of the theoretical results seven spectroscopic bands were assigned to excited states of RbCa, and one feature to an excitation of the Rb atom.

RbCa is the third AK-AKE molecule in a series of combined He nanodroplet and *ab initio* investigations. In contrast to LiCa and RbSr, the relaxation mechanisms seem to be more complicated and no fluorescence was observed. These mechanisms probably relate to the He environment.

Besides the current interest of the cold molecule community, there is the need for a deeper understanding of the bonding mechanisms in this group of molecules. The group of alkaline earth monohalides was well described in terms of ionic bonding models either based on mutual polarization of the atomic constituents [298, 299] or on a ligand field approach [300]. The ligand field theory was also successful in the development of a model for the electronic structure of alkaline earth oxides, first for CaO[301, 302], and later applied to SrO[303]. A large amount of experimental data was available for these molecules at that time, whereas we are just at the beginning of data collection for alkali-alkaline earth diatomic molecules. While we are currently working on an analysis of the common properties of these molecules, we can summarize already a few peculiarities found in this study of RbCa. If we concentrate on the $^2\Sigma^+$ and $^2\Pi$ states, the ground state exhibits the by far smallest bonding energy. Among the excited states, those correlating to excited states of Ca, show a smaller well depth than those correlating to excited Rb states. Up to $3^2\Sigma^+$ and $2^2\Pi$, the permanent electric dipole moment at $r_e = 4.37$ Å (ground state equilibrium internuclear distance) are positive irrespective of their asymptote. From $4^2\Sigma^+$ and $3^2\Pi$ up in energy, the dipole moment of most states is negative. Our studies have focused on combinations relevant for ultracold molecular physics. The helium nanodroplet isolation method shows promise for further investigations of diatomic molecules. Future applications of this approach may envisage the production of more exotic species, which are not easily accessible by conventional methods.

4.6 Remarks

The computational results presented here are sufficient to describe the vibronic spectra as they can be resolved by HENDI spectroscopy. However, for applications in ultracold molecular physics a higher accuracy is necessary. One step to increase the accuracy is the inclusion of spin-orbit coupling as it has been shown in chapter 3. Another possibility is the measurement of fluorescence spectra using the determined transitions or the measurement of rovibronic levels with high resolution spectroscopy.

Chapter 5

Permanent electric dipole moments of alkali-alkaline earth molecules

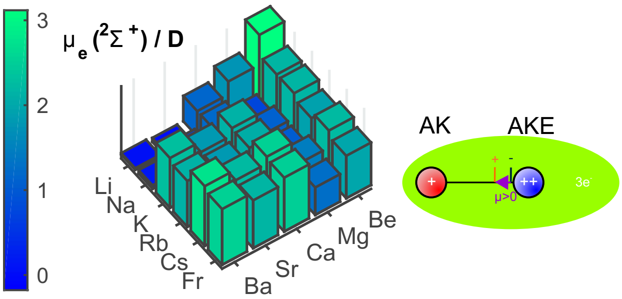

This chapter corresponds to the publication:
Electric dipole moments and chemical bonding of diatomic alkali - alkaline earth molecules
by Johann V. Pototschnig, Andreas W. Hauser, and Wolfgang E. Ernst
Physical Chemistry Chemical Physics, **2016**, *18*, 5964 which was written by the author of the thesis.

The author of the thesis was responsible for:

- author of the publication
- realization and implementation of the *ab initio* calculations
- interpretation of the result, analysis of correlation between dipole moment and other atomic and diatomic properties

The contributions of the co-authors are listed below:

- A. W. Hauser: supervision, editing, help with the interpretation of the results
- W. E. Ernst: supervision, editing, funding

Reproduced from ref. 10 with permission from the PCCP Owner Societies. The article is available at https://doi.org/10.1039/C5CP06598D.

Abstract

We investigate the properties of alkali-alkaline earth diatomic molecules in the lowest Σ^+ states of the doublet and quartet multiplicity by *ab initio* calculations. In all sixteen cases studied, the permanent electric dipole moment points in opposite directions for the two spin states. This peculiarity can be explained by molecular orbital theory. We further discuss dissociation energies and bond distances. We analyze trends and provide an empirically motivated model for the prediction of the permanent electric dipole moment for combinations of alkali and alkaline earth atoms not studied in this work.

5.1 Introduction

In the last years ultracold molecules have attracted a lot of attention due to their outstanding properties[28–33]. The low temperature reduces the decoherence, and ensembles of ultracold molecules can be used to simulate quantum systems[71, 72, 74–77] or perform quantum computations[80]. Most degrees of freedom are frozen out at these temperatures, which allows precise control of chemical reactions[85–87]. Another advantage is the reduction of the linewidth and noise in measurements of fundamental physical properties and constants[88] such as the proton to electron mass ratio[89–91], the electron electric dipole moment[97, 98] or the fine structure constant[93, 94].

The first molecules produced in the ultracold temperature regime were homonuclear alkali-dimers[42–44, 46], which do not have a permanent electric dipole moment. A few years later, ultracold heteronuclear alkali-dimers were produced[49–51, 54–56]. Their permanent electric dipole moment gives experimentalists an additional handle for manipulation via electric fields. In this sense, the next logical step is the production of ultracold molecules with a dipole moment plus an additional magnetic moment, originating from an unpaired electron spin. This magnetic moment causes additional interactions and enables control of these molecules via magnetic fields. Currently, the most promising candidates are alkali (AK)-alkaline earth (AKE) and AK-Yb diatomic molecules because the involved atoms are well under control in ultracold atomic physics. Bose-Einstein condensation, for example, has been achieved for most AK atoms[61] Ca,[63], Sr[64], and Yb[65]. In a series of recent studies combining experimental and computational efforts[2, 5–8] we found permanent electric dipole moments (PEDM) with opposite signs in the lowest Σ^+ states of the doublet and the quartet multiplicity for AK-AKE molecules. In this work we analyze this behavior and discuss the trends in greater detail. The magnitude of the permanent electric dipole moment (PEDM) is of special importance for future applications. A significant value is necessary to align molecules in an optical lattice[166, 167], to control interactions with an external microwave field[31, 76, 79], and it might even be useful to reach low vibrational levels[304].

Early on, there has been interest in the prediction of dipole moments for alkali halides and alkaline earth halides. These two groups of molecules with predominantly ionic bonding could successfully be described by electrostatic interaction models[305–307].

The Rittner model[305] for alkali halides assumes a complete charge transfer of one electron and considers the polarizabilities of the ions. Törring *et al.*[298, 299] applied a similar model to AKE halides. More sophisticated computations using ligand field theory were performed for AKE halides[300] and lanthanum containing diatomics[308, 309]. A model taking orbital mixing into account was applied to SrBr in ref. 310. However, these techniques assume a transfer of at least one electron and can therefore not be applied to AK-AKE molecules. Recently, an empirical model for the relation between dipole moment and vibrational frequencies was presented[311].

There are a few theoretical and experimental studies concerned with the properties of AK-AKE molecules. Bauschlicher *et al.*[312] performed one of the first calculations. Two theoretical studies examined the ground state of Li-AKE molecules by coupled cluster calculations[257, 260]. The ground states of neutral AK-Sr molecules and several states of the molecular ions have been investigated by a configuration interaction method[119, 313]. In ref. 258, the ground states of AK-Mg diatomic molecules were calculated at the coupled cluster level of theory. Using the same approach, Gopakumar *et al.*[167] recently investigated the AK-AKE molecules (Na, K, Rb)-(Ca, Sr). The combination of barium with an alkali atom has also been considered in the ground state[314]. Some older studies analyzed the ground and several excited states of LiBa[262, 265] and NaBa[315]. The most thoroughly studied representative of these diatomic molecules is LiCa, with experimental[24, 25, 316], theoretical[267, 268], and combined investigations[2, 266]. The first realization of a combined quantum degenerate mixture of Rb and Sr[26] was followed by a series theoretical and experimental publications[5–7, 179, 240, 241]. The excited states of LiSr[268], RbBa[317], LiMg[318], and RbCa[8] were calculated recently.

In this study, we investigate the energetically lowest electronic states of neutral AK (Li, Na, K, Rb) - AKE (Be, Mg, Ca, Sr) molecules in the doublet and quartet manifold. Throughout the article, the coordinate system is defined such that the AKE atom is on the negative side of the axis and the AK atom on the positive side. Therefore, a positive value of the PEDM corresponds to a dipole moment pointing in axis direction from the AKE to the AK atom (i.e., the center of the negative charge lies closer to the AKE atom).

This manuscript is structured as follows: In the next section details of the computational method are given, then an overview of the results and a comparison to previous results. After discussing trends for AK-AKE molecules we give a qualitative description of the situation for the lowest Σ^+ states in AK-AKE molecules. Finally, we present an empirical model in section 5.3.4.

5.2 Computational details

All *ab initio* calculations were carried out with the MOLPRO[140] software package. A multiconfigurational self consistent field calculation (MCSCF[125, 216]) was performed, followed by multireference configuration interaction including Davidson correction (MRCI[128, 217]). The quintuple-zeta basis set family of Peterson *et al.* covers most atoms of our study and was used where possible. All electrons basis sets[319] were applied for Li, Na, Be and Mg. For the heavier atoms the corresponding effective core potential basis sets[320] of Peterson were combined with the recommended effective core potentials[243, 244] of Lim *et al.* For K and Rb, however, no Peterson basis sets were available. In these cases, we fell back on the basis sets provided by Lim[243, 244], decontracted them, and added several diffuse functions to obtain a description of similar accuracy.[4] The same strategy has recently been applied to RbCa[8], yielding excitation energies in good agreement with experimental measurements.

We further applied core polarization potentials (CPPs) as introduced by Müller and Meyer[116] due to their importance for correct magnitudes of the permanent electric dipole moments[117, 321] (see figure 5.1). The parameters of the core polarization potential are given (see table 5.1) and were optimized for our effective core potentials and basis sets. This approach only allows basis functions with an angular quantum number below 5. Therefore, basis functions with higher quantum numbers were neglected. No core polarization was added for Li and Be due to their small cores and large energy difference between the core orbitals and valence orbitals compared to the other elements. With this approach the energy difference between the first excited state ($^2P_{AK}/^3P_{AKE}$) and the ground state agrees within 150 cm^{-1} (1%) with the atomic values[13] in the asymptotic limit.

Table 5.1: Parameters of the CPPs used in this study; α_{core} is the dipole polarizability and ρ is the cutoff parameter. The CPPs account for the polarizability of the innermost shells. These parameters have been adjusted for the best reproduction of atomic excitation energies.

AK	α_{core} / a.u.	ρ / Å^{-2}	AKE	α_{core} / a.u.	ρ / Å^{-2}
Na	1.00	1.27	Mg	1.20	0.60
K	5.61	0.46	Ca	7.16	0.25
Rb	9.74	0.35	Sr	9.28	0.28

It is known that the correlation or polarization of the core electrons has a significant influence on the dipole moment[117, 321]. The importance of this contribution can be estimated by looking at figure 5.1, where the results without (a)) and with (b)) core polarization potentials are compared. Typically, the PEDM is overestimated if the polarization of the core is neglected, which agrees well with the observations of ref. 117. This error increases with atomic mass. The largest deviation was found for RbSr, where the dipole moment is reduced by 1.65 D to about half its value after inclusion of core polarization. The PEDMs for the computations including core polarization potentials (see plot b of figure 5.1) were obtained by finite field calculations,[5] which we carried out

---

[4] the basis sets were completely decontracted and additional basis functions were added: K[s: 0.0037, 0.0017; p:0.0016, 0.00062; d: 4.34, 0.011; f: 0.0296]; Rb[s: 0.0036, p: 0.0042, d: 0.0116, 2.860, f: 0.0624 g: 0.33]

[5] This was necessary because the dipole moments determined by the MRCI routine in MOLPRO do not include the dipole moment of the polarized core. However, the difference between the dipole moments determined by the routine and the finite field calculations are smaller than 0.05 D in all

for different field strengths varying from 10^{-5} to $5 \cdot 10^{-3}$ $a.u.$ for all 16 molecules. For each field strength the PEDMs and polarizabilities were computed by three point and five point finite field approximations and compared to each other to estimate the size of numerical error. The values were then taken where the smallest deviation was observed. (The values and the field strengths for their calculation are listed in the appendix A)

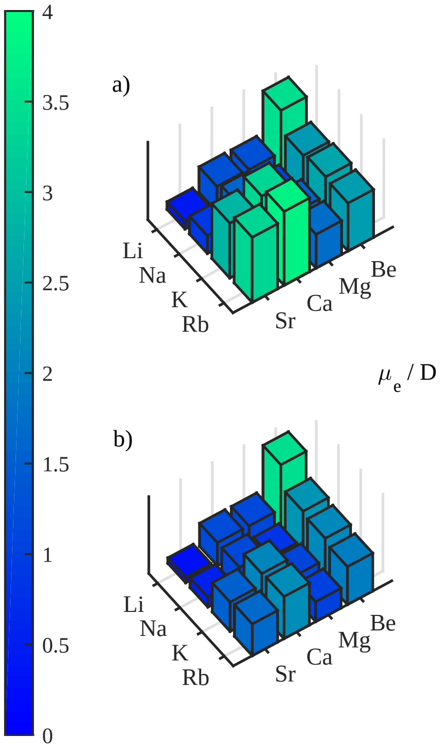

Figure 5.1: The permanent electric dipole moment of the doublet ground state at its equilibrium distance, obtained at the MCSCF+MRCI level of theory, without (a)) and with (b)) the inclusion of core polarization potentials.

The PEDMs for the lowest Σ^+ state of the quartet multiplicity were also changed significantly by the core polarization potential, especially for heavy molecules, but without a clear trend. An improvement of the potential depth of LiCa was achieved by a new set of recently adjusted core polarization parameters. The potential depth for LiCa obtained in this work (2613 cm^{-1}) now agrees better with the experimental value (2605 cm^{-1}[24]) than our previous calculation[2]. However, part of the improvement might originate also from the slightly different basis set. On average, the equilibrium distance was reduced by the core polarization potential, although some minor deviations occurred, especially for the quartet states.

In the MCSCF and MRCI calculation the same active space was applied, but it was necessary to adapt it to the different basis sets and effective core potentials. Details on the size and definition of the active space for the various diatomics can be found in

---

cases.

appendix A. Note that the lowest Σ^+ state in the quartet multiplicity is an electronically excited state accompanied by several excited states of the doublet manifold. Therefore, several excited states were calculated in both spin configurations to obtain a meaningful description of this state. In a combined MCSCF calculation 16 to 32 states of doublet multiplicity and 3 or 8 states of quartet multiplicity were optimized. The number of states was kept the same in the MRCI calculation for the quartet multiplicity, but the number of doublet states was reduced to 12-17 states. With this setup for the state-averaged calculations we obtained smooth potential energy curves up to an internuclear separation of 10 Å. At this distance, the deviation for the ground state from the asymptotic value is only 10 cm^{-1} for light atoms and about 25 cm^{-1} for heavy atoms.[3]

---

[3] Supplementary information available: Several tables regarding the calculations and their results as well as orbital pictures. See appendix A.

5.3 Results

5.3.1 Overview

The properties of 16 AK-AKE molecules have been calculated by MCSCF+MRCI and the values for the ground state are listed in table 5.2. Results for the lowest Σ^+ state in the quartet multiplicity are given in table 5.3.

Table 5.2: Results for the $^2\Sigma^+$ ground state, obtained at the MRCI level of theory, including core polarization potentials. Where available, values from the literature are given for comparison.

Mol.	Ref.	μ_e/D	r$_e$/Å	D$_e$/cm^{-1}	ω_e/cm^{-1}	$\alpha_{\|\|}{}^{a}$/a.u.
LiBe	This work	3.47	2.60	2427	313	365
	257	3.58	2.58	2406	300	
	312		2.61	2339	300	
	322 [b]		2.59		295	
LiMg	This work	1.18	3.10	1538	181	470
	318	1.22	3.10	1395	174	
	258	1.02	3.10	1445	180	
	260	0.86[c]	3.12	1332	187	482
	257	1.12	3.11	1432	206	
	312		3.11	1613	183	
	264 [b]			1331	190	
LiCa	This work	1.19	3.39	2613	200	588
	2		3.34	2883	203	
	268		3.40	2131	206	
	260	1.10[c]	3.40	2260	210	599
	257	1.12	3.36	2607	207	
	266		3.40	2178	204	
	267		3.30	2355	196	
	24 [b]		3.36	2605	202	
LiSr	This work	0.28	3.57	2471	181	653
	268		3.58	2074	181	
	260	0.31[c]	3.53	2223	196	640
	257	0.24	3.55	2401	184	
	119	0.34	3.48	2587	185	
NaBe	This work	2.33	2.97	1291	173	397
	312		3.05	1129	164	
NaMg	This work	0.86	3.47	946	90	432
	258	0.72	3.53	825	83	
	312		3.56	887	85	
NaCa	This work	1.18	3.67	1792	103	577
	167	1.01	3.72	1453	97	594

Table 3.3: *Continued.*

Mol.	Ref.	μ_e/D	r$_e$/Å	D$_e$/cm^{-1}	ω_e/cm^{-1}	$\alpha_{||}$^{a}/a.u.
NaSr	This work	0.51	3.84	1728	87	636
	167	0.49	3.89	1441	82	633
	119	0.62	3.82	1597	85	
KBe	This work	2.22	3.51	920	122	628
KMg	This work	1.08	3.99	779	64	656
	258	0.83	4.09	647	58	
KCa	This work	2.12	4.20	1455	71	869
	167	1.67	4.32	974	61	892
KSr	This work	1.52	4.39	1358	57	925
	167	1.27	4.53	964	48	942
	119	1.52	4.41	1166	52	
RbBe	This work	1.97	3.70	816	104	631
RbMg	This work	1.04	4.17	744	54	664
	258	0.79	4.29	586	47	
RbCa	This work	2.19	4.37	1337	57	922
	8	2.54	4.37	1406	58	
	167	1.75	4.53	921	49	961
RbSr	This work	1.64	4.56	1279	43	972
	7	1.80	4.59	1274	42	
	179		4.67	1041	38	
	241		4.67	1018	36	
	167	1.41	4.72	916	36	1009
	119	1.54	4.60	1073	32	

[a] Polarizabilities along the internuclear axis for the diatomic molecules

[b] Experimental results

[c] from atomic energy levels in the NIST-database[13].

Besides the *ab initio* calculations performed in this work, several other theoretical predictions as well as three experimental studies are listed in table 5.2. Overall agreement between the various studies is good except for significant differences in dissociation energies. LiCa, the best studied molecule in the literature, with data available from 8 different sources, shows a large variation of the dissociation energy. Our value and the value of ref. 257 agree best with recent experimental findings[24]. Two older experimental results[264, 322] are also listed in table 5.2. A recent experiment of our group[5] yielded a vibrational constant (ω_e) of (42 ± 5) cm^{-1} for RbSr, which is in good agreement with the theoretical results in table 5.2. The calculated PEDMs are all positive and differ on average by 0.16 D (13 %) from previous computations, with the largest difference observed for the PEDM of KCa in ref. 167. Note that the PEDM values listed in table 5.2 were evaluated for the respective equilibrium distance. When zero-point motion is considered, the PEDM is on average reduced by 0.03 D for the doublet states and by

Table 5.3: Results for the lowest $^4\Sigma^+$ state, obtained at the MRCI level of theory, including core polarization potentials. Where available, values from the literature are given for comparison.

mol.	Ref.	μ_e/D	r_e/Å	D_e/cm^{-1}	ω_e/cm^{-1}	$\alpha_{\|\|}{}^a$/a.u.
LiBe	This work	-0.61	5.51	59	25	223
LiMg	This work	-2.52	4.72	222	32	423
LiCa	This work	-4.58	4.59	522	55	1031
	2		4.33	608	67	
	268		5.01	265	30	
LiSr	This work	-6.61	4.59	692	61	1340
	268		4.60	401	47	
NaBe	This work	-0.45	5.84	50	18	229
NaMg	This work	-0.99	5.71	131	21	326
NaCa	This work	-1.62	5.74	237	24	686
NaSr	This work	-2.00	5.81	287	23	1200
KBe	This work	-0.72	5.99	48	16	300
KMg	This work	-1.58	5.73	157	20	338
KCa	This work	-2.50	5.73	343	26	950
KSr	This work	-2.99	5.95	376	22	1523
RbBe	This work	-0.79	6.03	47	15	363
RbMg	This work	-1.66	5.84	170	18	645
RbCa	This work	-2.13	6.05	316	19	922
	8		5.98	336	19	
RbSr	This work	-2.66	6.15	343	16	1491
	7		6.17	390	16	
	179		6.25	329	15	
	179		6.15	336	15	

a . . . polarizabilities along the internuclear axis for the diatomic molecules

0.06 D for the quartet states (details are provided in appendix A). The difference to other equilibrium distances is on average 0.05 Å (1 %) with the largest deviations occurring for RbSr and RbCa when compared to ref. 167. This deviation in the latter cases also explains the slight difference in the PEDM as the listed values are taken at the equilibrium separation. A small disagreement can also be found between the parallel polarizabilities (along the internuclear axis) listed in table 5.2. Note that only the polarizabilities ($\alpha_{||}$) at the equilibrium distances along the internuclear axis are given here. A more detailed treatment of polarizabilities and their experimental significance is provided in ref. 167 for AK-AKE molecules or in ref. 166 for AK-AK molecules.

A similar compilation of data for the lowest $^4\Sigma^+$ state is given in table 5.3, although fewer theoretical and experimental values are available.[6] In general, the equilibrium radius is larger and the potential depth and vibrational constant are smaller than corresponding quantities for the ground state. For the polarizability no clear trend can be observed.

5.3.2 Trends for AK-AKE molecules

A diatomic molecule formed by a single alkali atom and a single alkaline earth atom comprises three valence electrons. If excitations of core electrons and ionizations are neglected, these three electrons can only form a doublet or a quartet state. The AK atom, providing one unpaired electron, is always in a doublet state in the asymptotic limit of separated atoms. In contrast, the AKE atom can be either in a singlet or in a triplet state. A doublet state of the molecule is therefore either realized by the combination of a singlet AKE atom with the doublet AK atom, or by the combination of a triplet AKE atom with an anti-aligned electron from the AK atom. Quartet multiplicity can only arise if a triplet state of the AKE atom is combined with an aligned electron on the AK atom. The ground state of the molecule must be a doublet state, since the lowest state of the AKE atom is of singlet character. Only an excited triplet state of the AKE can result in a quartet state. For the AKE atoms considered in this study (Be-Sr), this is a ^3P state with excitation energies between 22000 cm^{-1} and 14500 cm^{-1}. For Ba and Ra the lowest excitation has ^3D character. The lowest excitation of the AK atom is a ^2P state with energies ranging from 12500 cm^{-1} to 17000 cm^{-1}. The energy difference between the lowest excitation of the AKE (^3P) and the AK atom (^2P) is plotted in graphics a) of figure 5.2. Note that there are negative values for combinations of light alkali atoms and heavy alkaline earth atoms. Rather than the ^3D-excitations, which are the lowest ones, the ^3P-excitations were used in figure 5.2 for Ba and Ra. In plot b) of figure 5.2 the difference in electronegativities (ENs) is shown with a behavior similar to the differences in excitation energies. A positive value of the electronegativity difference indicates that the electron density is pulled towards the AKE atom. Only combinations of light AK atoms with heavy AKE atoms have negative differences. Within our test set only LiSr has a negative EN difference. The difference in excitation energy or electronegativities characterizes the direction and magnitude of the pull at the electron density. Additionally, the polarizability is important as it measures the flexibility of the electron density. The atomic values for the polarizability range from 37 to 248 a.u. for AKE atoms and from 164 to 313 a.u. for AK atoms[161], with an increasing value for heavier atoms. The change in the orbital of the AK atom can be expected to be larger than the change for the AKE atom if atoms of similar mass are combined. Such a behavior was observed and is discussed in section 5.3.3.

Figure 5.3 shows the PEDMs (a)) and dissociation energies (b)) for the ground state of the 16 AK-AKE molecules within our test set. The smallest PEDM was obtained for LiSr, but unlike the difference in ENs, it still is positive. The largest EN difference for the

---

[6] Note that this is not the lowest state in the quartet multiplicity. The $1^4\Pi$ state has the same asymptote but is more strongly bound than the $1^4\Sigma^+$ state.

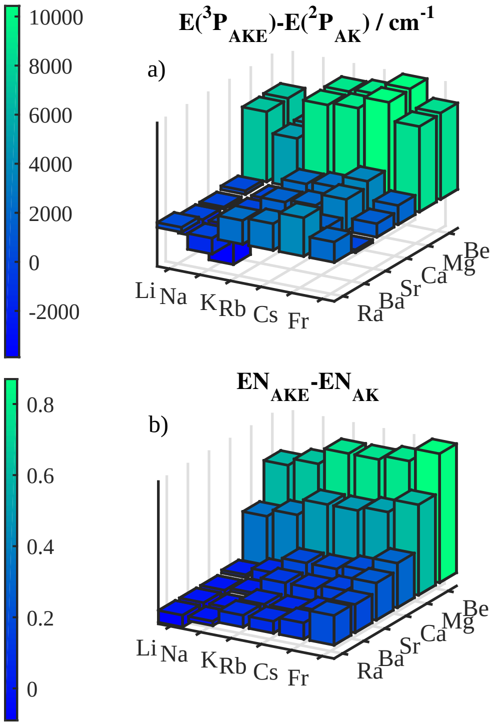

Figure 5.2: Differences between AK and AKE atoms for two atomic properties are shown in the figure, in the upper plot energy differences of the first P-excitations[13] and in the lower plot the differences in the electronegativities according to Pauling's scale[160].

calculated molecules is found for the RbBe molecule, but LiBe shows the largest dipole moment. The increase by going from light to heavy AK atoms and AKE atoms as seen in the difference of ENs in plot b) of figure 5.2 is not seen for the PEDMs. For KMg and RbMg small PEDMs are observable in figure 5.3. The small PEDMs for Mg containing molecules are probably related to the significantly smaller electronegativity difference for Mg than for Be, although they have similar differences in excitation energies (figure 5.2). Also, the potential depths are different. In plot b) of figure 5.3 the potential depths are shown and the values for molecules containing Mg are noticeably smaller than for the other AKE atoms, with no other trend being obvious for AKE atoms. However, there is a trend for AK atoms. The potential depth decreases seemingly exponentially in going from light to heavy AK atoms. The largest potential depth was determined for LiCa (2613 cm^{-1}), the smallest one for RbMg (744 cm^{-1}). In contrast to the PEDM and the equilibrium radii, the core polarization potential changes the potential depth in both directions. In cases where the AK atom is significantly lighter than the AKE atom the potential depth is reduced. However, if the AKE atom is lighter, the potential depth is increased. The equilibrium radii increase with inclusion of core polarization potentials. This effect is larger for heavier AK atoms, but shows no recognizable dependence on the AKE atom.[3]

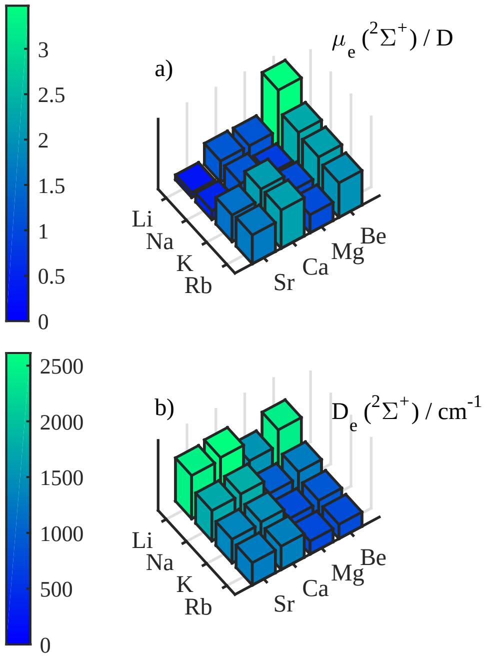

Figure 5.3: The permanent electric dipole moment (a)) and the potential depth (b)) for several AK-AKE molecules in their ground state ($^2\Sigma^+$) are shown.

In contrast to the strictly positive PEDM for the doublet ground states the PEDMs for the lowest Σ^+ state in the quartet manifold are negative, as can be seen in figure 5.4. The PEDMs for the quartet states show a correlation with the difference in ENs (b) in figure 5.2). The most negative PEDM is found for the only molecule with a negative EN difference (LiSr), while small PEDMs are obtained for strongly positive EN differences. Small PEDMs of the $^4\Sigma^+$ state are observable in plot a) in figure 5.4 for Na containing diatomic molecules including NaBe with the smallest value. This seems to be related to the first excitation energy of Na, which is the largest of all AK atoms. The large excitation energy leads to the small – and for some combinations with Na even negative – differences in the excitation energy, as can be seen in graphics a) of figure 5.2. The potential depth turns out to be a reliable descriptor for the magnitude of the PEDM, as is evident by comparing plot a) and b) of figure 5.4, but is less useful for the estimation of PEDMs in the doublet manifold. For the $^4\Sigma^+$ state the dissociation energy and the PEDM have a correlation coefficient of $R = -0.97$.

The equilibrium internuclear distances of the lowest Σ^+ states in the two multiplicities are given in the tables 5.2 and 5.3. The r_e values for the doublet state are all below 4.57 Å, those for the quartet states lie above this value. The equilibrium distances can be compared to the tabulated covalent[163] and van der Waals[162] radii.[3] The internuclear distances for the ground state minimum lie in between the covalent and van der Waals values. On average, they are off by 0.4 Å from the covalent radii and by 1.4 Å from the van der Waals radii. Them being closer to the covalent radii indicates

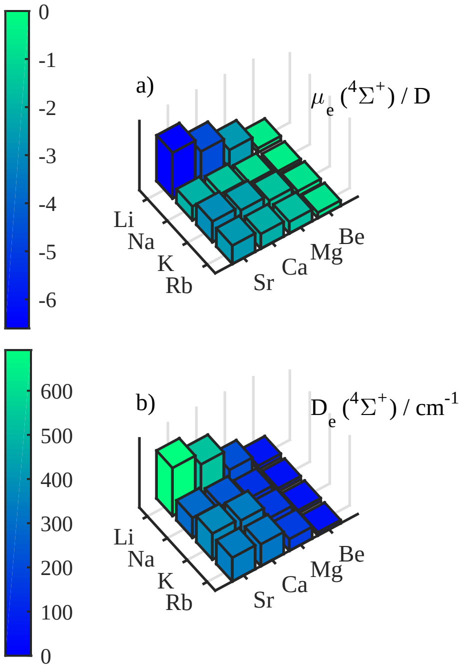

Figure 5.4: The upper plot shows the PEDMs for several AK-AKE molecules in the lowest $^4\Sigma^+$ state. Note that the axis is reversed so that the highest bar corresponds to the most negative value. The graphics below shows the corresponding dissociation energy for a direct comparison.

a covalent or ionic bond in the lowest state of the doublet manifold. The lowest $^4\Sigma^+$ states have equilibrium internuclear separations that are on average 0.5 Å larger than predicted by the tabulated van der Waals values, which indicates a weak bond.

The fraction of ionic character[305] can be estimated by dividing the determined dipole moment by the dipole moment obtained by shifting one electron by the equilibrium distance: $f_{Ion} = \frac{\mu}{e \cdot r_e}$. For the ground state, this fraction lies below 21 %, except for molecules containing Be, where the values are always above 21 %. As is obvious from the method of calculation, this quantity is correlated with the determined dipole moment and should be interpreted with caution. For the quartet states, particularly high values are observed for Li containing molecules.

With the finite field calculations, which we performed in order to determine the dipole moment, we could also determine the polarizabilities of the molecules along the internuclear axis. Graphics a) of figure 5.5 shows the polarizabilities for the ground state, which increase with atomic mass. These values are about 3.7 (with an variation from 3.4 to 4.0) times larger than the mean of the polarizability of the atoms involved. The polarizabilities for the quartet states show stronger variations (from 1.8 to 7.7 of the mean of the atomic pol.) than for the doublet states, as can be seen in graphics b) of figure 5.5. Furthermore, there is a pronounced increase of polarizability for heavy AKE atoms, but no clear trend for the AK atoms. This dependence is probably related to the lowering of the first excitation energy when going from light to heavy AKE atoms.

An increased mixing of the s-orbital of the AK atom and the p-orbital of the AKE atom facilitates a change in the electron density distribution.

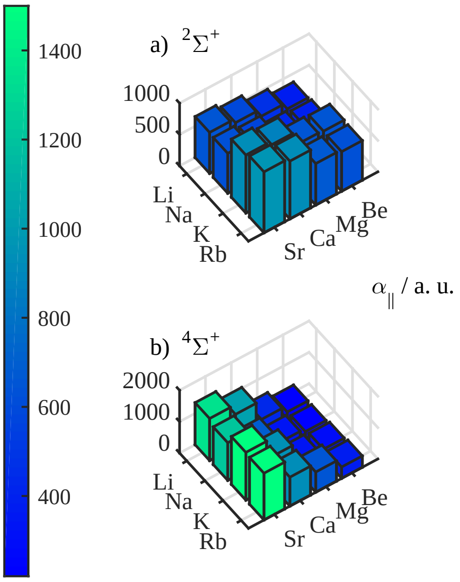

Figure 5.5: Finite-field polarizabilities in the doublet ground state (upper graphics) and the lowest $^4\Sigma^+$ state (lower graphics), calculated at the corresponding equilibrium geometry.

5.3.3 Qualitative picture

Typical potential energy curves and PEDM curves for the lowest Σ^+ states in the two multiplicities are shown in figure 5.6. The lowest $^2\Sigma^+$ is strongly bound with a positive PEDM. The PEDM approaches zero for large internuclear distances as expected for neutral molecules. In contrast, the lowest $^4\Sigma^+$ state is weakly bound with a negative PEDM. In general, the maximum ($^2\Sigma^+$) or minimum ($^4\Sigma^+$) of the PEDM curve is found for internuclear distances smaller than the equilibrium distance. The results displayed in figure 5.6 refer to LiBe, but the same behavior was previously observed for LiCa[2], RbCa[7], and RbSr[8]. In the current study, all 16 AK-AKE molecules confirm this trend. However, this behavior is not very pronounced for LiSr, and a different sign of the dipole moment can be expected in the ground state if Ba or Ra atoms are combined with Li. In fact, this has been observed by Gou *et al.*[314].

Our findings are summarized in figure 5.7. The ground state, displayed in graphics a), shows a smaller bond distance. The dipole moment is positive, the vector of the dipole moment points from the AKE atom (++) to the AK atom (+). This is the result of the center of charge of the electrons being closer to the AKE atom than the center of positive charge. The quartet state has a larger bond distance and a negative dipole moment. The center of electron charge is now closer to the AK atom than the center of positive

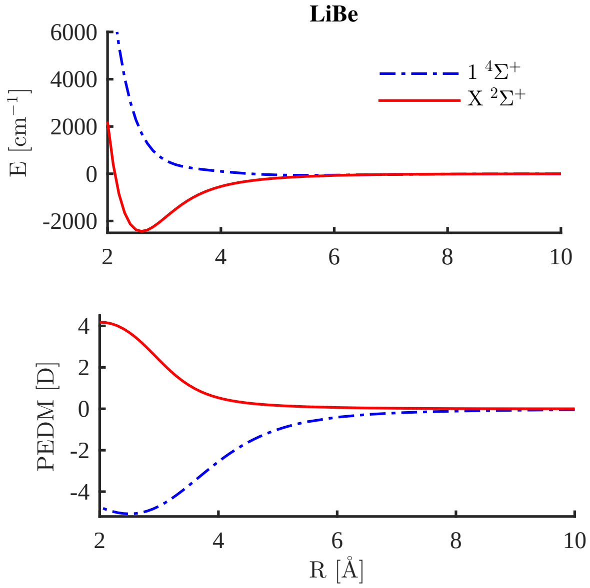

Figure 5.6: Potentials and PEDMs of the lowest Σ^+ state in the doublet and quartet multiplicity for the LiBe molecule.

charge. We explain this behavior by the orbital occupation indicated on the right side of figure 5.7. In the ground state (a)) the 1st orbital, mainly an s-orbital around the AKE atom,[7] is doubly occupied. The 2nd orbital, mainly a mixture of s-orbitals from the AK atom and p-orbitals from the AKE atom, is singly occupied. Because the AKE orbital mixes into it, it is not centered at the AK atom. Therefore, the center of negative charge is closer to the AKE atom, and a positive PEDM is obtained in our coordinate system. This agrees with the situation indicated by the atomic polarizabilities. In general, the AK atoms have larger polarizabilities than AKE atoms. In the ground state, the highest occupied AK orbital should deform more easily and mix with AKE orbitals. The situation is different for the lowest Σ^+ state in the quartet multiplicity (b) in figure 5.7). Since all spins need to be aligned, the Pauli principle does not allow for a double occupation of the 1st orbital. Therefore, one electron is transferred from this orbital into the 3rd orbital, which is a mixture of s-orbitals from the AK atom and p-orbitals from the AKE atom. For this reason, it has a probability density close to the AK atom, which changes the direction of the PEDM compared to the ground state. The 3rd orbital also mixes s- and p- orbital contributions in a similar way as the 2nd orbital does. However, unlike the 2nd orbital, it has an additional node between the atoms, not only at the center of the AKE core.[7] It corresponds, at least approximately, to the antibonding counterpart of the 2nd orbital, which explains the small dissociation energy of the lowest $^4\Sigma^+$ state.

---

[7] The isosurfaces of the three orbitals indicated on the left side in figure 5.7 can be found in appendix A.

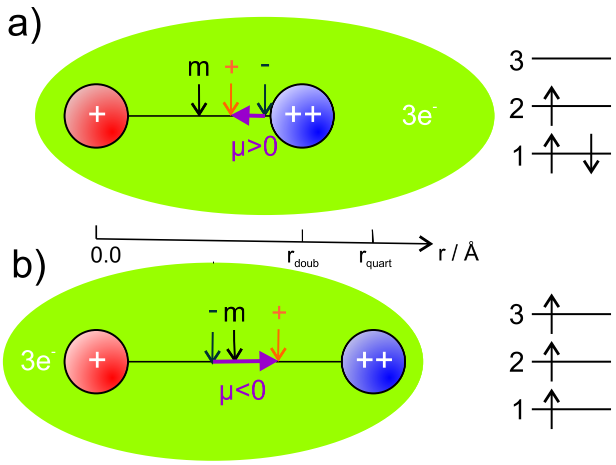

Figure 5.7: A visualization of the charge distribution in our set of 16 AK-AKE molecules (no absolute scale). The AK (+) atom is shown in red, the AKE (++) atom in blue. Center of mass, positive and negative charge are indicated by arrows. On the right side the orbital occupation discussed in the text is depicted. Calculated isosurfaces of the corresponding orbitals can be found in appendix A.

5.3.4 Dipole moment predictions

In this section we attempt to describe and predict the behavior of the dipole moment in the ground state due to its experimental importance for several applications mentioned in the introduction. The PEDMs of the lowest Σ^+ state of the quartet multiplicity are well correlated with the dissociation energy, which is not the case for the ground state. However, we find the following empirical equation to reproduce the dipole moments surprisingly well for all species under investigation:

$$\mu_e = a_1 \cdot \mathrm{sign}\,(\Delta EN) \cdot \sqrt{|\Delta EN|} + a_2 \cdot \bar{P_{at}} + \frac{a_3}{D_e} \tag{5.1}$$

This model requires the difference of electronegativities ΔEN, the mean of the atomic polarizabilities $\bar{P_{at}}$, and the dissociation energy D_e as input for the evaluation of the dipole moment. We note that it does not have yet a clear theoretical justification, as it was derived from an analysis of correlations between the dipole moment and atomic properties by a simple trial and error approach. However, it agrees very well with the available ab initio data, as can be seen from figure 5.8, although it only requires three fitting parameters a_1, a_2 and a_3. At least the occurrence of the atomic descriptors in the formula can be readily justified. The difference in ENs accounts for the pull on the electron density, and the corresponding contribution to the dipole moment must therefore be related to a charge transfer. We do not have an explanation for the square root dependence, which made it necessary to also introduce the sign function in order to have the sign of the EN difference correlate with the direction of dipole moment. Because the value of the EN difference covers only a region from -0.1 to 0.9 other functions might also be suitable to capture the behavior. Slightly worse results are obtained for functions like $a_3 \cdot \left(\Delta EN - \frac{\Delta EN^2}{2}\right)$ or the bounded $a_3 \cdot \tanh\left(\Delta EN\right)$. The increase of the PEDM with increasing mean polarizability is easily understood by the greater spatial flexibility of the electron distribution. However, an explanation for the third term in equation 5.1 is less straight-forward. The corresponding fitting parameter a_3 takes a negative value in the model, therefore reducing the dipole moment proportional to the inverse of the corresponding dissociation energy. In other words, the weaker the bond, the more effectively this term reduces the dipole moment. This last contribution is not fully understood, but both properties are related to the spatial distribution of the orbitals.

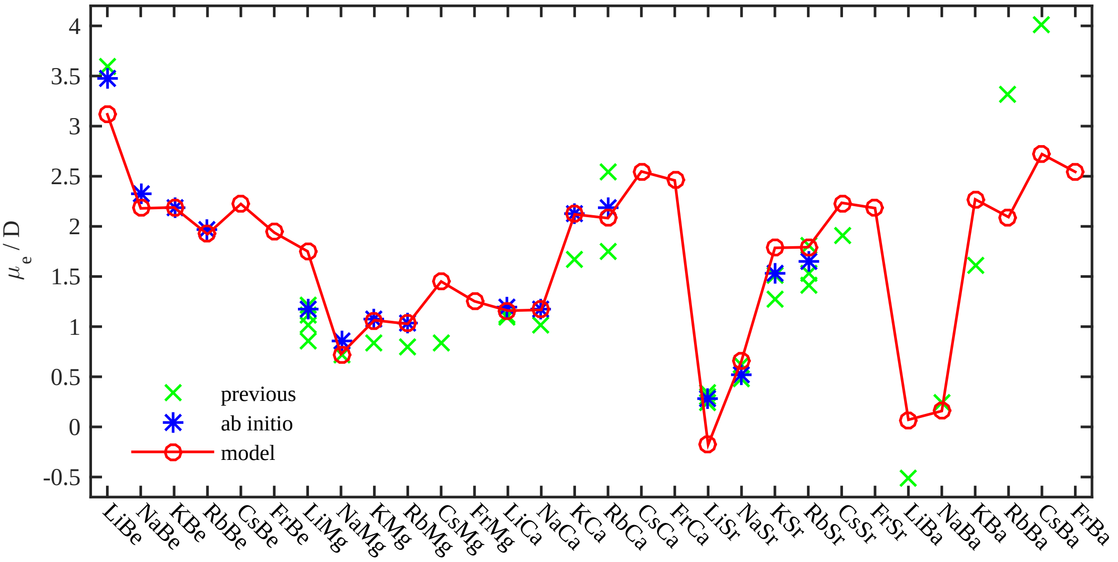

Figure 5.8: Dipole moment predictions as described in the text (○). The three parameters of the model were determined by fitting to the ab initio results of this work (∗). The resulting model shows good agreement with results from previous theoretical treatments (x) listed in table 5.2. Additional values have been added for the CsMg (ref. 119), CsSr (ref. 258) and AK-Ba molecules (ref. 314).

This empirical model allows us to predict the dipole moments for other AK-AKE molecules. However, while the required ENs and the atomic polarizabilities can be found in ref. 160 and 161, the dissociation energies need to be estimated. For Ba, the values from ref. 314 have been used. The potential depth of molecules including Cs or Fr were extrapolated with an exponential function from values for smaller AK atoms, since an exponential dependence was observed for the dissociation energy in figure 5.3. These results, together with previous theoretical results for AK-AKE molecules beyond our test set[119, 258, 314], are shown in figure 5.8. We note that Gou *et al.*[314] neglected the polarization of the cores, which might explain their larger amplitudes, similar to what we observed without core polarization potentials (figure 5.1). A detailed comparison between predicted and previous values is given in appendix A.

5.4 Conclusion

The lowest Σ^+ states in the doublet and quartet manifold for a selection of 16 AK-AKE molecules were analyzed at the MCSCF+MRCI level of theory. Trends for the PEDMs, equilibrium internuclear separations, dissociation energies, and polarizabilities along the internuclear axis were discussed. We find that the PEDMs of the lowest Σ^+ state in the doublet and quartet multiplicity are pointing in opposite directions for all molecules under investigation, which is in line with previous calculations. This behavior was explained in a molecular orbital picture. We further presented an empirical formula which describes the PEDM in the $^2\Sigma^+$ state as a function of two atomic descriptors (electronegativity, polarizability) and the dissociation energy. After fitting three parameters of the formula to our test set, we used this model to successfully predict the PEDM of several AK-AKE molecules beyond our initial test set.

The PEDM is important for applications of ultracold molecules, since it is the essential parameter for the interaction with microwaves, and, in combination with the polarizability, for the alignment in electric fields and optical lattices. A high PEDM is favorable because lower intensities and field strengths are sufficient to manipulate the molecules. In our study we find the highest PEDM for combinations with Be. However, handling these molecules might be a problem in the experiment due to the toxicity of beryllium. Good alternatives with high PEDM are RbCa, KCa, and RbSr, with the latter being the most promising candidate at present[26]. Our extrapolation formula indicates that CsCa might also be a promising choice.

5.5 Remarks

Tables containing additionally determined parameters are available in appendix A, which also contains pictures of the natural orbitals as determined in the MCSCF calculation. In order to obtain the results presented above it was necessary to determine several excited states for the 16 AK-AKE molecules. The potential energy curves as well as PEDMs and TDMs calculated by the implemented automated procedure are shown in appendix C.

In the discussion in the previous sections the changes introduced by the core polarization potential are discussed and the numerical values of the differences are given in appendix A in section A.1.10. If a CPP is included the core is not only described by a potential or frozen orbitals, but also has an electric dipole moment induced by an external electric field. This dipole moment changes the orbitals which leads to the significant changes in the permanent electric dipole moment (see above), which is reduced to about half its value. The automatically computed moments include the change of the dipole moment due to the change in the orbitals. But the dipole moment of the core due to

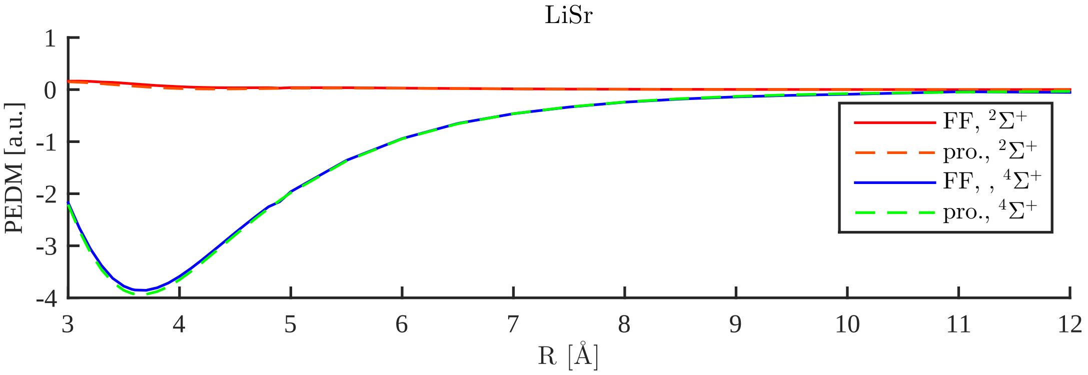

Figure 5.9: This figure show the PEDM dipole moment for LiSr in the $X\,^2\Sigma^+$ and $1\,^4\Sigma^+$ states determined by a finite field calcualtion and the values calculated by the implementation in Molpro[140].

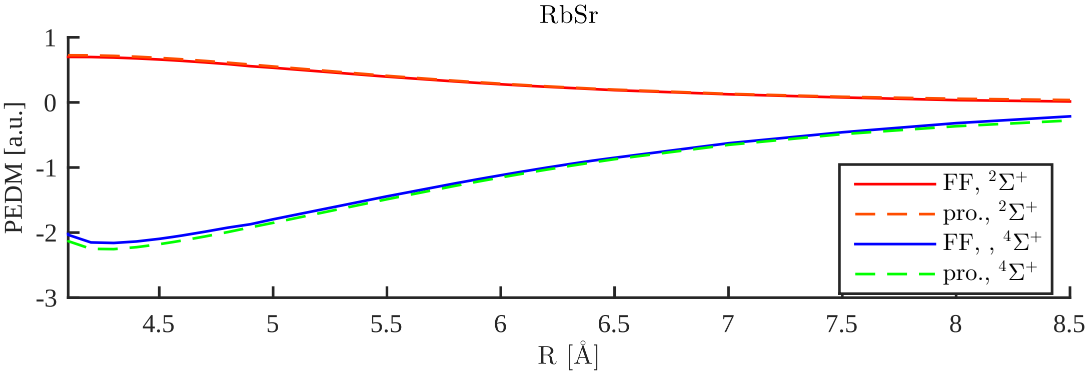

Figure 5.10: This figure show the PEDM dipole moment for RbSr in the $X\,^2\Sigma^+$ and $1\,^4\Sigma^+$ states determined by a finite field calcualtion and the values calculated by the implementation in Molpro[140].

the polarization is not included. We can estimate the influence of this contribution by comparing finite field calculations (which only need accurate energies) to the automated calculation. For LiBe, both results match exactly, which is expected if CPPs are not applied. The differences for other molecules are given in appendix A.1.11 and tend to be small. The dipole moment curves for two molecules (LiSr, RbSr) have been calculated by both approaches and are shown in figures 5.9 and 5.10. These small differences have a similar magnitude as other approximations used in these calculations and are smaller than the error introduced by a complete neglect of core polarization.

Chapter 6

Summary and outlook

This thesis presents theoretical studies of several diatomic molecules. The selected compounds have two features in common. Firstly, they have at least one open shell. The unpaired electron leads to a magnetic dipole moment. Secondly, we only considered heteronuclear molecules. This results in an often substantial charge transfer between the atoms leading to a large permanent electric dipole moment in several cases.

The first part of this thesis is devoted to the extension of previous calculations on the CrHe system[20] to additional multiplicities and contains an analysis in the context of recent experiments. 12 states of septet manifold and 12 states of quintet manifold were determined, corresponding asymptotically to the ground state, as well as 5 septet and 6 quintet states corresponding to excitations on the chromium atom. In general, the states are weakly bound with dissociation energies of a few cm^{-1} except for the $1\ {}^7\Pi$ state. For potential energy curves with the same asymptote ($\mathrm{z}\,{}^7\mathrm{P}^\circ$) spin-orbit coupling was included via the Breit-Pauli Hamiltonian.

In chapter 3 we present the results for RbSr, a follow up of our benchmark study of LiCa[2]. This molecule was selected due to the good control of its constituents in ultracold atomic physics[26]. Details of the experimental investigation can be found in previous publications[5, 6, 23]. In this thesis, 17 doublet and 5 quartet Hund's case (a) states are presented as determined by a multireference configuration interaction computation. Asymptotically, they correspond to the ground state, three doublet excitations of the Rb atom and two singlet and two triplet excitations of the Sr atom. A dissociation energy of about 1273 cm^{-1} was determined for the ground state, which differs from previous calculations on average by 200 cm^{-1}. The vibrational constant of the ground state agrees well with the experimental value, both at about 42 cm^{-1}. Five electronically excited states were identified in the experimental spectrum and their transition energies deviate by less than 500 cm^{-1} for levels below 15000 cm^{-1}. Additionally, several Hund's case (c) states were calculated by two different methods. The spectroscopic parameters of the seven lowest of these states are listed in chapter 3. These potentials were then used to simulate an observed laser induced fluorescence spectrum. The envelope of the signal can be explained without including spin-orbit coupling, but the structure is only observable after the inclusion of such effects. The Breit-Pauli computation was expected to be more accurate as it includes a change of the spin-orbit coupling strength, but we observed that the calculation based on a constant spin-orbit parameter and diagonlization yields better agreement with the experiment.

In the next step Sr was replaced by Ca, and a similar investigation was performed. 19 states in the doublet manifold and 5 states in the quartet manifold were determined by multireference configuration interaction for RbCa. They correspond asymptotically to the ground state, four doublet states of the Rb atom, and two singlet and two triplet states of the Ca atom. In addition, the ground state of the cation (RbCa+) was computed. Seven features in the measured spectrum up to 23000 cm^{-1} were assigned to electronically exited states with an error of about 500 cm^{-1} in total. There are some similarities between the electronic states of RbCa and RbSr: The 1 $^2\Pi$ state has the largest dissociation energy and smallest internuclear separation. The weakest bound state is the 1 $^4\Sigma^+$. The ground state the smallest dissociation energy among the other states below 20000 cm^{-1}. The 1 $^2\Delta$ electronic state is also strongly bound and shows the second largest dissociation energy. The equilibrium positions are about 0.2 Å smaller for RbCa than for RbSr.

In chapter 5 we only considered two electronic states, but investigated a set of 16 AK-AKE molecules. The spectroscopic parameters and permanent electric dipole moments were extracted for all molecules and trends were analyzed for the lowest Σ^+ state in the quartet and doublet manifold. These states show qualitatively different properties. The doublet ground state is significantly bound with values between 2600 and 700 cm^{-1}. It has a positive partial charge on the AK atom resulting in a positive PEDM for our definition of the coordinates. In contrast the quartet state shows a small dissociation energy and a negative PEDM. The dissociation energies of the $^4\Sigma^+$ states range from 700 to 40 cm^{-1}. They behave inversely to the difference in electronegativities, e.g. for RbBe the largest electronegativity difference and the shallowest potential can be observed. The amplitude of the permanent electric dipole moment shows the same trend as the dissociation energies but with a negative sign. In the case of the $^2\Sigma^+$ state, no clear correlation between the PEDM and a single atomic or molecular indicators could be observed. Three different quantities were necessary to describe the permanent electric dipole moment of this state. The mean of the atomic polarizability, the difference in electronegativities, and the dissociation energy of the doublet state were used to successfully capture the behavior of the PEDM. Large values of the PEDM, appreciated in experimental applications, were obtained for combinations with Be. However, the toxicity of Be keeps its applicability limited. High values were also obtained for combinations of heavy AK and heavy AKE atoms, as for example RbSr or RbCa. LiSr has the smallest PEDM and might be used in experiments that rather require a dominant magnetic dipole moment. The values of the equilibrium radii for the $^2\Sigma^+$ state were between the tabulated van der Waals and covalent radii, but closer to the second ones. Therefore, we assume that it is a covalent bond with a large ionic character for diatomic molecules consisting of Be and a AK atom. The equilibrium internuclear separation for the $^4\Sigma^+$ are close to or larger than the tabulated van der Waals distances. This, in combination with the small dissociation energies, leads to the conclusion that this is a van der Waals bond.

Our computations made extensive use of effective core potentials. They were compared to calculations using all electrons. In general, ECP results were closer to experimental observations, although this strongly depended on the quality of the effective core potentials used. Further improvement was achieved by the application of core polarization potentials, which simulate the response of the core to an external electron distribution. This approximate method was especially important for excitation energies and electric dipole moments. Equally important is the selection of a meaningful basis set. It should be sufficiently large and compatible with the atom and effective core potential, although we observed that several all electron basis sets give good results in combination with ECPs. Our theoretical results allowed to identify vibronic features in the experimental spectrum, but with deviations of about 500 cm^{-1} for the transition energies. The difference between measured and calculated vibrational constants was smaller. In order to reliably predict optical transitions and transfer schemes the error should be on the order of GHz (0.03 cm^{-1}) which can currently only be achieved by fitting to experimental data.

As a next step we want to investigate excited states of several AK-Ca/AK-Sr molecules in order to estimate the viability of optical transfer schemes with conventional laser systems. Additional experimental results are important for reliable predictions and hopefully will be available soon. For photoassociation, weakly bound excited states with long-range bonding are necessary. So far only the $^4\Sigma^+$ state of the AK-AKE molecules shows this feature, but this state can not be used because there is no transition dipole moment. Combinations with Cs might show weakly bound excited states with a significant TDM due to the low lying electronic excitations, but it is questionable if they can be accessed with conventional laser systems. Another interesting topic is the combination of chromium with alkali atoms. The resulting molecule should have five unpaired electrons like the d-orbitals of the transition metals. This model system might then be used to study the interesting magnetic properties of transition metals.

There are also several open question concerning superfluid helium droplets and the interactions with dopants. In the course of this work, several relaxations from one electronic state to another one were observed or assumed. Examples are the relaxation from a septet into a quintet state for CrHe molecule, the fluorescence stemming from a lower state than the excited one in RbSr, and the lack of fluorescence in RbCa. The energy transfer mechanisms responsible for these observations are yet unclear.

Danksagung

Nun möchte ich mir die Zeit nehmen mich bei den Menschen zu bedanken, die mir in den letzten Jahren zur Seite gestanden sind und ohne deren Unterstützung diese Arbeit nicht möglich gewesen wäre. Einen besonderen Dank möchte ich meinen Betreuer *Wolfgang E. Ernst* aussprechen, der mir dieses Thema zugetragen hat und mir die finanziellen Möglichkeiten eröffnet hat es durchzuführen. Durch seine Förderung war es mir möglich mein Wissen auf mehreren Konferenzen zu vertiefen und mich mit mehreren Gästen über meine Arbeit zu unterhalten, wie zum Beispiel Marius Lewerenz und Florian Schreck. Mein Dank gilt auch meinem Kobetreuer *Andreas W. Hauser*, der mich mit seiner fachlichen Kompetenz so manche Frage beantwortet hat und auch bereits vor seiner Vorlesung die Elektronenstrukturtheorie nahe gebracht hat. Seine Betreuung aus der Ferne unter anderem über Skype, sowie sein oftmaliges Korrekturlesen waren entscheidend für die Qualität meiner Arbeit.

Mein ehemaliger Bürokollege *Matin Ratschek* war mir eine große Hilfe, insbesondere beim Aufsetzen des Rechenservers und der Bedienung von Linux. Zusammen mit *Andreas Kautsch* und *Matthias Hasewend* haben wir oft über das Chrom Atom und seine Wechselwirkung mit Helium diskutiert und sie einigermaßen verstanden. Meine Kollegen *Florian Lackner* und *Günter Krois* haben mir den Einstieg in die Klasse der Alkali-Erdalkali Moleküle erleichtert und ihn zahlreichen gemeinsamen Rätselstunden haben wir gemeinsam das Spektrum einige solcher Moleküle analysiert. Des Weiteren bin ich *Patrick Kraus* für seine zahlreichen Ratschläge dankbar. Die Diskussionen mit ihm und *Markus Koch* waren interessant und haben mein Wissen erweitert. Mein Dank gilt auch den Nudel- und Toastköchen des Instituts, wie zum Beispiel *Christian Gösweiner*. Ihr Aufwand hat es mir ermöglicht beim Mittagessen mich an so manchen interessanten Gespräch zu beteiligen. Mit meinen jetzigen Bürokollegen *Ralf Meyer* und *Samuel Früwirth* konnte ich immer wieder über Probleme theoretischer Rechnungen sprechen um Lösungen zu finden und wir haben gemeinsam dieses Jahr eine Summer School besucht.

Zuletzt möchte ich mich noch bei meiner Familie, insbesondere bei meinen Eltern Johann und Waltraud, bedanken. Ohne ihre Unterstützung wäre mein Leben anders verlaufen.

Appendix A

Additional information for alkali - alkaline earth molecules

This appendix contains several additional tables providing more detailed information on the *ab initio* results. Some of these results are displayed as figures in chapter 5. In section A.1.1 predicted values of the formula in the text are compared to previous calculations. Additional orbital pictures are plotted in section A.2, which support the explanation in chapter 5.

Section A.1.2 contains the results of a multiconfigurational self consistent field calculation (MCSCF) in combination with an multireference configuration interaction (MRCI) for 16 different alkali-alkaline earth molecules. Details of the calculation can be found in chapter 5. The number of orbitals and states considered in the calculation are given in section A.1.6. Tabulated values describing the convergence of the dissociation energies for large internuclear separations and corresponding distances are listed in section A.1.3. Results without using the core polarization potentials (CPP) are given in section A.1.4 and for large internuclear distances in section A.1.5. The finite field values are listed in section A.1.7 together with applied field strengths. Section A.1.8 gives a comparison between the results for the equilibrium internuclear separations found in section A.1.2 and the tabulated covalent and van der Waals radii. The calculated polarizabilities (section A.1.7) are compared to the mean of the atomic polarizabilities in section A.1.9. The next two sections are concerned with comparisons between calculations with and without a CPP (section A.1.10) and between results obtained by the MRCI program and by finite field calculations (section A.1.11). In section A.1.13 the literature values for atomic properties are listed.

A.1 Tables

A.1.1 Predictions obtained with the empirical model and previous results for additional molecules

Table A.1: In this table the predicted values for the $^2\Sigma^+$ ground state of several AK-AKE molecules are listed alongside previous results obtained by *ab initio* calculations. The results are depicted in Fig. 8 in the manuscript.

mol.	Ref.	μ_e/D	r$_e$/Å	D$_e$/cm^{-1}	ω_e/cm^{-1}
LiBa	pred.	0.07		3646	
	260	-0.37	3.67	2871	205.5
	314	-0.52	3.73	3646	204.1
	265		3.58	3146	200.7
NaBa	pred.	0.16		2573	
	314	0.25	4.12	2573	92.3
	315		3.87	1920	89.2
KBa	pred.	2.27		1750	
	314	1.62	4.65	1750	59.4
RbBa	pred.	2.09		1472	
	314	3.32	4.93	1472	39.2
CsBe	pred.	2.22		776	
CsMg	pred.	1.45		729	
	258	0.83	4.54	544	43.2
CsCa	pred.	2.55		1282	
CsSr	pred.	2.22		1205	
	119	1.91	4.79	1084	33.8
CsBa	pred.	2.72		1466	
	314	4.02	5.19	1466	32.8
FrBe	pred.	1.94		764	
FrMg	pred.	1.25		726	
FrCa	pred.	2.46		1262	
FrSr	pred.	2.18		1183	
FrBa	pred.	2.54		1301	

A.1.2 Multireference configuration interaction

$^2\Sigma^+$ state

Table A.2: Permanent electric dipole moment of the $^2\Sigma^+$ ground state for the sixteen AK-AKE molecules in the test set as determined by MCSCF+MRCI calculations.

μ_e / D	Be	Mg	Ca	Sr
Li	3.460	1.141	1.123	0.175
Na	2.292	0.867	1.167	0.462
K	2.230	1.082	2.170	1.555
Rb	2.023	1.053	2.276	1.705

Table A.3: Dissociation energy of the $^2\Sigma^+$ ground state for the sixteen AK-AKE molecules in the test set as determined by MCSCF+MRCI calculations.

D_e / cm^{-1}	Be	Mg	Ca	Sr
Li	2427	1538	2613	2471
Na	1291	946	1792	1728
K	920	779	1455	1358
Rb	816	744	1337	1279

Table A.4: Equilibrium internuclear separation of the $^2\Sigma^+$ ground state for the sixteen AK-AKE molecules in the test set as determined by MCSCF+MRCI calculations.

r_e / Å	Be	Mg	Ca	Sr
Li	2.601	3.102	3.388	3.572
Na	2.966	3.465	3.665	3.843
K	3.506	3.994	4.196	4.392
Rb	3.704	4.173	4.369	4.564

Table A.5: Vibrational constant of the $^2\Sigma^+$ ground state for the sixteen AK-AKE molecules in the test set as determined by MCSCF+MRCI calculations.

ω_e / cm^{-1}	Be	Mg	Ca	Sr
Li	312.9	181.0	199.8	180.7
Na	173.0	89.6	102.9	87.2
K	121.7	64.3	71.3	56.7
Rb	104.2	54.1	57.0	42.6

Table A.6: Anharmonicity parameter of the $^2\Sigma^+$ ground state for the sixteen AK-AKE molecules in the test set as determined by MCSCF+MRCI calculations.

$\omega_e x_e$ / cm^{-1}	Be	Mg	Ca	Sr
Li	10.15	5.33	3.82	3.31
Na	5.80	2.13	1.48	1.10
K	4.03	1.32	0.87	0.59
Rb	3.32	0.98	0.61	0.35

Table A.7: Fraction of ionic character of the $^2\Sigma^+$ ground state for the sixteen AK-AKE molecules in the test set as determined by MCSCF+MRCI calculations. (Pauling criterion, equation 1.90)

f_{Ion} / %	Be	Mg	Ca	Sr
Li	52	14	13	2
Na	30	10	13	5
K	25	11	20	14
Rb	21	10	20	15

$^4\Sigma^+$ state

Table A.8: Permanent electric dipole moment of the lowest $^4\Sigma^+$ state for the sixteen AK-AKE molecules in the test set as determined by MCSCF+MRCI calculations.

μ_e / D	Be	Mg	Ca	Sr
Li	-0.621	-2.537	-4.640	-6.703
Na	-0.453	-0.988	-1.593	-2.040
K	-0.733	-1.652	-2.612	-3.008
Rb	-0.789	-1.628	-2.204	-2.710

Table A.9: Dissociation energy of the lowest $^4\Sigma^+$ state for the sixteen AK-AKE molecules in the test set as determined by MCSCF+MRCI calculations.

D_e / cm^{-1}	Be	Mg	Ca	Sr
Li	59	222	522	692
Na	50	131	237	287
K	48	157	343	376
Rb	47	170	316	343

Table A.10: Equilibrium internuclear separation of the lowest $^4\Sigma^+$ state for the sixteen AK-AKE molecules in the test set as determined by MCSCF+MRCI calculations.

r_e / Å	Be	Mg	Ca	Sr
Li	5.505	4.715	4.593	4.589
Na	5.837	5.713	5.736	5.807
K	5.992	5.731	5.727	5.947
Rb	6.027	5.844	6.054	6.148

Table A.11: Vibrational constant of the lowest $^4\Sigma^+$ state for the sixteen AK-AKE molecules in the test set as determined by MCSCF+MRCI calculations.

ω_e / cm^{-1}	Be	Mg	Ca	Sr
Li	24.7	31.9	54.5	61.4
Na	18.3	20.6	23.6	22.9
K	16.2	19.9	25.6	21.6
Rb	15.3	17.7	19.2	16.3

Table A.12: Anharmonicity parameter of the lowest $^4\Sigma^+$ state for the sixteen AK-AKE molecules in the test set as determined by MCSCF+MRCI calculations.

$\omega_e x_e$ / cm^{-1}	Be	Mg	Ca	Sr
Li	2.79	1.14	1.42	1.36
Na	1.68	0.81	0.59	0.46
K	1.37	0.63	0.48	0.31
Rb	1.25	0.47	0.29	0.19

Table A.13: Fraction of ionic character of the lowest $^4\Sigma^+$ state for the sixteen AK-AKE molecules in the test set as determined by MCSCF+MRCI calculations. (Pauling criterion, equation 1.90)

f_{Ion} / %	Be	Mg	Ca	Sr
Li	4	21	40	57
Na	3	7	11	14
K	5	11	18	20
Rb	5	11	14	17

A.1.3 Multireference configuration interaction - asymptotic convergence

Table A.14: Largest internuclear distances calculated to check asymptotic convergence in the MSCSCF+MRCI calculations.

r_{max} / Å	Be	Mg	Ca	Sr
Li	11	13	10	10
Na	10	12	11	11
K	10.5	12	30	25
Rb	10.5	10	11	13

$^2\Sigma^+$ state

Table A.15: Dissociation energy of the $^2\Sigma^+$ ground state for the sixteen AK-AKE molecules in the test set as determined by MCSCF+MRCI calculations with the asymptotic distances given in table A.14.

D_e / cm^{-1}	Be	Mg	Ca	Sr
Li	2429	1542	2613	2470
Na	1291	949	1797	1735
K	921	787	1476	1383
Rb	817	744	1348	1301

Table A.16: Differences in the dissociation energy of the $^2\Sigma^+$ ground state for the MCSCF+MRCI calculations between asymptotic limits of 10 Å and the distances given in table A.14.

ΔD_e / cm^{-1}	Be	Mg	Ca	Sr
Li	2	4	0	-1
Na	0	3	5	7
K	1	8	21	25
Rb	1	0	11	22

$^4\Sigma^+$ state

Table A.17: Dissociation energy of the lowest $^4\Sigma^+$ state for the sixteen AK-AKE molecules in the test set as determined by MCSCF+MRCI calculations with the asymptotic distances given in table A.14.

D_e / cm^{-1}	Be	Mg	Ca	Sr
Li	61	229	522	692
Na	50	138	246	302
K	49	173	381	427
Rb	47	170	334	387

Table A.18: Differences in the dissociation energy of the lowest $^4\Sigma^+$ state for the MCSCF+MRCI calculations between asymptotic limits of 10 Å and the distances given in table A.14.

ΔD_e / cm^{-1}	Be	Mg	Ca	Sr
Li	2	7	0	0
Na	0	7	9	15
K	1	16	38	51
Rb	0	0	18	44

A.1.4 Multireference configuration interaction without CPPs

$^2\Sigma^+$ state

Table A.19: Permanent electric dipole moment of the $^2\Sigma^+$ ground state for the sixteen AK-AKE molecules in the test set as determined by MCSCF+MRCI calculations without CPPs.

μ_e / D	Be	Mg	Ca	Sr
Li	3.460	1.297	1.312	0.395
Na	2.403	1.090	1.602	0.919
K	2.564	1.596	3.337	2.831
Rb	2.470	1.744	3.807	3.360

Table A.20: Dissociation energy of the $^2\Sigma^+$ ground state for the sixteen AK-AKE molecules in the test set as determined by MCSCF+MRCI calculations without CPPs.

D_e / cm^{-1}	Be	Mg	Ca	Sr
Li	2427	1648	2883	2870
Na	1223	953	1862	1882
K	823	744	1426	1425
Rb	695	659	1299	1288

Table A.21: Equilibrium internuclear separation of the $^2\Sigma^+$ ground state for the sixteen AK-AKE molecules in the test set as determined by MCSCF+MRCI calculations without CPPs.

r_e / Å	Be	Mg	Ca	Sr
Li	2.601	3.098	3.385	3.573
Na	3.034	3.547	3.750	3.930
K	3.644	4.162	4.361	4.561
Rb	3.881	4.396	4.578	4.782

Table A.22: Vibrational constant of the $^2\Sigma^+$ ground state for the sixteen AK-AKE molecules in the test set as determined by MCSCF+MRCI calculations without CPPs.

ω_e / cm^{-1}	Be	Mg	Ca	Sr
Li	312.9	187.7	208.7	190.3
Na	163.8	87.3	102.4	89.0
K	108.9	59.5	68.6	56.1
Rb	90.0	48.1	54.3	42.3

Table A.23: Anharmonicity parameter of the $^2\Sigma^+$ ground state for the sixteen AK-AKE molecules in the test set as determined by MCSCF+MRCI calculations without CPPs.

$\omega_e x_e$ / cm^{-1}	Be	Mg	Ca	Sr
Li	10.10	5.35	3.78	3.16
Na	5.48	2.00	1.41	1.05
K	3.60	1.19	0.82	0.55
Rb	2.91	0.88	0.57	0.33

Table A.24: Fraction of ionic character of the $^2\Sigma^+$ ground state for the sixteen AK-AKE molecules in the test set as determined by MCSCF+MRCI calculations without CPPs.(Pauling criterion, equation 1.90)

f_{Ion} / %	Be	Mg	Ca	Sr
Li	52	16	15	4
Na	31	12	17	9
K	28	15	30	24
Rb	25	16	33	28

$^4\Sigma^+$ state

Table A.25: Permanent electric dipole moment of the lowest $^4\Sigma^+$ state for the sixteen AK-AKE molecules in the test set as determined by MCSCF+MRCI calculations without CPPs.

μ_e / D	Be	Mg	Ca	Sr
Li	-0.621	-2.507	-4.501	-5.286
Na	-0.508	-1.170	-1.956	-2.317
K	-0.922	-2.159	-2.949	-3.511
Rb	-0.938	-2.094	-2.768	-3.258

Table A.26: Dissociation energy of the lowest $^4\Sigma^+$ state for the sixteen AK-AKE molecules in the test set as determined by MCSCF+MRCI calculations without CPPs.

D_e / cm^{-1}	Be	Mg	Ca	Sr
Li	59	215	521	620
Na	48	138	271	320
K	50	181	315	429
Rb	45	183	287	388

Table A.27: Equilibrium internuclear separation of the lowest $^4\Sigma^+$ state for the sixteen AK-AKE molecules in the test set as determined by MCSCF+MRCI calculations without CPPs.

r_e / Å	Be	Mg	Ca	Sr
Li	5.506	4.750	4.613	4.773
Na	5.872	5.705	5.675	5.788
K	6.023	5.699	5.906	5.992
Rb	6.189	5.884	6.145	6.244

Table A.28: Vibrational constant of the lowest $^4\Sigma^+$ state for the sixteen AK-AKE molecules in the test set as determined by MCSCF+MRCI calculations without CPPs.

ω_e / cm^{-1}	Be	Mg	Ca	Sr
Li	25.7	30.1	60.9	58.9
Na	17.7	20.9	25.9	24.4
K	15.6	21.1	24.1	23.3
Rb	13.8	18.9	19.3	17.7

Table A.29: Anharmonicity parameter of the lowest $^4\Sigma^+$ state for the sixteen AK-AKE molecules in the test set as determined by MCSCF+MRCI calculations without CPPs.

$\omega_e x_e$ / cm^{-1}	Be	Mg	Ca	Sr
Li	2.79	1.05	1.78	1.40
Na	1.62	0.79	0.62	0.47
K	1.20	0.62	0.46	0.32
Rb	1.06	0.49	0.32	0.20

Table A.30: Fraction of ionic character of the lowest $^4\Sigma^+$ state for the sixteen AK-AKE molecules in the test set as determined by MCSCF+MRCI calculations without CPPs. (Pauling criterion, equation 1.90)

f_{Ion} / %	Be	Mg	Ca	Sr
Li	4	21	38	44
Na	3	8	14	16
K	6	15	20	23
Rb	6	14	18	21

A.1.5 Multireference configuration interaction without CPPs - asymptotic convergence

Table A.31: Largest internuclear distances calculated to check asymptotic convergence in the MSCSCF+MRCI calculations without CPPs.

r_{max} / Å	Be	Mg	Ca	Sr
Li	11	100	100	100
Na	100	12	100	10
K	13	13	100	100
Rb	100	100	10.5	10

$^2\Sigma^+$ state

Table A.32: Dissociation energy of the $^2\Sigma^+$ ground state for the sixteen AK-AKE molecules in the test set as determined by MCSCF+MRCI calculations without CPPs with the asymptotic distances given in table A.31.

D_e / cm^{-1}	Be	Mg	Ca	Sr
Li	2429	1653	2896	2885
Na	1227	957	1872	1882
K	829	754	1457	1459
Rb	700	671	1307	1288

Table A.33: Differences in the dissociation energy of the $^2\Sigma^+$ ground state for the MCSCF+MRCI calculations without CPPs between asymptotic distances of 10 Å and the values given in table A.31.

ΔD_e / cm^{-1}	Be	Mg	Ca	Sr
Li	2	5	13	15
Na	4	4	10	0
K	6	10	31	34
Rb	5	12	8	0

$^4\Sigma^+$ state

Table A.34: Dissociation energy of the lowest $^4\Sigma^+$ state for the sixteen AK-AKE molecules in the test set as determined by MCSCF+MRCI calculations without CPPs with the asymptotic distances given in table A.31.

D_e / cm^{-1}	Be	Mg	Ca	Sr
Li	61	223	541	644
Na	51	141	294	320
K	52	151	358	488
Rb	35	193	300	388

Table A.35: Differences in the dissociation energy of the lowest $^4\Sigma^+$ state for the MCSCF+MRCI calculations without CPPs between asymptotic distances of 10 Å and the values given in table A.31.

ΔD_e / cm^{-1}	Be	Mg	Ca	Sr
Li	2	8	20	24
Na	3	3	23	0
K	2	-30	43	59
Rb	-10	10	13	0

A.1.6 Technical details of the multiconfigurational calculations

In this section we give details about orbital occupation and calculated states. The calculations were performed in the C_{2v} point group and the labels A_1, B_1, B_2, and A_2 refer to the irreducible representations.

Table A.36: The number of closed orbitals are listed for the different molecules in the MCSCF and MRCI calculations.

	Be				Mg				Ca				Sr			
	A_1	B_1	B_2	A_2	A_1	B_1	B_2	A_2	A_1	B_1	B_2	A_2	A_1	B_1	B_2	A_2
Li	2				4	1	1		3	1	1		3	1	1	
Na	4	1	1		6	2	2		5	2	2		5	2	2	
K	3	1	1		5	2	2		4	2	2		4	2	2	
Rb	3	1	1		5	2	2		4	2	2		4	2	2	

Table A.37: The number of occupied orbitals are listed for the different molecules in the MCSCF and MRCI calculations.

	Be				Mg				Ca				Sr			
	A_1	B_1	B_2	A_2	A_1	B_1	B_2	A_2	A_1	B_1	B_2	A_2	A_1	B_1	B_2	A_2
Li	11	4	4	1	13	5	5	1	12	5	5	1	12	5	5	1
Na	12	5	5	1	17	7	7	2	16	8	8	2	13	5	5	1
K	14	6	6	2	16	7	7	2	13	6	6	2	13	6	6	2
Rb	15	7	7	3	15	7	7	2	16	8	8	3	13	6	6	2

$^2\Sigma^+$ state

Table A.38: The number of states determined in the MCSCF for the doublet multiplicity are given.

	Be				Mg				Ca				Sr			
	A_1	B_1	B_2	A_2	A_1	B_1	B_2	A_2	A_1	B_1	B_2	A_2	A_1	B_1	B_2	A_2
Li	9	5	5	1	9	5	5	1	11	6	6	3	12	6	6	2
Na	7	4	4	1	10	5	5	2	12	7	7	3	10	5	5	2
K	10	5	5	2	10	5	5	2	8	4	4	2	8	4	4	2
Rb	11	6	6	3	13	8	8	3	11	6	6	3	10	5	5	2

Table A.39: The number of states determined in the MRCI for the doublet multiplicity are given.

	Be				Mg				Ca				Sr			
	A_1	B_1	B_2	A_2	A_1	B_1	B_2	A_2	A_1	B_1	B_2	A_2	A_1	B_1	B_2	A_2
Li	5	3	3	1	5	3	3	1	7	4	4	1	5	3	3	1
Na	6	3	3	1	6	3	3	1	7	4	4	2	7	4	4	2
K	7	4	4	1	7	4	4	1	6	3	3	1	5	3	3	1
Rb	7	4	4	1	6	3	3	1	6	5	5	1	7	4	4	2

$^4\Sigma^+$ state

Table A.40: The number of states determined in the MCSCF for the quartet multiplicity are given.

	Be				Mg				Ca				Sr			
	A_1	B_1	B_2	A_2	A_1	B_1	B_2	A_2	A_1	B_1	B_2	A_2	A_1	B_1	B_2	A_2
Li	1	1	1		1	1	1		3	2	2	1	3	2	2	1
Na	1	1	1		1	1	1		3	2	2	1	3	2	2	1
K	1	1	1		1	1	1		3	2	2	1	3	2	2	1
Rb	1	1	1		1	1	1		3	2	2	1	3	2	2	1

Table A.41: The number of states determined in the MRCI for the quartet multiplicity are given.

	Be				Mg				Ca				Sr			
	A_1	B_1	B_2	A_2	A_1	B_1	B_2	A_2	A_1	B_1	B_2	A_2	A_1	B_1	B_2	A_2
Li	1	1	1		1	1	1		3	2	2	1	3	2	2	1
Na	1	1	1		1	1	1		3	2	2	1	3	2	2	1
K	1	1	1		1	1	1		3	2	2	1	3	2	2	1
Rb	1	1	1		1	1	1		1	1	1		3	2	2	1

A.1.7 Finite field calculations

$^2\Sigma^+$ state

Table A.42: Permanent electric dipole moment of the $^2\Sigma^+$ ground state for the sixteen AK-AKE molecules in the test set as determined by finite field calculations for MCSCF+MRCI results.

μ_e / D	Be	Mg	Ca	Sr
Li	3.467	1.184	1.192	0.285
Na	2.326	0.857	1.182	0.511
K	2.219	1.083	2.122	1.523
Rb	1.970	1.037	2.188	1.645

Table A.43: Polarizabilities along the internuclear axis of the $^2\Sigma^+$ ground state for the sixteen AK-AKE molecules in the test set as determined by finite field calculations for MCSCF+MRCI results.

$\alpha_{\|\|}$ / a. u.	Be	Mg	Ca	Sr
Li	365	470	588	653
Na	397	432	577	636
K	628	656	869	925
Rb	631	664	922	972

Table A.44: Field strength for the finite field calculation of the $^2\Sigma^+$ ground state properties.

field / a. u.	Be	Mg	Ca	Sr
Li	2.50E-04	2.50E-04	5.00E-05	2.50E-04
Na	1.25E-04	2.50E-04	2.50E-04	1.25E-04
K	1.25E-04	5.00E-05	2.50E-04	2.50E-05
Rb	1.25E-04	1.25E-04	5.00E-05	1.25E-04

$^4\Sigma^+$ state

Table A.45: Permanent electric dipole moment of the lowest $^4\Sigma^+$ state for the sixteen AK-AKE molecules in the test set as determined by finite field calculations for MCSCF+MRCI results.

μ_e / D	Be	Mg	Ca	Sr
Li	-0.613	-2.519	-4.578	-6.606
Na	-0.452	-0.986	-1.619	-2.003
K	-0.719	-1.581	-2.501	-2.989
Rb	-0.790	-1.662	-2.130	-2.661

Table A.46: Polarizabilities along the internuclear axis of the lowest $^4\Sigma^+$ state for the sixteen AK-AKE molecules in the test set as determined by finite field calculations for MCSCF+MRCI results.

$\alpha_{\|\|}$ / a. u.	Be	Mg	Ca	Sr
Li	223	423	1031	1340
Na	229	326	686	1200
K	300	338	950	1523
Rb	363	645	922	1491

Table A.47: Field strength for the finite field calculation of the lowest $^4\Sigma^+$ state properties.

field / a. u.	Be	Mg	Ca	Sr
Li	1.25E-04	2.50E-04	1.25E-04	1.25E-04
Na	1.25E-04	1.25E-04	2.50E-05	1.25E-04
K	5.00E-05	5.00E-05	5.00E-05	1.25E-04
Rb	5.00E-05	2.50E-05	3.75E-05	1.25E-05

A.1.8 Radii

Table A.48: Covalent radii for the sixteen AK-AKE molecules in the test set as determined with tabulated values[163].

r_{cov} / Å	Be	Mg	Ca	Sr
Li	2.24	2.69	3.04	3.23
Na	2.62	3.07	3.42	3.61
K	2.99	3.44	3.79	3.98
Rb	3.16	3.61	3.96	4.15

Table A.49: Van der Waals radii for the sixteen AK-AKE molecules in the test set as determined with tabulated values[162].

r_{vdW} / Å	Be	Mg	Ca	Sr
Li	4.10	4.63	4.74	4.96
Na	4.48	5.01	5.12	5.34
K	4.71	5.24	5.35	5.57
Rb	5.19	5.72	5.83	6.05

$^2\Sigma^+$ state

Table A.50: Difference between the covalent radii (table A.48) and the equilibrium internuclear separation of the $^2\Sigma^+$ ground state (table A.4) for the sixteen AK-AKE molecules in the test set.

r_e-r_{cov} / Å	Be	Mg	Ca	Sr
Li	0.36	0.41	0.35	0.34
Na	0.35	0.40	0.25	0.23
K	0.52	0.55	0.41	0.41
Rb	0.54	0.56	0.41	0.41

Table A.51: Difference between the van der Waals radii (table A.49) and the equilibrium internuclear separation of the $^2\Sigma^+$ ground state (table A.4) for the sixteen AK-AKE molecules in the test set.

r_{vdW}-r_e / Å	Be	Mg	Ca	Sr
Li	1.50	1.53	1.35	1.39
Na	1.51	1.55	1.46	1.50
K	1.20	1.25	1.15	1.18
Rb	1.49	1.55	1.46	1.49

$^4\Sigma^+$ state

Table A.52: Difference between the covalent radii (table A.48) and the equilibrium internuclear separation of the lowest $^4\Sigma^+$ state (table A.10) for the sixteen AK-AKE molecules in the test set.

r_e-r_{cov} / Å	Be	Mg	Ca	Sr
Li	3.27	2.03	1.55	1.36
Na	3.22	2.64	2.32	2.20
K	3.00	2.29	1.94	1.97
Rb	2.87	2.23	2.09	2.00

Table A.53: Difference between the van der Waals radii (table A.49) and the equilibrium internuclear separation of the lowest $^4\Sigma^+$ state (table A.10) for the sixteen AK-AKE molecules in the test set.

r_{vdW}-r_e / Å	Be	Mg	Ca	Sr
Li	-1.41	-0.09	0.15	0.37
Na	-1.36	-0.70	-0.62	-0.47
K	-1.28	-0.49	-0.38	-0.38
Rb	-0.84	-0.12	-0.22	-0.10

A.1.9 Polarizabilities

Table A.54: Mean of the atomic polarizabilities using tabulated values[161].

α_{atom} / a. u.	Be	Mg	Ca	Sr
Li	101	118	167	175
Na	100	117	166	174
K	164	181	230	238
Rb	178	195	244	252

$^2\Sigma^+$ state

Table A.55: Factor between the atomic polarizabilities (table A.54) and the polarizabilities along the internuclear axis of the $^2\Sigma^+$ ground states as determined by finite field calculations for MCSCF+MRCI results (table A.43).

$\alpha_{\|\|}/\alpha_{atom}$ / a. u.	Be	Mg	Ca	Sr
Li	3.62	3.98	3.53	3.73
Na	3.96	3.69	3.48	3.65
K	3.82	3.62	3.78	3.88
Rb	3.54	3.40	3.78	3.85

$^4\Sigma^+$ state

Table A.56: Factor between the atomic polarizabilities (table A.54) and the polarizabilities along the internuclear axis of the lowest $^4\Sigma^+$ state as determined by finite field calculations for MCSCF+MRCI results (table A.46).

$\alpha_{\|\|}/\alpha_{atom}$ / a. u.	Be	Mg	Ca	Sr
Li	2.21	3.59	6.19	7.65
Na	2.29	2.78	4.14	6.88
K	1.83	1.86	4.13	6.39
Rb	2.04	3.30	3.78	5.91

A.1.10 Geometry and energy comparisons: with and without CPPs

$^2\Sigma^+$ state

Table A.57: Differences in the permanent electric dipole moments of the $^2\Sigma^+$ ground state for the sixteen AK-AKE molecules in the test set as determined by MCSCF+MRCI calculations with (table A.2) and without (table A.19) CPPs.

μ_e(no CPP)-μ_e(with CPP) / D	Be	Mg	Ca	Sr
Li	0.000	0.156	0.189	0.220
Na	0.111	0.223	0.435	0.456
K	0.334	0.515	1.167	1.276
Rb	0.447	0.691	1.531	1.655

Table A.58: Difference in the dissociation energies of the $^2\Sigma^+$ state as determined by MCSCF+MRCI calculations with (table A.3) and without (table A.20) CPPs.

D$_e$(no CPP)-D$_e$(with CPP) / cm^{-1}	Be	Mg	Ca	Sr
Li	0	110	270	399
Na	-68	7	70	154
K	-97	-35	-29	67
Rb	-121	-85	-38	9

Table A.59: Difference in equilibrium internuclear separation of the $^2\Sigma^+$ ground state as determined by MCSCF+MRCI calculations with (table A.4) and without (table A.21) CPPs.

r$_e$(no CPP)-r$_e$(with CPP) / Å	Be	Mg	Ca	Sr
Li	0.000	-0.004	-0.003	0.001
Na	0.068	0.082	0.085	0.087
K	0.138	0.168	0.165	0.169
Rb	0.177	0.223	0.209	0.218

$^4\Sigma^+$ state

Table A.60: Differences in the permanent electric dipole moments of the lowest $^4\Sigma^+$ state for the sixteen AK-AKE molecules in the test set as determined by MCSCF+MRCI calculations with (table A.8) and without (table A.25) CPPs.

μ_e(no CPP)-μ_e(with CPP) / D	Be	Mg	Ca	Sr
Li	0.000	0.030	0.152	1.418
Na	-0.056	-0.182	-0.364	-0.276
K	-0.189	-0.507	-0.338	-0.503
Rb	-0.150	-0.466	-0.564	-0.547

Table A.61: Difference in the dissociation energies of the $^4\Sigma^+$ state as determined by MCSCF+MRCI calculations with (table A.9) and without (table A.26) CPPs.

D$_e$(no CPP)-D$_e$(with CPP) / cm^{-1}	Be	Mg	Ca	Sr
Li	0	-7	-1	-72
Na	-2	7	34	33
K	2	24	-28	53
Rb	-2	13	-29	45

Table A.62: Difference in equilibrium internuclear separation of the lowest $^4\Sigma^+$ state as determined by MCSCF+MRCI calculations with (table A.10) and without (table A.27) CPPs.

r$_e$(no CPP)-r$_e$(with CPP) / Å	Be	Mg	Ca	Sr
Li	0.001	0.035	0.020	0.184
Na	0.035	-0.008	-0.061	-0.019
K	0.031	-0.032	0.179	0.045
Rb	0.162	0.040	0.091	0.096

A.1.11 Comparison between internally evaluated MRCI permanent electric dipole moments and finite field results

$^2\Sigma^+$ state

Table A.63: Differences in the permanent electric dipole moments of the $^2\Sigma^+$ ground state for the sixteen AK-AKE molecules in the test set as determined by the MRCI routine (table A.2) and by finite field calculations (table A.42).

μ_e(FF)-μ_e(MRCI) / D	Be	Mg	Ca	Sr
Li	0.007	0.044	0.069	0.110
Na	0.034	-0.011	0.015	0.048
K	-0.011	0.001	-0.047	-0.033
Rb	-0.053	-0.016	-0.087	-0.061

$^4\Sigma^+$ state

Table A.64: Differences in the permanent electric dipole moments of the lowest $^4\Sigma^+$ state for the sixteen AK-AKE molecules in the test set as determined by the MRCI routine (table A.8) and by finite field calculations (table A.45).

μ_e(FF)-μ_e(MRCI) / D	Be	Mg	Ca	Sr
Li	0.008	0.018	0.075	0.097
Na	0.000	0.002	-0.026	0.037
K	0.013	0.071	0.111	0.019
Rb	-0.002	-0.035	0.074	0.049

A.1.12 Vibrationally averaged permanent electric dipole moment

$^2\Sigma^+$ state

Table A.65: Vibrationally averaged permanent electric dipole moment of the $^2\Sigma^+$ ground state for the sixteen AK-AKE molecules in the test set as determined by MCSCF+MRCI calculations.

μ_0 / D	Be	Mg	Ca	Sr
Li	3.377	1.103	1.104	0.169
Na	2.216	0.844	1.153	0.458
K	2.150	1.061	2.146	1.544
Rb	1.953	1.037	2.255	1.695

Table A.66: Change of the permanent electric dipole moment by vibrational averaging. (see table A.2 and table A.65)

$\mu_e - \mu_0$ / D	Be	Mg	Ca	Sr
Li	0.083	0.038	0.019	0.007
Na	0.075	0.022	0.014	0.004
K	0.079	0.020	0.023	0.012
Rb	0.069	0.017	0.021	0.011

$^4\Sigma^+$ state

Table A.67: Vibrationally averaged permanent electric dipole moment of the lowest $^4\Sigma^+$ state for the sixteen AK-AKE molecules in the test set as determined by MCSCF+MRCI calculations.

μ_0 / D	Be	Mg	Ca	Sr
Li	-0.575	-2.421	-4.514	-6.498
Na	-0.422	-0.957	-1.558	-2.007
K	-0.688	-1.606	-2.500	-2.922
Rb	-0.739	-1.585	-2.169	-2.713

Table A.68: Change of the permanent electric dipole moment by vibrational averaging. (see table A.8 and table A.67)

$\mu_e - \mu_0$ / D	Be	Mg	Ca	Sr
Li	-0.046	-0.116	-0.126	-0.205
Na	-0.031	-0.031	-0.034	-0.033
K	-0.045	-0.046	-0.111	-0.087
Rb	-0.050	-0.043	-0.035	0.003

A.1.13 Atomic properties as obtained from literature

Table A.69: The literature values[13] for differences in the lowest excitation energies are listed. These values are depicted in Fig. 1 in the manuscript. For Ba and Ra the lowest ^3P state was used.

ΔE_{ex} / cm^{-1}	Be	Mg	Ca	Sr	Ba	Ra
Li	7076	6987	359	-201	-1821	487
Na	5013	4923	-1705	-2265	-3884	-1577
K	8957	8867	2239	1679	60	2367
Rb	9243	9154	2526	1965	346	2654
Cs	10433	10343	3715	3155	1536	3843
Fr	8618	8529	1901	1341	-279	2029

Table A.70: The literature values[160] for differences in electronegativities are listed. These values are depicted in Fig. 1 in the manuscript.

ΔEN / Pauling	Be	Mg	Ca	Sr	Ba	Ra
Li	0.59	0.33	0.02	-0.03	-0.09	-0.08
Na	0.64	0.38	0.07	0.02	-0.04	-0.03
K	0.75	0.49	0.18	0.13	0.07	0.08
Rb	0.75	0.49	0.18	0.13	0.07	0.08
Cs	0.78	0.52	0.21	0.16	0.1	0.11
Fr	0.87	0.61	0.3	0.25	0.19	0.2

A.2 Isosurface plots of molecular orbitals

Isosurfaces of the first three partly occupied orbitals in the irreducible representation A_1 in the C_{2v} point group are displayed. The natural orbitals were determined by states averaged MCSCF calculations. The sign of the orbital is indicated by colors (red or blue).

A.2.1 1st orbital

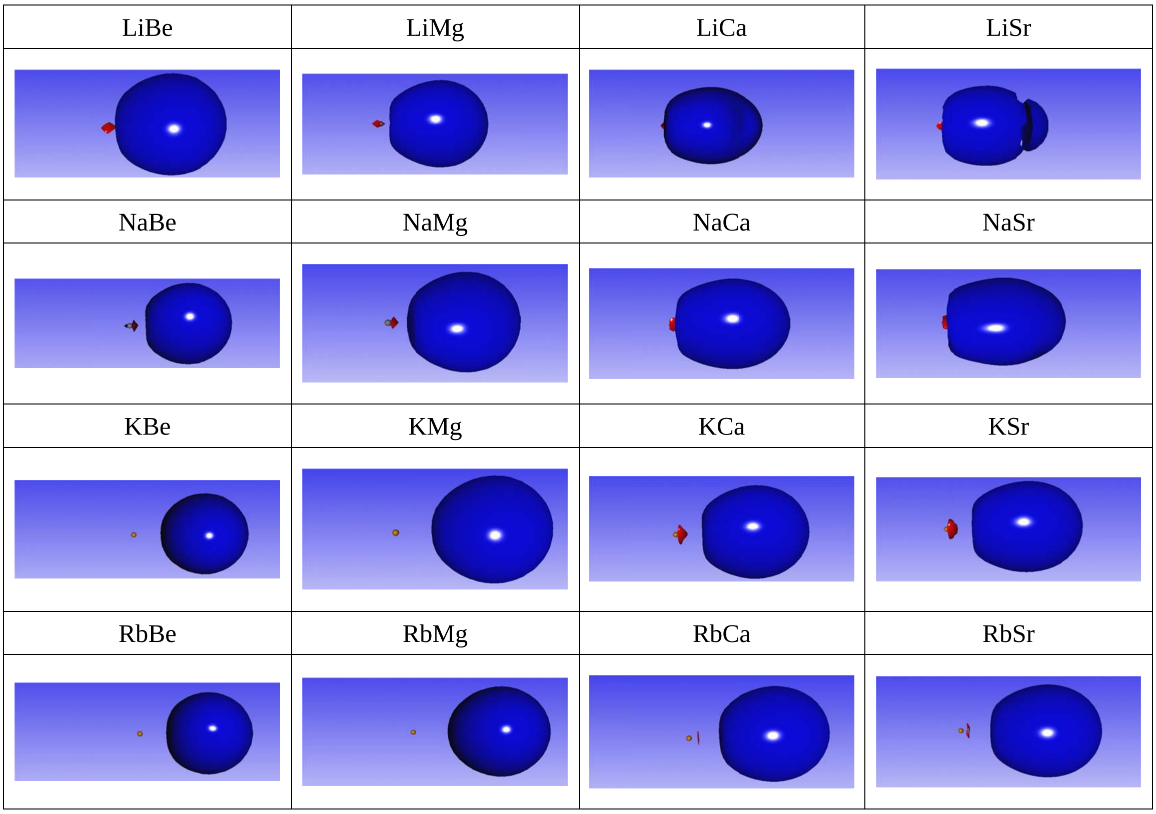

Figure A.1: These plots depict the isosurfaces for the first orbital as denoted in Sec. 3.3 and in Fig. 7 in the manuscript. They are isosurfaces of orbitals determined by a state averaged MCSCF calculation[140].

A.2.2 2nd orbital

LiBe	LiMg	LiCa	LiSr
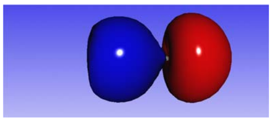	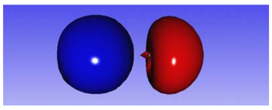	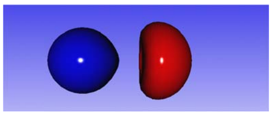	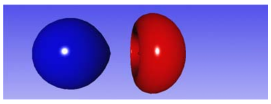
NaBe	NaMg	NaCa	NaSr
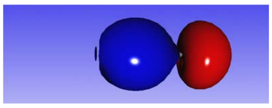	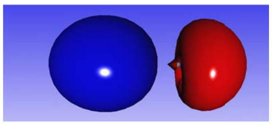	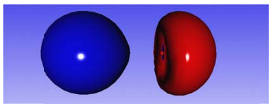	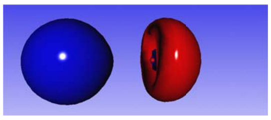
KBe	KMg	KCa	KSr
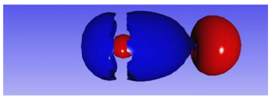	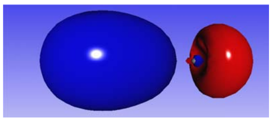	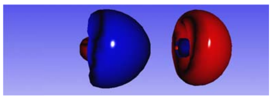	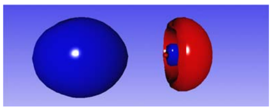
RbBe	RbMg	RbCa	RbSr
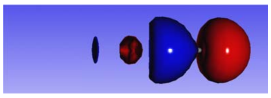	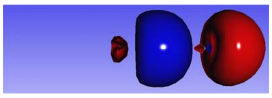	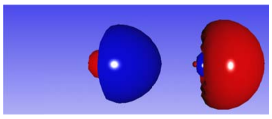	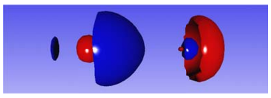

Figure A.2: These plots depict the isosurfaces for the second orbital as denoted in Sec. 3.3 and in Fig. 7 in the manuscript. They are isosurfaces of orbitals determined by a state averaged MCSCF calculation[140].

A.2.3 3^{rd} orbital

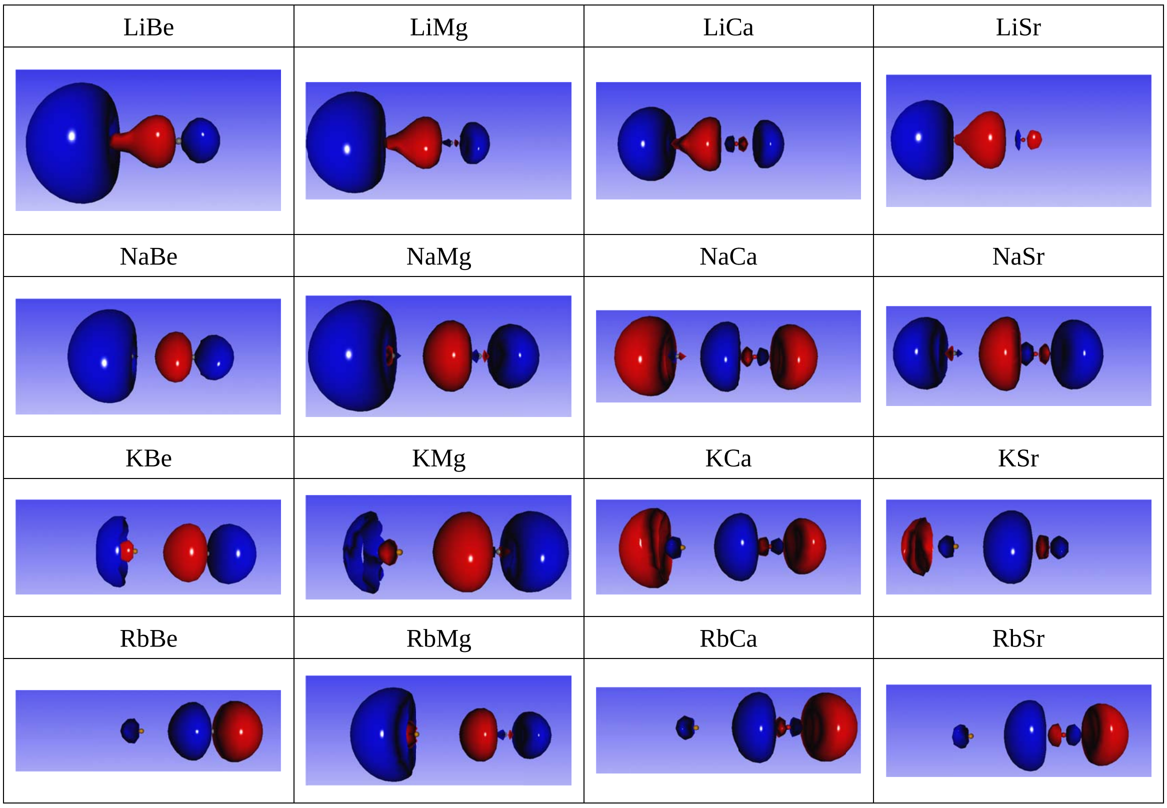

Figure A.3: These plots depict the isosurfaces for the third orbital as denoted in Sec. 3.3 and in Fig. 7 in the manuscript. They are isosurfaces of orbitals determined by a state averaged MCSCF calculation[140].

Appendix B

Models for the permanent electric dipole moment

In chapter 5 we determined the permanent electric dipole moment of several AK-AKE molecules and developed an empirical model for them. This appendix provides additional background information about previous predictive formulas for the permanent electric dipole moment. Several models can be found in the literature, but were mainly used and developed for alkali-halides and similar molecules where a strong charge transfer occurs (the electron of the alkali atom closes the shell of the halides). The chemical bond of these diatomic molecules can be classified as ionic which simplifies the modeling.

B.1 Electronegativity

The difference of the electronegativities of the atoms involved can serve as a first estimate of the direction (sign) and the amplitude of the permanent electric dipole moment:

$$\mu_{12} = c * (EN_1 - EN_2)\,, \tag{B.1}$$

with c being a positive constant. However, this approximation is too crude to give good values for the dipole moment, although attempts have been made to predict the dipole moment based on electronegativities, see e. g. ref. 323.

B.2 Rittner model

The Rittner model was developed early on to estimate the binding energy and dipole moments of alkali halide molecules. It is based on the assumption that the atoms can be approximated by two ions (AK^+, X^-), which are polarized by the field of each other. The dipole moment is then given by the dipole moment of the ionic complex plus the additional induced moments of each atom:

$$\mu_{Ritt} = e \cdot r_e - (\mu_1 + \mu_2)\,, \tag{B.2}$$

with r_e denoting the equilibrium distance between the atoms and μ_n the induced dipole moments of the n^{th} ion.

The induced moments can be calculated via:

$$\mu_1 = \alpha_1 * E_1 = \alpha_1 \left[\frac{e}{r^2} + 2\frac{\mu_2}{r^3}\right],$$
$$\mu_2 = \alpha_2 \left[\frac{e}{r^2} + 2\frac{\mu_1}{r^3}\right], \tag{B.3}$$

where the field acting on the n^{th} ion is given by E_n and α_n is its free ion polarizability. Such polarizabilities and their calculation are discussed in ref. 161.

Solving these coupled equations yields:

$$\mu_1 = \frac{r^4 e\alpha_1 + 2re\alpha_1\alpha_2}{r^6 - 4\alpha_1\alpha_2} \approx \frac{e\alpha_1}{r^2} + \frac{2e\alpha_1\alpha_2}{r^5} + \frac{4e\alpha_1^2\alpha_2}{r^8} + \ldots,$$
$$\mu_2 = \frac{r^4 e\alpha_2 + 2re\alpha_1\alpha_2}{r^6 - 4\alpha_1\alpha_2} \approx \frac{e\alpha_2}{r^2} + \frac{2e\alpha_1\alpha_2}{r^5} + \frac{4e\alpha_1\alpha_2^2}{r^8} + \ldots, \tag{B.4}$$

which results in the following dipole moment:

$$\mu_{Ritt}(r) = e \cdot r_e - \frac{r_e^4 e(\alpha_1 + \alpha_2) + 4r_e e\alpha_1\alpha_2}{r_e^6 - 4\alpha_1\alpha_2} \tag{B.5}$$
$$\approx e \cdot r_e - \frac{e(\alpha_1 + \alpha_2)}{r_e^2} + \frac{4e\alpha_1\alpha_2}{r_e^5}. \tag{B.6}$$

The latter approximation is only valid for $r_e^6 >> 4\alpha_1\alpha_2$.

The electrostatic energy for the two polarizable ions is then given by:

$$\phi_{Ritt}(r) = -\frac{e^2}{r} - \frac{\mu_1 e}{r^2} - \frac{\mu_2 e}{r^2} - \frac{2\mu_1\mu_2}{r^3} + \frac{\mu_1^2}{2\alpha_1} + \frac{\mu_2^2}{2\alpha_2} = \tag{B.7}$$
$$-\frac{e^2}{r} - \frac{e^2(\alpha_1 + \alpha_2)}{2r^4} - \frac{2e^2\alpha_1\alpha_2}{r^7}. \tag{B.8}$$

The second line is obtained using the first two terms in the approximation in equation B.4. By adding a repulsive short range and a van der Waals long range interaction one gets the potential:

$$V_{Ritt}(r) = Ae^{-\frac{r}{\rho}} - \frac{C}{r^6} - \frac{e^2}{r} - \frac{\mu_1 e}{r^2} - \frac{\mu_2 e}{r^2} - \frac{2\mu_1\mu_2}{r^3} + \frac{\mu_1^2}{2\alpha_1} + \frac{\mu_2^2}{2\alpha_2} = \tag{B.9}$$
$$Ae^{-\frac{r}{\rho}} - \frac{C}{r^6} - \frac{e^2}{r} - \frac{e^2(\alpha_1 + \alpha_2)}{2r^4} - \frac{2e^2\alpha_1\alpha_2}{r^7}, \tag{B.10}$$

with parameters A and ρ defining the repulsive behavior and the Van der Waals coefficient C. Note that this model uses the polarizabilities of the singly charged ions (AK^+, X^-).

B.3 T-Rittner model

The truncated Rittner model can be derived from a quantum mechanical treatment[306] and gives the expression:

$$V_{T-Ritt}(r) = Ae^{-\frac{r}{\rho}} - \frac{e^2}{r} - \frac{e^2(\alpha_1 + \alpha_2)}{2r^4} - \frac{C}{r^6}. \tag{B.11}$$

It was shown that the term $\frac{2e^2\alpha_1\alpha_2}{r^7}$ arises from a higher order in perturbation theory. The dipole moment can than be calculated via

$$\mu_{T-Ritt}(r) = er_e - e\frac{\alpha_1 + \alpha_2}{r_e^2}. \tag{B.12}$$

B.4 Electrostatic polarization model

Törring *et al.*[298, 299, 310] developed a model for alkaline earth halides assuming that one electron is completely transferred from the AKE atom to the halide (resulting in AKE$^+$ and X$^-$). The distance between the cores AKE^{++} and X$^-$ is denoted as r, the distance between the center of the AKE^{++} and the valence electron (completing it to AKE$^+$) as Δr. The additional dipole moment is introduced by a shift of charge $\mu = e \cdot \Delta r$. Using this expression, the polarization of the AKE-part can be calculated as follows:

$$\mu_{AKE} = e \cdot \Delta r = \alpha_{AKE}\left(\frac{e}{(r+\Delta r)^2} + \frac{2\mu_X}{(r+\Delta r)^3}\right), \tag{B.13}$$

and the polarization of the halide-part similarly as:

$$\mu_X = \alpha_X\left(\frac{2e}{r^2} - \frac{e}{(r+\Delta r)^2}\right). \tag{B.14}$$

This leads to an equation determining the charge shift

$$\Delta r = \frac{\alpha_{AKE}}{(r+\Delta r)^2} + \frac{4\alpha_{AKE}\alpha_X}{r^2(r+\Delta r)^3} - \frac{2\alpha_{AKE}\alpha_X}{(r+\Delta r)^5} \tag{B.15}$$

which can be solved self-consistently. The electrostatic potential and dipole moment take the following form:

$$\phi_{Toerr}(r) = -\frac{2e^2}{r} + \frac{e^2}{(r+\Delta r)} - \frac{2e\mu_X}{r^2} + \frac{e\mu_X}{(r+\Delta r)^2} + \frac{(\mu_X^2)}{2\alpha_X} + \frac{(\mu_{AKE}^2)}{2\alpha_{AKE}} \tag{B.16}$$

$$= -\frac{2e^2}{r} + \frac{e^2}{(r+\Delta r)} + \frac{(\mu_X^2)}{2\alpha_X} + \frac{(\mu_{AKE}^2)}{2\alpha_{AKE}} \tag{B.17}$$

$$\mu_{Toerr} = e \cdot r_e - \frac{2e\alpha_X}{r_e^2} + \frac{e(\alpha_X + \alpha_{AKE})}{(r_e+\Delta r)^2} - \frac{4e\alpha_X\alpha_{AKE}}{r_e^2(r_e+\Delta r)^3} + \frac{2e\alpha_X\alpha_{AKE}}{(r_e+\Delta r)^5} \tag{B.18}$$

This model was developed to describe the strong polarization of the open shell of the alkaline earth atom, which is not the case in alkali-alkaline earth molecules. In the latter, the multipole expansion of the AKE$^+$ field at the AKE^{++} center is poorly convergent.

Extension to excited states: In ref. 299 this model was extended to calculate excited states of alkaline earth halides. Since excited states can not be assumed to render spherical symmetry, the electrostatic interaction of the point charge with the quadrupole moment is taken into account and the potential becomes

$$V_{ex} = T_{ion} + Ae^{-\frac{r}{\rho}} - \frac{C}{r^6} - \frac{e^2}{r} + \frac{e^2 Q}{2r^3} + \phi_{pol}, \tag{B.19}$$

with T_{ion} being the excitation energy of the free ion and $Q = \int \psi^* r^2 (3cos^2\Theta - 1)\psi dV$ as the quadrupole moment of the unpaired electron. Assuming similar short and long range behavior, the excitation energy can be calculated by:

$$T = T_{ion} + \frac{e^2 Q}{2r^3} - \phi_{pol} + \Phi_{pol}^{ground}. \tag{B.20}$$

μ_{AKE} and μ_X can be calculated as described above and the dipole moment is calculated in the same manner.

B.5 Polarization of AK-AKE molecules

In this section an attempt will be made to apply the above mentioned models to AK-AKE molecules. The previous models assume a significant charge transfer due to the high electronegativity of the halogens. For alkali-alkaline earth molecules, in contrast, no electron is removed from the alkaline earth or the alkali atom. The AK partner is more strongly polarized, since its polarizability is larger. At first, a simple model applying atomic polarizabilities yields:

$$\mu_{pol} = -\left(\mu_1 + \mu_2\right), \tag{B.21}$$

with the induced moments

$$\mu_1 = \alpha_1 \frac{2\mu_2}{r^3} \quad \text{and} \quad \mu_2 = \alpha_2 \frac{2\mu_1}{r^3}.$$

The solution to these coupled equations is, of course, $\mu_1 = \mu_2 = 0$. As expected there is no induced dipole moment if there is no field.

Therefore, we consider a charge shift Δr on the alkali atom due to its higher polarizability:

$$\mu_{AK} = e \cdot \Delta r. \tag{B.22}$$

The polarization of the AKE atom then becomes

$$\mu_{AKE} = \alpha_{AKE} e \left(\frac{1}{r^2} - \frac{1}{(r + \Delta r)^2} \right), \tag{B.23}$$

and the polarization of the AK atom is given by

$$\mu_{AK} = \alpha_{AK} \left(\frac{e}{(r + \Delta r)^2} + \frac{2\mu_{AKE}}{(r + \Delta r)^3} \right). \tag{B.24}$$

From this, we obtain

$$\Delta r = \frac{e\alpha_{AK}}{(r+\Delta r)^2} + \frac{2e\alpha_{AK}\alpha_{AKE}}{(r+\Delta r)^3}\left(\frac{1}{r^2} - \frac{1}{(r+\Delta r)^2}\right), \tag{B.25}$$

where Δr and the dipole moment are determined by the polarizabilities of the neutral atoms.

This model yields dipole moments which increase monotonically with increasing polarizabilities. This simple picture is not sufficient, as the *ab initio* dipole moments in chapter 5 show a different behavior. The simple empirical model for the PEDM presented in chapter 5 yields a better description of the PEDM. The polarizabilities are one ingredient of this model, but electronegativities and dissociation energies are used as well.

B.6 Ligand field calculations

A ligand is an ion, atom, or molecule that binds or interacts with a central atom or molecule. In the case of diatomic ligand field calculations we have a central ion (C^+ / C^{2+}) which is interacting with other atoms or ions (ligands, L^- / L^{2-}). This models deals with compounds where at least one charge is transferred from one atom to another. The basic idea is to calculate the disturbance of the central ion by the surrounding charge distribution (mainly monopole, but higher multipoles might be included). The central ion is split into a closed shell ion core (C^{2+} / C^{3+}) and a single valence electron.

Field *et al.*[300, 309] used this method for alkaline earth halides. A more recent example (LaO) with a short introduction for this method can be found in ref. 308.

B.7 Potential parameters

There are empirical models using atomic or potential parameters for the prediction of dipole moments of diatomic molecules. One recent example is the model by Hou *et al.*[311, 324, 325]. They assumed the following empirical relationship:

$$\frac{q^2}{4\pi\epsilon_0}\frac{1}{R_d^2} = \frac{1}{\hbar^2} m_{red} r_e E_0^2, \tag{B.26}$$

with a s m_{red} the reduced mass of the molecule, $\hbar$ as the Planck constant, r_e as the equilibrium distance of the molecules, E_0 as the zero point energy, q as the effective charge and R_d as an effective radius. The effective charge and the effective radius can be used to calculate the dipole moment via

$$\mu_d = 4.8032\, qR_d, \tag{B.27}$$

where the constant is valid for following units: q needs to be given in e and R_d in Å in order to obtain μ_d in units of Debye. For alkali halide molecules the effective charge q is assumed to be one; a complete transfer of an electrons is assumed. For other molecules this can be adjusted using electronegativity differences. The effective radius can then be calculated from the effective charge and potential parameters via

$$R_d = 3957.6371 \frac{q}{\sqrt{r_e m_{red} \omega_e^2}}. \tag{B.28}$$

This yields following formula for the dipole moment:

$$\mu_d = 19009.3405 \frac{q^2}{\sqrt{r_e m_{red} \omega_e^2}}. \tag{B.29}$$

This last formula has a qualitatively different behavior from the linear formula for point charges: $\mu = q r_e$. However, such a relationship was not found for AK-AKE molecules. Therefore, we applied our home-brewed model in chapter 5.

Appendix C

Excited states of several alkali - alkaline earth molecules

In this appendix the results for the different electronic states obtained with the method presented in chapter 5 are listed. We show The PECs, PEDMs, and TDMs. A small error is present in the results for the PEDM and an even smaller error for the TDMs, see section 5.5 for a more detailed discussion. The values in the tables were determined with mean atomic masses and for potentials ending at 10 Å.

C.1 Molecules

C.1.1 LiBe

LiBe is the molecule consisting of the two lightest atoms. In this calculation core polarization potentials were not applied.

Table C.1: Spectroscopic parameters of several electronic states of LiBe obtained with the approach described in chapter 5.

state	D_e/cm^{-1}	r_e/Å	ω_e/cm^{-1}	$\omega_e x_e$/cm^{-1}	μ_e/D
X $^2\Sigma^+$	2428	2.601	312.9	10.08	3.46
1 $^2\Pi$	12817	2.261	495.7	4.79	4.40
2 $^2\Sigma^+$	7482	2.610	345.5	3.99	-2.33
2 $^2\Pi$	5438	2.977	217.8	2.18	0.10
3 $^2\Sigma^+$	2567	3.516	146.1	2.08	-0.88
1 $^4\Pi$	4974	2.514	361.2	6.56	5.96
1 $^4\Sigma^+$	59	5.521	24.7	2.57	-0.61
4 $^2\Sigma^+$	4954	2.765	369.2	6.88	4.02

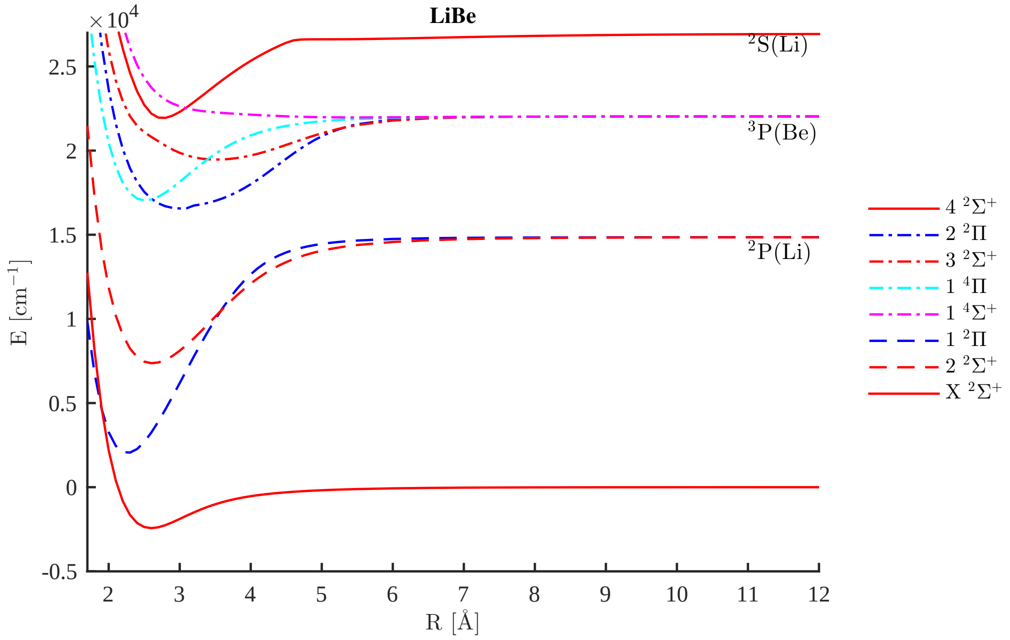

Figure C.1: PEC of LiBe

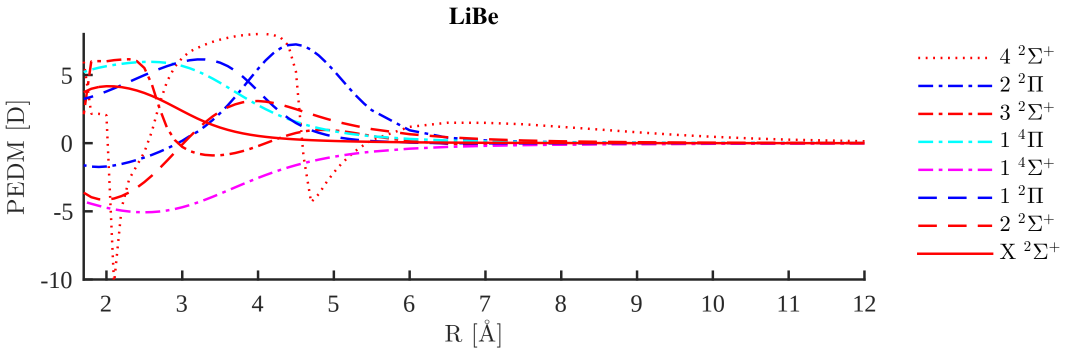

Figure C.2: PEDM of LiBe

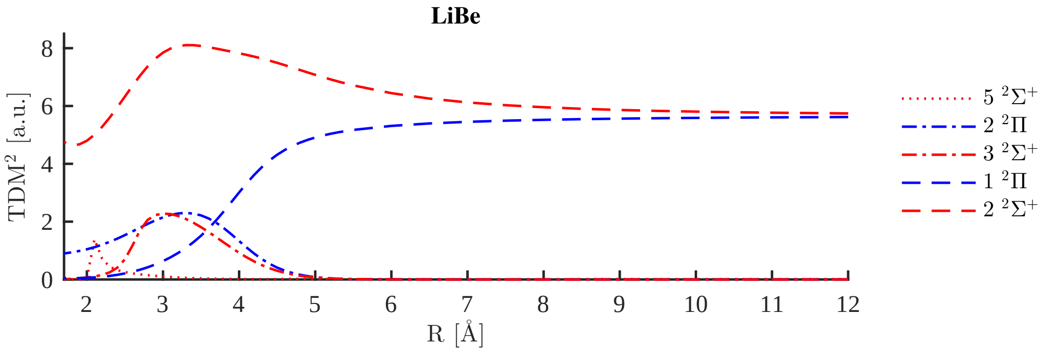

Figure C.3: TDM of LiBe

C.1.2 NaBe

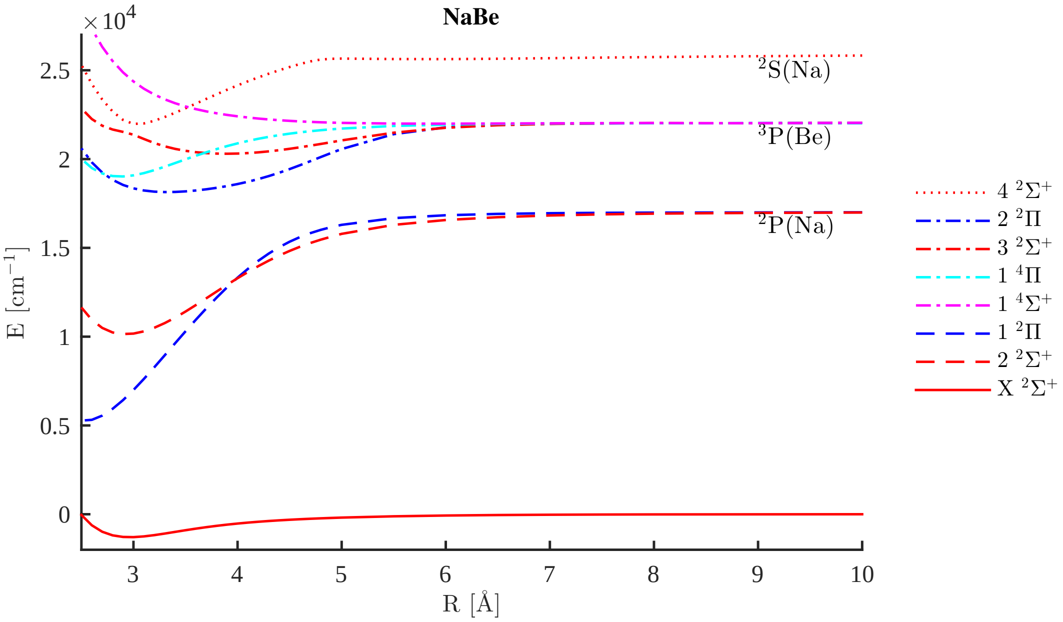

Figure C.4: PEC of NaBe

Table C.2: Spectroscopic parameters of several electronic states of NaBe obtained with the approach described in chapter 5.

state	D_e/cm^{-1}	$r_e/\text{Å}$	$\omega_e/\mathrm{cm}^{-1}$	$\omega_e x_e/\mathrm{cm}^{-1}$	μ_e/D
X $^2\Sigma^+$	1291	2.966	173.0	5.80	2.29
1 $^2\Pi$[a]	11865	2.529	349.8	2.58	6.11
2 $^2\Sigma^+$	6851	2.923	247.9	2.24	0.42
2 $^2\Pi$	3890	3.326	128.1	1.05	-1.22
3 $^2\Sigma^+$	1744	3.891	98.4	1.39	-2.26
1 $^4\Pi$	3010	2.874	221.5	4.07	5.75
1 $^4\Sigma^+$	50	5.837	18.3	1.68	-0.45
4 $^2\Sigma^+$	3831	3.071	277.4	5.02	3.71

[a] … obtained by a slightly modified calculation, points at smaller internuclear separations were required

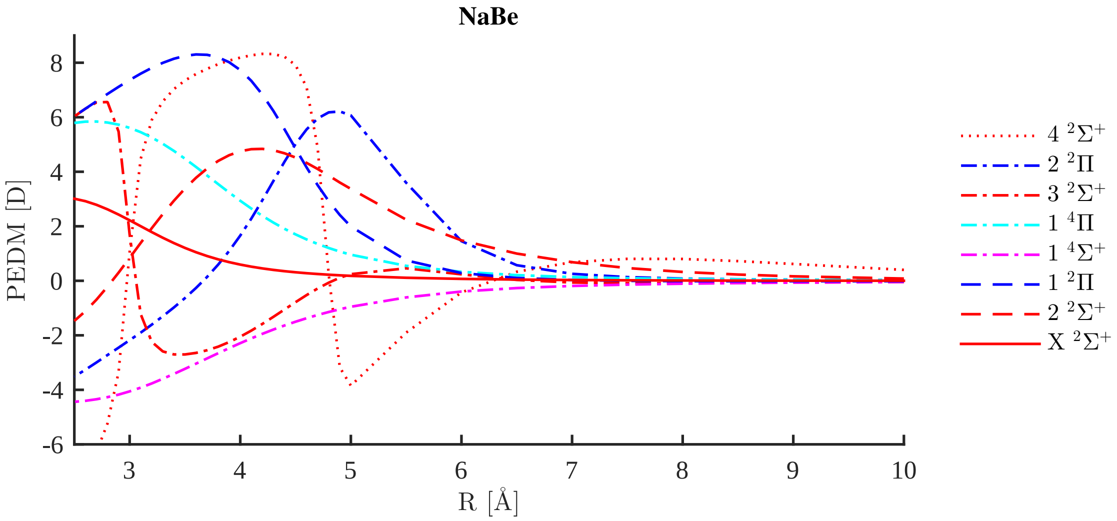

Figure C.5: PEDM of NaBe

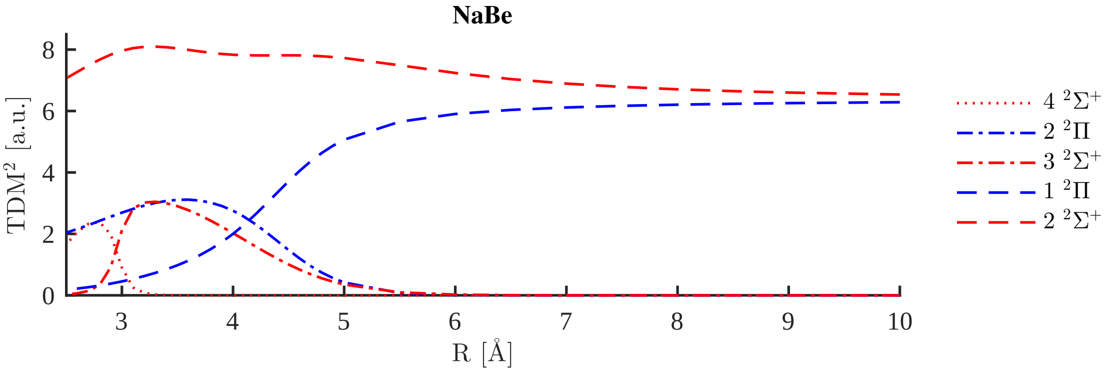

Figure C.6: TDM of NaBe

C.1.3 KBe

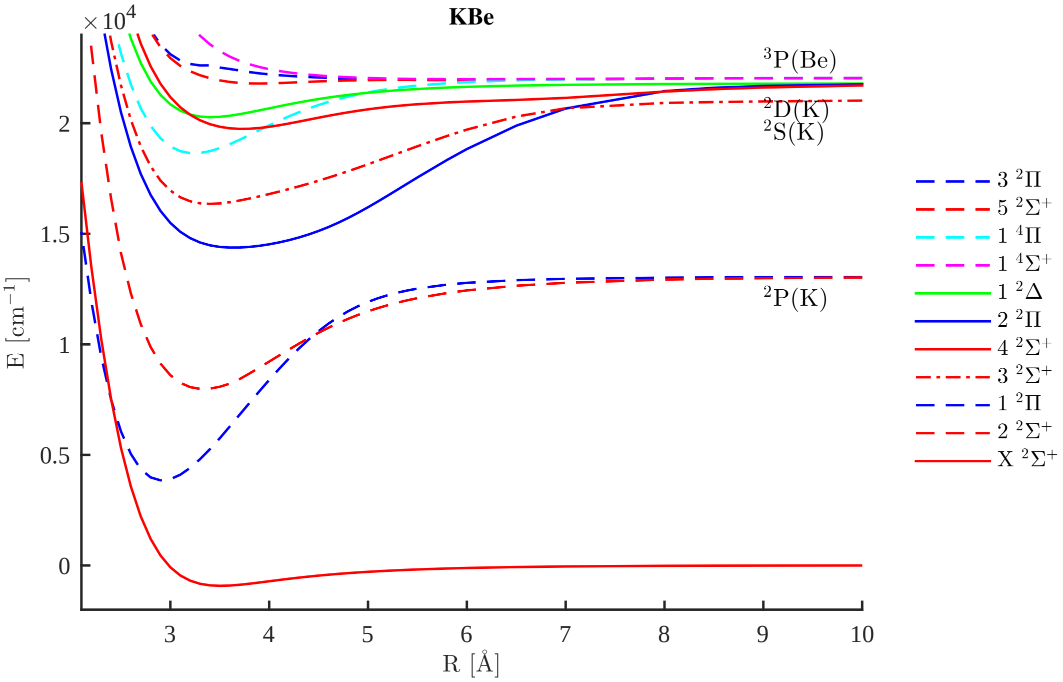

Figure C.7: PEC of KBe

Table C.3: Spectroscopic parameters of several electronic states of KBe obtained with the approach described in chapter 5.

state	D_e/cm^{-1}	$r_e/\mathrm{Å}$	$\omega_e/\mathrm{cm}^{-1}$	$\omega_e x_e/\mathrm{cm}^{-1}$	μ_e/D
X $^2\Sigma^+$	920	3.506	121.7	4.03	2.23
1 $^2\Pi$	9193	2.919	286.8	2.24	8.87
2 $^2\Sigma^+$	5046	3.340	200.7	2.00	3.49
2 $^2\Pi$	7385	3.648	116.4	0.46	-2.50
3 $^2\Sigma^+$	4671	3.398	147.3	1.16	-0.45
1 $^4\Pi$	3398	3.239	199.6	2.93	7.99
1 $^4\Sigma^+$	49	5.960	18.0	1.67	-0.75
4 $^2\Sigma^+$	1963	3.728	119.5	1.82	-3.73
1 $^2\Delta$	1522	3.407	141.6	3.29	-0.47
5 $^2\Sigma^+$	242	3.883	74.5	5.72	-5.08
3 $^2\Pi$	91	5.858	24.2	1.63	-0.29

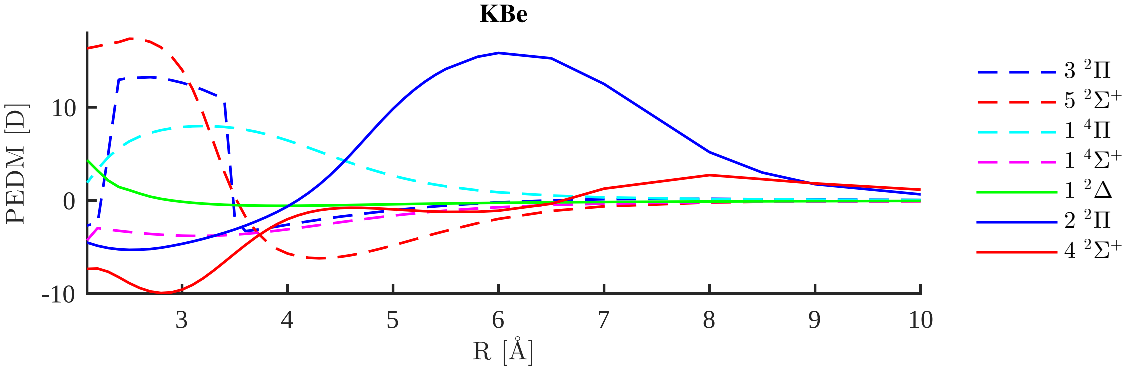

Figure C.8: PEDM of KBe

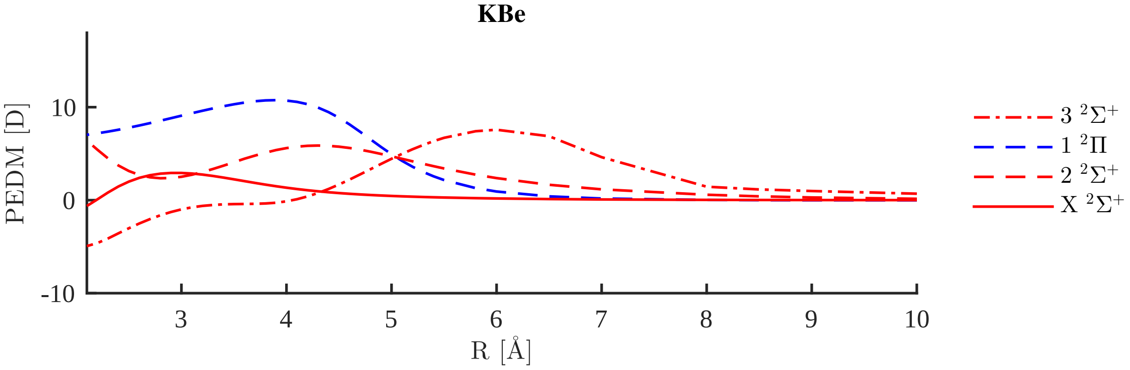

Figure C.9: PEDM of KBe

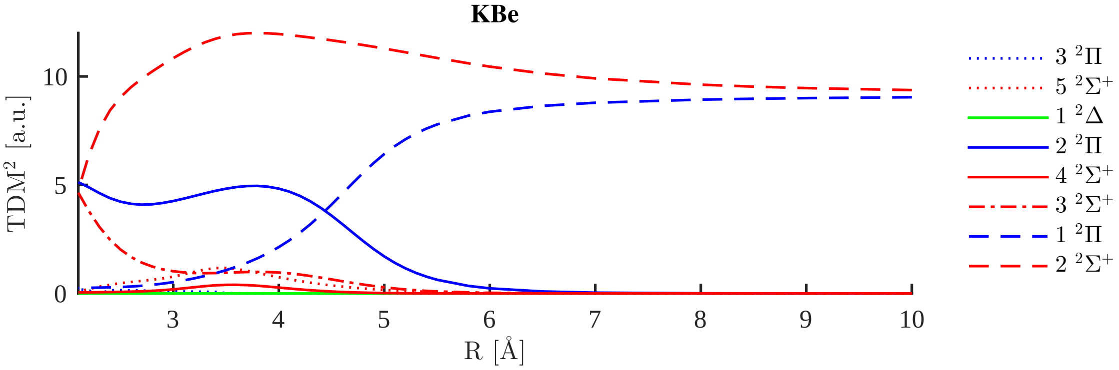

Figure C.10: TDM of KBe

C.1.4 RbBe

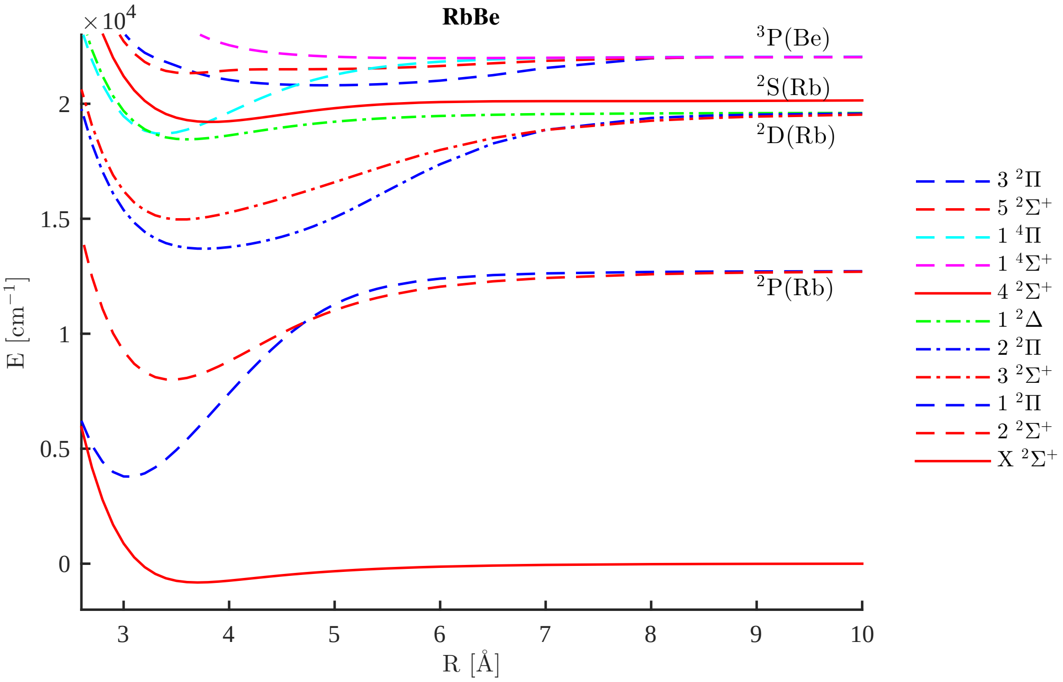

Figure C.11: PEC of RbBe

Table C.4: Spectroscopic parameters of several electronic states of RbBe obtained with the approach described in chapter 5.

state	D_e/cm^{-1}	$r_e/\mathrm{Å}$	$\omega_e/\mathrm{cm}^{-1}$	$\omega_e x_e/\mathrm{cm}^{-1}$	μ_e/D
X $^2\Sigma^+$	816	3.704	104.1	3.32	2.02
1 $^2\Pi$	8946	3.054	262.1	1.92	9.69
2 $^2\Sigma^+$	4695	3.455	184.6	1.82	5.15
2 $^2\Pi$	5878	3.761	108.3	0.50	-3.82
3 $^2\Sigma^+$	4563	3.547	138.2	1.05	-3.11
1 $^4\Pi$	3350	3.367	182.5	2.48	8.40
1 $^4\Sigma^+$	47	5.976	16.4	1.42	-0.82
4 $^2\Sigma^+$	936	3.826	102.4	2.80	-4.69
1 $^2\Delta$	1145	3.600	118.1	3.04	-0.54
5 $^2\Sigma^+$	700	3.618	111.0	4.40	10.52
3 $^2\Pi$	1242	4.915	40.4	0.33	0.77

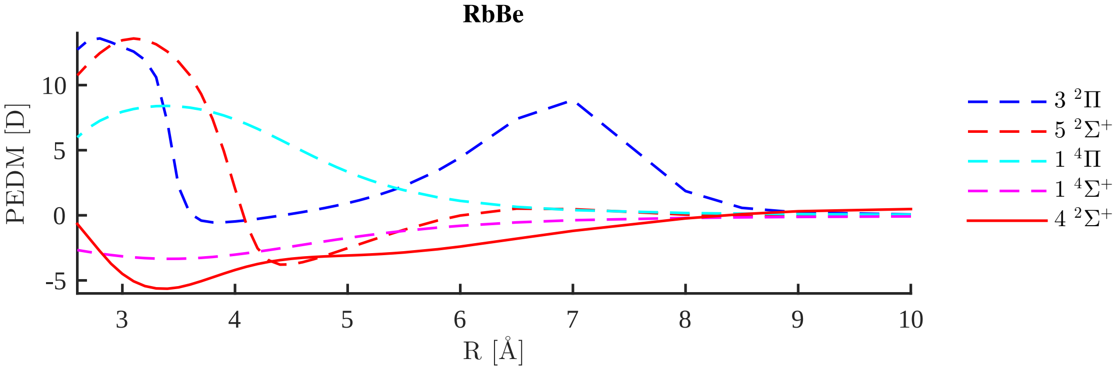

Figure C.12: PEDM of RbBe

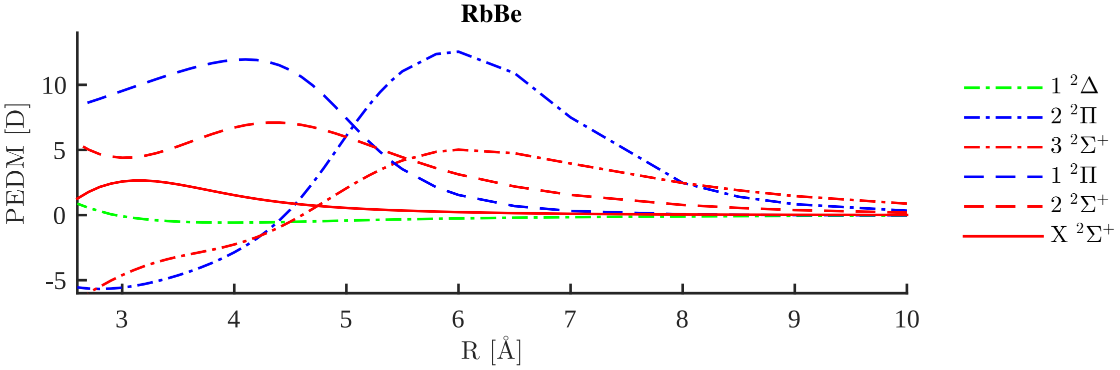

Figure C.13: PEDM of RbBe

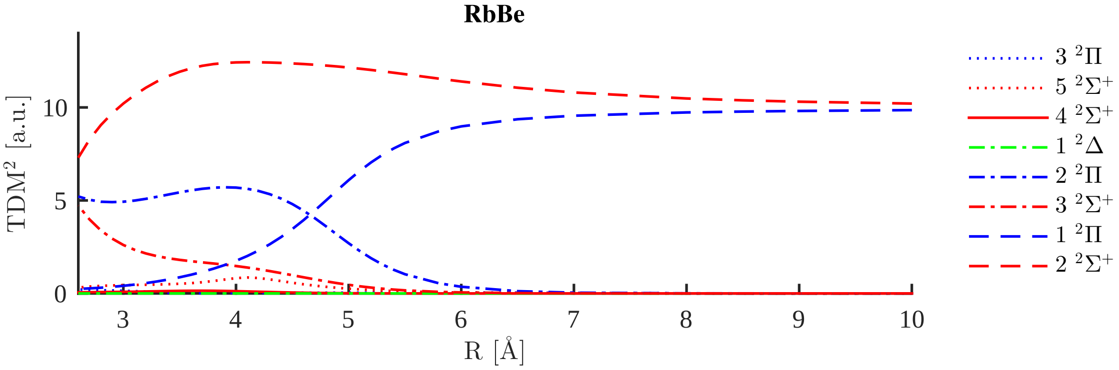

Figure C.14: TDM of RbBe

C.1.5 LiMg

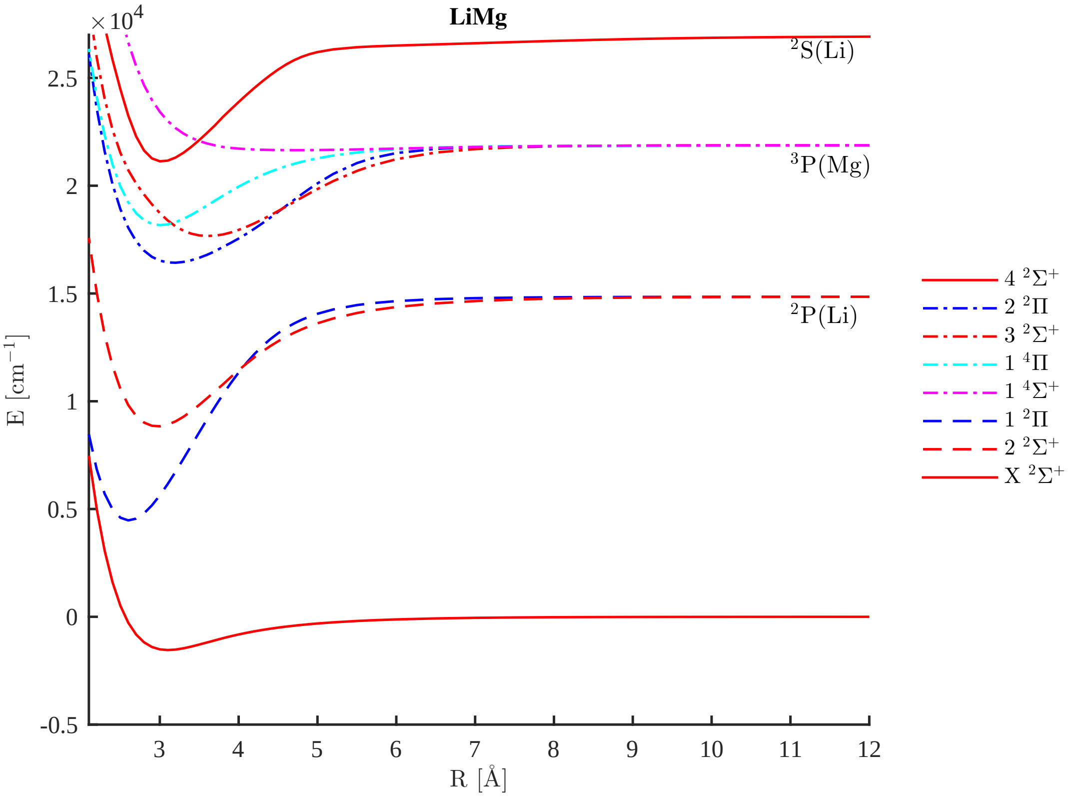

Figure C.15: PEC of LiMg

Table C.5: Spectroscopic parameters of several electronic states of LiMg obtained with the approach described in chapter 5.

state	D_e/cm^{-1}	$r_e/\text{Å}$	$\omega_e/\mathrm{cm}^{-1}$	$\omega_e x_e/\mathrm{cm}^{-1}$	μ_e/D
X $^2\Sigma^+$	1538	3.104	180.6	5.30	1.14
1 $^2\Pi$	10372	2.606	357.0	3.08	2.84
2 $^2\Sigma^+$	5997	2.970	257.7	2.77	-1.29
2 $^2\Pi$	5430	3.175	191.9	1.70	1.86
3 $^2\Sigma^+$	4205	3.612	166.5	1.65	-0.61
1 $^4\Pi$	3678	3.008	233.6	3.71	3.65
1 $^4\Sigma^+$	222	4.715	31.9	1.14	-2.54
4 $^2\Sigma^+$	5733	3.035	300.5	3.94	3.72

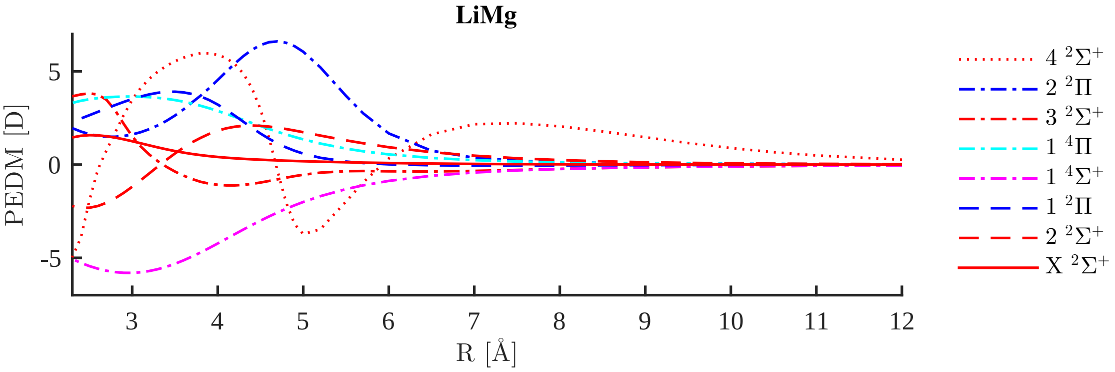

Figure C.16: PEDM of LiMg

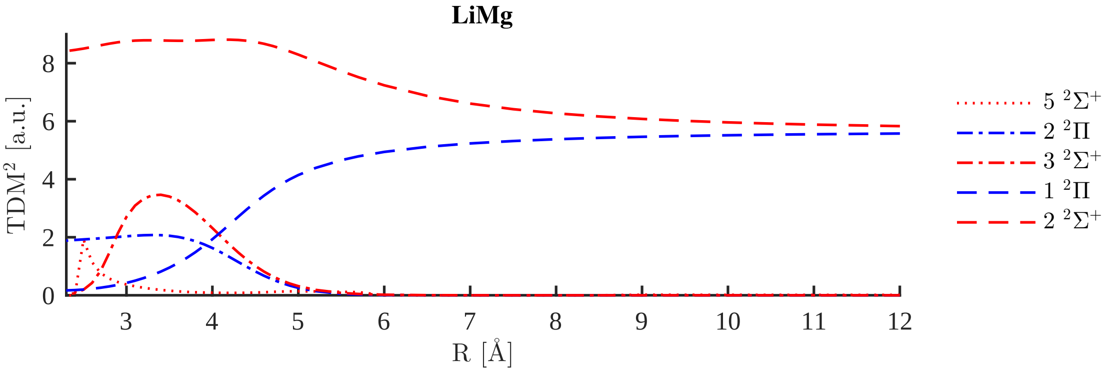

Figure C.17: TDM of LiMg

C.1.6 NaMg

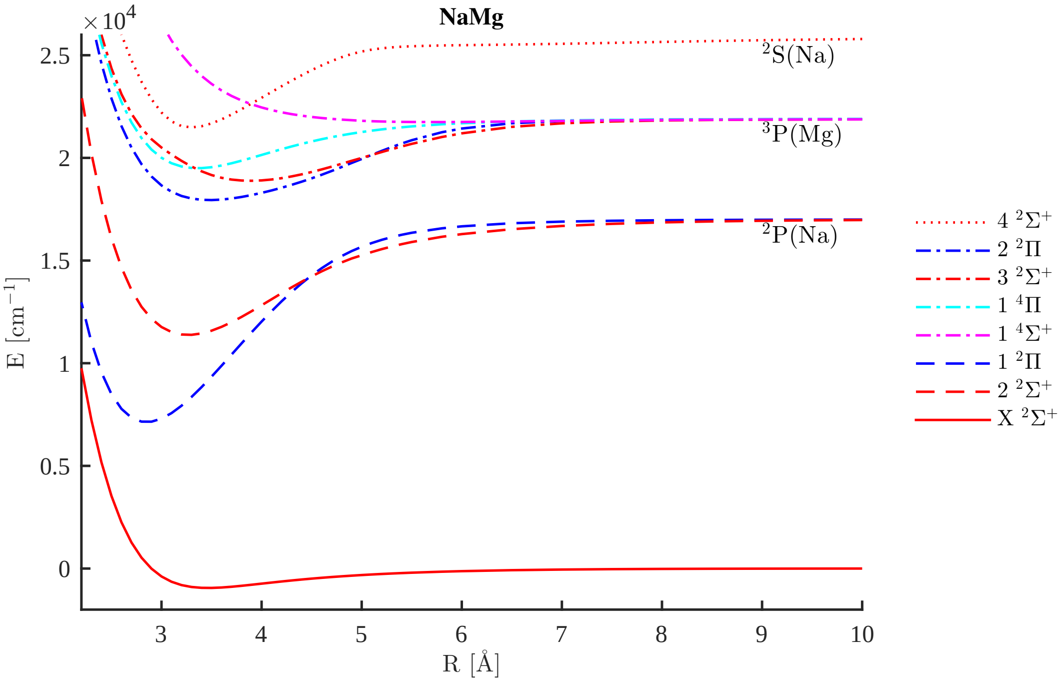

Figure C.18: PEC of NaMg

Table C.6: Spectroscopic parameters of several electronic states of NaMg obtained with the approach described in chapter 5.

state	D_e/cm^{-1}	$r_e/\text{Å}$	ω_e/cm^{-1}	$\omega_e x_e/\text{cm}^{-1}$	μ_e/D
X $^2\Sigma^+$	945	3.465	89.4	2.12	0.87
1 $^2\Pi$	9863	2.850	219.7	1.22	4.68
2 $^2\Sigma^+$	5595	3.266	159.7	1.14	0.63
2 $^2\Pi$	3944	3.484	106.0	0.71	-0.21
3 $^2\Sigma^+$	2990	3.888	93.2	0.73	-1.94
1 $^4\Pi$	2391	3.360	126.3	1.67	3.76
1 $^4\Sigma^+$	131	5.708	20.8	0.82	-0.99
4 $^2\Sigma^+$	4300	3.304	180.6	1.90	2.81
5 $^2\Sigma^+$	5171	3.337	124.4	0.75	-7.00
1 $^2\Delta$	4921	3.040	176.4	1.58	0.62

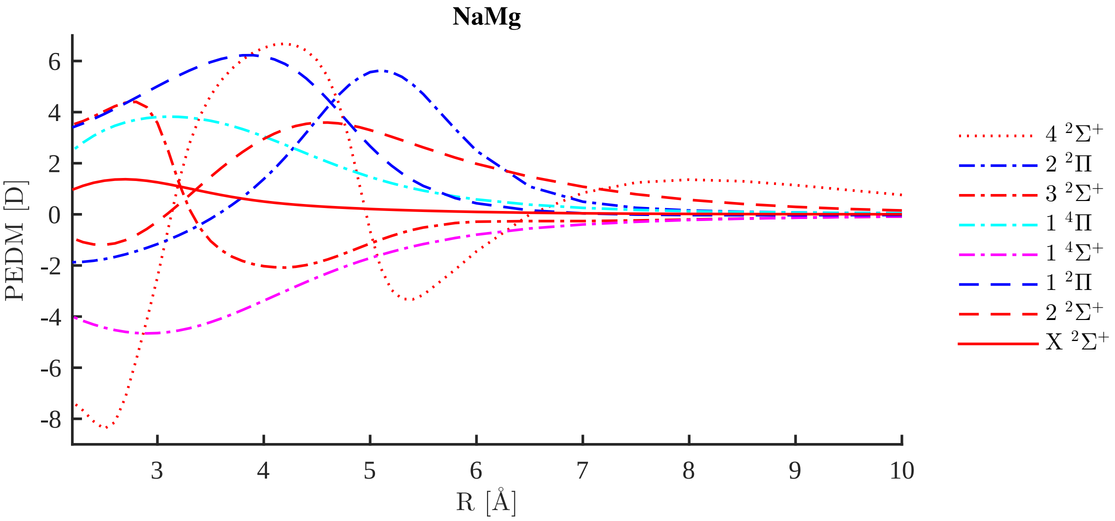

Figure C.19: PEDM of NaMg

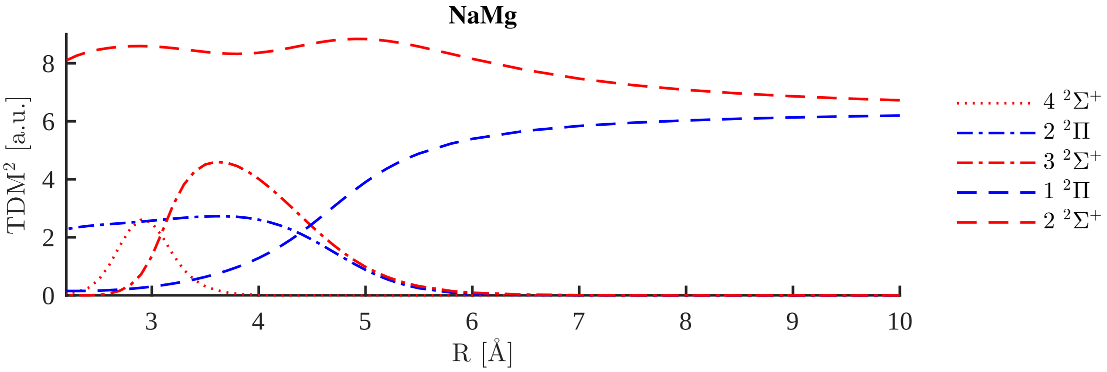

Figure C.20: TDM of NaMg

C.1.7 KMg

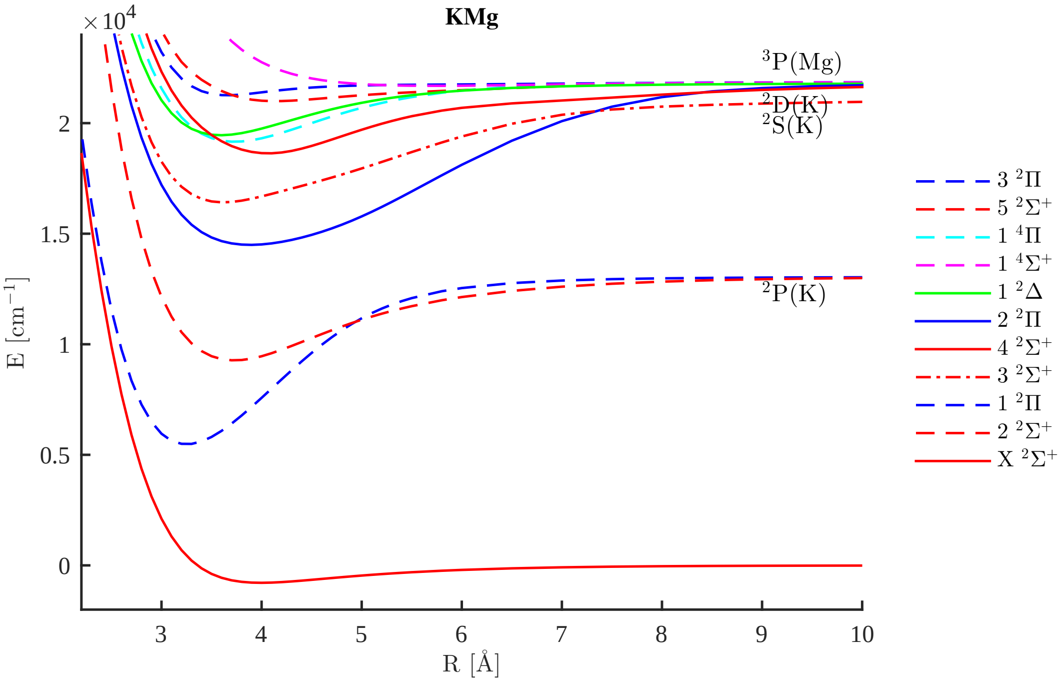

Figure C.21: PEC of KMg

Table C.7: Spectroscopic parameters of several electronic states of KMg obtained with the approach described in chapter 5.

state	D_e/cm^{-1}	$r_e/\mathrm{Å}$	$\omega_e/\mathrm{cm}^{-1}$	$\omega_e x_e/\mathrm{cm}^{-1}$	μ_e/D
X $^2\Sigma^+$	779	3.994	64.3	1.33	1.08
1 $^2\Pi$	7551	3.250	168.7	0.94	7.71
2 $^2\Sigma^+$	3721	3.728	117.1	0.92	3.35
2 $^2\Pi$	7222	3.891	88.2	0.27	-1.86
3 $^2\Sigma^+$	4542	3.615	109.3	0.66	1.41
1 $^4\Pi$	2690	3.730	107.7	1.08	5.92
1 $^4\Sigma^+$	158	5.728	20.0	0.63	-1.66
3 $^2\Pi$	585	3.654	89.3	3.40	5.08
4 $^2\Sigma^+$	2997	4.065	97.7	0.80	-1.72
5 $^2\Sigma^+$	848	4.131	64.7	1.23	-8.60
1 $^2\Delta$	2329	3.591	108.0	1.25	-0.21

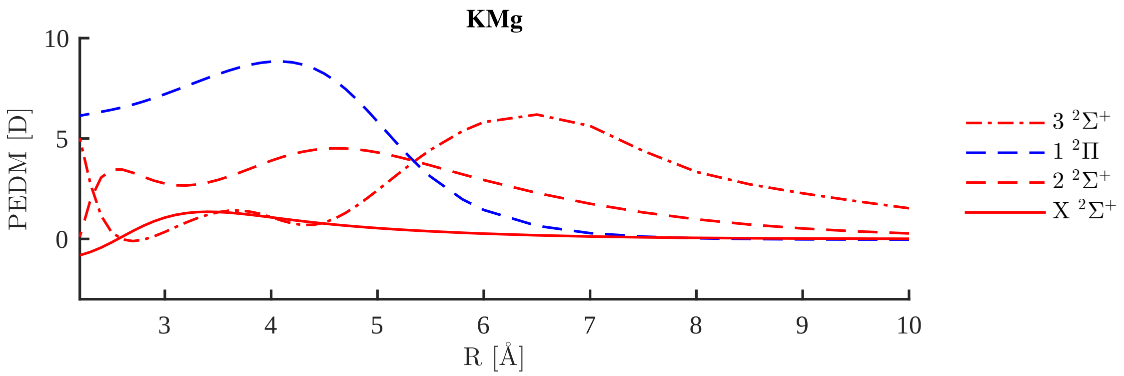

Figure C.22: PEDM of KMg

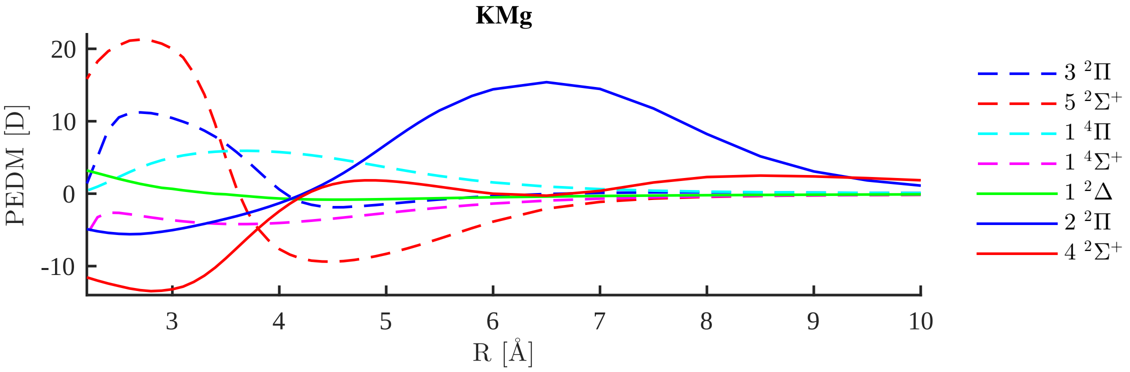

Figure C.23: PEDM of KMg

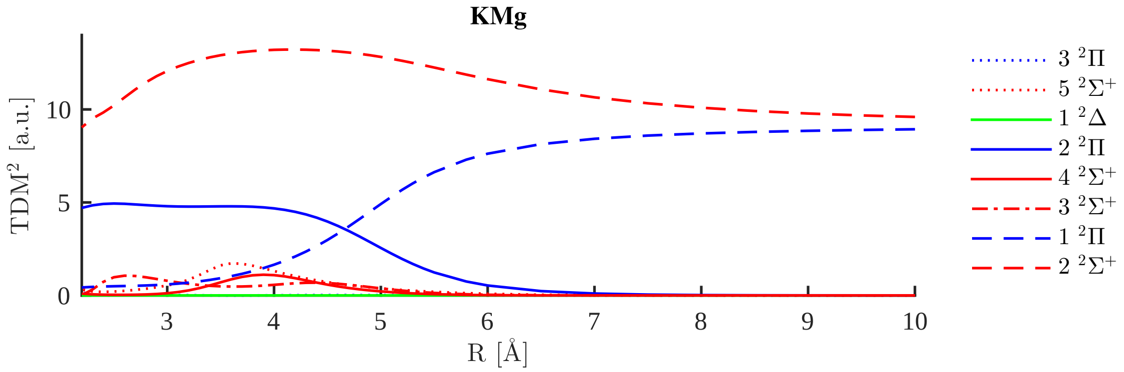

Figure C.24: TDM of KMg

C.1.8 RbMg

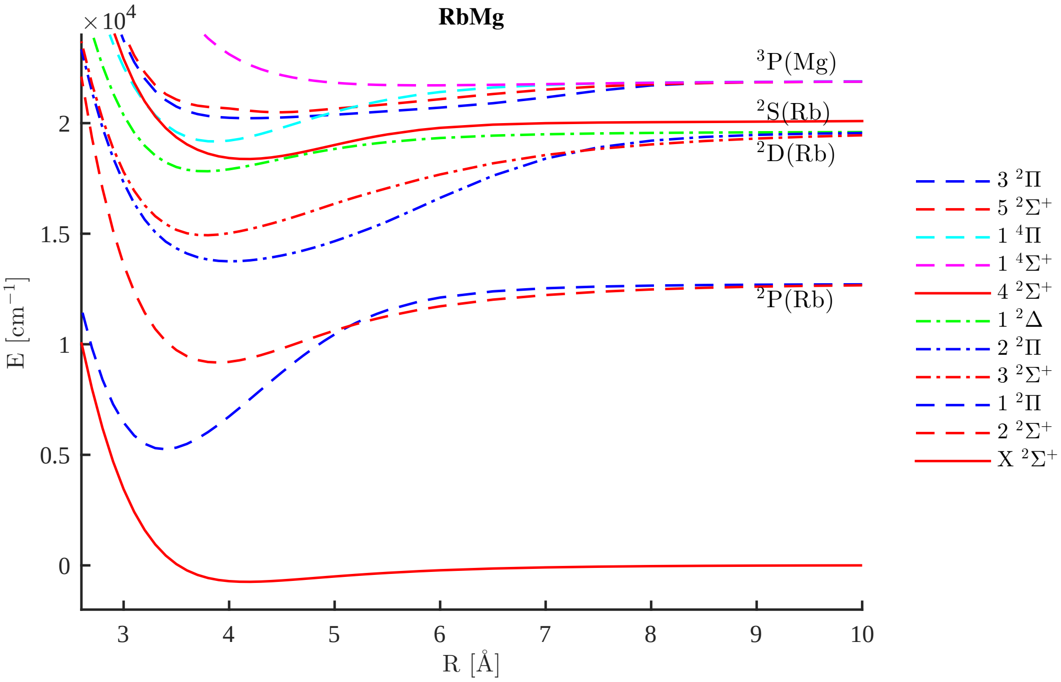

Figure C.25: PEC of RbMg

Table C.8: Spectroscopic parameters of several electronic states of RbMg obtained with the approach described in chapter 5.

state	D_e/cm^{-1}	r_e/Å	$\omega_e/\mathrm{cm}^{-1}$	$\omega_e x_e/\mathrm{cm}^{-1}$	μ_e/D
X $^2\Sigma^+$	744	4.173	54.2	0.99	1.05
1 $^2\Pi$	7455	3.386	147.3	0.73	8.78
2 $^2\Sigma^+$	3492	3.890	98.1	0.69	4.95
2 $^2\Pi$	5804	4.016	73.9	0.24	-3.71
3 $^2\Sigma^+$	4521	3.780	91.8	0.47	-1.49
1 $^4\Pi$	2715	3.862	93.8	0.81	6.32
1 $^4\Sigma^+$	169	5.852	17.6	0.46	-1.62
3 $^2\Pi$	1660	4.191	40.0	0.24	3.00
4 $^2\Sigma^+$	1718	4.165	73.3	0.78	-4.03
5 $^2\Sigma^+$	1382	4.467	52.4	0.50	-6.58
1 $^2\Delta$	1771	3.765	86.4	1.05	-0.49

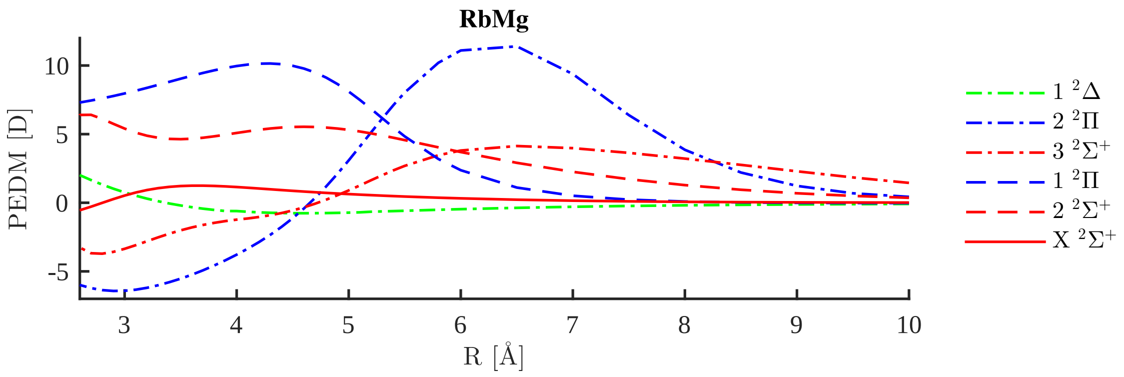

Figure C.26: PEDM of RbMg

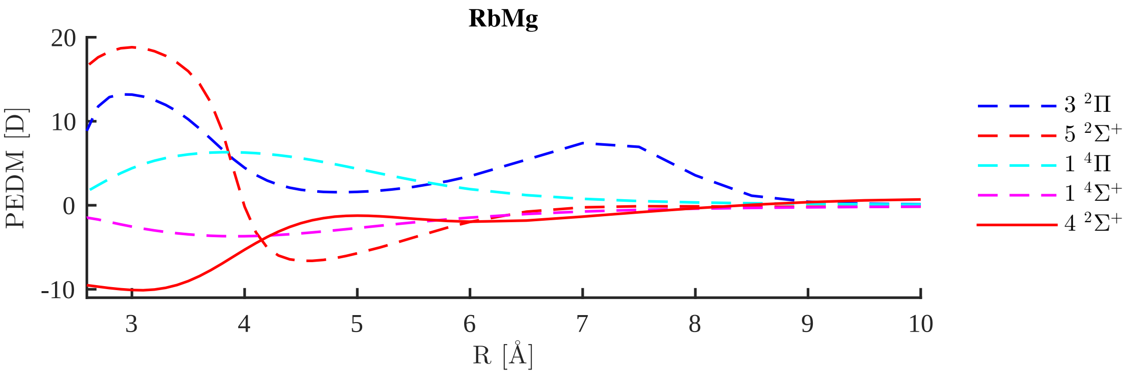

Figure C.27: PEDM of RbMg

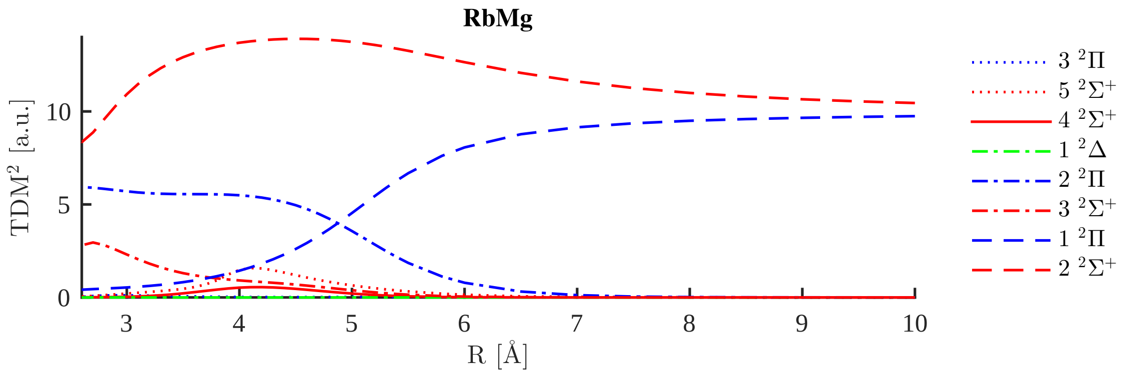

Figure C.28: TDM of RbMg

C.1.9 LiCa

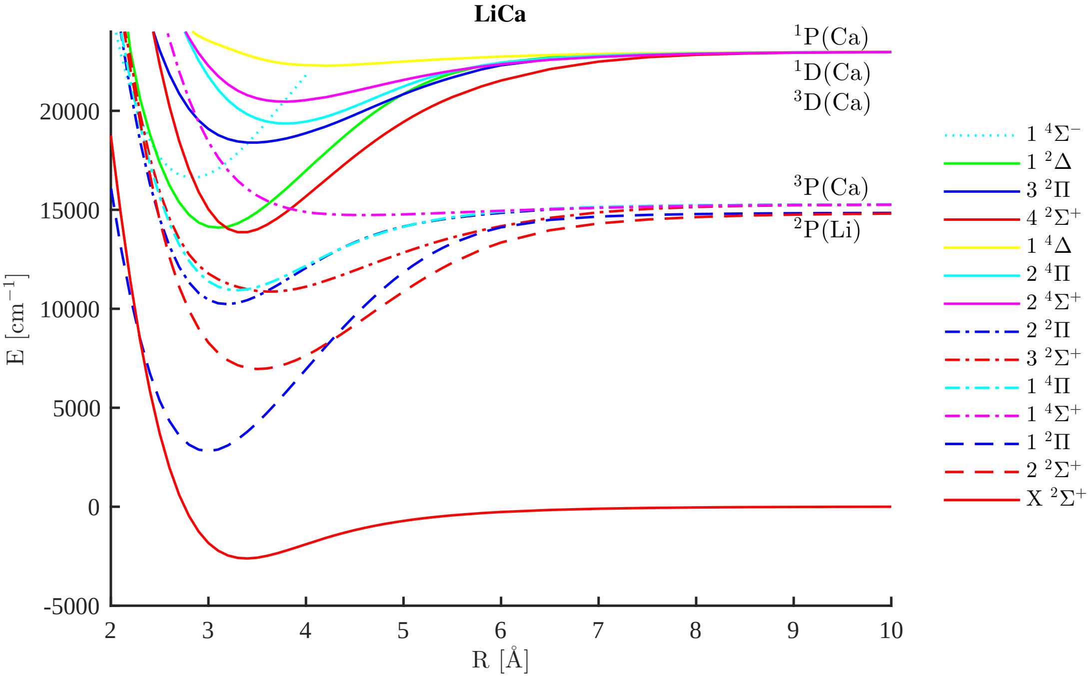

Figure C.29: PEC of LiCa

Table C.9: Spectroscopic parameters of several electronic states of LiCa obtained with the approach described in chapter 5.

state	D_e/cm^{-1}	r_e/Å	ω_e/cm^{-1}	$\omega_e x_e$/cm^{-1}	μ_e/D
X $^2\Sigma^+$	2612	3.388	199.8	3.82	1.12
1 $^2\Pi$	12033	2.994	295.2	1.81	0.59
2 $^2\Sigma^+$	7851	3.514	206.1	3.51	-3.42
2 $^2\Pi$	5035	3.189	246.7	3.02	4.70
3 $^2\Sigma^+$	4388	3.628	151.0	1.30	2.12
1 $^4\Pi$	4331	3.291	220.1	2.80	1.77
1 $^4\Sigma^+$	522	4.581	55.2	1.46	-4.69
4 $^2\Sigma^+$	9108	3.346	288.0	2.28	0.53
1 $^2\Delta$	8892	3.095	267.8	2.02	1.46
3 $^2\Pi$	4578	3.455	163.2	1.45	-4.27
5 $^2\Sigma^+$	4511	3.303	275.8	4.22	5.41
4 $^2\Pi$	3871	3.411	188.7	2.30	-4.83
2 $^4\Sigma^+$	2504	3.774	140.7	1.98	5.50
1 $^4\Delta$	690	4.202	77.0	2.15	2.21
2 $^4\Pi$	3608	3.790	167.7	1.95	4.49

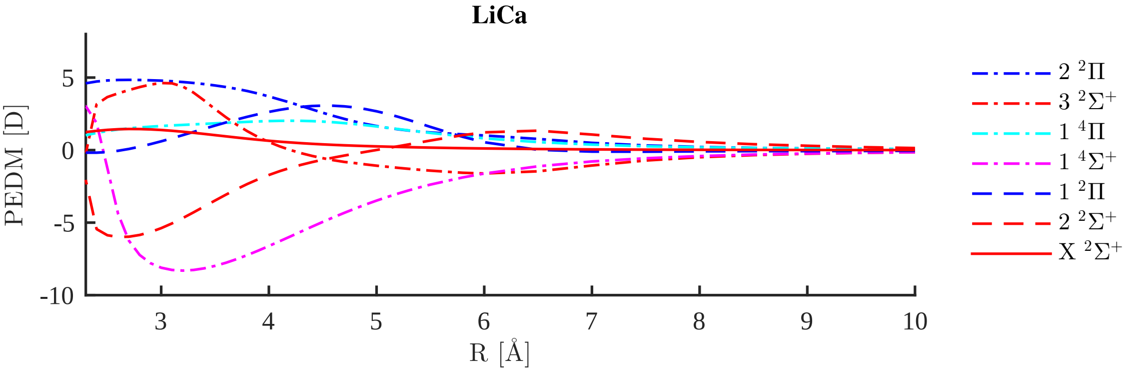

Figure C.30: PEDM of LiCa

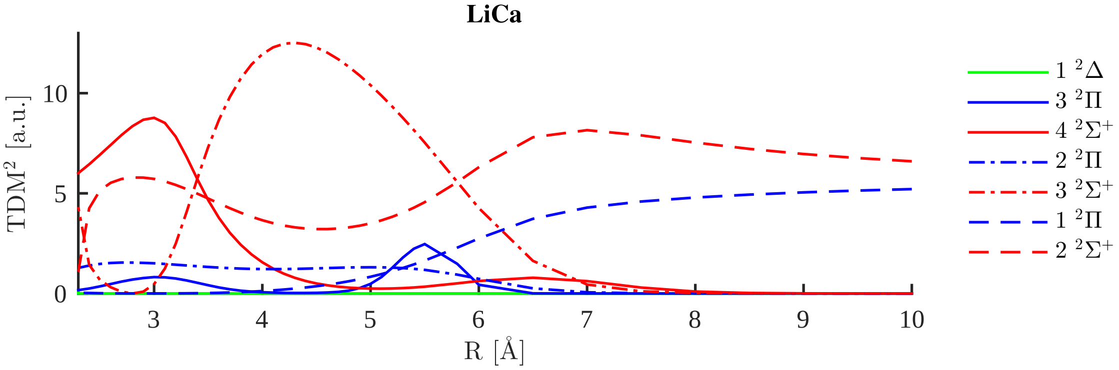

Figure C.31: TDM of LiCa

C.1.10 NaCa

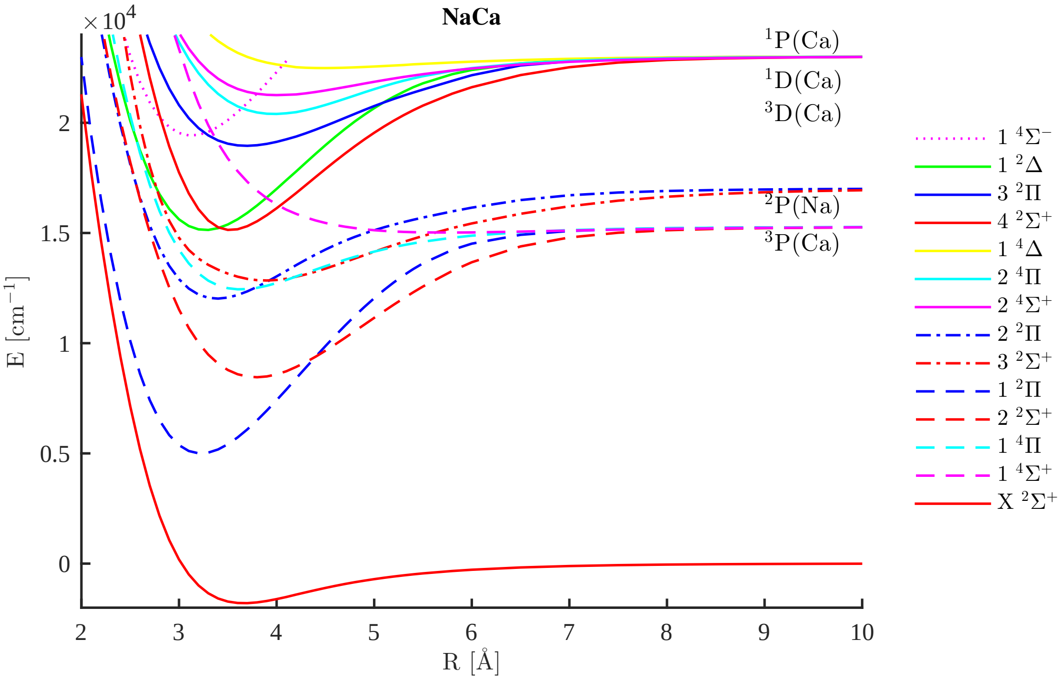

Figure C.32: PEC of NaCa

Table C.10: Spectroscopic parameters of several electronic states of NaCa obtained with the approach described in chapter 5.

state	D_e/cm^{-1}	r_e/Å	ω_e/cm^{-1}	$\omega_e x_e$/cm^{-1}	μ_e/D
X $^2\Sigma^+$	1792	3.665	102.9	1.48	1.17
1 $^2\Pi$	10262	3.224	172.1	0.72	2.28
2 $^2\Sigma^+$	6799	3.795	124.6	0.57	-0.54
2 $^2\Pi$	4977	3.390	141.1	1.00	4.61
3 $^2\Sigma^+$	4092	3.889	92.4	0.52	0.36
1 $^4\Pi$	2819	3.630	113.0	1.13	2.48
1 $^4\Sigma^+$	237	5.733	23.9	0.60	-1.60
4 $^2\Sigma^+$	7904	3.481	179.6	1.02	1.17
1 $^2\Delta$	7864	3.271	160.2	0.82	2.18
3 $^2\Pi$	4041	3.689	103.9	0.67	-4.37
4 $^2\Pi$	3041	3.728	94.9	0.74	-3.86
1 $^4\Delta$	1136	4.098	57.4	0.73	3.36

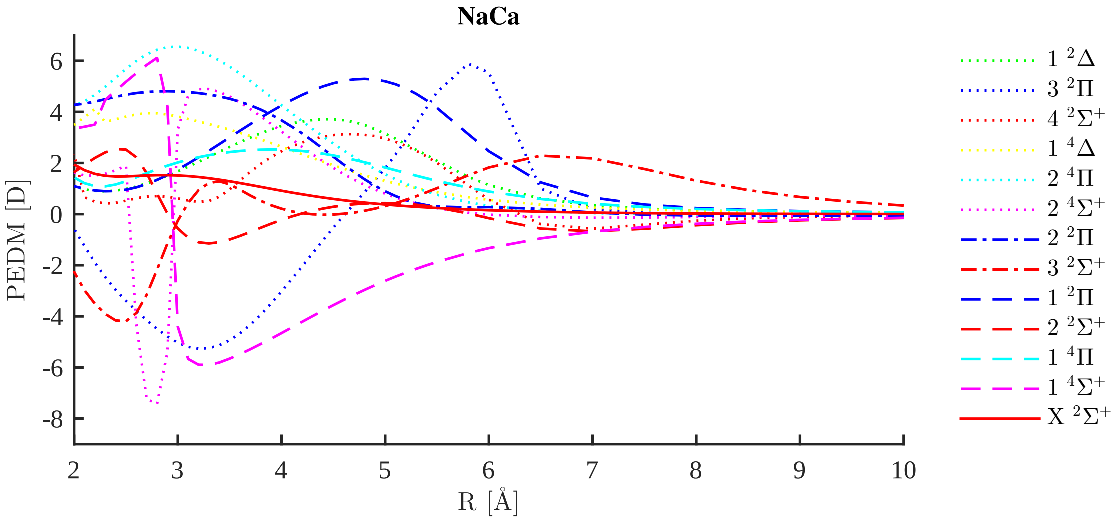

Figure C.33: PEDM of NaCa

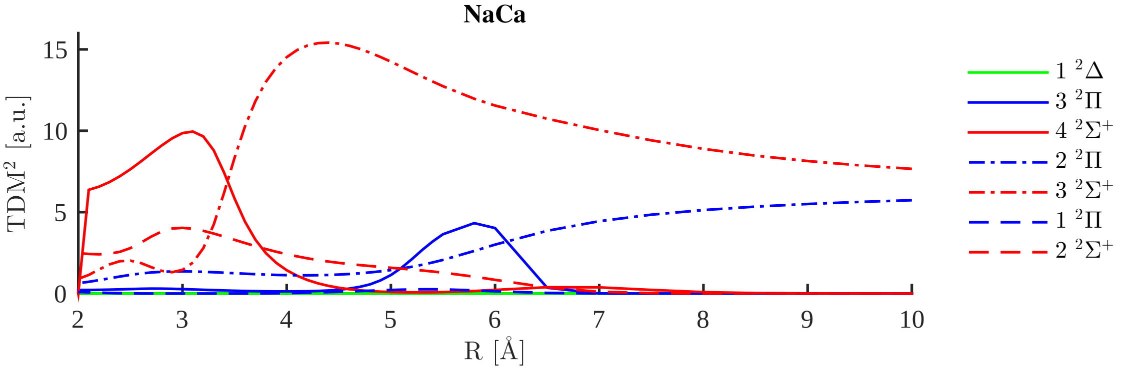

Figure C.34: TDM of NaCa

C.1.11 KCa

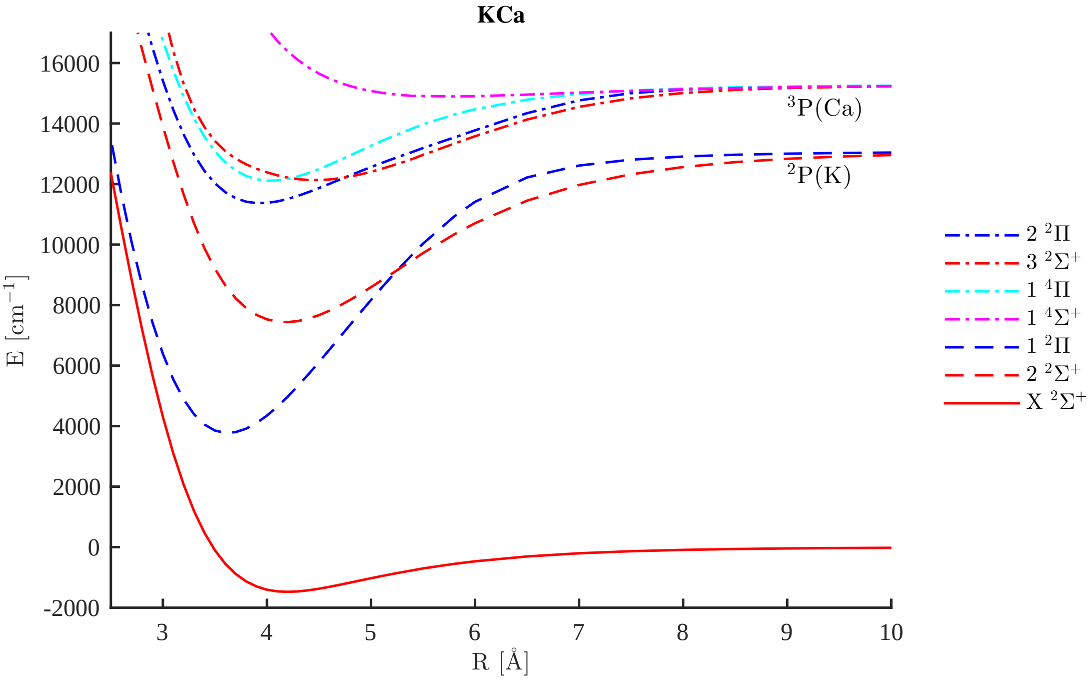

Figure C.35: PEC of KCa

Table C.11: Spectroscopic parameters of several electronic states of KCa obtained with the approach described in chapter 5.

state	D_e/cm^{-1}	r_e/Å	ω_e/cm^{-1}	$\omega_e x_e$/cm^{-1}	μ_e/D
X $^2\Sigma^+$	1455	4.196	71.3	0.87	2.17
1 $^2\Pi$	9267	3.622	129.7	0.45	5.78
2 $^2\Sigma^+$	5523	4.178	95.0	0.41	1.04
2 $^2\Pi$	3876	3.937	91.2	0.54	6.09
3 $^2\Sigma^+$	3099	4.461	61.3	0.30	2.91
1 $^4\Pi$	3135	4.037	90.7	0.66	4.91
1 $^4\Sigma^+$	343	5.727	25.6	0.48	-2.61

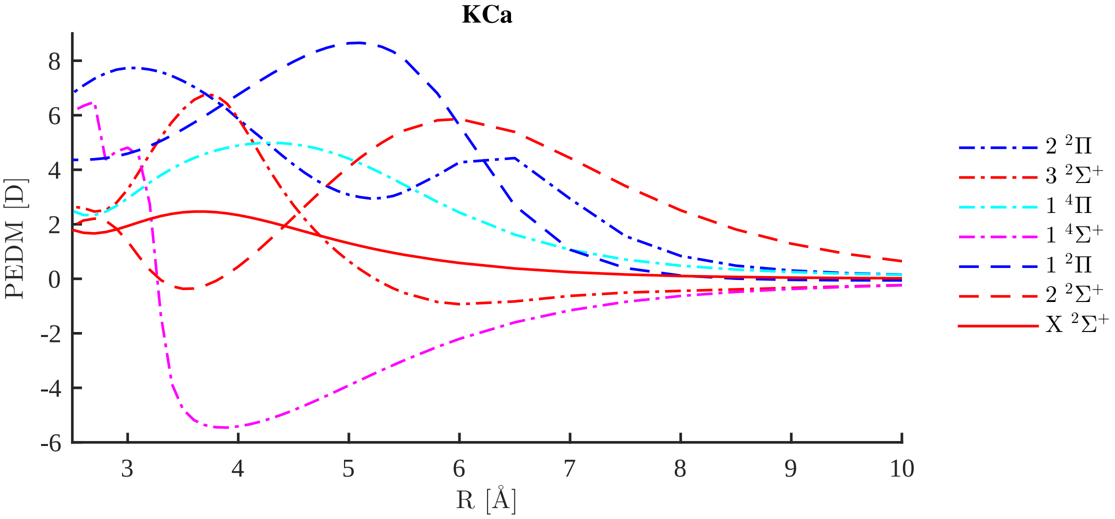

Figure C.36: PEDM of KCa

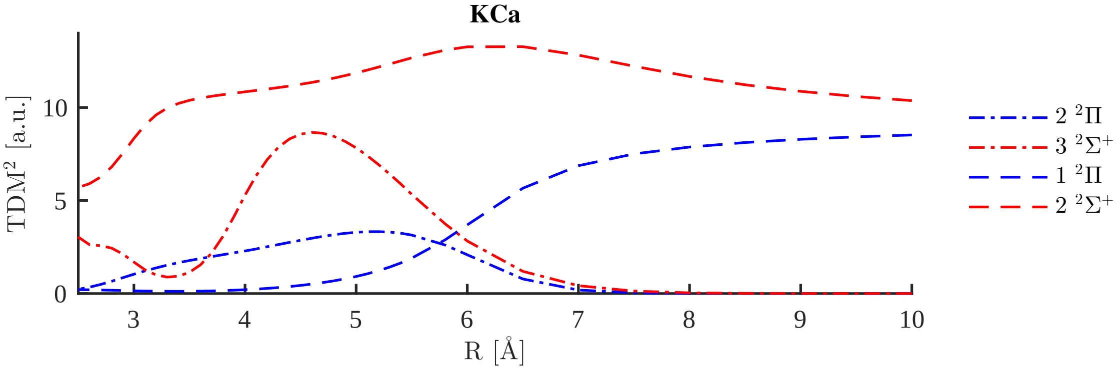

Figure C.37: TDM of KCa

C.1.12 RbCa

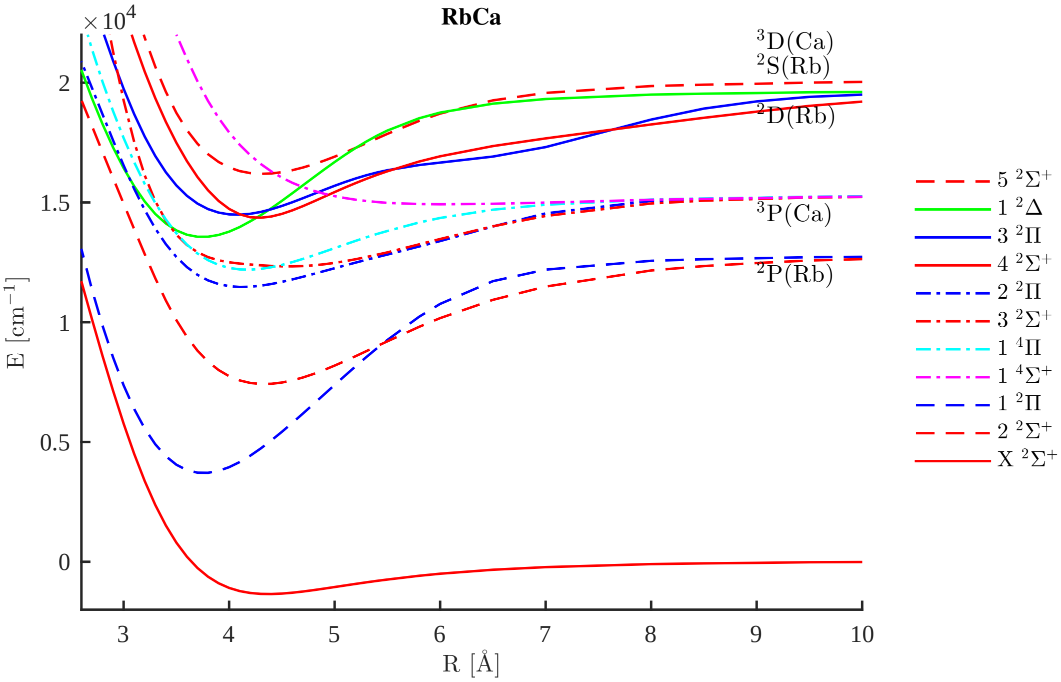

Figure C.38: PEC of RbCa

Table C.12: Spectroscopic parameters of several electronic states of RbCa obtained with the approach described in chapter 5.

state	D_e/cm^{-1}	$r_e/\text{Å}$	$\omega_e/\mathrm{cm}^{-1}$	$\omega_e x_e/\mathrm{cm}^{-1}$	μ_e/D
X $^2\Sigma^+$	1337	4.369	57.0	0.61	2.28
1 $^2\Pi$	9024	3.755	106.6	0.31	6.92
2 $^2\Sigma^+$	5216	4.332	78.2	0.29	2.40
2 $^2\Pi$	3776	4.126	70.6	0.33	5.96
3 $^2\Sigma^+$	2897	4.524	40.1	0.14	4.68
1 $^4\Pi$	3054	4.172	74.8	0.46	5.48
1 $^4\Sigma^+$	315	6.051	19.2	0.29	-2.21
4 $^2\Sigma^+$	4844	4.281	95.5	0.47	-3.72
1 $^2\Delta$	6052	3.748	98.8	0.40	5.49
3 $^2\Pi$	5013	4.074	80.5	0.32	-4.68
5 $^2\Sigma^+$	3838	4.314	74.3	0.36	0.98

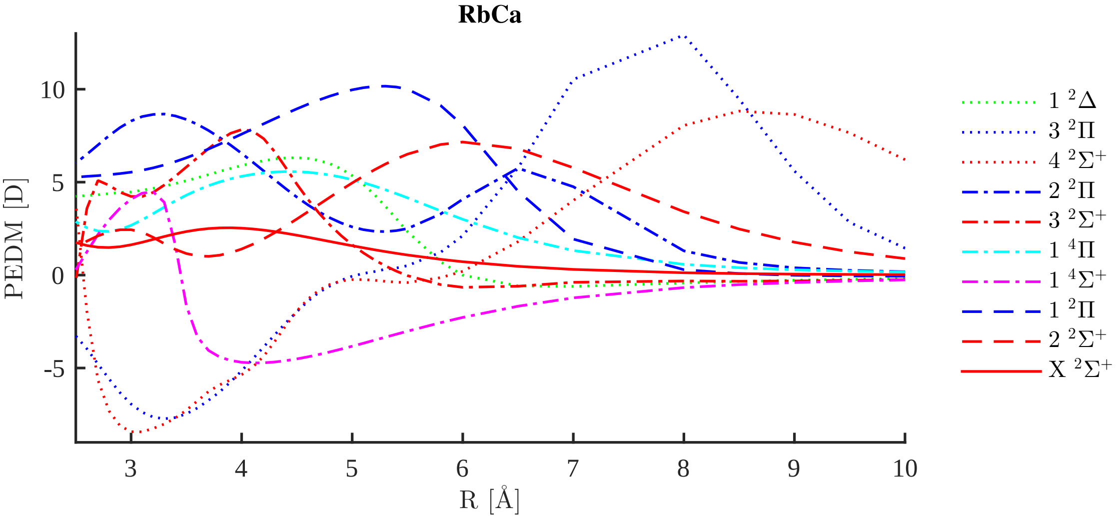

Figure C.39: PEDM of RbCa

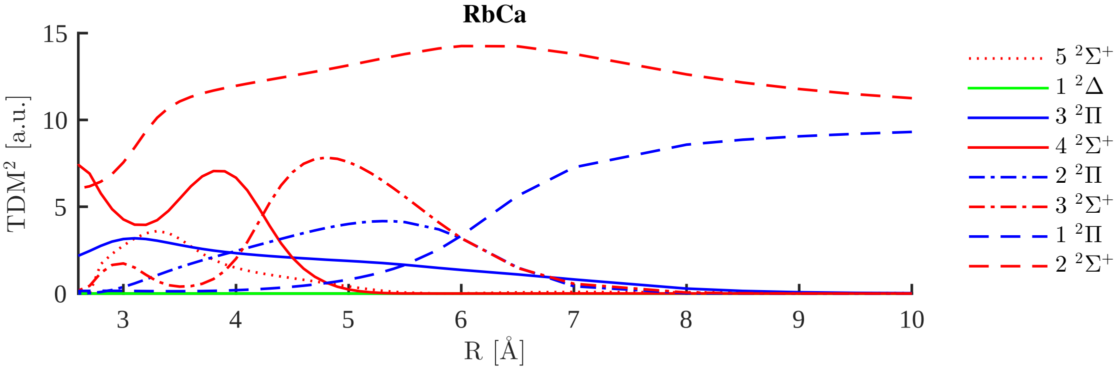

Figure C.40: TDM of RbCa

C.1.13 LiSr

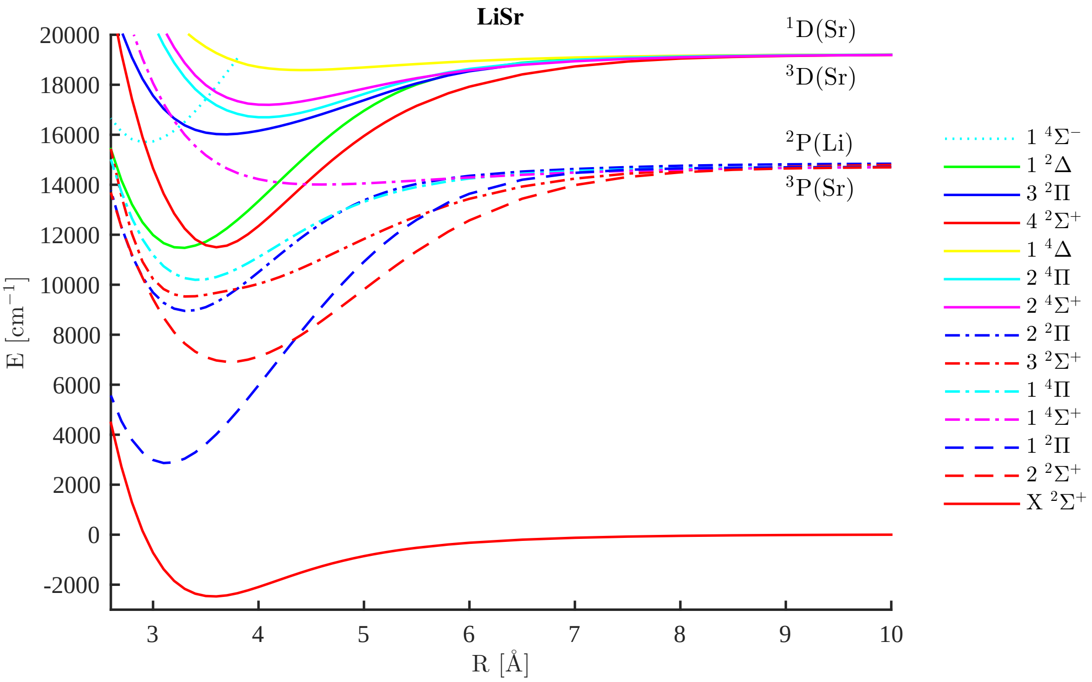

Figure C.41: PEC of LiSr

Table C.13: Spectroscopic parameters of several electronic states of LiSr obtained with the approach described in chapter 5.

state	D_e/cm^{-1}	r_e/Å	$\omega_e/\mathrm{cm}^{-1}$	$\omega_e x_e/\mathrm{cm}^{-1}$	μ_e/D
X $^2\Sigma^+$	2471	3.572	180.7	3.31	0.18
1 $^2\Pi$	11850	3.132	269.6	1.53	-0.87
2 $^2\Sigma^+$	7783	3.728	183.8	1.09	-3.77
2 $^2\Pi$	5889	3.324	240.5	2.46	5.26
3 $^2\Sigma^+$	5258	3.345	180.4	1.55	3.78
1 $^4\Pi$	4517	3.425	207.1	2.37	-0.08
1 $^4\Sigma^+$	692	4.590	61.4	1.36	-6.70
4 $^2\Sigma^+$	7669	3.606	258.7	2.18	0.71
1 $^2\Delta$	7731	3.275	243.4	1.92	0.65
3 $^2\Pi$	3185	3.680	138.0	1.49	-4.90
2 $^4\Sigma^+$	1997	4.068	129.5	2.10	6.31
1 $^4\Delta$	618	4.416	72.6	2.13	1.98
2 $^4\Pi$	2505	4.053	138.7	1.92	6.01

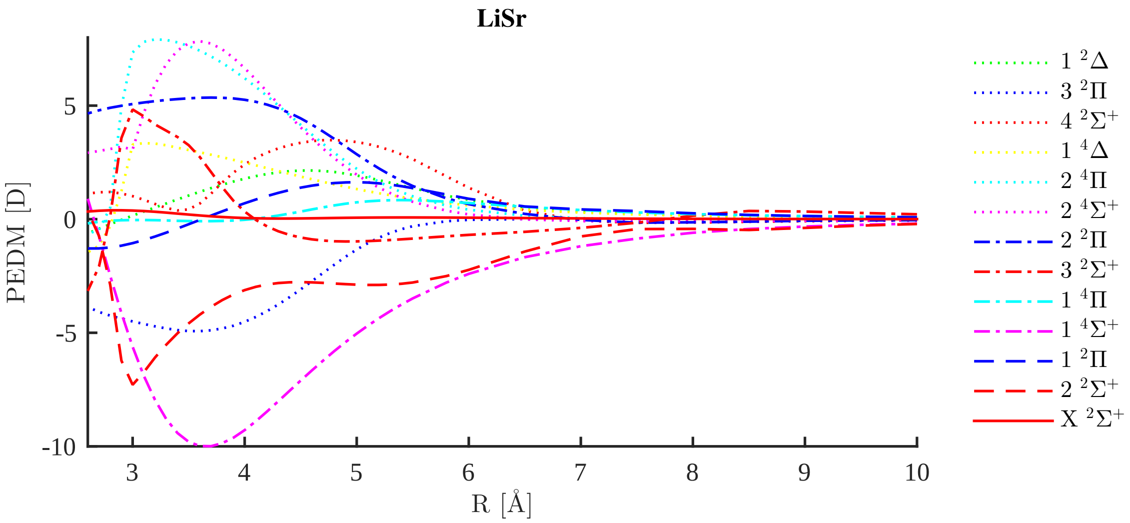

Figure C.42: PEDM of LiSr

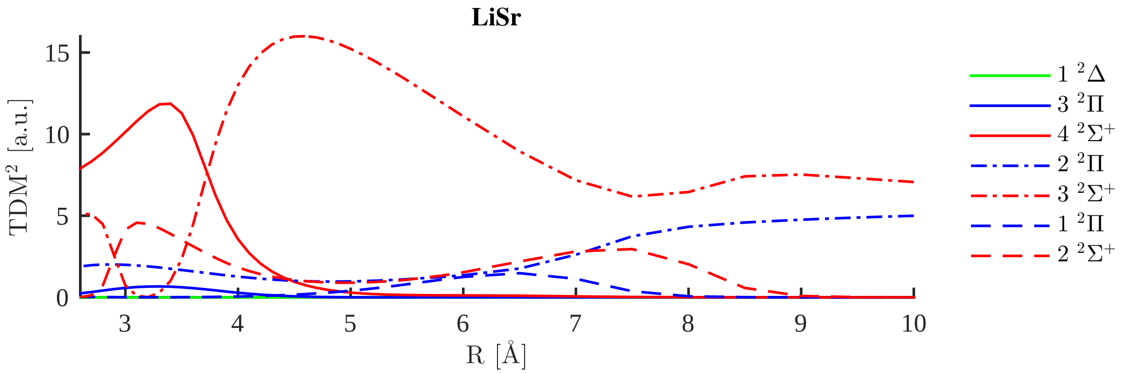

Figure C.43: TDM of LiSr

C.1.14 NaSr

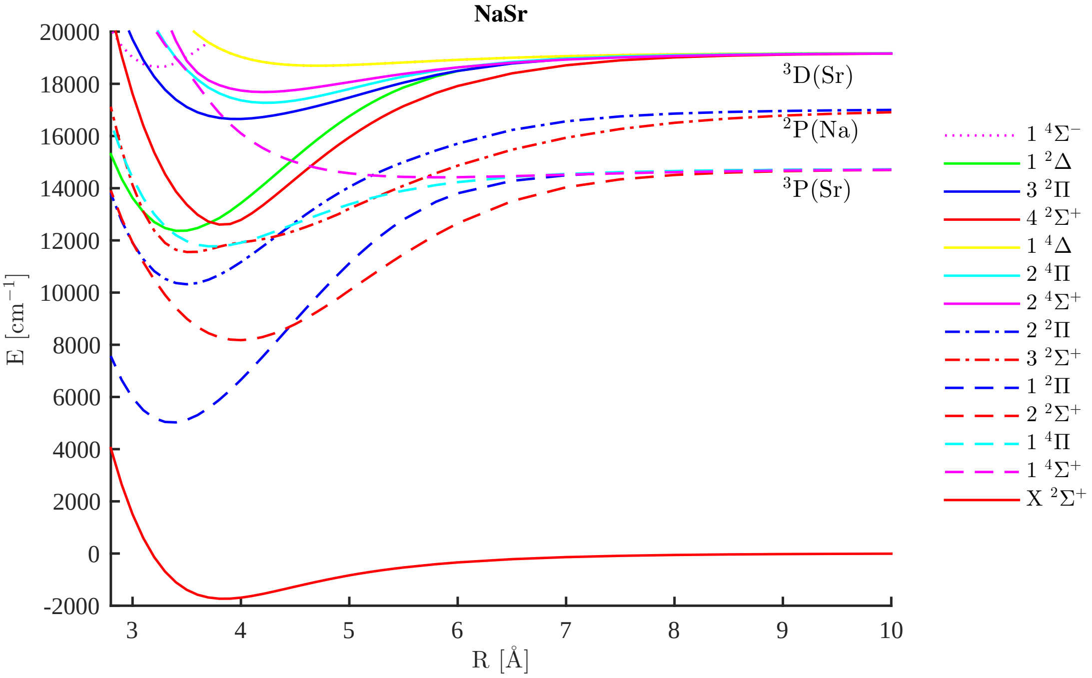

Figure C.44: PEC of NaSr

Table C.14: Spectroscopic parameters of several electronic states of NaSr obtained with the approach described in chapter 5.

state	D_e/cm^{-1}	r_e/Å	ω_e/cm^{-1}	$\omega_e x_e$/cm^{-1}	μ_e/D
X $^2\Sigma^+$	1728	3.843	87.2	1.10	0.46
1 $^2\Pi$	9699	3.363	146.9	0.56	0.64
2 $^2\Sigma^+$	6523	3.987	103.4	0.41	-0.80
2 $^2\Pi$	6679	3.497	131.3	0.65	5.33
3 $^2\Sigma^+$	5384	3.538	145.3	0.98	-0.98
1 $^4\Pi$	2952	3.747	100.8	0.86	0.62
1 $^4\Sigma^+$	287	5.806	22.9	0.46	-2.04
4 $^2\Sigma^+$	6544	3.822	150.8	0.87	0.78
1 $^2\Delta$	6812	3.444	134.3	0.66	1.32
3 $^2\Pi$	2518	3.960	75.1	0.56	-4.64
2 $^4\Sigma^+$	1475	4.206	64.7	0.71	3.41
1 $^4\Delta$	480	4.703	37.0	0.71	1.75
2 $^4\Pi$	1898	4.234	74.0	0.72	5.31
5 $^2\Sigma^+$	2385	3.697	119.7	1.50	4.11
2 $^2\Delta$	1065	4.386	50.8	0.61	2.79

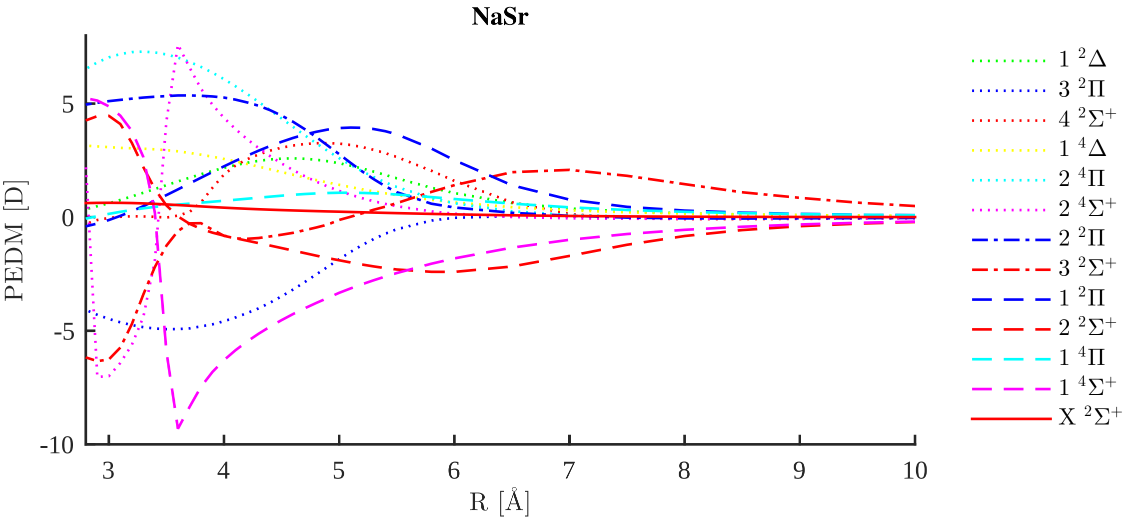

Figure C.45: PEDM of NaSr

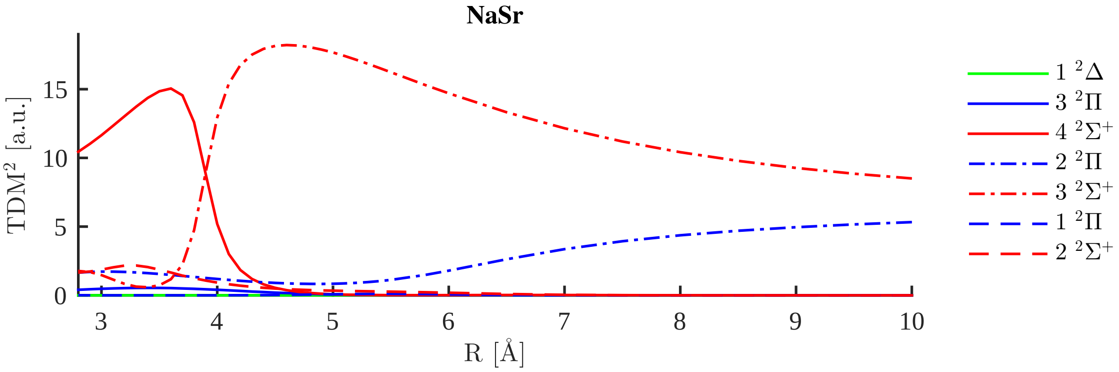

Figure C.46: TDM of NaSr

C.1.15 KSr

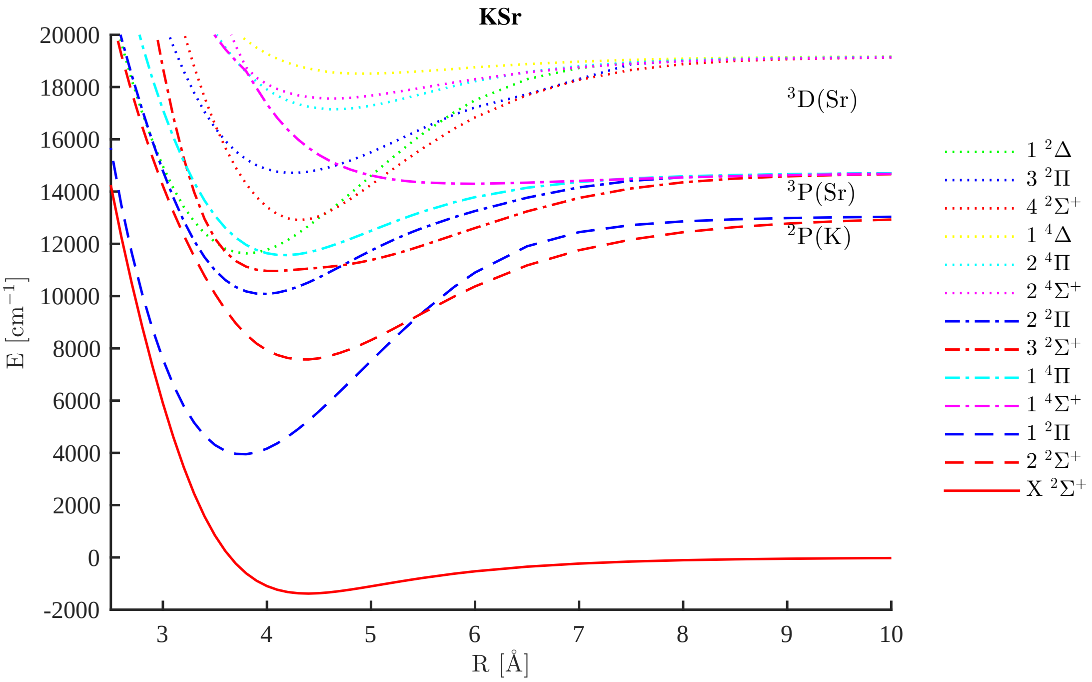

Figure C.47: PEC of KSr

Table C.15: Spectroscopic parameters of several electronic states of KSr obtained with the approach described in chapter 5.

state	D_e/cm^{-1}	r_e/Å	$\omega_e/\mathrm{cm}^{-1}$	$\omega_e x_e/\mathrm{cm}^{-1}$	μ_e/D
X $^2\Sigma^+$	1358	4.392	56.7	0.59	1.56
1 $^2\Pi$	9090	3.765	105.2	0.30	4.31
2 $^2\Sigma^+$	5358	4.350	78.0	0.28	0.67
2 $^2\Pi$	4615	3.968	88.1	0.42	8.69
3 $^2\Sigma^+$	3706	4.053	61.4	0.25	6.10
1 $^4\Pi$	3131	4.170	75.9	0.46	3.04
1 $^4\Sigma^+$	376	5.944	21.6	0.31	-3.01
4 $^2\Sigma^+$	6214	4.315	104.1	0.44	0.26
1 $^2\Delta$	7528	3.809	98.9	0.32	4.70
3 $^2\Pi$	4434	4.242	71.9	0.29	-7.28
2 $^4\Sigma^+$	1574	4.627	49.3	0.39	5.02
1 $^4\Delta$	652	4.919	33.2	0.42	2.82
2 $^4\Pi$	1997	4.652	57.3	0.41	6.51

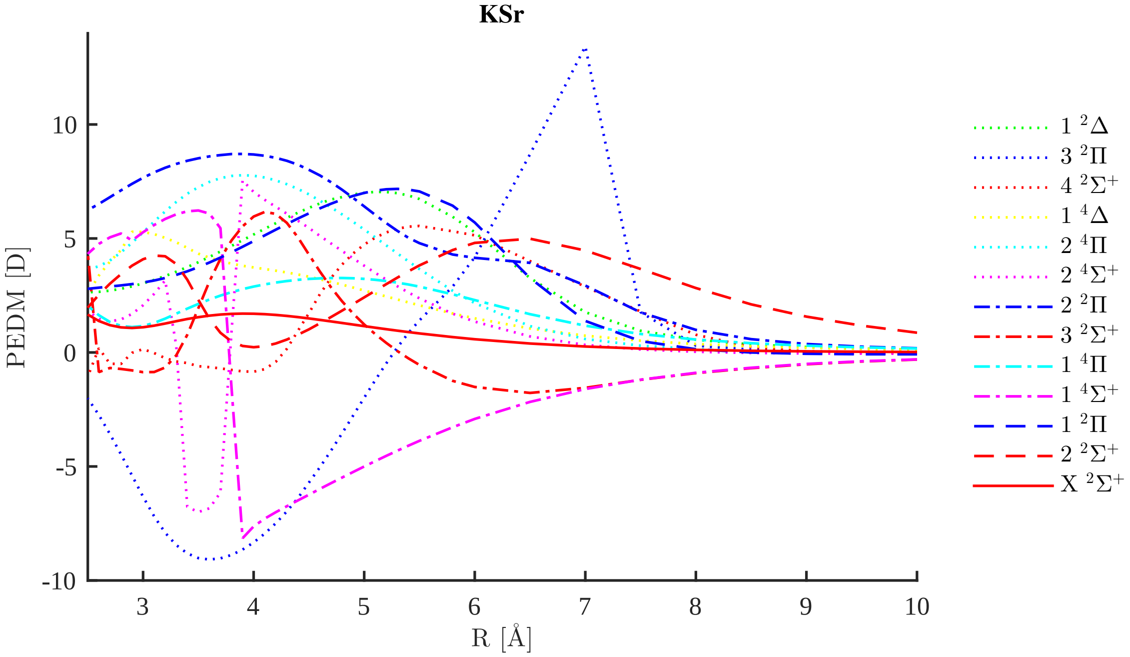

Figure C.48: PEDM of KSr

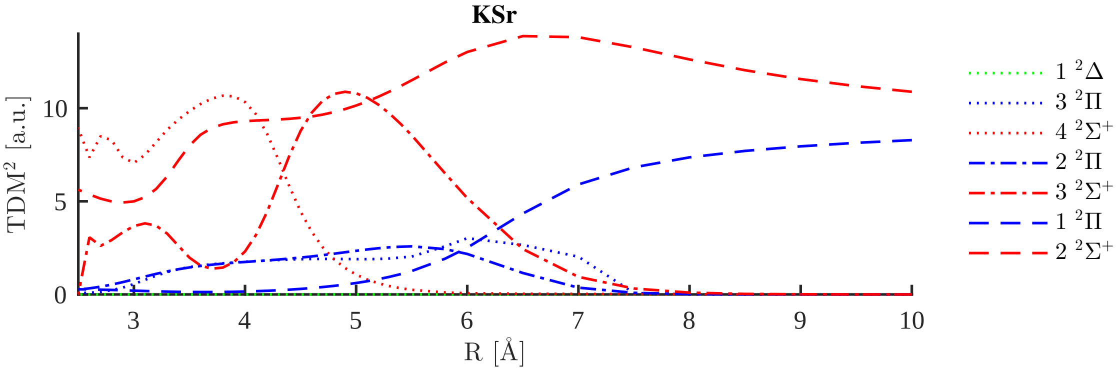

Figure C.49: TDM of KSr

C.1.16 RbSr

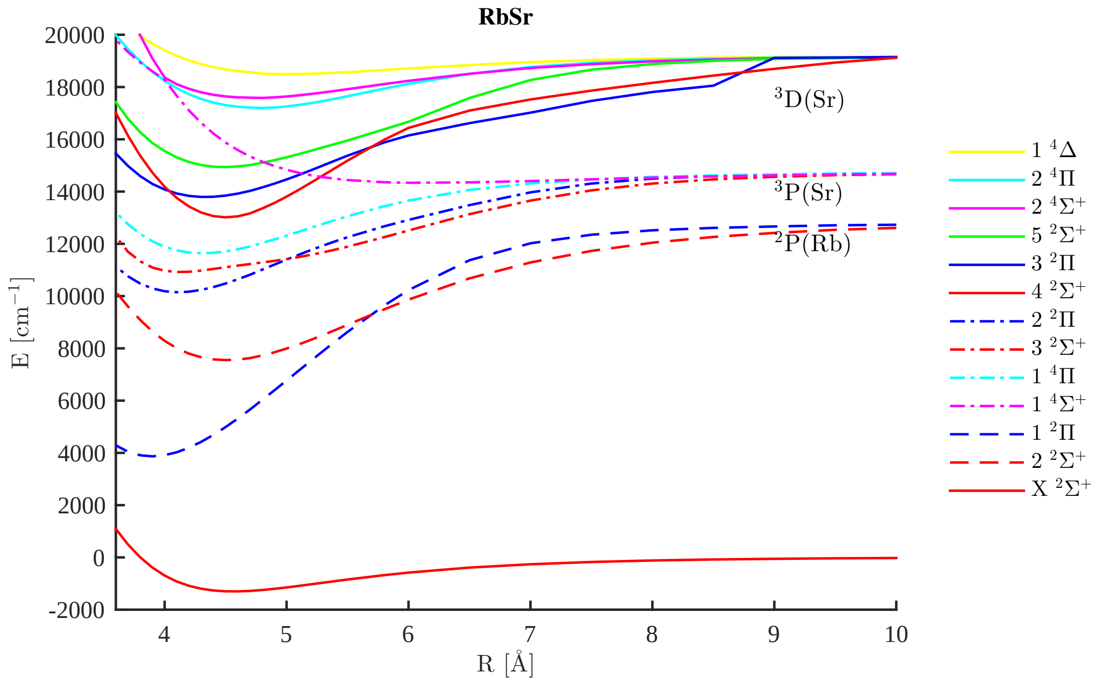

Figure C.50: PEC of RbSr

Table C.16: Spectroscopic parameters of several electronic states of RbSr obtained with the approach described in chapter 5.

state	D_e/cm^{-1}	$r_e/\text{Å}$	ω_e/cm^{-1}	$\omega_e x_e/\text{cm}^{-1}$	μ_e/D
X $^2\Sigma^+$	1279	4.564	42.6	0.35	1.71
1 $^2\Pi$	8861	3.895	80.0	0.18	5.54
2 $^2\Sigma^+$	5059	4.506	59.8	0.18	2.02
2 $^2\Pi$	4548	4.114	65.5	0.24	9.62
3 $^2\Sigma^+$	3737	4.137	57.8	0.22	7.10
1 $^4\Pi$	3059	4.312	57.5	0.27	3.65
1 $^4\Sigma^+$	343	6.147	16.3	0.19	-2.71

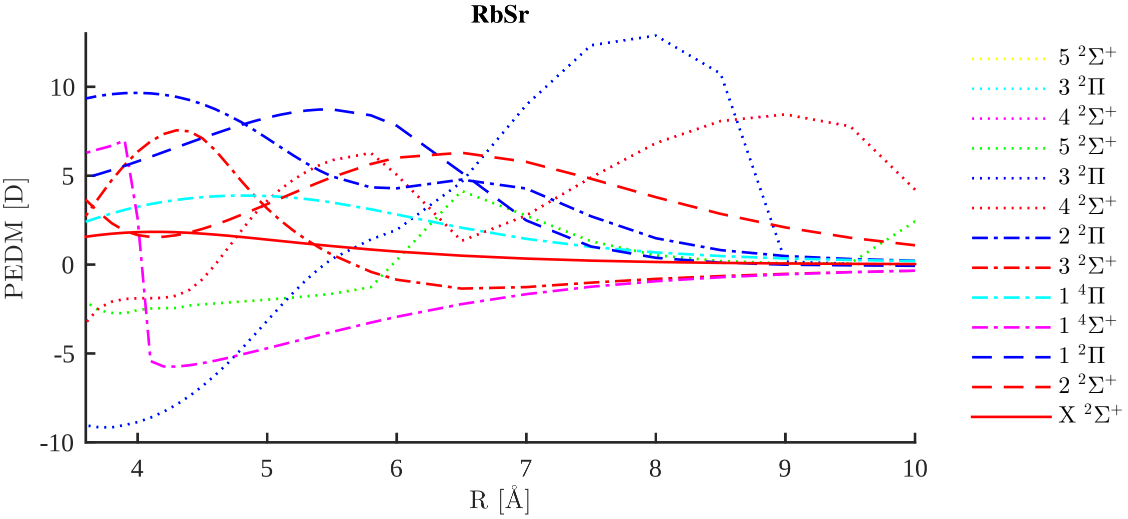

Figure C.51: PEDM of RbSr

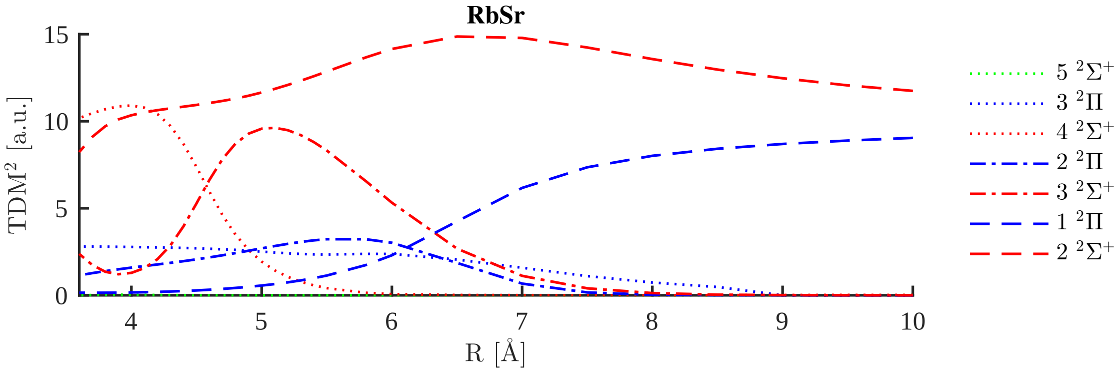

Figure C.52: TDM of RbSr

Bibliography

[1] F. Lackner, J. Poms, G. Krois, J. V. Pototschnig, and W. E. Ernst. Spectroscopy of Lithium Atoms and Molecules on Helium Nanodroplets. *J. Phys. Chem. A*, 117 (46):11866–11873, November 2013. URL `https://doi.org/10.1021/jp4030238`.

[2] G. Krois, J. V. Pototschnig, F. Lackner, and W. E. Ernst. Spectroscopy of Cold LiCa Molecules Formed on Helium Nanodroplets. *J. Phys. Chem. A*, 117(50): 13719–13731, 2013. URL `http://pubs.acs.org/doi/abs/10.1021/jp407818k`.

[3] J. V. Pototschnig, M. Ratschek, A. W. Hauser, and W. E. Ernst. An ab initio study of the CrHe diatomic molecule: the effect of van der Waals distortion on a highly magnetic multi-electron system. *Phys. Chem. Chem. Phys.*, 16(20):9469–9478, 2014. URL `https://doi.org/10.1039/c4cp00559g`.

[4] M. Ratschek, J. V. Pototschnig, A. W. Hauser, and W. E. Ernst. Solvation and Spectral Line Shifts of Chromium Atoms in Helium Droplets Based on a Density Functional Theory Approach. *J. Phys. Chem. A*, 118(33):6622–6631, August 2014. URL `https://doi.org/10.1021/jp5034036`.

[5] F. Lackner, G. Krois, T. Buchsteiner, J. V. Pototschnig, and W. E. Ernst. Helium Nanodroplet Assisted Preparation of Cold RbSr Molecules. *Phys. Rev. Lett.*, 113: 153001, 2014. URL `https://doi.org/10.1103/PhysRevLett.113.153001`.

[6] G. Krois, F. Lackner, J. V. Pototschnig, T. Buchsteiner, and W. Ernst. Characterization of RbSr Molecules: A Spectral Analysis on Helium Droplets. *Phys. Chem. Chem. Phys.*, 16:22373–22381, 2014. URL `https://doi.org/10.1039/C4CP03135K`.

[7] J. V. Pototschnig, G. Krois, F. Lackner, and W. E. Ernst. Ab initio Study of the RbSr electronic Structure: Potential Energy Surfaces, Transition Dipole Moments and Permanent Electric Dipole Moments. *J. Chem. Phys.*, 141:234309, 2014. URL `https://doi.org/10.1063/1.4903791`.

[8] J. V. Pototschnig, G. Krois, F. Lackner, and W. E. Ernst. Investigation of the RbCa molecule: Experiment and theory. *J. Mol. Spectrosc.*, 310:126–134, April 2015. URL `https://doi.org/10.1016/j.jms.2015.01.006`.

[9] A. W. Hauser, J. V. Pototschnig, and W. E. Ernst. A classic case of Jahn-Teller effect theory revisited: Ab initio simulation of hyperfine coupling and pseudorotational tunneling in the 1^2E ' state of Na_3. *Chem. Phys.*, 460:2–13, October 2015. URL `https://doi.org/10.1016/j.chemphys.2015.07.027`.

[10] J. V. Pototschnig, A. W. Hauser, and W. E. Ernst. Electric dipole moments and chemical bonding of diatomic alkali - alkaline earth molecules. *Phys. Chem. Chem. Phys.*, 18:5964, 2016. URL `https://doi.org/10.1039/C5CP06598D`.

[11] D. Feller. The role of databases in support of computational chemistry calculations. *J. Comp. Chem.*, 17(13):1571–1586, October 1996. URL `https://doi.org/10.1002/(SICI)1096-987X(199610)17:13<1571::AID-JCC9>3.0.CO;2-P`.

[12] K. L. Schuchardt, B. T. Didier, T. Elsethagen, L. S. Sun, V. Gurumoorthi, J. Chase, J. Li, and T. L. Windus. Basis set exchange: A community database for computational sciences. *J. Chem. Inf. Model.*, 47(3):1045–1052, May 2007. URL `https://doi.org/10.1021/ci600510j`.

[13] Y. Ralchenko, A.E. Kramida, J. Reader, and NIST ASD Team. NIST Atomic Spectra Database (ver. 4.1.0), [Online]. *National Institute of Standards and Technology, Gaithersburg, MD*, 2015. URL `http://physics.nist.gov/asd`.

[14] M. Koch. *Magnetic Resonance Spectroscopy of Single Alkali-Metal Atoms Isolated in Superfluid Helium Nanodroplets.* Doctoral Thesis, Graz University of Technology, 2009.

[15] M. Koch, C. Callegari, and W. E. Ernst. Alkali-metal electron spin density shift induced by a helium nanodroplet. *Mol. Phys.*, 108(7-9):1005–1011, 2010. URL `https://doi.org/10.1080/00268971003623401`.

[16] Andreas Kautsch. *Photoinduced Dynamics of Transition Metal Atoms and Clusters in Helium Nanodroplets.* Doctoral Thesis, Graz University of Technology, 2014.

[17] A. Kautsch, M. Hasewend, M. Koch, and W. E. Ernst. Fano resonances in chromium photoionization spectra after photoinduced ejection from a superfluid helium nanodroplet. *Phys. Rev. A*, 86(3):033428, September 2012. URL `https://doi.org/10.1103/PhysRevA.86.033428`.

[18] Andreas Kautsch, Markus Koch, and Wolfgang E. Ernst. Electronic Relaxation after Resonant Laser Excitation of Cr in Superfluid Helium Nanodroplets. *J. Phys. Chem. A*, 117(39):9621–9625, 2013. URL `http://pubs.acs.org/doi/abs/10.1021/jp312336m`.

[19] M. Koch, A. Kautsch, F. Lackner, and W. E. Ernst. One- and Two-Color Resonant Photoionization Spectroscopy of Chromium-Doped Helium Nanodroplets. *J. Phys. Chem. A*, 118(37):8373–8379, September 2014. URL `https://doi.org/10.1021/jp501285r`.

[20] Johann V. Pototschnig. Theoretical Investigation of the Interaction between Chromium and Helium. Master Thesis, Graz Unversity of Technology, 2012.

[21] Martin Ratschek. -. Doctoral Thesis, Graz University of Technology, expected 2016.

[22] Günter Krois. Heavy alkali and alkaline earth metals on cold helium droplets: First comparison of excitation spectra. Master Thesis, Graz University of Technology, 2011.

[23] Günter Krois. *Alkali - alkaline earth metal molecules on cold helium droplets.* Doctoral Thesis, Graz University of Technology, 2014.

[24] A. Stein, M. Ivanova, A. Pashov, H. Knöckel, and E. Tiemann. Spectroscopic Study of the $2^2\Sigma^+$ and the $4^2\Sigma^+$ Excited States of LiCa. *J. Chem. Phys.*, 138(11): 114306, 2013. URL `http://link.aip.org/link/?JCP/138/114306/1`.

[25] M. Ivanova, A. Stein, A. Pashov, A. V. Stolyarov, H. Knockel, and E. Tiemann. The $X^2\Sigma^+$ state of LiCa studied by Fourier-transform spectroscopy. *J. Chem. Phys.*, 135(17):174303, November 2011. URL `https://doi.org/10.1063/1.3652755`.

[26] B. Pasquiou, A. Bayerle, S. M. Tzanova, S. Stellmer, J. Szczepkowski, M. Parigger, R. Grimm, and F. Schreck. Quantum degenerate mixtures of strontium and rubidium atoms. *Phys. Rev. A*, 88(2):023601, August 2013. URL `https://doi.org/10.1103/PhysRevA.88.023601`.

[27] Michael L. Wall. *Quantum Many-Body Physics of Ultracold Molecules in Optical Lattices.* Springer Theses. Springer International Publishing, 2015. URL `https://doi.org/10.1007/978-3-319-14252-4`.

[28] J. Ulmanis, J. Deiglmayr, M. Repp, R. Wester, and M. Weidemuller. Ultracold Molecules Formed by Photoassociation: Heteronuclear Dimers, Inelastic Collisions, and Interactions with Ultrashort Laser Pulses. *Chem. Rev.*, 112(9):4890–4927, September 2012. URL `https://doi.org/10.1021/cr300215h`.

[29] G. Quéméner and P. S. Julienne. Ultracold Molecules under Control! *Chem. Rev.*, 112(9, SI):4949–5011, SEP 2012. ISSN 0009-2665. URL `https://doi.org/10.1021/cr300092g`.

[30] I. Bloch and P. Zoller. Chapter 5 - Ultracold Atoms and Molecules in Optical Lattices. In *Ultracold Bosonic and Fermionic Gases*, volume 5 of *Contemporary Concepts of Condensed Matter Science*, pages 121 – 156. Elsevier, 2012. URL `http://dx.doi.org/10.1016/B978-0-444-53857-4.00005-2`. editors: K. Levin, A. L. Fetter and D. M. Stamper-Kurn,.

[31] L. D. Carr, D. DeMille, R. V. Krems, and J. Ye. Cold and ultracold molecules: science, technology and applications. *New J. Phys.*, 11:055049, May 2009. URL `https://doi.org/10.1088/1367-2630/11/5/055049`.

[32] J Doyle, B Friedrich, RV Krems, and F Masnou-Seeuws. Quo vadis, cold molecules? *EPJ D*, 31(2):149–164, NOV 2004. ISSN 1434-6060. URL `https://doi.org/10.1140/epjd/e2004-00151-x`.

[33] M. Baranov, L. Dobrek, K. Goral, L. Santos, and M. Lewenstein. Ultracold dipolar gases - a challenge for experiments and theory. *Phys. Scripta*, T102:74–81, 2002. URL `https://doi.org/10.1238/Physica.Topical.102a00074`.

[34] E. S. Shuman, J. F. Barry, D. R. Glenn, and D. DeMille. Radiative Force from Optical Cycling on a Diatomic Molecule. *Phys. Rev. Lett.*, 103(22):223001, November 2009. URL `https://doi.org/10.1103/PhysRevLett.103.223001`.

[35] E. S. Shuman, J. F. Barry, and D. DeMille. Laser cooling of a diatomic molecule. *Nature*, 467(7317):820–823, October 2010. URL `http://dx.doi.org/10.1038/nature09443`.

[36] C. Chin, R. Grimm, P. Julienne, and E. Tiesinga. Feshbach resonances in ultracold gases. *Rev. Mod. Phys.*, 82:1225–1286, Apr 2010. URL `http://link.aps.org/doi/10.1103/RevModPhys.82.1225`.

[37] W. C. Stwalley. Efficient conversion of ultracold Feshbach-resonance-related polar molecules into ultracold ground state ($X^1\Sigma^+$ v=0, J=0) molecules. *EPJ D*, 31(2):221–225, November 2004. URL `https://doi.org/10.1140/epjd/e2004-00147-6`.

[38] F. Vewinger, M. Heinz, B. W. Shore, and K. Bergmann. Amplitude and phase control of a coherent superposition of degenerate states. I. Theory. *Phys. Rev. A*, 75(4), APR 2007. ISSN 1050-2947. URL `https://doi.org/10.1103/PhysRevA.75.043406`.

[39] W. C. Stwalley and H. Wang. Special review lecture - Photoassociation of ultracold atoms: A new spectroscopic technique. *J. Mol. Spectrosc.*, 195(2):194–228, June 1999. URL `https://doi.org/10.1006/jmsp.1999.7838`.

[40] H. Wang and W. C. Stwalley. Ultracold photoassociative spectroscopy of heteronuclear alkali-metal diatomic molecules. *J. Chem. Phys.*, 108(14):5767–5771, April 1998. URL `https://doi.org/10.1063/1.475987`.

[41] K. Bergmann, H. Theuer, and B. W. Shore. Coherent population transfer among quantum states of atoms and molecules. *Rev. Mod. Phys.*, 70:1003–1025, Jul 1998. URL `http://link.aps.org/doi/10.1103/RevModPhys.70.1003`.

[42] A. Fioretti, D. Comparat, A. Crubellier, O. Dulieu, F. Masnou-Seeuws, and P. Pillet. Formation of cold Cs_2 molecules through photoassociation. *Phys. Rev. Lett.*, 80 (20):4402–4405, May 1998. URL `https://doi.org/10.1103/PhysRevLett.80.4402`.

[43] T. Takekoshi, B. M. Patterson, and R. J. Knize. Observation of optically trapped cold cesium molecules. *Phys. Rev. Lett.*, 81(23):5105–5108, December 1998. URL `https://doi.org/10.1103/PhysRevLett.81.5105`.

[44] T. Takekoshi, B. M. Patterson, and R. J. Knize. Observation of cold ground-state cesium molecules produced in a magneto-optical trap. *Phys. Rev. A*, 59(1):R5–R7, January 1999. URL `https://doi.org/10.1103/PhysRevA.59.R5`.

[45] J. G. Danzl, M. J. Mark, E. Haller, M. Gustavsson, R. Hart, A. Liem, H. Zellmer, and H. C. Nagerl. Deeply bound ultracold molecules in an optical lattice. *New J. Phys.*, 11:055036, May 2009. URL `https://doi.org/10.1088/1367-2630/11/5/055036`.

[46] A. N. Nikolov, E. E. Eyler, X. T. Wang, J. Li, H. Wang, W. C. Stwalley, and P. L. Gould. Observation of ultracold ground-state potassium molecules. *Phys. Rev. Lett.*, 82(4):703–706, January 1999. URL `https://doi.org/10.1103/PhysRevLett.82.703`.

[47] C. Gabbanini, A. Fioretti, A. Lucchesini, S. Gozzini, and M. Mazzoni. Cold rubidium molecules formed in a magneto-optical trap. *Phys. Rev. Lett.*, 84(13):2814–2817, March 2000. URL `https://doi.org/10.1103/PhysRevLett.84.2814`.

[48] S. Stellmer, B. Pasquiou, R. Grimm, and F. Schreck. Creation of Ultracold Sr-2 Molecules in the Electronic Ground State. *Phys. Rev. Lett.*, 109(11):115302, September 2012. URL `https://doi.org/10.1103/PhysRevLett.109.115302`.

[49] M. W. Mancini, G. D. Telles, A. R. L. Caires, V. S. Bagnato, and L. G. Marcassa. Observation of ultracold ground-state heteronuclear molecules. *Phys. Rev. Lett.*, 92(13):133203, April 2004. URL `https://doi.org/10.1103/PhysRevLett.92.133203`.

[50] D. Wang, J. Qi, M. F. Stone, O. Nikolayeva, H. Wang, B. Hattaway, S. D. Gensemer, P. L. Gould, E. E. Eyler, and W. C. Stwalley. Photoassociative production and trapping of ultracold KRb molecules. *Phys. Rev. Lett.*, 93(24):243005, December 2004. URL `https://doi.org/10.1103/PhysRevLett.93.243005`.

[51] D. Wang, J. Qi, M. F. Stone, O. Nikolayeva, B. Hattaway, S. D. Gensemer, H. Wang, W. T. Zemke, P. L. Gould, E. E. Eyler, and W. C. Stwalley. The photoassociative spectroscopy, photoassociative molecule formation, and trapping of ultracold ^{39}K^{85}Rb. *EPJ D*, 31(2):165–177, November 2004. URL `https://doi.org/10.1140/epjd/e2004-00162-7`.

[52] K. K. Ni, S. Ospelkaus, M. H. G. de Miranda, A. Pe'er, B. Neyenhuis, J. J. Zirbel, S. Kotochigova, P. S. Julienne, D. S. Jin, and J. Ye. A high phase-space-density gas of polar molecules. *Science*, 322(5899):231–235, October 2008. URL `https://doi.org/10.1126/science.1163861`.

[53] S. Ospelkaus, K. K. Ni, D. Wang, M. H. G. de Miranda, B. Neyenhuis, G. Quéméner, P. S. Julienne, J. L. Bohn, D. S. Jin, and J. Ye. Quantum-State Controlled Chemical Reactions of Ultracold Potassium-Rubidium Molecules. *Science*,

327(5967):853–857, February 2010. URL https://doi.org/10.1126/science.1184121.

[54] A. J. Kerman, J. M. Sage, S. Sainis, T. Bergeman, and D. DeMille. Production and state-selective detection of ultracold RbCs molecules. *Phys. Rev. Lett.*, 92(15):153001, April 2004. URL https://doi.org/10.1103/PhysRevLett.92.153001.

[55] A. J. Kerman, J. M. Sage, S. Sainis, T. Bergeman, and D. DeMille. Production of ultracold, polar RbCs* molecules via photoassociation. *Phys. Rev. Lett.*, 92(3):033004, January 2004. URL https://doi.org/10.1103/PhysRevLett.92.033004.

[56] J. M. Sage, S. Sainis, T. Bergeman, and D. DeMille. Optical production of ultracold polar molecules. *Phys. Rev. Lett.*, 94(20):203001, May 2005. URL https://doi.org/10.1103/PhysRevLett.94.203001.

[57] C. Haimberger, J. Kleinert, M. Bhattacharya, and N. P. Bigelow. Formation and detection of ultracold ground-state polar molecules. *Phys. Rev. A*, 70(2):021402, August 2004. URL https://doi.org/10.1103/PhysRevA.70.021402.

[58] J. Deiglmayr, A. Grochola, M. Repp, K. Mortlbauer, C. Gluck, J. Lange, O. Dulieu, R. Wester, and M. Weidemuller. Formation of ultracold polar molecules in the rovibrational ground state. *Phys. Rev. Lett.*, 101(13):133004, September 2008. URL https://doi.org/10.1103/PhysRevLett.101.133004.

[59] V. Zhelyazkova, A. Cournol, T. E. Wall, A. Matsushima, J. J. Hudson, E. A. Hinds, M. R. Tarbutt, and B. E. Sauer. Laser cooling and slowing of CaF molecules. *Phys. Rev. A*, 89(5):053416, May 2014. URL https://doi.org/10.1103/PhysRevA.89.053416.

[60] M. H. Anderson, J. R. Ensher, M. R. Matthews, C. E. Wieman, and E. A. Cornell. Observation of Bose-einstein Condensation In A Dilute Atomic Vapor. *Science*, 269(5221):198–201, July 1995. URL https://doi.org/10.1126/science.269.5221.198.

[61] A. J. Leggett. Bose-Einstein condensation in the alkali gases: Some fundamental concepts. *Rev. Mod. Phys.*, 73(2):307–356, April 2001. URL https://doi.org/10.1103/RevModPhys.73.307.

[62] T. Weber, J. Herbig, M. Mark, H. C. Nagerl, and R. Grimm. Bose-einstein condensation of cesium. *Science*, 299(5604):232–235, January 2003. URL https://doi.org/10.1126/science.1079699.

[63] S. Kraft, F. Vogt, O. Appel, F. Riehle, and U. Sterr. Bose-Einstein Condensation of Alkaline Earth Atoms: ^{40}Ca. *Phys. Rev. Lett.*, 103(13):130401, September 2009. URL https://doi.org/10.1103/PhysRevLett.103.130401.

[64] S. Stellmer, M. K. Tey, B. Huang, R. Grimm, and F. Schreck. Bose-Einstein Condensation of Strontium. *Phys. Rev. Lett.*, 103(20):200401, November 2009. URL `https://doi.org/10.1103/PhysRevLett.103.200401`.

[65] Y. Takasu, K. Maki, K. Komori, T. Takano, K. Honda, M. Kumakura, T. Yabuzaki, and Y. Takahashi. Spin-singlet Bose-Einstein condensation of two-electron atoms. *Phys. Rev. Lett.*, 91(4):040404, July 2003. URL `https://doi.org/10.1103/PhysRevLett.91.040404`.

[66] A. Griesmaier, J. Werner, S. Hensler, J. Stuhler, and T. Pfau. Bose-einstein condensation of chromium. *Phys. Rev. Lett.*, 94(16):160401, April 2005. URL `https://doi.org/10.1103/PhysRevLett.94.160401`.

[67] G. Bismut, B. Pasquiou, D. Ciampini, B. Laburthe-Tolra, E. Marechal, L. Vernac, and O. Gorceix. Optimized loading of an optical dipole trap for the production of chromium BECs. *Appl. Phys. B*, 102(1):1–9, January 2011. URL `https://doi.org/10.1007/s00340-010-4171-y`.

[68] A. H. Hansen, A. Y. Khramov, W. H. Dowd, A. O. Jamison, B. Plotkin-Swing, R. J. Roy, and S. Gupta. Production of quantum-degenerate mixtures of ytterbium and lithium with controllable interspecies overlap. *Phys. Rev. A*, 87(1):013615, January 2013. URL `https://doi.org/10.1103/PhysRevA.87.013615`.

[69] H. Hara, Y. Takasu, Y. Yamaoka, J. M. Doyle, and Y. Takahashi. Quantum Degenerate Mixtures of Alkali and Alkaline-Earth-Like Atoms. *Phys. Rev. Lett.*, 106(20):205304, May 2011. URL `https://doi.org/10.1103/PhysRevLett.106.205304`.

[70] A. H. Hansen, A. Khramov, W. H. Dowd, A. O. Jamison, V. V. Ivanov, and S. Gupta. Quantum degenerate mixture of ytterbium and lithium atoms. *Phys. Rev. A*, 84(1):011606, July 2011. URL `https://doi.org/10.1103/PhysRevA.84.011606`.

[71] L. Santos, G. V. Shlyapnikov, P. Zoller, and M. Lewenstein. Bose-Einstein condensation in trapped dipolar gases. *Phys. Rev. Lett.*, 85(9):1791–1794, August 2000. URL `https://doi.org/10.1103/PhysRevLett.85.1791`.

[72] K. Goral, L. Santos, and M. Lewenstein. Quantum phases of dipolar bosons in optical lattices. *Phys. Rev. Lett.*, 88(17):170406, April 2002. URL `https://doi.org/10.1103/PhysRevLett.88.170406`.

[73] L. Santos, G. V. Shlyapnikov, and M. Lewenstein. Roton-maxon spectrum and stability of trapped dipolar Bose-Einstein condensates. *Phys. Rev. Lett.*, 90(25):250403, June 2003. URL `https://doi.org/10.1103/PhysRevLett.90.250403`.

[74] L. D. Carr, G. V. Shlyapnikov, and Y. Castin. Achieving a BCS transition in an atomic Fermi gas. *Phys. Rev. Lett.*, 92(15):150404, April 2004. URL `https://doi.org/10.1103/PhysRevLett.92.150404`.

[75] M. A. Baranov, L. Dobrek, and M. Lewenstein. Superfluidity of trapped dipolar Fermi gases. *Phys. Rev. Lett.*, 92(25):250403, June 2004. URL `https://doi.org/10.1103/PhysRevLett.92.250403`.

[76] H. P. Buchler, E. Demler, M. Lukin, A. Micheli, N. Prokof'ev, G. Pupillo, and P. Zoller. Strongly correlated 2D quantum phases with cold polar molecules: Controlling the shape of the interaction potential. *Phys. Rev. Lett.*, 98(6):060404, February 2007. URL `https://doi.org/10.1103/PhysRevLett.98.060404`.

[77] M. A. Baranov, M. Dalmonte, G. Pupillo, and P. Zoller. Condensed Matter Theory of Dipolar Quantum Gases. *Chem. Rev.*, 112(9):5012–5061, September 2012. URL `https://doi.org/10.1021/cr2003568`.

[78] K. R. A. Hazzard, B. Gadway, M. Foss-Feig, B. Yan, S. A. Moses, J. P. Covey, N. Y. Yao, M. D. Lukin, J. Ye, D. S. Jin, and A. M. Rey. Many-Body Dynamics of Dipolar Molecules in an Optical Lattice. *Phys. Rev. Lett.*, 113(19):195302, November 2014. URL `https://doi.org/10.1103/PhysRevLett.113.195302`.

[79] A. Micheli, G. K. Brennen, and P. Zoller. A toolbox for lattice-spin models with polar molecules. *Nat. Phys.*, 2(5):341–347, May 2006. URL `https://doi.org/10.1038/nphys287`.

[80] D. DeMille. Quantum computation with trapped polar molecules. *Phys. Rev. Lett.*, 88:067901, Jan 2002. URL `http://link.aps.org/doi/10.1103/PhysRevLett.88.067901`.

[81] S. Marx, D. A. Smith, M. J. Abel, T. Zehentbauer, G. Meijer, and G. Santambrogio. Imaging Cold Molecules on a Chip. *Phys. Rev. Lett.*, 111(24):243007, December 2013. URL `https://doi.org/10.1103/PhysRevLett.111.243007`.

[82] S. A. Meek, H. Conrad, and G. Meijer. Trapping Molecules on a Chip. *Science*, 324(5935):1699–1702, June 2009. URL `https://doi.org/10.1126/science.1175975`.

[83] A. Andre, D. DeMille, J. M. Doyle, M. D. Lukin, S. E. Maxwell, P. Rabl, R. J. Schoelkopf, and P. Zoller. A coherent all-electrical interface between polar molecules and mesoscopic superconducting resonators. *Nat. Phys.*, 2(9):636–642, September 2006. URL `https://doi.org/10.1038/nphys386`.

[84] P. Rabl, D. DeMille, J. M. Doyle, M. D. Lukin, R. J. Schoelkopf, and P. Zoller. Hybrid quantum processors: Molecular ensembles as quantum memory for solid state circuits. *Phys. Rev. Lett.*, 97(3):033003, July 2006. URL `https://doi.org/10.1103/PhysRevLett.97.033003`.

[85] B. K. Stuhl, M. T. Hummon, and J. Ye. Cold State-Selected Molecular Collisions and Reactions. *Annu. Rev. Phys. Chem.*, 65:501–518, 2014. URL `https://doi.org/10.1146/annurev-physchem-040513-103744`.

[86] R. V. Krems. Cold controlled chemistry. *Phys. Chem. Chem. Phys.*, 10(28):4079–4092, 2008. URL `https://doi.org/10.1039/b802322k`.

[87] E. R. Hudson, C. Ticknor, B. C. Sawyer, C. A. Taatjes, H. J. Lewandowski, J. R. Bochinski, J. L. Bohn, and J. Ye. Production of cold formaldehyde molecules for study and control of chemical reaction dynamics with hydroxyl radicals. *Phys. Rev. A*, 73(6):063404, June 2006. URL `https://doi.org/10.1103/PhysRevA.73.063404`.

[88] C. Chin, V. V. Flambaum, and M. G. Kozlov. Ultracold molecules: new probes on the variation of fundamental constants. *New J. Phys.*, 11:055048, May 2009. URL `https://doi.org/10.1088/1367-2630/11/5/055048`.

[89] M. Kajita, G. Gopakumar, M. Abe, and M. Hada. Sensitivity of vibrational spectroscopy of optically trapped SrLi and CaLi molecules to variations in $\mathrm{m}_p/\mathrm{m}_e$. *J. Phys. B*, 46(2):025001, January 2013. URL `https://doi.org/10.1088/0953-4075/46/2/025001`.

[90] M. Kajita, G. Gopakumar, M. Abe, and M. Hada. Characterizing of variation in the proton-to-electron mass ratio via precise measurements of molecular vibrational transition frequencies. *J. Mol. Spectrosc.*, 300:99–107, June 2014. URL `https://doi.org/10.1016/j.jms.2014.03.009`.

[91] V. V. Flambaum and M. G. Kozlov. Enhanced sensitivity to the time variation of the fine-structure constant and $\mathrm{m}_p/\mathrm{m}_e$ in diatomic molecules. *Phys. Rev. Lett.*, 99 (15):150801, October 2007. URL `https://doi.org/10.1103/PhysRevLett.99.150801`.

[92] D. DeMille, S. Sainis, J. Sage, T. Bergeman, S. Kotochigova, and E. Tiesinga. Enhanced sensitivity to variation of $\mathrm{m}_e/\mathrm{m}_p$ in molecular spectra. *Phys. Rev. Lett.*, 100(4):043202, February 2008. URL `https://doi.org/10.1103/PhysRevLett.100.043202`.

[93] K. Beloy, A. W. Hauser, A. Borschevsky, V. V. Flambaum, and P. Schwerdtfeger. Effect of alpha variation on the vibrational spectrum of Sr_2. *Phys. Rev. A*, 84 (6):062114, DEC 21 2011. ISSN 1050-2947. URL `https://doi.org/10.1103/PhysRevA.84.062114`.

[94] E. R. Hudson, H. J. Lewandowski, B. C. Sawyer, and J. Ye. Cold molecule spectroscopy for constraining the evolution of the fine structure constant. *Phys. Rev. Lett.*, 96(14):143004, April 2006. URL `https://doi.org/10.1103/PhysRevLett.96.143004`.

[95] E. A. Hinds. Testing time reversal symmetry using molecules. *Phys. Scripta*, T70: 34–41, 1997. URL `https://doi.org/10.1088/0031-8949/1997/T70/005`.

[96] J. J. Hudson, B. E. Sauer, M. R. Tarbutt, and E. A. Hinds. Measurement of the electron electric dipole moment using YbF molecules. *Phys. Rev. Lett.*, 89(2): 023003, July 2002. URL `https://doi.org/10.1103/PhysRevLett.89.023003`.

[97] E. R. Meyer and J. L. Bohn. Electron electric-dipole-moment searches based on alkali-metal- or alkaline-earth-metal-bearing molecules. *Phys. Rev. A*, 80(4): 042508, October 2009. URL `https://doi.org/10.1103/PhysRevA.80.042508`.

[98] E. R. Meyer, J. L. Bohn, and M. P. Deskevich. Candidate molecular ions for an electron electric dipole moment experiment. *Phys. Rev. A*, 73(6):062108, June 2006. URL `https://doi.org/10.1103/PhysRevA.73.062108`.

[99] A. E. Leanhardt, J. L. Bohn, H. Loh, P. Maletinsky, E. R. Meyer, L. C. Sinclair, R. P. Stutz, and E. A. Cornell. High-resolution spectroscopy on trapped molecular ions in rotating electric fields: A new approach for measuring the electron electric dipole moment. *J. Mol. Spectrosc.*, 270(1):1–25, November 2011. URL `https://doi.org/10.1016/j.jms.2011.06.007`.

[100] J. J. Hudson, D. M. Kara, I. J. Smallman, B. E. Sauer, M. R. Tarbutt, and E. A. Hinds. Improved measurement of the shape of the electron. *Nature*, 473(7348): 493–U232, May 2011. URL `https://doi.org/10.1038/nature10104`.

[101] A. Borschevsky, M. Ilias, V. A. Dzuba, V. V. Flambaum, and P. Schwerdtfeger. Relativistic study of nuclear-anapole-moment effects in diatomic molecules. *Phys. Rev. A*, 88(2):022125, August 2013. URL `https://doi.org/10.1103/PhysRevA.88.022125`.

[102] M. G. Kozlov and L. N. Labzosky. Parity Violation Effects In Diatomics. *J. Phys. B*, 28(10):1933–1961, May 1995. URL `https://doi.org/10.1088/0953-4075/28/10/008`.

[103] H. Lefebvre-Brion and R. W. Field. *Perturbations in the Spectra of Diatomic Molecules*. Academic Press Inc., 1986.

[104] W. Domcke, D. R. Yarkony, and C. Köppl, editors. *Conical Intersections - Theory, Computation and Experiment*, volume 17 of *Advanced Series in Physical Chemistry*. World Scientific Publishing Co. Pte. Ltd., 2011. URL `http://dx.doi.org/10.1142/9789814313452`.

[105] Gerhard Herzberg. *Molecular Spectra and Molecular Structure - I. Spectra of Diatomic Molecules*. Van Nostrand Reinhold Company, 1950.

[106] R. J. Le Roy. Level 8.0. University of Waterloo Chemical Physics Research Report CP-663, University of Waterloo, 2007. URL `http://leroy.uwaterloo.ca/programs`. A Computer Program for Solving the Radial Schrödinger Equation for Bound and Quasibound Levels.

[107] EMSL Basis set Exchange, Nov. 2015. URL `https://bse.pnl.gov/bse/portal`.

[108] Frank Jensen. *Introduction to Computational Chemistry*. John Wiley & Sons, Ltd, 2007.

[109] S. F. Boys and F. Bernadi. Calculation of Small Molecular Interactions By Differences of Separate Total Energies - Some Procedures With Reduced Errors. *Mol. Phys.*, 19(4):553–&, 1970. URL `https://doi.org/10.1080/00268977000101561`.

[110] T. Helgaker, W. Klopper, H. Koch, and J. Noga. Basis-set convergence of correlated calculations on water. *J. Chem. Phys.*, 106(23):9639–9646, June 1997. URL `https://doi.org/10.1063/1.473863`.

[111] H. J. Werner and P. J. Knowles. *MOLPRO Users Manual Version 2010.1*. University College Cardiff Consultants Limited, 2008.

[112] Stuttgart/Cologne energy-consistent (ab initio) pseudopotentials suitable for wavefunction-based and density functional calculations, Nov. 2015. URL `http://www.tc.uni-koeln.de/PP/index.en.html`.

[113] M. M. Hurley, L. F. Pacios, P. A. Christiansen, R. B. Ross, and W. C. Ermler. Ab initio Relativistic Effective Potentials With Spin-orbit Operators: 2. K Through Kr. *J. Chem. Phys.*, 84(12):6840–6853, June 1986. URL `https://doi.org/10.1063/1.450689`.

[114] L. A. LaJohn, P. A. Christiansen, R. B. Ross, T. Atashroo, and W. C. Ermler. Ab initio Relativistic Effective Potentials With Spin Orbit Operators: 3. Rb through Xe. *J. Chem. Phys.*, 87(5):2812–2824, September 1987. URL `https://doi.org/10.1063/1.453069`.

[115] P. Fuentealba, H. Preuss, H. Stoll, and L. von Szentpaly. A Proper Account of Core-polarization With Pseudopotentials - Single Valence-electron Alkali Compounds. *Chem. Phys. Lett.*, 89(5):418–422, 1982. URL `https://doi.org/10.1016/0009-2614(82)80012-2`.

[116] W. Müller, J. Flesh, and W. Meyer. Treatment of Intershell Correlation-effects In Abinitio Calculations By Use of Core Polarization Potentials - Method and Application To Alkali and Alkaline-earth Atoms. *J. Chem. Phys.*, 80(7):3297–3310, 1984. URL `http://dx.doi.org/10.1063/1.447083`.

[117] W. Müller and W. Meyer. Ground-state Properties of Alkali Dimers and Their Cations (including the Elements Li, Na, and K) From Ab initio Calculations With Effective Core Polarization Potentials. *J. Chem. Phys.*, 80(7):3311–3320, 1984. URL `https://doi.org/10.1063/1.447084`.

[118] P. Fuentealba, H. Stoll, and A. Savin. Atomic Correlation-energy Differences By Means of A Polarization Potential. *Phys. Rev.*, 38(1):483–486, July 1988. URL `https://doi.org/10.1103/PhysRevA.38.483`.

[119] R. Guerout, M. Aymar, and O. Dulieu. Ground state of the polar alkali-metal-atom-strontium molecules: Potential energy curve and permanent dipole moment. *Phys. Rev. A*, 82(4):042508, October 2010. URL `https://doi.org/10.1103/PhysRevA.82.042508`.

[120] M. Aymar, S. Azizi, and O. Dulieu. Model-potential calculations for ground and excited Sigma states of Rb_2+, Cs_2+ and RbCs+ ions. *J. Phys. B*, 36(24):4799–4812, December 2003. URL `https://doi.org/10.1088/0953-4075/36/24/004`.

[121] Attila Szabo and Neil S. Ostlund. *Modern Qauntum Chemistry - Introduction to Advanced Electronic Structure Theory.* Dover Publication Inc., 1996.

[122] H.-J. Werner and W. Meyer. A quadratically convergent MCSCF method for the simultaneous optimization of several states. *J. Chem. Phys.*, 74(10):5794–5801, 1981. URL `https://doi.org/10.1063/1.440892`.

[123] H. J. Werner and W. Meyer. A Quadratically Convergent Multiconfiguration-self-consistent Field Method With Simultaneous-optimization of Orbitals and Cl Coefficients. *J. Chem. Phys.*, 73(5):2342–2356, 1980. URL `https://doi.org/10.1063/1.440384`.

[124] B. O. Roos, P. R. Taylor, and P. E. M. Siegbahn. A Complete Active Space Scf Method (CASSCF) Using A Density-matrix Formulated Super-CI Approach. *Chem. Phys.*, 48(2):157–173, 1980. URL `https://doi.org/10.1016/0301-0104(80)80045-0`.

[125] H.-J. Werner and P. J. Knowles. A second order MCSCF method with optimum convergence. *J. Chem. Phys.*, 82:5053, 1985. URL `http://dx.doi.org/10.1063/1.448627`.

[126] P. G. Szalay, T. Muller, G. Gidofalvi, H. Lischka, and R. Shepard. Multiconfiguration Self-Consistent Field and Multireference Configuration Interaction Methods and Applications. *Chem. Rev.*, 112(1):108–181, January 2012. URL `https://doi.org/10.1021/cr200137a`.

[127] P. J. Knowles and H.-J. Werner. An Efficient Method for the Evaluation of Coupling Coefficients in Configuration Interaction Calculations. *Chem. Phys. Lett.*, 145:514–522, 1988. URL `http://dx.doi.org/10.1016/0009-2614(88)87412-8`.

[128] H.-J. Werner and P. J. Knowles. An Efficient Internally Contracted Multiconfiguration Reference CI Method. *J. Chem. Phys.*, 89:5803–5814, 1988. URL `http://dx.doi.org/10.1063/1.455556`.

[129] M. Kallay, P. G. Szalay, and P. R. Surjan. A general state-selective multireference coupled-cluster algorithm. *J. Chem. Phys.*, 117(3):980–990, July 2002. URL `https://doi.org/10.1063/1.1483856`.

[130] T. Fleig, L. K. Sorensen, and J. Olsen. A relativistic 4-component general-order multi-reference coupled cluster method: initial implementation and application to HBr. *Theor. Chem. Acc.*, 118(5-6):979, DEC 2007. URL `https://doi.org/10.1007/s00214-007-0381-8`.

[131] X. Z. Li and J. Paldus. N-reference, M-state coupled-cluster method: Merging the state-universal and reduced multireference coupled-cluster theories. *J. Chem. Phys.*, 119(11):5334–5345, September 2003. URL `https://doi.org/10.1063/1.1599302`.

[132] S. Chattopadhyay, U. S. Mahapatra, and D. Mukherjee. Development of a linear response theory based on a state-specific multireference coupled cluster formalism. *J. Chem. Phys.*, 112(18):7939–7952, May 2000. URL `https://doi.org/10.1063/1.481395`.

[133] J. F. Stanton and R. J. Bartlett. The Equation of Motion Coupled-cluster Method - A Systematic Biorthogonal Approach To Molecular-excitation Energies, Transition-probabilities, and Excited-state Properties. *J. Chem. Phys*, 98 (9):7029–7039, May 1993. URL `https://doi.org/10.1063/1.464746`.

[134] A. I. Krylov. Equation-of-motion coupled-cluster methods for open-shell and electronically excited species: The Hitchhiker's guide to Fock space. *Annu. Rev. Phys. Chem.*, 59:433–462, 2008. URL `https://doi.org/10.1146/annurev.physchem.59.032607.093602`.

[135] R. J. Bartlett and M. Musial. Coupled-cluster theory in quantum chemistry. *Rev. Mod. Phys.*, 79(1):291–352, January 2007. URL `https://doi.org/10.1103/RevModPhys.79.291`.

[136] E. R. Davidson and D. W. Silver. Size consistency in dilute helium gas electronic-structure. *Chem. Phys. Lett.*, 52(3):403–406, 1977. URL `https://doi.org/10.1016/0009-2614(77)80475-2`.

[137] K. Jankowski, L. Meissner, and J. Wasilewki. Davidson-type Corrections For Quasi-degenerate States. *Int. J. Quant. Chem.*, 28(6):931–942, December 1985. URL `https://doi.org/10.1002/qua.560280622`.

[138] J. T. Hougen. Strategies for advanced applications of permutation-inversion groups to the microwave spectra of molecules with large amplitude motions. *J. Mol. Spectrosc.*, 256(2):170–185, August 2009. URL `https://doi.org/10.1016/j.jms.2009.04.011`.

[139] M. Schnell. Understanding High-Resolution Spectra of Nonrigid Molecules Using Group Theory. *ChemPhysChem*, 11(4):758–780, March 2010. URL `https://doi.org/10.1002/cphc.200900760`.

[140] H.-J. Werner, P. J. Knowles, G. Knizia, F. R. Manby, M. Schütz, P. Celani, T. Korona, R. Lindh, A. Mitrushenkov, G. Rauhut, K. R. Shamasundar, T. B. Adler, R. D. Amos, A. Bernhardsson, A. Berning, D. L. Cooper, M. J. O. Deegan, A. J. Dobbyn, F. Eckert, E. Goll, C. Hampel, A. Hesselmann, G. Hetzer, T. Hrenar, G. Jansen, C. Köppl, Y. Liu, A. W. Lloyd, R. A. Mata, A. J. May, S. J. McNicholas, W. Meyer, M. E. Mura, A. Nicklass, D. P. O'Neill, P. Palmieri, D. Peng, K. Pflüger, R. Pitzer, M. Reiher, T. Shiozaki, H. Stoll, A. J. Stone, R. Tarroni, T. Thorsteinsson, and M. Wang. Molpro, version 2012.1, a package of ab initio programs, 2012. see http://www.molpro.net.

[141] P. O. Lödwin and H. Shull. Natural Orbitals In the Quantum Theory of 2-electron Systems. *Phys. Rev.*, 101(6):1730–1739, 1956. URL `https://doi.org/10.1103/PhysRev.101.1730`.

[142] E. R. Davidson. Properties and Uses of Natural Orbitals. *Rev. Mod. Phys.*, 44(3): 451–&, 1972. URL `https://doi.org/10.1103/RevModPhys.44.451`.

[143] J. Pipek and P. G. Mezey. A Fast Intrinsic Localization Procedure Applicable For Ab initio and Semiempirical Linear Combination of Atomic Orbital Wavefunctions. *J. Chem. Phys.*, 90(9):4916–4926, May 1989. URL `https://doi.org/10.1063/1.456588`.

[144] E. D. Glendening, J. K. Badenhoop, A. E. Reed, J. E. Carpenter, J. A. Bohmann, C. M. Morales, C. R. Landis, and F. Weinhold. NBO 6.0, 2013. URL `http://nbo6.chem.wisc.edu/index.htm`. Theoretical Chemistry Institute, University of Wisconsin, Madison.

[145] E. D. Glendening, C. R. Landis, and F. Weinhold. NBO 6.0: Natural bond orbital analysis program. *J. Comp. Chem.*, 34(16):1429–1437, June 2013. URL `https://doi.org/10.1002/jcc.23266`.

[146] N. Marzari and D. Vanderbilt. Maximally localized generalized Wannier functions for composite energy bands. *Phys. Rev. B*, 56(20):12847–12865, November 1997. URL `https://doi.org/10.1103/PhysRevB.56.12847`.

[147] J. V. Ortiz. Brueckner orbitals, Dyson orbitals, and correlation potentials. *Int. J. Quant. Chem.*, 100(6):1131–1135, December 2004. URL `https://doi.org/10.1002/qua.20204`.

[148] C. D. Sherrill, A. I. Krylov, E. F. C. Byrd, and M. Head-Gordon. Energies and analytic gradients for a coupled-cluster doubles model using variational Brueckner orbitals: Application to symmetry breaking in $O_4(+)$. *J. Chem. Phys.*, 109(11): 4171–4181, September 1998. URL `https://doi.org/10.1063/1.477023`.

[149] C. M. Oana and A. I. Krylov. Dyson orbitals for ionization from the ground and electronically excited states within equation-of-motion coupled-cluster formalism:

Theory, implementation, and examples. *J. Chem. Phys.*, 127(23):234106, December 2007. URL `https://doi.org/10.1063/1.2805393`.

[150] C. M. Oana and A. I. Krylov. Cross sections and photoelectron angular distributions in photodetachment from negative ions using equation-of-motion coupled-cluster Dyson orbitals. *J. Chem. Phys.*, 131(12):124114, September 2009. URL `https://doi.org/10.1063/1.3231143`.

[151] J. E. Jones. On the determination of molecular fields - II From the equation of state of a gas. *Proc. R. Soc. A*, 106(738):463–477, October 1924. URL `https://doi.org/10.1098/rspa.1924.0082`.

[152] J. E. Lennard-Jones. The equation of state of gases and critical phenomena. *Physica*, 4:0941–0956, 1937. URL `https://doi.org/10.1016/S0031-8914(37)80191-3`.

[153] G. Mie. Kinetic theory of monatomic bodies. *Annalen Der Physik*, 11(8):657–697, June 1903.

[154] P. M. Morse. Diatomic Molecules According to the Wave Mechanics. II. Vibrational Levels. *Phys. Rev.*, 34:57–64, 1929. URL `http://link.aps.org/doi/10.1103/PhysRev.34.57`.

[155] J. L. Dunham. The energy levels of a rotating vibrator. *Phys. Rev.*, 41(6):721–731, September 1932. URL `https://doi.org/10.1103/PhysRev.41.721`.

[156] Y. P. Varshni and R. C. Shukla. Potential Energy Functions For Alkali Halide Molecules. *J. Mol. Spectrosc.*, 16(1):63–&, 1965. URL `https://doi.org/10.1016/0022-2852(65)90085-8`.

[157] R. J. Le Roy. Level 8.2. *University of Waterloo - Chemical Physics Research Report*, 668, 2015. URL `http://scienide2.uwaterloo.ca/~rleroy/level/`.

[158] R. J. Le Roy. betaFit 2.1. University of Waterloo Chemical Physics Research Report CP-666, University of Waterloo, 2013. URL `http://leroy.uwaterloo.ca/programs`. A Computer Program to Fit Pointwise Potentials to Selected Analytic Functions.

[159] J. Jiang, Y. J. Cheng, and J. Mitroy. Long-range interactions between alkali and alkaline-earth atoms. *J. Phys. B*, 46(12):125004, June 2013. URL `https://doi.org/10.1088/0953-4075/46/12/125004`.

[160] David R. Lide, editor. *CRC Handbook of Chemistry and Physics.* CRC Press, 85 edition, 2004. URL `www.crcpress.com`.

[161] J. Mitroy, M. S. Safronova, and C. W. Clark. Theory and applications of atomic and ionic polarizabilities. *J. Phys. B*, 43(20):202001, October 2010. URL `https://doi.org/10.1088/0953-4075/43/20/202001`.

[162] S. Alvarez. A cartography of the van der Waals territories. *Dalton Trans.*, 42(24): 8617–8636, 2013. URL `https://doi.org/10.1039/c3dt50599e`.

[163] B. Cordero, V. Gomez, A. E. Platero-Prats, M. Reves, J. Echeverria, E. Cremades, F. Barragan, and S. Alvarez. Covalent radii revisited. *Dalton Trans.*, -(21):2832–2838, 2008. URL `https://doi.org/10.1039/b801115j`.

[164] C. Callegari and W. E. Ernst. *Handbook of High-Resolution Spectroscopy*, chapter : Helium Droplets as Nanocryostats for Molecular Spectroscopy - from the Vacuum Ultraviolet to the Microwave Regime, pages 1551–1594. John Wiley & Sons, Chichester, 2011. URL `https://doi.org/10.1002/9780470749593`. eds. M. Quack and F. Merkt.

[165] D. R. Herrick. Connecting Pauling and Mulliken electronegativities. *J. Chem. Theory Comput.*, 1(2):255–260, March 2005. URL `https://doi.org/10.1021/ct049942a`.

[166] J. Deiglmayr, M. Aymar, R. Wester, M. Weidemüller, and O. Dulieu. Calculations of static dipole polarizabilities of alkali dimers: Prospects for alignment of ultracold molecules. *J. Chem. Phys.*, 129(6):064309, AUG 2008. ISSN 0021-9606. URL `https://doi.org/10.1063/1.2960624`.

[167] G. Gopakumar, M. Abe, M. Hada, and M. Kajita. Dipole polarizability of alkali-metal (Na, K, Rb) alkaline-earth-metal (Ca, Sr) polar molecules: Prospects for alignment. *J. Chem. Phys.*, 140(22):224303, 2014. URL `http://scitation.aip.org/content/aip/journal/jcp/140/22/10.1063/1.4881396`.

[168] G. H. F. Diercksen and A. J. Sadlej. Perturbation-theory of the Electron Correlation-effects For Atomic and Molecular-properties - 2nd-order and 3rd-order Correlation Corrections To Molecular Dipole-moments and Polarizabilities. *J. Chem. Phys.*, 75(3):1253–1266, 1981. URL `https://doi.org/10.1063/1.442175`.

[169] P. K. Mukherjee, T. Minato, and D. P. Chong. Finite-field Calculations of Molecular Polarizabilities Using Field-induced Polarization Functions .2. 2nd-order and 3rd-order Perturbation Correlation Corrections To the Coupled Hartree-fock Polarizability of Hf. *Int. J. Quant. Chem.*, 23(2):447–457, 1983. URL `https://doi.org/10.1002/qua.560230213`.

[170] I. V. Hertel and C.-P. Schulz. *Atome, Moleküle und optische Physik 1.* Springer-Verlag Berlin Heidelberg, 2008.

[171] T. Saue, L. Visscher, H. J. A. Jensen, and R. Bast. DIRAC, a relativistic ab initio electronic structure program. Release DIRAC14, 2014. URL `http://www.diracprogram.org`. with contributions from V. Bakken, K. G. Dyall, S. Dubillard, U. Ekström, E. Eliav, T. Enevoldsen, E. Faßhauer, T. Fleig, O. Fossgaard, A. S. P. Gomes, T. Helgaker, J. K. Lærdahl, Y. S. Lee, J. Henriksson, M. Iliaš, Ch. R. Jacob, S. Knecht, S. Komorovský, O. Kullie, C. V. Larsen,

H. S. Nataraj, P. Norman, G. Olejniczak, J. Olsen, Y. C. Park, J. K. Pedersen, M. Pernpointner, R. di Remigio, K. Ruud, P. Sałek, B. Schimmelpfennig, J. Sikkema, A. J. Thorvaldsen, J. Thyssen, J. van Stralen, S. Villaume, O. Visser, T. Winther, and S. Yamamoto.

[172] A. Wolf, M. Reiher, and B. A. Hess. The generalized Douglas-Kroll transformation. *J. Chem. Phys.*, 117(20):9215–9226, November 2002. URL `https://doi.org/10.1063/1.1515314`.

[173] M. Reiher and A. Wolf. Exact decoupling of the Dirac Hamiltonian. I. General theory. *J. Chem. Phys.*, 121(5):2037–2047, August 2004. URL `https://doi.org/10.1063/1.1768160`.

[174] M. Reiher and A. Wolf. Exact decoupling of the Dirac Hamiltonian. II. The generalized Douglas-Kroll-Hess transformation up to arbitrary order. *J. Chem. Phys.*, 121(22):10945–10956, December 2004. URL `https://doi.org/10.1063/1.1818681`.

[175] M. Reiher. Douglas–Kroll–Hess Theory: a relativistic electrons-only theory for chemistry. *Theor. Chem. Acc.*, 116(1):241–252, 2006. ISSN 1432-2234. URL `http://dx.doi.org/10.1007/s00214-005-0003-2`.

[176] Peter Schwerdtfeger, editor. *Relativistic Electronic Structure Theory - Part 1. Fundamentals*, volume 11 of *Theoretical and Compuational Chemistry*. Elsevier Science B.V., first edition, 2002.

[177] J. Autschbach. Perspective: Relativistic effects. *J. Chem. Phys.*, 136(15):150902, April 2012. URL `https://doi.org/10.1063/1.3702628`.

[178] H. Haken and H. C. Wolf. *Atom- und Quantenphysik*. Springer-Verlag Berlin Heidelberg, 1996.

[179] P. S. Zuchowski, R. Guerout, and O. Dulieu. Ground- and excited-state properties of the polar and paramagnetic RbSr molecule: A comparative study. *Phys. Rev. A*, 90(1):012507, July 2014. URL `https://doi.org/10.1103/PhysRevA.90.012507`.

[180] B. A. Hess, R. J. Buenker, and P. Chandra. Toward the Variational Treatment of Spin-orbit and Other Relativistic Effects For Heavy-atoms and Molecules. *Int. J. Quant. Chem.*, 29(4):737–753, April 1986. URL `https://doi.org/10.1002/qua.560290414`.

[181] A. Berning, M. Schweizer, H. J. Werner, P. J. Knowles, and P. Palmieri. Spin-orbit matrix elements for internally contracted multireference configuration interaction wavefunctions. *Mol. Phys.*, 98(21):1823–1833, November 2000. URL `https://doi.org/10.1080/00268970009483386`.

[182] M. D. Morse. Clusters of Transition-metal Atoms. *Chem. Rev.*, 86(6):1049–1109, December 1986. URL `https://doi.org/10.1021/cr00076a005`.

[183] J. A. Alonso. Electronic and atomic structure, and magnetism of transition-metal clusters. *Chem. Rev.*, 100(2):637–677, February 2000. URL `https://doi.org/10.1021/cr980391o`.

[184] F. Baletto and R. Ferrando. Structural properties of nanoclusters: Energetic, thermodynamic, and kinetic effects. *Rev. Mod. Phys.*, 77:371–423, May 2005. URL `http://link.aps.org/doi/10.1103/RevModPhys.77.371`.

[185] S. Hensler, A. Griesmaier, J. Werner, A. Gorlitz, and T. Pfau. A two species trap for chromium and rubidium atoms. *J. Mod. Opt.*, 51(12):1807–1816, August 2004. URL `https://doi.org/10.1080/09500340410001667590`.

[186] C. Kohl and G. F. Bertsch. Noncollinear magnetic ordering in small chromium clusters. *Phys. Rev. B*, 60:4205–4211, Aug 1999. URL `http://link.aps.org/doi/10.1103/PhysRevB.60.4205`.

[187] A. Proykova and D. Stauffer. Classical simulations of magnetic structures for chromium clusters: Size effects. *Cent. Eur. J. Phys.*, 3:209–220, 2005. URL `http://dx.doi.org/10.2478/BF02475588`. 10.2478/BF02475588.

[188] P. Ruiz-Díaz, J. L. Ricardo-Chávez, J. Dorantes-Dávila, and G. M. Pastor. Magnetism of small Cr clusters: Interplay between structure, magnetic order, and electron correlations. *Phys. Rev. B*, 81:224431, Jun 2010. URL `http://link.aps.org/doi/10.1103/PhysRevB.81.224431`.

[189] M. B. Knickelbein. Photoionization studies of chromium clusters: Ionization energies of Cr_4 to Cr_{25}. *Phys. Rev. A*, 67(1):013202 1–6, January 2003. URL `https://doi.org/10.1103/PhysRevA.67.013202`.

[190] F. W. Payne, W. Jiang, and L. A. Bloomfield. Magnetism and magnetic isomers in free chromium clusters. *Phys. Rev. Lett.*, 97(19):193401, November 2006. URL `https://doi.org/10.1103/PhysRevLett.97.193104`.

[191] M. Ratschek, M. Koch, and W. E. Ernst. Doping helium nanodroplets with high temperature metals: Formation of chromium clusters. *J. Chem. Phys.*, 136(10): 104201, March 2012. URL `https://doi.org/10.1063/1.3692330`.

[192] E. Fawcett. Spin-density-wave antiferromagnetism in chromium. *Rev. Mod. Phys.*, 60:209–283, Jan 1988. URL `http://link.aps.org/doi/10.1103/RevModPhys.60.209`.

[193] J. P. Toennies and A. F. Vilesov. Superfluid helium droplets: A uniquely cold nanomatrix for molecules and molecular complexes. *Angew. Chem. Int. Ed.*, 43 (20):2622–2648, 2004. URL `https://doi.org/10.1002/anie.200300611`.

[194] J. Nagl, G. Auboeck, A. W. Hauser, O. Allard, C. Callegari, and W. E. Ernst. High-spin alkali trimers on helium nanodroplets: Spectral separation and analysis.

J. Chem. Phys., 128(15), APR 21 2008. ISSN 0021-9606. URL `https://doi.org/10.1063/1.2906120`.

[195] J. Nagl, G. Auböck, A. W. Hauser, O. Allard, C. Callegari, and W. E. Ernst. Heteronuclear and homonuclear high-spin alkali trimers on helium nanodroplets. *Phys. Rev. Lett.*, 100:063001, 2008. URL `https://doi.org/10.1103/PhysRevLett.100.063001`.

[196] A. Przystawik, P. Radcliffe, S. G. Gode, K. H. Meiwes-Broer, and J. Tiggesbaumker. Spectroscopy of silver dimers in triplet states. *J. Phys. B*, 39(19):S1183–S1189, October 2006. URL `https://doi.org/10.1088/0953-4075/39/19/S25`.

[197] A. W. Hauser, C. Callegari, and W. E. Ernst. *Advances in the Theory of Atomic and Molecular Systems: Dynamics, Spectroscopy, Clusters and Nanostructures*, volume 20 of *Progress in Theoretical Chemistry and Physics*, chapter : Level-structure and magnetic properties from one-electron atoms to clusters with delocalized electronic orbitals: shell model for alkali trimers, pages 201–215. Springer Science+Business Media B.V., 2009. URL `https://doi.org/10.1007/978-90-481-2985-0`. eds. Piecuch, P. and Maruani, J. and Delgado-Barrio, G. and Wilson, S.

[198] M. Hartmann, J. P. Miller, R. E.and Toennies, and A. F. Vilesov. Rotationally Resolved Spectroscopy of SF_6 In Liquid-helium Clusters - A Molecular Probe of Cluster Temperature. *Phys. Rev. Lett.*, 75(8):1566–1569, August 1995. URL `https://doi.org/10.1103/PhysRevLett.75.1566`.

[199] J. Higgins, W. E. Ernst, C. Callegari, J. Reho, K. K. Lehmann, G. Scoles, and M. Gutowski. Spin Polarized Alkali Clusters: Observation of Quartet States of the Sodium Trimer. *Phys. Rev. Lett.*, 77(22):4532–4535, Nov 1996. URL `https://doi.org/10.1103/PhysRevLett.77.4532`.

[200] J. Higgins, C. Callegari, J. Reho, F. Stienkemeier, W. E. Ernst, K. K. Lehmann, M. Gutowski, and G. Scoles. Photoinduced chemical dynamics of high-spin alkali trimers. *Science*, 273:629, 1996. URL `https://doi.org/10.1126/science.273.5275.629`.

[201] H. Partridge and C. W. Bauschlicher. Theoretical-study of the Low-lying States of TiHe+, TiNe+, TiAr+, VAr+, CrHe+, CrAr+, FeHe+, FeAr+, CoHe+, and CoAr+. *J. Phys. Chem*, 98(9):2301–2306, March 1994. URL `https://doi.org/10.1021/j100060a016`.

[202] D. J. D. Wilson, C. J. Marsden, and E. I. von Nagy-Felsobuki. Ab initio structures and stabilities of HeTM3+ (TM = Sc-Cu). *Chem. Phys.*, 284(3):555–563, November 2002. URL `https://doi.org/10.1016/S0301-0104(02)00798-X`.

[203] D. J. D. Wilson, C. J. Marsden, and E. I. von Nagy-Felsobuki. Ab initio calculations on first row transition metal hydrides TMH_n+ and helides $TMHe_{n+1}+$

(TM = Sc-Cu, n=0-2) . *Phys. Chem. Chem. Phys.*, 5(2):252–258, 2003. URL `https://doi.org/10.1039/b208640a`.

[204] D. J. D. Wilson and E. I. von Nagy-Felsobuki. The electronic structure of transition metal dihelide dications. *Phys. Chem. Chem. Phys.*, 8(29):3399–3409, August 2006. URL `https://doi.org/10.1039/b606467a`.

[205] J. D. Weinstein, R. deCarvalho, C. I. Hancox, and J. M. Doyle. Evaporative cooling of atomic chromium. *Phys. Rev. A*, 65(2):021604, February 2002. URL `https://doi.org/10.1103/PhysRevA.65.021604`.

[206] E. J. Thomas, J. S. Murray, C. J. O'Connor, and P. Politzer. The Cr_2 molecule: some perspectives. *J. Mol. Struc. - Theochem*, 487(1-2):177–182, September 1999. URL `http://dx.doi.org/10.1016/S0166-1280(99)00152-9`.

[207] M. Brynda, L. Gagliardi, and B. O. Roos. Analysing the chromium-chromium multiple bonds using multiconfigurational quantum chemistry. *Chem. Phys. Lett.*, 471(1-3):1–10, March 2009. URL `https://doi.org/10.1016/j.cplett.2009.02.006`.

[208] K. Hongo and R. Maezono. A benchmark quantum Monte Carlo study of the ground state chromium dimer. *Int. J. Quant. Chem.*, 112(5):1243–1255, March 2012. URL `https://doi.org/10.1002/qua.23113`.

[209] F. Ruiperez, M. Piris, J. M. Ugalde, and J. M. Matxain. The natural orbital functional theory of the bonding in Cr_2, Mo_2 and W_2. *Phys. Chem. Chem. Phys.*, 15(6):2055–2062, 2013. URL `https://doi.org/10.1039/c2cp43559d`.

[210] K. Andersson. The electronic spectrum of Cr_2. *Chem. Phys. Lett.*, 237(3-4):212–221, May 1995. URL `https://doi.org/10.1016/0009-2614(95)00328-2`.

[211] F. Ruipérez, J. M. Ugalde, and I. Infante. Electronic Structure and Bonding in Heteronuclear Dimers of V, Cr, Mo, and W: a CASSCF/CASPT2 Study. *Inorg. Chem.*, 50(19):9219–9229, 2011. URL `https://doi.org/10.1021/ic200061h`.

[212] A. de Paz, A. Sharma, A. Chotia, E. Marechal, J. H. Huckans, P. Pedri, L. Santos, O. Gorceix, L. Vernac, and B. Laburthe-Tolra. Nonequilibrium Quantum Magnetism in a Dipolar Lattice Gas. *Phys. Rev. Lett.*, 111(18):185305, October 2013. URL `https://doi.org/10.1103/PhysRevLett.111.185305`.

[213] N. B. Balabanov and K. A. Peterson. Systematically convergent basis sets for transition metals. I. All-electron correlation consistent basis sets for the 3d elements Sc-Zn. *J. Chem. Phys.*, 123(6):064107, August 2005. URL `https://doi.org/10.1063/1.1998907`.

[214] D. E. Woon and T. H.. Dunning. Gaussian-basis Sets For Use In Correlated Molecular Calculations .4. Calculation of Static Electrical Response Properties.

J. Chem. Phys., 100(4):2975–2988, February 1994. URL `https://doi.org/10.1063/1.466439`.

[215] J. D. Watts, J. Gauss, and R. J. Bartlett. Coupled-cluster methods with noniterative triple excitations for restricted open-shell Hartree–Fock and other general single determinant reference functions. Energies and analytical gradients. *J. Chem. Phys.*, 98(11):8718–8733, June 1993. URL `http://dx.doi.org/10.1063/1.464480`.

[216] P. J. Knowles and H.-J. Werner. An efficient second order MCSCF method for long configuration expansions. *Chem. Phys. Letters*, 115:259–267, 1985. URL `http://dx.doi.org/10.1016/0009-2614(85)80025-7`.

[217] P. J. Knowles and H.-J. Werner. Internally Contracted Multiconfiguration Reference Configuration Interaction Calculations for Excited States. *Theor. Chem. Acc.*, 84:95–103, 1992. URL `https://doi.org/10.1007/BF01117405`.

[218] P. R. Kemper, M. T. Hsu, and M. T. Bowers. Transition-metal Ion Rare-gas Clusters - Bond Strengths and Molecular-parameters For Co+$(\mathrm{He/Ne})_n$, Ni+$(\mathrm{He/Ne})_n$, and Cr+$(\mathrm{He/Ne/Ar})_n$. *J. Phys. Chem.*, 95(26):10600–10609, December 1991. URL `https://doi.org/10.1021/j100179a022`.

[219] G. von Helden, P. R. Kemper, M. T. Hsu, and M. T. Bowers. Determination of Potential-energy Curves For Ground and Metastable Excited-state Transition-metal Ions Interacting With Helium and Neon Using Electronic State Chromatography. *J. Chem. Phys.*, 96(9):6591–6605, May 1992. URL `https://doi.org/10.1063/1.462598`.

[220] T. J. Lee and P. R. Taylor. A Diagnostic For Determining the Quality of Single-reference Electron Correlation Methods. *Int. J. Quant. Chem.*, 36:199–207, 1989. URL `https://doi.org/10.1002/qua.560360824`.

[221] C. L. Janssen and I. M. B. Nielsen. New diagnostics for coupled-cluster and Moller-Plesset perturbation theory. *Chem. Phys. Lett.*, 290(4-6):423–430, July 1998. URL `https://doi.org/10.1016/S0009-2614(98)00504-1`.

[222] D. Dell'Angelo, G. Guillon, and A. Viel. Excited Li and Na in He-n: Influence of the dimer potential energy curves. *J. Chem. Phys.*, 136(11):114308, March 2012. URL `https://doi.org/10.1063/1.3693766`.

[223] H. Boutarfa, K. Alioua, M. Bouledroua, A. R. Allouche, and M. Aubert-Frecon. Photoabsorption profile and satellite features of the potassium 4s -> 4p transition perturbed by ground-state helium atoms. *Phys. Rev. A*, 86(5):052504, November 2012. URL `https://doi.org/10.1103/PhysRevA.86.052504`.

[224] J. Pacale. Use of L-dependent Pseudopotentials In the Study of Alkali-metal-atom-He Systems - the Adiabatic Molecular Potentials. *Phys. Rev. A*, 28(2):632–644, 1983. URL `https://doi.org/10.1103/PhysRevA.28.632`.

[225] M. Mella, G. Calderoni, and F. Cargnoni. Predicting atomic dopant solvation in helium clusters: The MgHe_n case. *J. Chem. Phys.*, 123(5):054328, August 2005. URL `https://doi.org/10.1063/1.1982787`.

[226] E. Czuchaj, M. Krosnicki, and H. Stoll. Valence ab initio calculation of the potential energy curves for Ca-rare gas van der Waals molecules. *Chem. Phys.*, 292(1): 101–110, July 2003. URL `https://doi.org/10.1016/S0301-0104(03)00274-X`.

[227] F. Cargnoni and M. Mella. Solubility of Metal Atoms in Helium Droplets: Exploring the Effect of the Well Depth Using the Coinage Metals Cu and Ag. *J. Phys. Chem. A*, 115(25):7141–7152, June 2011. URL `https://doi.org/10.1021/jp112408d`.

[228] F. Cargnoni, T. Kus, M. Mella, and R. J. Bartlett. Ground state potential energy surfaces and bound states of M-He dimers (M=Cu,Ag,Au): A theoretical investigation. *J. Chem. Phys.*, 129(20):204307, November 2008. URL `https://doi.org/10.1063/1.3020706`.

[229] S. M. Younger, J. R. Fuhr, G. A. Martin, and W. L. Wiese. Atomic Transition-probabilities For Vanadium, Chromium, and Manganese - Critical Data Compilation of Allowed Lines. *J. Phys. Chem. Ref. Data*, 7(2):495–629, 1978. URL `http://dx.doi.org/10.1063/1.555576`.

[230] M. J. Pellin, D. M. Gruen, T. Fisher, and T. Foosnaes. Emission, Optical-optical Double-resonance, and Excited-state Absorption-spectroscopy of Matrix-isolated Chromium and Molybdenum Atoms. *J. Phys. Chem.*, 79(12):5871–5886, 1983. URL `https://doi.org/10.1063/1.445757`.

[231] F. Ancilotto, P. B. Lerner, and M. W. Cole. Physics of solvation. *J. Low Temp. Phys.*, 101(5-6):1123–1146, December 1995. URL `https://doi.org/10.1007/BF00754527`.

[232] H. L. Alberts and E. S. Fisher. Note On the Pressure-dependence of the Spin-flip Transition In Chromium. *Phys. Status Solidi B*, 98(1):K21–K24, 1980. URL `https://doi.org/10.1002/pssb.2220980147`.

[233] R. L. Stillwell, D. E. Graf, W. A. Coniglio, T. P. Murphy, E. C. Palm, J. H. Park, D. VanGennep, P. Schlottmann, and S. W. Tozer. Pressure-driven Fermi surface reconstruction of chromium. *Phys. Rev. B*, 88(12):125119, September 2013. URL `https://doi.org/10.1103/PhysRevB.88.125119`.

[234] R. Soulairol, C. C. Fu, and C. Barreteau. Structure and magnetism of bulk Fe and Cr: from plane waves to LCAO methods. *J. Phys. Condens. Matter*, 22(29): 295502, July 2010. URL `https://doi.org/10.1088/0953-8984/22/29/295502`.

[235] F. Dalfovo, A. Lastri, L. Pricaupenko, S. Stringari, and J. Treiner. Structural and Dynamical Properties of Superfluid-helium - A Density-functional Approach. *Phys.*

Rev. B, 52(2):1193–1209, July 1995. URL `https://doi.org/10.1103/PhysRevB.52.1193`.

[236] C. Callegari, K. K. Lehmann, R. Schmied, and G. Scoles. Helium nanodroplet isolation rovibrational spectroscopy: Methods and recent results. *J. Chem. Phys.*, 115 (22):10090–10110, December 2001. URL `https://doi.org/10.1063/1.1418746`.

[237] K. K. Lehmann and C. Callegari. Quantum hydrodynamic model for the enhanced moments of inertia of molecules in helium nanodroplets: Application to SF_6. *J. Chem. Phys.*, 117(4):1595–1603, July 2002. URL `https://doi.org/10.1063/1.1486443`.

[238] S. Giorgini, L. P. Pitaevskii, and S. Stringari. Theory of ultracold atomic Fermi gases. *Rev. Mod. Phys.*, 80(4):1215–1274, October 2008. URL `https://doi.org/10.1103/RevModPhys.80.1215`.

[239] M. Aymar and O. Dulieu. Calculations of transition and permanent dipole moments of heteronuclear alkali dimers NaK, NaRb and NaCs. *Mol. Phys.*, 105 (11-12):1733–1742, 2007. URL `https://doi.org/10.1080/00268970701494016`.

[240] P. S. Zuchowski, J. Aldegunde, and J. M. Hutson. Ultracold RbSr Molecules Can Be Formed by Magnetoassociation. *Phys. Rev. Lett.*, 105(15):153201, October 2010. URL `https://doi.org/10.1103/PhysRevLett.105.153201`.

[241] T. Chen, S. B. Zhu, X. L. Li, J. Qian, and Y. Z. Wang. Prospects for transferring ^{87}Rb^{84}Sr dimers to the rovibrational ground state based on calculated molecular structures. *Phys. Rev. A*, 89(6):063402, June 2014. URL `https://doi.org/10.1103/PhysRevA.89.063402`.

[242] M. Tomza, F. Pawlowski, M. Jeziorska, C. P. Koch, and R. Moszynski. Formation of ultracold SrYb molecules in an optical lattice by photoassociation spectroscopy: theoretical prospects. *Phys. Chem. Chem. Phys.*, 13(42):18893–18904, 2011. URL `https://doi.org/10.1039/c1cp21196j`.

[243] I. S. Lim, P. Schwerdtfeger, B. Metz, and H. Stoll. All-electron and relativistic pseudopotential studies for the group 1 element polarizabilities from K to element 119. *J. Chem. Phys.*, 122(10):104103, March 2005. URL `https://doi.org/10.1063/1.185451`.

[244] I. S. Lim, H. Stoll, and P. Schwerdtfeger. Relativistic small-core energy-consistent pseudopotentials for the alkaline-earth elements from Ca to Ra. *J. Chem. Phys.*, 124(3):034107, January 2006. URL `https://doi.org/10.1063/1.2148945`.

[245] A. Nicklass, K. A. Peterson, A. Berning, H. J. Werner, and P. J. Knowles. Convergence of Breit-Pauli spin-orbit matrix elements with basis set size and configuration interaction space: The halogen atoms F, Cl, and Br. *J. Chem. Phys.*, 112 (13):5624–5632, April 2000. URL `https://doi.org/10.1063/1.481137`.

[246] S. Ghosal, R. J. Doyle, C. P. Koch, and J. M. Hutson. Stimulating the production of deeply bound RbCs molecules with laser pulses: the role of spin-orbit coupling in forming ultracold molecules. *New J. Phys.*, 11:055011, May 2009. doi: 10.1088/1367-2630/11/5/055011. URL `https://doi.org/10.1088/1367-2630/11/5/055011`.

[247] M. L. Gonzalez-Martinez and J. M. Hutson. Magnetically tunable Feshbach resonances in Li + Yb(^{3}P$_J$). *Phys. Rev. A*, 88(2):020701, August 2013. URL `https://doi.org/10.1103/PhysRevA.88.020701`.

[248] M. Borkowski, P. S. Zuchowski, R. Ciurylo, P. S. Julienne, D. Kedziera, L. Mentel, P. Tecmer, F. Munchow, C. Bruni, and A. Gorlitz. Scattering lengths in isotopologues of the RbYb system. *Phys. Rev. A*, 88(5):052708, November 2013. URL `https://doi.org/10.1103/PhysRevA.88.052708`.

[249] D. A. Brue and J. M. Hutson. Prospects of forming ultracold molecules in $^2\Sigma$ states by magnetoassociation of alkali-metal atoms with Yb. *Phys. Rev. A*, 87(5):052709, May 2013. URL `https://doi.org/10.1103/PhysRevA.87.052709`.

[250] M. Kajita, G. Gopakumar, M. Abe, and M. Hada. Elimination of the Stark shift from the vibrational transition frequency of optically trapped ^{174}Yb^{6}Li molecules. *Phys. Rev. A*, 84(2):022507, August 2011. URL `https://doi.org/10.1103/PhysRevA.84.022507`.

[251] G. Gopakumar, M. Abe, B. P. Das, M. Hada, and K. Hirao. Relativistic calculations of ground and excited states of LiYb molecule for ultracold photoassociation spectroscopy studies. *J. Chem. Phys.*, 133(12):124317, September 2010. URL `https://doi.org/10.1063/1.3475568`.

[252] F. Baumer, F. Munchow, A. Gorlitz, S. E. Maxwell, P. S. Julienne, and E. Tiesinga. Spatial separation in a thermal mixture of ultracold ^{174}Yb and ^{87}Rb atoms. *Phys. Rev. A*, 83(4):040702, April 2011. URL `https://doi.org/10.1103/PhysRevA.83.040702`.

[253] F. Munchow, C. Bruni, M. Madalinski, and A. Gorlitz. Two-photon photoassociation spectroscopy of heteronuclear YbRb. *Phys. Chem. Chem. Phys.*, 13(42):18734–18737, 2011. URL `https://doi.org/10.1039/c1cp21219b`.

[254] W. E. Ernst, J. Kändler, S. Kindt, and T. Torring. Electric-dipole Moment of SrF X $^2\Sigma^+$ from High-precision Stark-effect Measurements. *Chem. Phys. Lett.*, 113(4):351–354, 1985. URL `https://doi.org/10.1016/0009-2614(85)80379-1`.

[255] W. E. Ernst and J. Kändler. Different Polarization of the A $^2\Pi$ and C $^2\Pi$ State Wave-functions In CaF Observed By Visible and Uv Stark Spectroscopy. *Phys. Rev. A*, 39(3):1575–1578, February 1989. URL `https://doi.org/10.1103/PhysRevA.39.1575`.

[256] Y. Huang, J. Qi, H. K. Pechkis, D. Wang, E. E. Eyler, P. L. Gould, and W. C. Stwalley. Formation, detection and spectroscopy of ultracold Rb_2 in the ground $X^1\Sigma^+$ state. *J. Phys. B*, 39(19):S857–S869, October 2006. URL `https://doi.org/10.1088/0953-4075/39/19/S04`.

[257] S. Kotochigova, A. Petrov, M. Linnik, J. Klos, and P. S. Julienne. Ab initio properties of Li-group-II molecules for ultracold matter studies. *J. Chem. Phys.*, 135(16):164108, October 2011. URL `https://doi.org/10.1063/1.3653974`.

[258] L. Augustovičová and P. Soldán. Ab initio properties of MgAlk (Alk = Li, Na, K, Rb, Cs). *J. Chem. Phys.*, 136(8):084311, February 2012. URL `https://doi.org/10.1063/1.3690459`.

[259] G. Gopakumar, M. Abe, M. Hada, and M. Kajita. Magnetic-field effects in transitions of X Li molecules (X: even isotopes of group II atoms). *Phys. Rev. A*, 84(4): 045401, October 2011. URL `https://doi.org/10.1103/PhysRevA.84.045401`.

[260] G. Gopakumar, M. Abe, M. Kajita, and M. Hada. Ab initio study of permanent electric dipole moment and radiative lifetimes of alkaline-earth-metal-Li molecules. *Phys. Rev. A*, 84(6):062514, December 2011. URL `https://doi.org/10.1103/PhysRevA.84.062514`.

[261] R. Stringat, G. Fabre, A. Boulezhar, J. D'Incan, C. Effantin, J. Vérges, and A. Bernard. The $X^2\Sigma^+$, (2) $^2\Sigma^+$, and $(2)^2\Pi$ States of BaLi. *J. Mol. Spectrosc.*, 168 (2):514–521, December 1994. URL `https://doi.org/10.1006/jmsp.1994.1298`.

[262] J. D'Incan, C. Effantin, A. Bernard, G. Fabre, R. Stringat, A. Boulezhar, and J. Vérges. Electronic-structure of BaLi .2. First Observation of the $Ba^{6,7}Li$ Spectrum - Analysis of the $2^2\Pi$-$X^2\Sigma^+$ System. *J. Chem. Phys.*, 100(2):945–949, January 1994. URL `https://doi.org/10.1063/1.466576`.

[263] J. Vérges, J. D'Incan, C. Effantin, A. Bernard, G. Fabre, R. Stringat, and A. Boulzhar. Electronic-structure of BaLi - the $(2)^2\Sigma^+$State. *J. Phys. B*, 27(8): L153–L155, April 1994. URL `https://doi.org/10.1088/0953-4075/27/8/004`.

[264] K. R. Berry and M. A. Duncan. Photoionization spectroscopy of LiMg. *Chem. Phys. Lett.*, 279(1-2):44–49, November 1997. URL `https://doi.org/10.1016/S0009-2614(97)00991-3`.

[265] A. R. Allouche and M. Aubert-Frécon. Electronic-structure of BaLi .1. Theoretical-study. *J. Chem. Phys.*, 100(2):938–944, January 1994. URL `https://doi.org/10.1063/1.466575`.

[266] L. M. Russon, G. K. Rothschopf, M. D. Morse, A. I. Boldyrev, and J. Simons. Two-photon ionization spectroscopy and all-electron ab initio study of LiCa. *J. Chem. Phys.*, 109(16):6655–6665, October 1998. URL `https://doi.org/10.1063/1.477317`.

[267] A. R. Allouche and M. Aubert-Frécon. Theoretical-study of the Low-lying Electronic States of the CaLi Molecule. *Chem. Phys. Lett.*, 222(5):524–528, May 1994. URL `https://doi.org/10.1016/0009-2614(94)00371-8`.

[268] Geetha Gopakumar, Minori Abe, Masahiko Hada, and Masatoshi Kajita. Ab initio study of ground and excited states of ^{6}Li^{40}Ca and ^{6}Li^{88}Sr molecules. *J. Chem. Phys.*, 138(19):194307–14, May 2013. URL `http://dx.doi.org/10.1063/1.4804622`.

[269] Takatoshi Aoki, Yuki Yamanaka, Makoto Takeuchi, Yoshio Torii, and Yasuhiro Sakemi. Photoionization loss in simultaneous magneto-optical trapping of Rb and Sr. *Phys. Rev. A*, 87:063426, Jun 2013. URL `http://link.aps.org/doi/10.1103/PhysRevA.87.063426`.

[270] F. H. J. Hall, M. Aymar, N. Bouloufa-Maafa, O. Dulieu, and S. Willitsch. Light-assisted ion-neutral reactive processes in the cold regime: Radiative molecule formation versus charge exchange. *Phys. Rev. Lett.*, 107(24):243202, December 2011. URL `https://doi.org/10.1103/PhysRevLett.107.243202`.

[271] M. Tacconi, F. A. Gianturco, and A. K. Belyaev. Computing charge-exchange cross sections for Ca+ collisions with Rb at low and ultralow energies. *Phys. Chem. Chem. Phys.*, 13(42):19156–19164, 2011. URL `https://doi.org/10.1039/c1cp20916g`.

[272] A. K. Belyaev, S. A. Yakovleva, M. Tacconi, and F. A. Gianturco. Resonances in Ca^{+} + Rb nonadiabatic collisions at ultralow energies. *Phys. Rev. A*, 85(4):042716, April 2012. URL `https://doi.org/10.1103/PhysRevA.85.042716`.

[273] April 27, 2000. vol. 104, number 16. *J. Phys. Chem. A*, , vol. 104, number 16, 2000.

[274] M. E. Jacox. On Walking in the Footprints of Giants. *Annu. Rev. Phys. Chem.*, 61:1–18, 2010. URL `https://doi.org/10.1146/annurev.physchem.012809.103439`.

[275] F. Stienkemeier, J. Higgins, W. E. Ernst, and G. Scoles. Laser Spectroscopy of Alkali-doped Helium Clusters. *Phys. Rev. Lett.*, 74(18):3592–3595, May 1995. URL `https://doi.org/10.1103/PhysRevLett.74.3592`.

[276] G. Scoles and K. K. Lehmann. Molecular spectroscopy - Nanomatrices are cool. *Science*, 287(5462):2429–2430, March 2000. URL `https://doi.org/10.1126/science.287.5462.2429`.

[277] F. Stienkemeier, J. Higgins, C. Callegari, S. I. Kanorsky, W. E. ERnst, and G. Scoles. Spectroscopy of alkali atoms (Li, Na, K) attached to large helium clusters. *Z. Phys. D*, 38(3):253–263, October 1996.

[278] F. R. Brühl, R. A. Trasca, and W. E. Ernst. Rb-He exciplex formation on helium nanodroplets. *J. Chem. Phys.*, 115(22):10220–10224, December 2001. URL `http://dx.doi.org/10.1063/1.1410118`.

[279] O. Bünermann, M. Mudrich, M. Weidemüller, and F. Stienkemeier. Spectroscopy of Cs attached to helium nanodroplets. *J. Chem. Phys.*, 121(18):8880–8886, November 2004. URL `https://doi.org/10.1063/1.1805508`.

[280] O. Bünermann, M. Dvorak, F. Stienkemeier, A. Hernando, R. Mayol, M. Pi, M. Barranco, and F. Ancilotto. Calcium atoms attached to mixed helium droplets: A probe for the ^{3}He-^{4}He interface. *Phys. Rev. B*, 79(21):214511, June 2009. URL `https://doi.org/10.1103/PhysRevB.79.214511`.

[281] J. Higgins, C. Callegari, J. Reho, F. Stienkemeier, W. E. Ernst, M. Gutowski, and G. Scoles. Helium cluster isolation spectroscopy of alkali dimers in the triplet manifold. *J. Phys. Chem. A*, 102(26):4952–4965, June 1998. URL `https://doi.org/10.1021/jp981115g`.

[282] J. Allard, O.and Nagl, G. Auböck, C. Callegari, and W. E. Ernst. Investigation of KRb and Rb_2 Formed on Cold Helium Nanodroplets. *J. Phys. Chem. B*, 39(19): 1169, 2006. URL `https://doi.org/10.1088/0953-4075/39/19/S24`.

[283] A. W. Hauser, G. Auböck, and W. E. Ernst. *Vibronic Interactions and the Jahn-Teller Effect: Theory and Applications*, volume 23 of *Progress in Theoretical Chemistry and Physics*, chapter : Jahn-Teller Effect and Spin-Orbit Coupling in Heavy Alkali Trimers, pages 301–316. Springer Science+Business Media B.V., 2012. URL `https://doi.org/10.1007/978-94-007-2384-9`. eds. Atanasov, M. and Daul, C. and Tregenna-Piggot, P.

[284] J. Koput and K. A. Peterson. Ab initio potential energy surface and vibrational-rotational energy levels of X $^2\Sigma^+$ CaOH. *J. Phys. Chem. A*, 106(41):9595–9599, October 2002. URL `https://doi.org/10.1021/jp026283u`.

[285] J. Nagl, A. W. Hauser, G. Auböck, C. Callegari, and W. E. Ernst. Optical Spectroscopy of Potassium-Doped Argon Clusters. Experiments and Quantum-Chemistry Calculations. *J. Phys. Chem. A*, 111(49):12386–12397, December 2007. URL `https://doi.org/10.1021/jp075951e`.

[286] F. Lackner, G. Krois, M. Theisen, M. Koch, and W. E. Ernst. Spectroscopy of nS, nP, and nD Rydberg Series of Cs Atoms on Helium Nanodroplets. *Phys. Chem. Chem. Phys.*, 13:18781–18788, 2011. URL `https://doi.org/10.1039/C1CP21280J`.

[287] M. Lewerenz, B. Schilling, and J. P. Toennies. Successive Capture and Coagulation of Atoms and Molecules To Small Clusters In Large Liquid-helium Clusters. *J. Chem. Phys.*, 102(20):8191–8207, May 1995. URL `https://doi.org/10.1063/1.469231`.

[288] M. Theisen, F. Lackner, and W. E. Ernst. Cs atoms on helium nanodroplets and the immersion of Cs(+) into the nanodroplet. *J. Chem. Phys.*, 135(7):074306, August 2011. URL `https://doi.org/10.1063/1.3624840`.

[289] E. Loginov, D. Rossi, and M. Drabbels. Photoelectron Spectroscopy of Doped Helium Nanodroplets. *Phys. Rev. Lett.*, 95(16):163401, October 2005. URL `https://doi.org/10.1103/PhysRevLett.95.163401`.

[290] J. L. Persson, Q. Hui, M. Nakamura, and M. Takami. Optical-spectra of Metal Dimers and Trimers In Superfluid-helium. *Phys. Rev. A*, 52(3):2011–2015, September 1995. URL `https://doi.org/10.1103/PhysRevA.52.2011`.

[291] M. Theisen, F. Lackner, F. Ancilotto, C. Callegari, and W. E. Ernst. Two-step excitation of Rb atoms on He nanodroplets. *EPJ D*, 61(2):403–408, January 2011. URL `https://doi.org/10.1140/epjd/e2010-10504-5`.

[292] F. Lackner, G. Krois, and W. E. Ernst. Rydberg-Ritz analysis and quantum defects for Rb and Cs atoms on helium nanodroplets. *Mol. Phys.*, 111(14-15):2118–2125, August 2013. URL `https://doi.org/10.1080/00268976.2013.788792`.

[293] F. Lackner, G. Krois, M. Koch, and W. E. Ernst. Rubidium on Helium Droplets: Analysis of an Exotic Rydberg Complex for n* $<$ 20 and 0 $<=$ l $<=$ 3. *J. Phys. Chem. Lett.*, 3(10):1404–1408, May 2012. URL `https://doi.org/10.1021/jz300381y`.

[294] L. Fechner, B. Gruner, A. Sieg, C. Callegari, F. Ancilotto, F. Stienkemeier, and M. Mudrich. Photoionization and imaging spectroscopy of rubidium atoms attached to helium nanodroplets. *Phys. Chem. Chem. Phys.*, 14(11):3843–3851, 2012. URL `https://doi.org/10.1039/c2cp22749e`.

[295] A. Pifrader, O. Allard, G. Aubock, C. Callegari, W. E. Ernst, R. Huber, and F. Ancilotto. One- and two-photon spectroscopy of highly excited states of alkali-metal atoms on helium nanodroplets. *J. Chem. Phys.*, 133(16):164502, October 2010. URL `https://doi.org/10.1063/1.3500397`.

[296] F. Lackner. *Rydberg States of Alkali-Metal Atoms on Superfluid Helium Nanodroplets.* Doctoral Thesis, Graz Universtiy of Technology, 2012.

[297] M. Theisen, F. Lackner, and W. E. Ernst. Forming Rb(+) snowballs in the center of He nanodroplets. *Phys. Chem. Chem. Phys.*, 12(45):14861–14863, 2010. URL `https://doi.org/10.1039/c0cp01283a`.

[298] T. Törring, W. E. Ernst, and S. Kindt. Dipole moments and potential energies of alkline earth monhalides from an ionic model. *J. Chem. Phys.*, 81(10):4614–4619, 1984. URL `https://doi.org/10.1063/1.447394`.

[299] T. Törring, W. E. Ernst, and J. Kändler. Energies and Electric-dipole Moments of the Low-lying Electronic States of the Alkaline-earth Monohalides From An Electrostatic Polarization Model. *J. Chem. Phys.*, 90(9):4927–4932, May 1989. URL `https://doi.org/10.1063/1.456589`.

[300] S. F. Rice, H. Martin, and R. W. Field. The Electronic-structure of the Calcium Monohalides - A Ligand-field Approach. *J. Chem. Phys.*, 82(11):5023–5034, 1985. URL `https://doi.org/10.1063/1.448676`.

[301] R. W. Field, D. P. Baldwin, E. J. Hill, M. G. Li, and M. C. McCarthy. Spectroscopy beyond molecular-constants. *Spectrochimica Acta*, 45A:75–89, 1989. URL `https://doi.org/10.1016/S0584-8539(89)80090-X`. (special supplement).

[302] D. P. Baldwin, E. J. Hill, and R. W. Field. Electron-affinity of O- and Diabatic CaO(g) Integer Charge Potential Curves. *J. Am. Chem. Soc.*, 112(25):9156–9161, December 1990. URL `https://doi.org/10.1021/ja00181a019`.

[303] R. F. W. Herrmann, G. K. Sumnicht, M. Stein, and W. Ernst. The Orange Band System of SrO - 1st Details about the Triplet Transitions. *J. Mol. Spectrosc.*, 156 (2):487–500, December 1992. URL `https://doi.org/10.1016/0022-2852(92)90248-M`.

[304] S. Kotochigova. Prospects for making polar molecules with microwave fields. *Phys. Rev. Lett.*, 99(7):073003, August 2007. URL `https://doi.org/10.1103/PhysRevLett.99.073003`.

[305] E. S. Rittner. Binding Energy and Dipole Moment of Alkali Halide Molecules. *J. Chem. Phys.*, 19(8):1030–1035, 1951. URL `https://doi.org/10.1063/1.1748448`.

[306] P. Brumer and M. Karplus. Perturbation-theory and Ionic Models For Alkali-Halide Systems .1. Diatomics. *J. Chem. Phys.*, 58(9):3903–3918, 1973. URL `https://doi.org/10.1063/1.1679747`.

[307] R. L. Matcha and S. C. King. Theory of Chemical Bond .2. Dipole-moments of Alkali-halide Molecules, Bond Polarity, and Differential Charge Affinity. *J. Am. Chem. Soc.*, 98(12):3420–3432, 1976. URL `https://doi.org/10.1021/ja00428a005`.

[308] J. Schamps, M. Bencheikh, J. C. Barthelat, and R. W. Field. The Electronic-structure of LaO - Ligand-field Versus Ab-initio Calculations. *J. Chem. Phys.*, 103(18):8004–8013, November 1995. URL `https://doi.org/10.1063/1.470219`.

[309] H. Schall, M. Dulick, and R. W. Field. The Electronic-structure of LaF - A Multiconfiguration Ligand-field Calculation. *J. Chem. Phys.*, 87(5):2898–2912, September 1987. URL `https://doi.org/10.1063/1.453078`.

[310] W. E. Ernst and J. O. Schröder. Polarization Spectroscopy of ^{79}SrBr and ^{81}SrBr - Analysis of the $X^2\Sigma^+$ and $B^2\Sigma^+$ Hyperfine-structure. *Z. Phys. D*, 1(1):103–112, 1986. URL `https://doi.org/10.1007/BF01384664`.

[311] S. Hou and P. F. Bernath. Relationship between Dipole Moments and Harmonic Vibrational Frequencies in Diatomic Molecules. *J. Phys. Chem. A*, 119(8):1435–8, February 2015. URL `https://doi.org/10.1021/acs.jpca.5b00993`.

[312] C. W. Bauschlicher, S. R. Langhoff, and H. Partridge. Theoretical-study of the BeLi, BeNa, MgLi, MgNa, and AlBe molecules and their negative-Ions. *J. Chem. Phys*, 96(2):1240–1247, January 1992. URL `https://doi.org/10.1063/1.462160`.

[313] M. Aymar, R. Guerout, and O. Dulieu. Structure of the alkali-metal-atom plus strontium molecular ions: Towards photoassociation and formation of cold molecular ions. *J. Chem. Phys.*, 135(6):064305, August 2011. URL `https://doi.org/10.1063/1.3611399`.

[314] D. Z. Gou, X. Y. Kuang, Y. F. Gao, and D. M. Huo. Theoretical study on the ground state of the polar alkali-metal-barium molecules: Potential energy curve and permanent dipole moment. *J. Chem. Phys.*, 142(3):034308, January 2015. URL `https://doi.org/10.1063/1.4906049`.

[315] N. Boutassetta, A. R. Allouche, and M. Aubert-Frécon. Theoretical-study of the Low-lying Electronic States of the BaNa Molecule. *Chem. Phys.*, 189(1):33–39, November 1994. URL `https://doi.org/10.1016/0301-0104(94)80005-7`.

[316] C. H. Wu, H. R. Ihle, and K. A. Gingerich. A Mass-spectrometric Study of the Alkaline-earth Diatomic-molecules - Dissociation-energies of Mg_2, Ca_2 and CaLi. *Int. J. Mass Spectrom.*, 47(JAN):235–238, 1983. URL `https://doi.org/10.1016/0020-7381(83)87178-2`.

[317] S. Knecht, L. K. Sorensen, H. J. A. Jensen, T. Fleig, and C. M. Marian. Accurate calculations of the ground state and low-lying excited states of the RbBa+ molecular ion: a proposed system for ultracold reactive collisions. *J. Phys. B*, 43(5): 055101, March 2010. URL `https://doi.org/10.1088/0953-4075/43/5/055101`.

[318] Y. F. Gao and T. Gao. Ab initio study of ground and low-lying excited states of MgLi and MgLi+ molecules with valence full configuration interaction and MRCI method. *Mol. Phys.*, 112(23):3015–3023, December 2014. URL `https://doi.org/10.1080/00268976.2014.926030`.

[319] B. P. Prascher, D. E. Woon, K. A. Peterson, T. H. Dunning, and A. K. Wilson. Gaussian basis sets for use in correlated molecular calculations. VII. Valence, core-valence, and scalar relativistic basis sets for Li, Be, Na, and Mg. *Theor. Chem. Acc.*, 128(1):69–82, January 2011. URL `http://tyr0.chem.wsu.edu/~kipeters/basis.html`.

[320] H. D. Li, H. Feng, W. G. Sun, Y. Zhang, Q. C. Fan, K. A. Peterson, Y. M. Xie, and H. F. Schaefer. The alkaline earth dimer cations (Be_2+, Mg_2+, Ca_2+, Sr_2+, and Ba_2+). Coupled cluster and full configuration interaction studies. *Mol. Phys.*, 111(14-15):2292–2298, August 2013. URL `https://doi.org/10.1080/00268976.2013.802818`.

[321] D. A. Fedorov, A. Derevianko, and S. A. Varganov. Accurate potential energy, dipole moment curves, and lifetimes of vibrational states of heteronuclear alkali dimers. *J. Chem. Phys.*, 140(18):184315, MAY 14 2014. ISSN 0021-9606. URL `https://doi.org/10.1063/1.4875038`.

[322] R. Schlachta, I. Fischer, P. Rosmus, and V. E. Bondybey. The Simplest Heteronuclear Metal Cluster - LiBe. *Chem. Phys. Lett.*, 170(5-6):485–491, July 1990. URL `https://doi.org/10.1016/S0009-2614(90)87089-A`.

[323] D. C. Ghosh and T. Chakraborty. Computation of the dipole moments of some heteronuclear diatomic molecules in terms of the revised electronegativity scale of Gordy. *J. Mol. Struc. - Theochem*, 916(1-3):47–52, December 2009. URL `https://doi.org/10.1016/j.theochem.2009.09.009`.

[324] S. Hou. Relations between harmonic frequencies of diatomic molecules. *Phys. Chem. Chem. Phys.*, 15(4):1154–63, 2013. URL `https://doi.org/10.1039/c2cp43630b`.

[325] S. L. Hou and P. F. Bernath. Relationships between dipole moments of diatomic molecules. *Phys. Chem. Chem. Phys.*, 17(6):4708–4713, 2015. URL `https://doi.org/10.1039/c4cp05255b`.